Motion gating for x-ray guided interventional electrophysiology procedures

Panayiotou, Maria

Awarding institution:
King's College London

King's College London

Doctoral Thesis

Motion gating for X-ray guided interventional electrophysiology procedures

Author:
Maria PANAYIOTOU

Supervisor:
Kawal S. RHODE, Ph.D.
Andrew P. KING, Ph.D.

A thesis submitted in fulfilment of the requirements
for the degree of Doctor of Phylosophy
in the

Division of Imaging Sciences & Biomedical Engineering
School of Medicine

January 2015

"Imagination is more important than knowledge. Knowledge is limited. Imagination encircles the world."

Albert Einstein

Abstract

Atrial fibrillation (AF) is a common supraventricular arrhythmia, characterized by irregular and uncoordinated contraction of the atrium. Although AF itself is not lethal, it accounts for secondary diseases and morbidity and mortality. The minimally-invasive radiofrequency ablation (RFA) procedure is a commonly performed treatment option for AF, guided by X-ray fluoroscopy. While it provides high temporal and spatial resolution, X-ray fluoroscopy has poor soft-tissue contrast. In order to enhance image guidance, volumetric roadmaps overlaid on live X-ray fluoroscopy may be used. However, these roadmaps are often static and do not reflect cardiorespiratory motion. Real-time roadmap update is important to compensate for this motion and maintain the accuracy of the guidance information, thereby allowing accurate determination of catheter-based ablation treatment sites. Motion gating is crucial for achieving this accuracy. Four novel and clinically applicable robust-to-noise motion gating techniques are developed and presented in this thesis.

The first proposed technique, Tracked-principal component analysis (PCA), is based on the formation of a novel statistical model of the motion of a coronary sinus (CS) catheter using PCA of tracked electrode locations from monoplane X-ray fluoroscopy images. Motion gating was later further extended to be applicable to more types of minimally invasive procedures, such as Cardiac resynchronisation therapy, where the CS catheter is not present in the X-ray images. This is achieved by the development of two robust to varying image-content techniques, the hierarchical manifold learning based and the Masked-PCA techniques. To avoid the limitation of the requirement to build a separate model for each X-ray view, an X-ray system View-angle independent technique was developed based on learning CS catheter motion using PCA and then applying the derived motion model to unseen images taken at arbitrary projections.

Applications of the motion gating techniques spanning from basic research to clinical tasks are demonstrated. These include catheter reconstruction in 3D from catheter tracking in gated sequential biplane X-ray images that can effectively achieve 2D/3D registration of 3D cardiac data (CT or MRI) to X-ray fluoroscopy; motion gating of 3D rotational X-ray angiography sequences where the angulation of the scanner is changed between frames; and motion compensation on unseen images taken at any arbitrary projection, by integrating cardiorespiratory motion into MRI-derived roadmaps fused with live X-ray fluoroscopy. This thesis is devoted to the development of robust-to-noise motion gating techniques and their use for improved procedure guidance while at the same time minimising patient and staff exposure to radiation, by allowing the use of lower-dose fluoroscopy. Results indicate that, within the constraints of acceptable accuracy, the achievable dose reduction factor is $\frac{1}{25}$ for the HML-based and Masked-PCA techniques, indicating a dose reduction of more than 25 times, between $\frac{1}{10}$ and $\frac{1}{25}$ for the Tracked-PCA technique and around $\frac{1}{10}$ for the View-angle independent technique.

Acknowledgements

I would like to express my deepest gratitude to my supervisors, Kawal Rhode and Andy King. They have been perfect mentors, constantly guiding and supporting me during these years, and teaching me, besides most of the technical aspects, how to be a good scientist. I enjoyed their availability and spontaneity as well as the freedom they allowed in the project. All these created a nice and productive working environment, which I hope they enjoyed as well. I am very thankful to Kawal for the opportunity to continue our collaboration in the future.

During these three years in the department of Imaging Sciences and Biomedical Engineering, I have expanded and deepened my knowledge about medical imaging, image acquisition and image processing and for this I have to thank James Housden, Yingliang Ma, Kanwal Bhatia and Rashed Karim who helped me in this learning process, sharing their knowledge and experience. I am very thankful to the clinical fellows and radiographers in the department for their precious help and very useful opinions.

I would like to give a special thanks to James Housden, for his valuable help and support throughout these three years, useful and essential advices, and especially for his constant presence and never ending patience.

I would like to acknowledge the Department of Health via the National Institute for Health Research (NIHR) comprehensive Biomedical Research Centre award to Guy's & St Thomas' NHS Foundation Trust in partnership with King's College London and King's College Hospital NHS Foundation Trust, for the financial support of the research contained in this thesis. Furthermore, the Engineering and Physical Sciences Research Council (EPSRC) for funding my thesis.

Finally, I want to thank my family and friends. Nothing would have been possible without their infinite love, support and trust. A big thank you also goes to the readers.

Maria Panayiotou, November 2014

Contents

List of Figures

List of Tables

Abbreviations

1D	One Dimensional
2D	Two Dimensional
3D	Three Dimensional
AF	Atrial Fibrillation
AP	Anteroposterior
AV	Atrioventricular
CAUD	Caudal
CFM	Circumferential Mapping
CRAN	Cranial
CRPM	Cardiac Respiratory Parametric Model
CRT	Cardiac Resynchronisation Therapy
CS	Coronary Sinus
CT	Computed Tomography
ECG	Electrocardiogram
EI	End-Inspiration
EP	Electrophysiology
EX	End-Expiration
FOV	Field Of View
FV	Frangi Vesselness
HML	Hierarchical Manifold Learning
ICA	Independent Component Analysis
LAO	Left Anterior Oblique
LBBB	Left Bundle Branch Block
LE	Laplacian Eigenmaps
LQTS	Long QT syndrome
LV	Left Ventricular
ML	Manifold Learning
MRI	Magnetic Resonance Imaging
MSCT	Multi Slice Computed Tomography

NCC	Normalised Cross Correlation
PCA	Principal Component Analysis
PC(s)	Principal Component(s)
PET	Positron Emission Tomography
PV	Pulmonary Veins
RAO	Right Anterior Oblique
RFA	Radiofrequency Ablation
RT	Radiotherapy
RXA	Rotational X-ray Angiography
SNR	Signal-to-Noise ratio
SPECT	Single Photon Emission Computed Tomography
SVT	Supraventricular Tachycardias
US	Ultrasound
VT	Ventricular Tachycardia
WPW	Wolff-Parkinson-White

Chapter 1

Introduction

Contents

The heart is a vital muscular pumping organ responsible for circulating blood through blood vessels to all body tissues. If this organ is malfunctioning, serious complications may occur, even resulting in death. The development of modern angiography systems has induced a growing trend in the clinical community to move towards a minimally-invasive approach to surgery in treating many of the cardiovascular diseases [1–4]. Minimally-invasive procedures are favoured because of reduced post-operative discomfort, faster healing times and lowered risk of infections or complications [5]. These procedures make treatment possible for patients who were previously considered to be too at risk for traditional open-heart surgery due to age or medical history.

In order to treat a patient minimally invasively, imaging technology needs to be applied. Imaging of the heart is difficult due to its rapid change in shape and size while pumping blood throughout the body, and its continuous change of position throughout the respiratory cycle. Guidance,

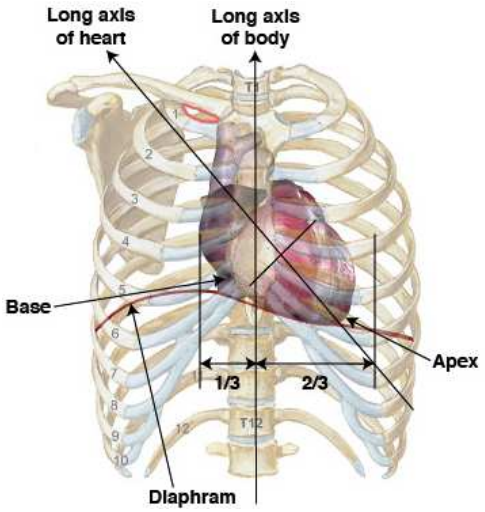

FIGURE 1.1: Anterior view of the heart in the thoracic cavity. Reproduced with permission from [10]. Copyright Lippincott Williams and Wilkins.

however, is very specific for the targeted application. This thesis is devoted to improved image guidance for cardiac catheterisation procedures. The aim of this chapter is to provide in detail the motivation and background of the work behind this thesis. It starts with a general description of the heart and its functioning role as an organ within the body. Cardiac arrhythmias are then described which may compromise the heart's function, focussing on atrial fibrillation (AF), the most common cardiac arrhythmia. It then goes on by describing ventricular dyssynchrony that can reduce cardiac efficiency and is correlated with heart failure. The chapter then goes through the current state-of-the-art treatment options, ending with the clinical motivation underlying the work of this thesis.

1.1 Cardiac anatomy and physiology

The heart, together with the blood and the blood vessels, make up the cardiovascular system. The heart is roughly the size of a clenched fist [6]. It rests on the diaphragm, near the midline of the thoracic cavity. It lies in the mediastinum, an anatomical region that extends from the sternum to the vertebral column, the first rib to the diaphragm, and between the lungs [7, 8]. About two-thirds of the mass of the heart lies to the left of the body's midline, illustrated in Figure 1.1. The wall of the heart consists of three layers, the epicardium (external layer), the myocardium (middle layer), and the endocardium (inner layer). The middle myocardium, which is cardiac muscle tissue, makes up about 95% of the heart and is responsible for its pumping action [9–11].

The heart has four chambers. The two superior receiving chambers are the atria, and the two inferior pumping chambers are the ventricles. Between the right atrium and the left atrium is a

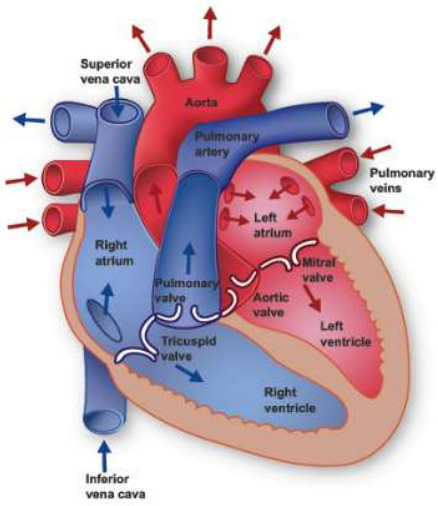

FIGURE 1.2: Blood flow through the heart. Deoxygenated blood, illustrated with blue arrows flows into the right atrium from the systemic circulation and is pumped into the right ventricle. The blood is then pumped from the right ventricle into the pulmonary artery, which delivers it to the lungs, the blood releases its carbon dioxide and absorbs oxygen. Reoxygenated blood, illustrated with red arrows, is returned to the left atrium, then flows into the left ventricle, which pumps it to the rest of the body. Reproduced with permission from [13]. Copyright by the estate of Robert M. Anderson, MD.

thin partition called the interatrial septum. Internally, the right ventricle is separated from the left ventricle by a partition called the interventricular septum [12].The right atrium forms the right border of the heart and receives deoxygenated blood from the superior and inferior vena cava (SVC & IVC) and the coronary sinus (CS) vein. When the right atrium contracts blood passes from the right atrium into the right ventricle through the tricuspid valve. The valves in the heart operate only by pressure differences and are responsible for preventing backflow of blood. Consequently, the tricuspid valve prevents blood from flowing back from the right ventricle to the right atrium. Blood passes from the right ventricle through the pulmonary valve into the pulmonary artery that takes blood away from the heart into the lungs. Oxygenated blood from the lungs flows into the left atrium via four pulmonary veins (PVs). On contraction of the left atrium, blood passes from the left atrium into the left ventricle through the bicuspid (mitral) valve. From the left ventricle, the blood is passed throughout the aortic valve into the ascending aorta from which the oxygenated blood spreads to the whole body [13]. Figure 1.2 illustrates the blood flow through the heart.

1.1.1 Conduction system

An inherent and rhythmical electrical activity is the reason for the heart's lifelong beat. The source of this electrical activity is a network of specialised cardiac muscle fibres called autorhythmic fibres because they are self-excitable. Autorhythmic fibres repeatedly generate action potentials that trigger heart contractions. As action potentials propagate through the heart, they

generate electrical currents that can be detected at the surface of the body [14], Figure 1.3a.

An electrocardiogram, abbreviated either ECG or EKG (from the German word *Elektrokardiogram*), is a recording of these electrical signals. The ECG is a composite record of action potentials produced by all the heart muscle fibres during each heartbeat. The instrument used to record the changes is an electrocardiograph. In clinical practice, electrodes are positioned on the arms and legs (limb leads) and at six positions on the chest (chest leads) to record the ECG. The electrocardiograph amplifies the heart's electrical signals and produces 12 different tracings from different combinations of limb and chest leads. Each limb and chest electrode records slightly different electrical activity because of the difference in its position relative to the heart. By comparing these records with one another and with normal records, it is possible to determine if the conducting pathway is abnormal, if the heart is enlarged, if certain regions of the heart are damaged and the cause of chest pain [15].

Cardiac action potentials propagate through the conduction system in the following sequence. Cardiac excitation normally begins in the sinoatrial (SA) node, located in the right atrial wall just inferior and lateral to the opening of the superior vena cava, Figure 1.3b. Each action potential from the SA node propagates throughout both atria via gap junctions in the intercalated discs of atrial muscle fibres. Following the action potential, the atria contracts, Figure 1.3c. The P wave, represented by a small upward deflection on the ECG, marks the contraction of the atria, Figure 1.3d. By conducting along atrial muscle fibres, the action potential reaches the atrioventricular (AV) node, located in the intertribal septum, just anterior to the opening of the CS. Here it is slowed for an instant to allow the ventricles to fill with blood. On the ECG, this interval is represented by the start of the line segment between the P and Q wave, Figure 1.3e. From the AV node, the action potential enters the atrioventricular (AV) bundle, also known as the bundle of His. This bundle is the only site where action potentials can conduct from the atria to the ventricles. After propagating along the AV bundle, the action potential enters both the right and left bundle branches. The bundle branches extend through the interventicular septum towards the apex of the heart. On the ECG, this is represented by the Q wave, Figure 1.3f. Finally, the large-diameter Purkinje fibres rapidly conduct the action potential beginning at the apex of the heart upward to the remainder of the ventricular myocardium [16], Figure 1.3g. The ventricles contract, pushing the blood upward towards the semilunar valves. The ventricles do not contract at exactly the same moment. The left ventricle contracts an instant before the right ventricle, Figure 1.3h. On the ECG, the R wave marks the contraction of the left ventricle, Figure 1.3i. The S wave marks the contraction of the right ventricle, Figure 1.3j. The contraction of the right ventricle pushes blood through the pulmonary valve to the lungs. The contraction of the left ventricle pushes blood through the aortic valve to the rest of the body, Figure 1.3k. As the signal passes, the walls of the ventricles relax and await the next signal. On the ECG, the T wave marks the point at which the ventricles are relaxing, Figure 1.3 [17].

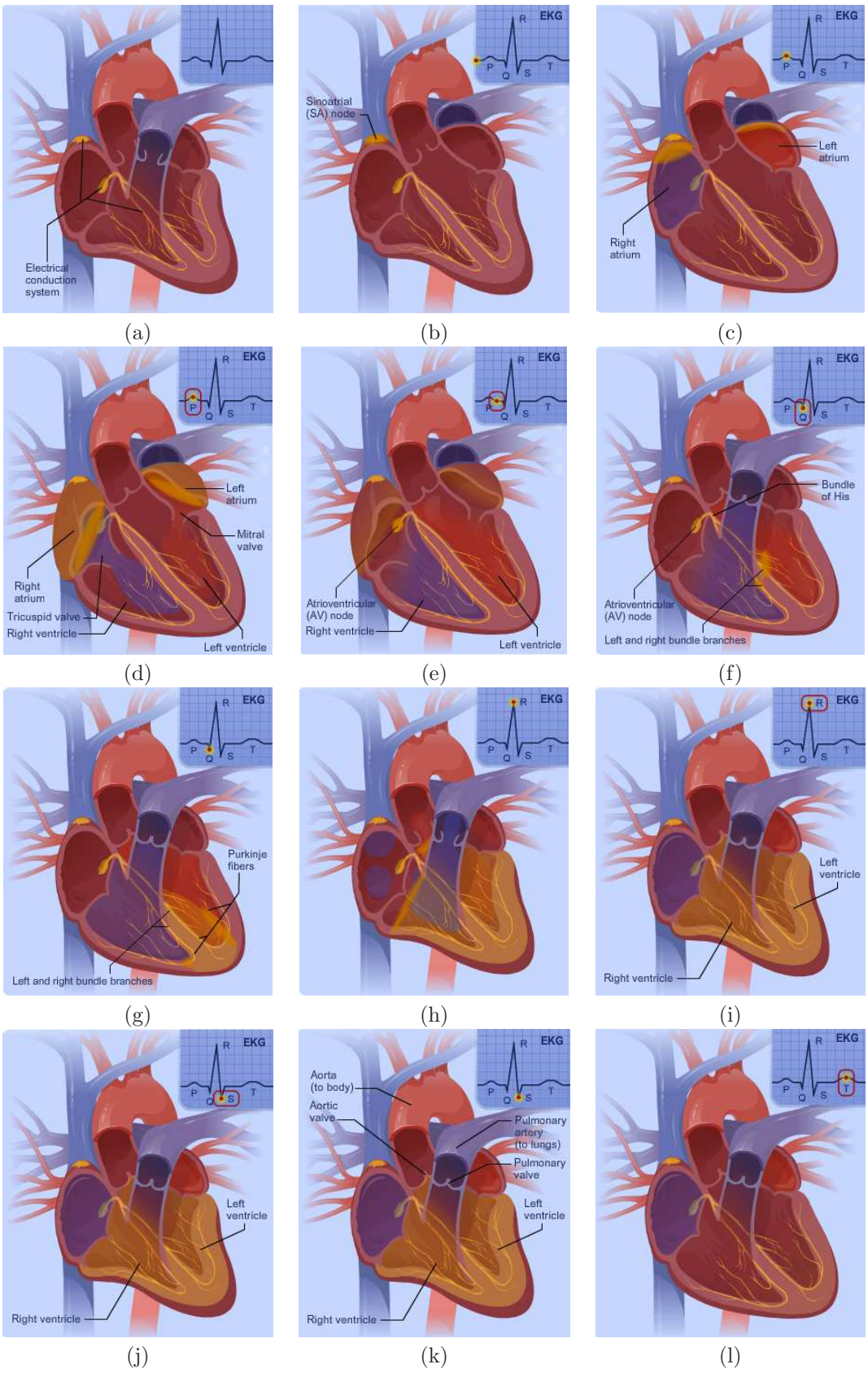

FIGURE 1.3: The cardiac conduction system illustrating its main components (SA node, AV node, bundle of His, bundle branches, Purkinje fibres) and their position on the ECG. The yellow highlighting demonstrated on the figures illustrates the cardiac electrical activity. Reproduced with permission from [17]. Copyright Springer.

1.2 Cardiac arrhythmias

Cardiac arrhythmias are disturbances in the heart's electrical impulses, causing the heart to beat too rapidly (tachycardia) or too slowly (bradycardia) [18]. Tachycardia is considered to be when the heart beat is faster than 100 beats per minute (bpm), whereas bradycardia describes an unusually slow heart beat of less than 60 bpm. Cardiac arrhythmias may feel like a fluttering or racing heart, and they're often harmless. However, some cardiac arrhythmias may be life-threatening, resulting in cardiac arrest [19].

Arrhythmias are classified not only by the speed of heart rate they cause but also by where they originate (atria or ventricles). Arrhythmias that originate in the atria are called atrial or supraventricular (above the ventricles) arrhythmias, while arrhythmias that originate in the ventricles are called ventricular arrhythmias. Common atrial tachycardias include Atrial fibrillation (AF), Atrial flutter, Supraventricular tachycardias (SVT) and Wolff-Parkinson-White (WPW) syndrome. Common ventricular tachycardias include Ventricular tachycardia (VT), Ventricular fibrillation and long QT syndrome. Common bradycardias include the Sick sinus and Conduction block.

AF is characterised by rapid and uncoordinated electrical stimulation of the atrial chambers causing them to quiver and contract inefficiently or not at all. Atrial flutter causes a rapid but coordinated electrical stimulation of the atrial chambers. AF and atrial flutter are associated with an increased long-term risk of stroke, heart failure, and all-cause mortality. SVTs usually cause a burst of rapid but regular heartbeats that begins and ends suddenly and can last from seconds to hours. These bursts often start when the electrical impulse from a heartbeat begins to circle repeatedly through an extra pathway [20]. SVT is rarely dangerous, but can cause a drop in blood pressure, causing lightheadedness or near-fainting episodes, and, rarely, fainting episodes. WPW syndrome is a special type of SVT. This syndrome involves episodes of a rapid heart rate caused by abnormal electrical connection in the heart. In people with Wolff-Parkinson-White syndrome, there is an extra (accessory) connection between the top and bottom chambers of the heart [20]. Patients with WPW syndrome may develop AF and are at increased risk for developing a dangerous ventricular arrhythmia when this occurs.

VT is characterised by rapid, regular heartbeats caused by abnormal electrical impulses that start in the ventricles. Often these are due to a problem with the electrical impulse traveling around a scar from a previous heart attack. In ventricular fibrillation, rapid, irregular electrical impulses cause the ventricles to quiver uselessly instead of pumping blood. As a result, ventricular pumping stops, blood ejection ceases, and circulatory failure and death occur unless there is an immediate medical intervention. Long QT syndrome (LQTS) is a heart disorder that carries an increased risk of fast, irregular heartbeats. LQTS disorder can result in blackouts, fainting (syncope), loss of consciousness or sudden cardiac death.

Sick sinus is a syndrome that is caused when the sinus node (heart's pacemaker) does not fire its signals properly, so that the heart rate slows down. Sometimes the rate changes back and forth between a slow and fast rate. Sick sinus can also be caused by scarring near the sinus node that slows, disrupts or blocks the travel of impulses. Possible complication to the sick sinus syndrome include angina, decreased exercised capacity, fainting (syncope), poor heart pumping and consequently heart failure. Conduction block is a block of the heart's electrical pathways that can occur in or near the AV node. A block can also occur along other pathways to each ventricle. Depending on the location and type of block, the impulses between the upper and lower halves of the heart may be slowed or blocked. If the signal is completely blocked, certain cells in the AV node or ventricles can make a steady, although usually slower, heartbeat [21].

ECG is probably the most frequently used diagnostic tool for cardiac arrhythmias [22]. Various tests can also be performed, including Holter and event monitors that record the heart's electrical signals for a period of 24 to 48 hours and simple graded exercise testing. Transesophageal echocardiography can be used to detect structural changes that may indicate an arrhythmia. Additionally, the electrophysiology study (EPS) test can be performed to assess serious arrhythmias. This test requires a catheterisation of the patient, where a thin, flexible wire is passed through a vein in the patient's groin (upper thigh) or arm to the heart. The wire records the heart's electrical signals.

The cardiac arrhythmia that is targeted here is AF, the most common sustained arrhythmia [23].

1.2.1 Atrial fibrillation

AF is the most common clinically significant cardiac arrhythmia and is characterised by irregular excitation waves and fast, irregular contraction of the atria [24]. During AF the heart rate is increased to 400-600 bpm. It is not directly mortal but favours the formation of thrombi in the atria which can potentially cause ischemic stroke. AF accounts for approximately 15% of all strokes in the United States [25]. Several epidemiological studies have shown strong associations between AF and increased risk of cerebral thrombo-embolism, development of heart failure, and increased mortality [26, 27].

There are three different types of AF. These include paroxysmal, persistent and permanent AF. Paroxysmal AF is recurrent AF of more that 2 episodes that terminates spontaneously within seven days. Persistent AF is sustained beyond seven days, or lasting less than seven days but necessitating pharmacological or electrical cardioversion. Included within the category of persistent AF is the longstanding persistent AF, which is sustained beyond one year. Permanent AF is AF in which cardioversion has either failed or not been attempted and the sinus rhythm cannot be restored by any means. Figure 1.5 illustrates an ECG recording of a patient with

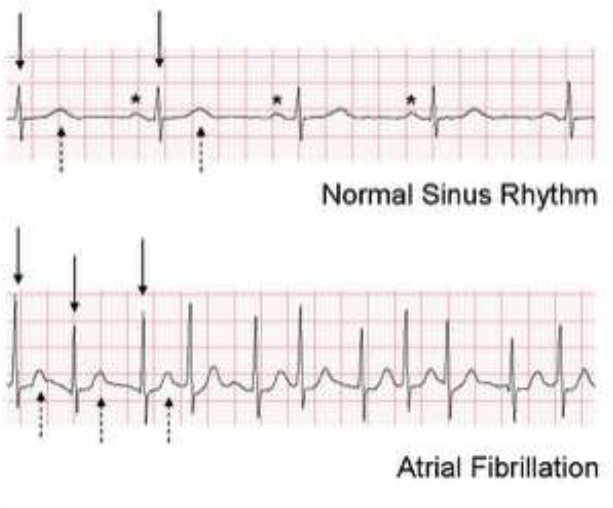

FIGURE 1.4: Example ECG traces. The top recording demonstrates normal sinus rhythm, with deflections called P waves (denoted by asterisks) that represent normally conducting atria. Each P wave is followed by a QRS complex, representing ventricular depolarization (solid arrows). Each QRS complex is followed by a T wave, representing repolarization of the ventricles (dashed arrows). The bottom recording is from the same patient while in atrial fibrillation. Note the absence of P waves and a subtle irregular undulation of the baseline representing atrial fibrillation. In the QRS complexes, ventricular activation occurs more rapidly and in an irregular pattern. Reproduced with permission from [28]. Copyright Lippincott Williams and Wilkins.

normal sinus rhythm (top) and a recording from the same patient while in atrial fibrillation (bottom).

1.2.1.1 Mechanisms

The hypotheses in the medical literature are the multiple wavelet hypothesis [29] and focal triggers [30, 31]. Until the mid to late 1980s, the multiple wavelet hypothesis for AF was widely accepted as the dominant AF mechanism. According to this hypothesis, AF results from the presence of multiple reentrant wavelets occurring simultaneously in the left and right atria, propagating in an abnormal atria-tissue substrate, Later, Haissaguerre *et al.* [32], after studying 45 patients with frequent episodes of atrial fibrillation, made the observation that the vast majority of AF is triggered by a focal source, and that the radiofrequency ablation (RFA) of that focal trigger can eliminate AF. By means of intracardiac mapping, fluoroscopy, and angiographic imaging they found that foci of rapid ectopic activity are often located in muscular sleeves that extend from the left atrium into the proximal parts of the PVs. Less frequently, focal initiation of AF may result from ectopic activity that arises from muscular sleeves in the proximal superior vena cava, from the ligament of Marshall, or other parts of the right and left atria. Besides such triggers, pathological substrate in the atria is needed to sustain the arrhythmia [33]. Considerable progress has been made in defining the mechanisms of initiation

and perpetuation of AF. However, they remain incompletely understood. Because of this, it is not possible to precisely tailor an ablation strategy to a particular AF mechanism.

1.2.1.2 Treatment

Therapies targeting AF can either manage the symptoms of the disease using drugs (palliative therapy) or try to eliminate the substrate and triggers causing AF (curative therapy). This is sometimes done using open heart surgery, although the most commonly employed curative therapy is the catheter RFA therapy which has been shown to result in better long-term success rates than antiarrhythmic drug therapy [34]. However, the kind of treatment strongly depends on the state of AF of the individual patient, the expected improvement in quality of life and the health economical cost.

1.2.2 Ventricular dyssynchrony

Along with AF, left ventricular (LV) dyssynchrony, also known as intraventricular dyssynchrony, characterised by a unique heart failure phenotype is also targeted throughout this thesis. LV dyssynchrony due to conduction system disease creates cardiac inefficiency even in normal hearts. Left ventricular dysfunction is often associated with myocardial conduction slowing, which is usually seen clinically as left bundle branch block (LBBB) on the surface ECG. LBBB causes asynchronous contraction of the left ventricle with the ventricular septum contracting early and the lateral left ventricular wall contracting late. This leads to a reduction in cardiac output and myocardial contraction efficiency and systolic mitral regurgitation worsens [35, 36]. Figure **??** illustrates an ECG recording from a patient while in LV dyssynchrony. In the figure, the QRS duration is shown, which is one of the indicators of dyssynchrony.

1.2.2.1 Mechanisms

Due to the relationship between temporal electrical activation and mechanical function, intraventricular (mechanical) dyssynchrony is the result of an abnormal electrical activation pattern, so-called electrical dyssynchrony. In heart failure patients, conduction defects due to LBBB or slow intra-myocardial conduction are common and result in regionally delayed electrical activation. Abnormal temporal electrical activation of the complex myocardial fibre architecture reduces pump efficiency and cardiac performance. Although conduction defects are common, this is not always the case and patients with heart failure may have LV dyssynchrony in the absence of regionally delayed electrical activation. Consequently, intraventricular dyssynchrony can result from one of two mechanisms [38, 39]. First, LV dyssynchrony may be the result of temporal delay in electrical activation of one region vs. another. A characteristic example

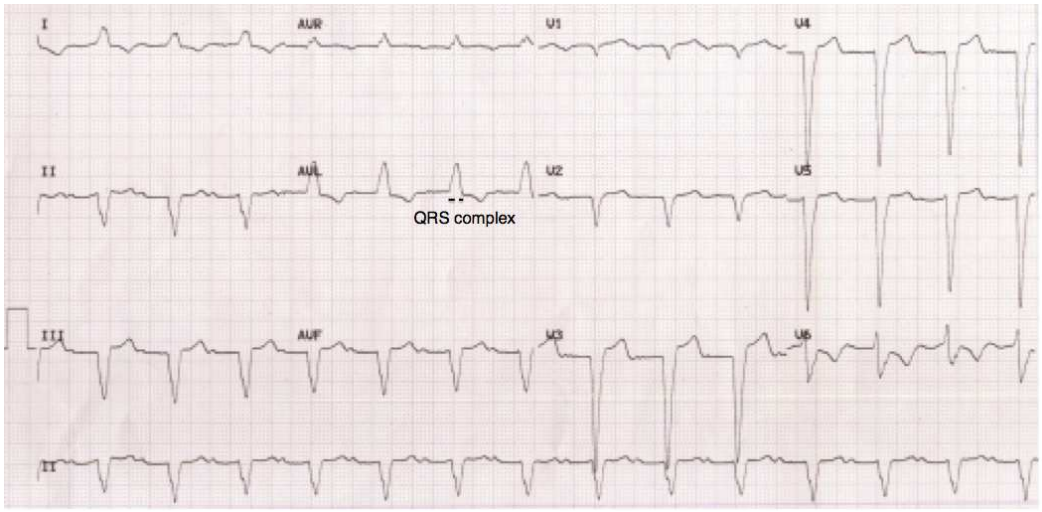

FIGURE 1.5: An ECG recording of a patient with LBBB with first degree AV block. The recording illustrates a QRS duration of more than 120 milliseconds with LBBB pattern in a person with refractory heart failure. Reproduced with permission from [37]. Copyright Elsevier.

is LBBB where electrical activation occurs first in the septum and then propagates slowly via intra-myocardial conduction to the lateral wall. A second mechanism of dyssynchrony occurs in the setting of normal temporal electrical activation. Relaxation delay and dyssynchrony can be induced by abnormal loading of the heart [40]. Echocardiography, often referred to as a cardiac echo, is a sonogram of the heart. Echocardiography uses standard two-dimensional, three-dimensional, and Doppler ultrasound to create images of the heart. Echocardiography and tissue Doppler imaging (TDI) are both needed to fully diagnose the different types of ventricular dyssynchrony [41].

1.2.2.2 Treatment

In cases where LV dyssynchrony is the result of temporal delay in electrical activation, simply restoring electrical synchrony with cardiac resynchronisation therapy (CRT) not only improves global heart function and exercise capacity, but also has a profound beneficial effect on the molecular and cellular phenotype. CRT has been proposed as an adjunct therapy in patients with drug-refractory heart failure [42, 43]. It is hypothesised that LV dyssynchrony is the most important determinant of response to CRT, and various techniques to detect and quantify LV dyssynchrony are currently under investigation [44]. However, no large studies have focused on the prediction of benefit from CRT based on the degree of LV dyssynchrony. More important, it is unclear whether patients with LV dyssynchrony who respond to CRT have a better prognosis than patients without dyssynchrony [39]. On the other hand, abnormal myocardial loading, which is characteristic in heart failure patients, can in itself contribute to dyssynchrony and this type of dyssynchrony may not be amenable to electrical resynchronisation.

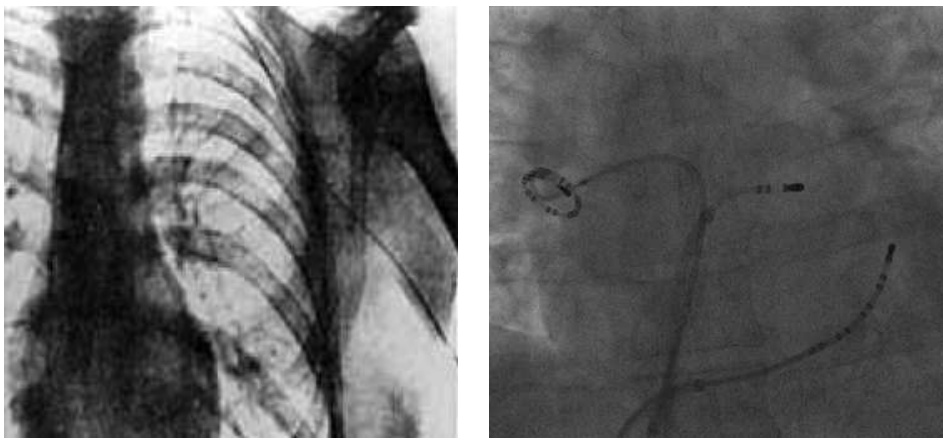

(a) (b)

FIGURE 1.6: (a) X-ray picture of the first catheter inserted into the human right atrium. Reproduced with permission from [48]. Copyright The Society of Thoracic Surgeons. Published by Elsevier Inc. (b) A recently taken X-ray picture of a patient undergoing an RFA procedure with the CS, ablation and CFM catheters introduced into the heart.

1.3 Cardiac catheterisation procedures

The development of the invasive diagnostic and therapeutic modalities of cardiac catheterisation is considered one of the greatest achievements in cardiovascular medicine. Clinical applications of image-guided interventions on the heart have been investigated by a large number of groups, leading in some cases to the acceptance of the procedure as a clinical standard [45, 46]. Cardiac catheterisation is a procedure used to diagnose and treat cardiovascular conditions. During cardiac catheterisation a narrow tube called a catheter is inserted into the blood vessels of the heart. The catheter is guided through the blood vessels to the heart with the aid of X-ray fluoroscopy images. The history of cardiac catheterisation dates back to Claude Bernard (1813-1878), who used it on animal models [47]. Clinical application of cardiac catheterisation began with Werner Forssmann in the 1930s, who inserted a catheter into the vein of his own forearm, guided it fluoroscopically into his right atrium, and took an X-ray picture of it, illustrated in Figure 1.6 [48, 49]. On the same figure a recently taken X-ray picture of a patient undergoing an RFA procedure, with the CS, ablation and CFM catheters introduced into the heart, illustrates the improvement of healthcare technology.

The electrophysiology (EP) procedure, a special type of cardiac catheterisation, is an invasive diagnostic test to evaluate the electrical system of the heart. During an EP procedure, specialised electrode catheters are positioned inside the heart, and the cardiac electrical system is mapped, showing the abnormal electrical pathways that are often responsible for producing the arrhythmia. In cases where an arrhythmia is found, EP procedures may be accompanied by a RFA procedure.

1.3.1 Radio-frequency ablation

RFA is a minimally-invasive procedure performed to treat paroxysmal and persistent AF (curative therapy). During the past decade, RFA of AF has evolved rapidly from a highly experimental unproven procedure, to its current status as a commonly performed ablation procedure in many major hospitals throughout the world [24]. RFA involves only a small incision, usually in the groin, and a catheter can be inserted through the femoral veins. During an RFA intervention, the ablation, mapping and CS catheters are introduced into the heart via the femoral veins. Access to the left heart is obtained by a transseptal puncture in the atria [50]. By applying radiofrequency currents via the ablation catheter, the clinician tries to electrically isolate tissue regions, mostly in the left atrium, which are thought to be causing the arrhythmia. The myocardium is thereby heated with radiofrequency current until it is necrotic and thus electrically isolated. Specifically, RFA involves the isolation of the PVs by creation of circumferential lesions around the right and the left PV ostia [51]. A schematic of common lesion sets employed in AF ablation is illustrated in Figure 1.7. Other less common trigger sites for AF, including the vein and ligament of Marshall and the posterior left atrial wall, are also encompassed by this lesion set. The circumferential lesions may also alter the arrhythmogenic substrate by elimination of tissue located near the atrial-PV junction that provides a substrate for reentrant circuits that may generate or perpetuate AF, and/or by reduction of the mass of atrial tissue needed to sustain reentry [52].

1.3.2 Cardiac resynchronisation therapy

CRT or biventricular pacing is a novel adjunctive therapy for patients with advanced heart failure. As previously mentioned in Section 1.2.2, many patients with severe heart failure have a LBBB or an intraventricular conduction delay. Up to 25% of patients with a QRS $> 120ms$, suffer from significant LV dyssynchrony and a high mortality rate. Patients with this combination of findings may benefit from the implantation of a pacing system that aims to normalise conduction and "resynchronise" the ventricles. This mode of cardiac stimulation is referred to as biventricular pacing and relies on the implantation of an additional pacing lead on the epicardial surface of the left ventricle. This is achieved by selectively cannulating the CS and passing a pacing lead via a posterolateral CS tributary to an appropriate location. This lead, as well as the two conventional right atrial and right ventricular leads, is then attached to a specialised pacemaker, to detect heart rate irregularities and emit tiny pulses of electricity to correct them. The procedure may be challenging and usually takes 1-2 hours depending on the operator's experience. The QRS complex shortens as the lateral wall of the left ventricle becomes "pre-excited" and contracts in concert with the ventricular septum [53, 54] .

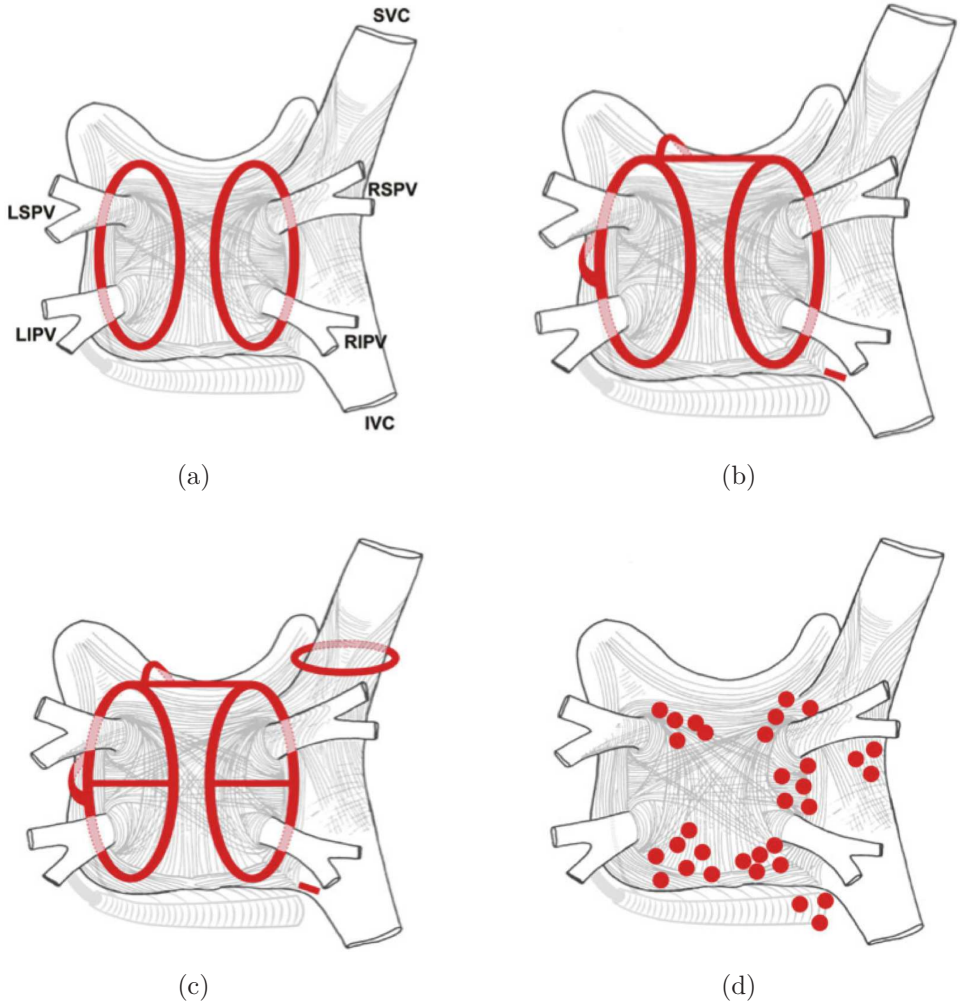

FIGURE 1.7: Schematic of common lesion sets employed in AF ablation. (a) The pulmonary vein isolation lesions. The left and right superior pulmonary veins (LSPV & RSPV), the left and right inferior pulmonary veins (LIPV & RIPV) and the SVC & IVC are illustrated in this figure. (b) Some common sites of linear ablation lesions. These include a "roof line" connecting the lesions encircling the left and right PVs, a "mitral isthmus" line connecting the mitral valve and the lesion encircling the left PVs at the level of the left inferior PV, and an anterior linear lesion connecting either the "roof line" or the left or right circumferential lesion to the mitral annulus anteriorly. Also shown is a linear lesion created at the cavotricuspid isthmus. (c) The addition of linear ablation lesions between the superior and inferior PVs and an encircling lesion of the SVC directed at electrical isolation of the superior vena cava. SVC isolation is performed in cases were focal firing from the SVC can be demonstrated. (d) Some of the most common sites of ablation lesions when complex fractionated electrograms are targeted. Reproduced with permission from [24]. Copyright European Society of Cardiology.

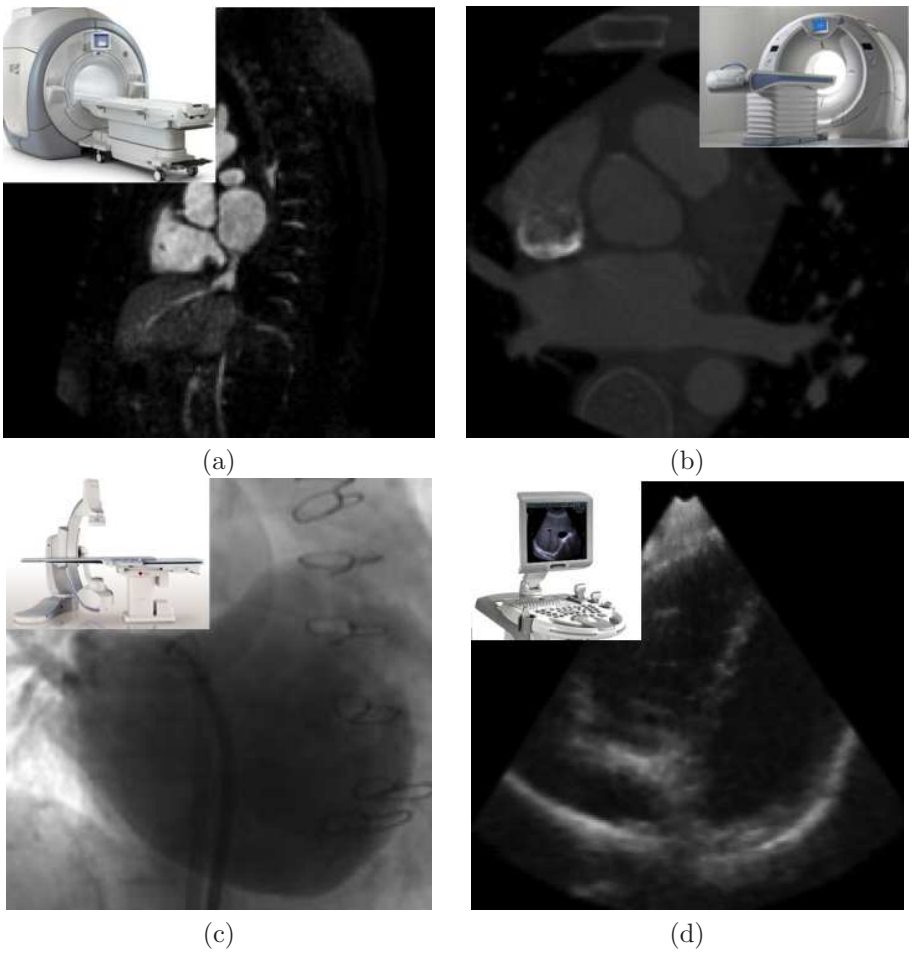

(a) (b)

(c) (d)

FIGURE 1.8: Examples of pre-procedural imaging: top left: contrast-enhanced 3D steady-state-free-precession MR image; top right: prospectively-gated, contrast-enhanced CT image; bottom left: rotational X-ray angiography of left atrium; bottom right: live 3D ultrasound. Reproduced with permission from [60]. Copyright IEEE.

1.4 Pre- and intra-procedural guidance

EP procedures involve the use of pre- and intra-procedural images to help cardiologists perform the procedures more safely and effectively. Pre-procedural anatomical imaging of the heart offers the ability to determine the cardiac geometry and identify the position of target tissues. Computed tomography (CT) [55, 56], magnetic resonance imaging (MRI) [57], ultrasound (echo) [58], and rotational X-ray angiography (RXA) [59] imaging modalities can be used to image EP patients prior to the intervention. These modalities are suitable for this purpose due to their excellent soft-tissue contrast and 3D imaging capabilities. Examples of pre-procedural imaging are illustrated in Figure 1.8.

The use of electro-anatomic mapping systems (EAMS) are a common form of intra-procedure imaging. EAMS are extensively used during EP procedures for guidance and electrical mapping. These systems are able to reconstruct anatomical models of the heart by tracking and recording

the position of a catheter that is moved along the endocardial surface. Two commercial examples of these EAMS are the *CARTO* system (Biosense Webster, USA) [61] and the *EnSite NavX* system (St. Jude Medical, UAS) [62]. While they promise to save X-ray dose, their expense and the additional preparatory time must be justified. In some instances, the registration of these systems may even be off with respect to the underlying anatomy [63]. Specifically, for the *CARTO* system disadvantages include requiring the use of a specialized (NaviSTAR) catheter, inability to easily relocate a displaced reference catheter and the inability to record or display the location of diagnostic/reference catheters [64]. Regarding the *EnSite NavX* system, disadvantages include limited utility against non-sustained arrhythmias and inaccurate rendition of complex anatomic structures unless meticulous contact mapping is performed in such areas [65]. Consequently, EAMS must never replace fundamental principles of arrhythmia diagnosis; at most, such systems must be used as an adjunctive tool when approaching a target arrhythmia. Wholly relying on data from an incorrectly acquired map may lead to an erroneously diagnosed arrhythmia mechanism, inaccurate site of tachycardia origination, or creation of a confusing, unhelpful activation map. Such errors may counteract any possible benefit offered by EAM, and may ultimately prolong procedure time [66].

Recently, robotic technology has emerged as a potentially important new enabling tool for AF ablation and other complicated electrophysiology procedures. Robotic ablation is catheter ablation of cardiac arrhythmias performed by an electrophysiologist using a robotic system. The robotic system consists of a robotic sheath that manipulates cardiac catheters, which are inserted into the femoral veins, operated remotely at a nearby control station. There are currently 2 robotic systems designed for use in the EP lab (from Stereotaxis, St. Louis, Missouri, and Hansen Medical, Mountain View, California) [67]. Although manual catheter ablation of most arrhythmias has become standardized, low risk and successful [68], certain challenges remain. Manipulation of catheters to precise locations within the heart and keeping them stable in the desired position can be challenging by hand, and manipulation by the robot can be helpful in this respect. Achieving adequate tissue contact, ideally with a small amount of pressure being applied by the catheter during ablation, is essential to effectively destroy the heart tissue responsible for the arrhythmia. By controlling catheter movement using the robot, the physician can automatically adjust and titrate the contact force to achieve the desired location and position. There is evidence that robotic ablation causes quicker more effective burns [69]. On the basis of limited clinical experience to date with these devices, it appears that robotically guided mapping and ablation may improve both the ease and outcomes of AF ablation, and potentially enable less-experienced operators to perform the procedure with greater safety and efficacy. However, robotic systems are expensive to purchase and install, and it is as yet unclear whether the clinical benefits will justify this extra expense.

An additional form of intra-procedure cardiac imaging is X-ray fluoroscopy. X-rays are ionising

electromagnetic radiation that penetrates bone and soft tissues and can either be absorbed, scattered or remain unchanged depending on the density of the tissues. The variation in absorption of different tissues is what is detected and depicted in the resulting image. X-ray imaging can be used for single static images or for real-time sequences, called fluoroscopy imaging. In modern fluoroscopy, the detector is an X-ray image intensifier, which allows low intensity X-rays to be converted to a visible light output and captures the light image with a digital video camera at real-time frame rates, up to 30 frames per second (fps). This has the advantage of capturing X-ray video sequences that can be displayed on computer monitors and/or electronically stored for offline review. The tube and detector are usually housed in a C-shaped gantry (C-arm) with a patient table placed between the ends of the C, as illustrated in Figure 1.9. The system allows rotational movement of the C-arm so that different views of the patient can be acquired without having to move either the patient or the table [70]. Specifically, the C-arm can rotate towards the left and right hand sides of the patient, (left and right anterior oblique projections (LAO/RAO)) or towards the head end and foot end of the patient (cranial and caudal directions (CRAN/CAUD)) [71]. The ability to take videos of the beating heart is essential for real-time cardiac imaging, and makes fluoroscopy suitable for guiding cardiac catheterisation procedures. Additional advantages of this form of intra-procedural guidance are its high-device visibility, low-cost, and widespread availability. On the other hand, in catheter-based cardiac procedures, such as EP studies, CRT and RFA for atrial fibrillation and flutter, the cardiologist must accurately and remotely position catheters into the heart. The limited visibility of the heart offered by fluoroscopy makes catheter navigation difficult, time-consuming and potentially dangerous since there is a chance that the catheter may puncture through the vessel wall. These result in significant X-ray exposure to the patient and staff, repeat toxic radio-opaque contrast agent injections, and often suboptimal success rates [72, 73].

While in a monoplane X-ray imaging system a single tube-detector system is used, acquiring images from a single view, in a biplane system two complete X-ray tube-detector systems are used to simultaneously acquire images from two approximately orthogonal (or oblique) views. In order to reconstruct optically opaque objects seen in X-ray images in 3D, like vessels, interventional devices and more importantly catheters, at least two oblique views must be acquired and synchronised in both respiratory and cardiac cycle motion phases. However, the majority of interventional cardiology X-ray systems are monoplane system. Biplane X-ray images could be acquired from two different angle views using a monoplane X-ray system. Typically, one is the anteroposterior (AP) view and the other is the left/right anterior oblique 30° view. The acquisition of these images is called sequential biplane imaging.

FIGURE 1.9: Photograph of a C-arm fluoroscopy unit with patient bed. The C-arm can rotate towards the left (LAO) and right (RAO), or towards the head (CRAN) and foot (CAUD). Reproduced from http://www.healthcare.philips.com/connectivity. Copyright Philips Healthcare.

1.5 Clinical motivation

As highlighted in the previous section minimally-invasive catheterisation procedures are carried out under X-ray fluoroscopic image guidance to guide the insertion and movement of catheters. However, while X-ray fluoroscopy provides high temporal and spatial resolution it provides only 2D projections and the guidance of such procedures is compromised by the inability of X-ray to effectively visualise soft tissues. In order to enhance image guidance for such cardiac interventions, intra-procedure X-ray fluoroscopy images can be registered and overlaid with pre-procedural 3D anatomical models derived from other imaging modalities. MRI has been used as a source of pre-procedure imaging data which is then registered to the intra-procedure fluoroscopy images or electrophysiology data [74, 75]. Such techniques can be performed in an XMR suite [76, 77], where an X-ray angiographic system is coaxially aligned with an MR system in the operating room, allowing the registration of the MR and fluoroscopy images during the same acquisition session. A further extension is represented by the integration of an X-ray system within the MR scanner, known as a closed-bore XMR system (CXMR) [78], which allows the simultaneous acquisition of fluoroscopy and MR data. Also CT imaging has been employed as the source of the 3D pre-procedure roadmap [79, 80]. Ector *et al.* [81] used a CT-based 3D model of the heart in combination with biplane fluoroscopy to guide the instrument navigation. In addition, modern cardiac interventional X-ray systems [82, 83] can perform 3D volumetric reconstruction in a CT like manner following intravascular injection of contrast agent. These techniques, known as C-arm CT or 3D rotational X-ray angiography (3DRXA), can also be used to form 3D roadmaps for guiding EP procedures, which is particularly suited to the clinical workflow. By achieving 3D visualisation of the cardiac soft tissue in relation to the catheter, good access and clear walkways are ensured, something particularly important to enhance procedure safety [59, 84–86].

The 2D-3D registration can be achieved using specialised hybrid imaging systems [87]. However, achieving the registration in a conventional monoplane catheter laboratory is challenging. A promising solution is the use of catheters to constrain the registration [88]. A recent implementation of this approach uses 3D catheter reconstructions from sequential biplane X-ray images [89]. This technique requires both cardiac and respiratory phase matching of the biplane images. In Truong *et al.* [89], this was achieved manually, but an automatic technique would significantly speed up the clinical workflow. A similar requirement for automatic frame matching exists when catheter positional information needs to be measured with reference to a registered anatomical model. This can be useful for recording the position of electrical measurements, pacing locations and ablation treatments [76, 90]. The co-registered anatomical and functional data can be used in combination with cardiac biophysical modelling to obtain patient-specific predictions. For personalised planning and guidance, there is a need to adjust the parameters of these models in order to fit to specific patient clinical data, such as those derived from catheter-based measurements [91, 92].

While image fusion is a powerful tool that has a promising outcome for patients undergoing EP procedures, the roadmap images produced will be static and will not update with the intra-procedural situation. Cardiorespiratory motion causes mis-registration of these models, compromising the guidance accuracy. Successful reduction of these misalignments is therefore a necessary, although very challenging, task. One way to achieve this is by motion gating of the real-time images. Motion gating is therefore useful both for catheter reconstruction for registration and for overlay of pre-procedural images with X-ray fluoroscopy to reduce the effects of respiratory motion.

Motivated by the necessity of cardiac catheterisation procedures to achieve the required accuracy for image guidance, the main scientific focus of this work was to develop novel and clinically useful techniques for cardiac and respiratory motion gating of interventional X-ray images.

EP procedures result in substantial patient and staff radiation doses due to the long fluoroscopy duration and radiation exposure [73]. Acute radiation-induced skin injuries or radiation-induced cancer are important risks associated with diagnostic and therapeutic procedures that require fluoroscopic imaging. It is necessary to minimise patient dose in order to outweigh the radiation risk by the benefit of the interventional procedure. Therefore, developing robust-to-noise gating techniques can potentially minimise patient exposure to radiation by allowing the use of lower dose fluoroscopy. This is an additional clinical motivation underlying the work of this thesis where its application for the purposes of motion gating of very low dose scenarios is demonstrated.

1.6 Objectives

As a form of translational research, the algorithms developed in this thesis must be suitable for deployment in cardiac catheterisation procedures and therefore must provide minimum disruption to the already existing clinical workflow. Disruption can be avoided if the motion gating algorithms make use of images that are already part of the clinical protocol, and therefore no additional imaging is required. Additionally, the techniques should be fully automatic. High degrees of accuracy and robustness are two further criteria that the motion gating algorithms must have for suitable deployment in the clinical environment, as any inaccurate information provided to the interventionalist may result in misleading guidance information, compromising the accuracy and success of the intervention. To achieve these aims, some quantitative objectives will be set for the development and validation of the algorithms developed in this thesis.

For cardiac catheterisation procedures such as RF ablation, CS catheter tracking accuracy within 2mm is an acceptable tolerance [93]. Throughout this thesis, the proposed algorithms should be able to achieve accuracies within this tolerance at least 90% of the time. Below 90%, at least one of the electrodes on a ten-electrode catheter is expected to be misdetected.

Applications of the motion gating techniques spanning from basic research to clinical tasks are demonstrated in this thesis. These clinical applications include 3D catheter reconstruction; motion gating of 3D rotational X-ray angiography sequences; and motion compensation. The motion gating accuracy objective set in this thesis is based on these targeted clinical applications. Consequently, two different objectives are needed, one for the motion compensation application and one for the other two. For motion compensation, the maximum allowable gating error is 1 second, which is derived from the maximum clinically acceptable registration error of 5mm [94–96] due to gating errors in respiratory motion. This 5mm is specified by the fact that in most EP procedures, the smallest structures encountered are the pulmonary veins, which are more than 10mm in diameter for most adults. Therefore it was estimated that the clinical accuracy requirement for EP procedures is 5 mm for adults and slightly less for children [94].

For the rotational gating and the phase matching for 3D reconstruction, both applications will use the diastolic phase. This is because the heart is more relaxed in this phase, and it is expected that its shape will be more repeatable over several cycles. Additionally, when registering a 3D model, the model is almost always from a diastolic image. Since the heart will be relatively stationary in the diastolic phase for a period of about 0.3s, the motion gating accuracy objective is set to 0.1s. This 0.1s objective is set based on the cardiac gating. Since the respiratory motion is slower, larger gating errors could be allowed if only respiratory motion were important, as is the case for the motion compensation application, whereas for these two applications, cardiac motion is the limiting factor. The final objective of this thesis is to determine the maximum dose reduction factor possible within the constraints of these accuracy objectives.

1.7 Scientific contributions

This thesis provides scientific progress within the current research fields regarding electrophysiology procedures and contributions to the community of computer-assisted interventions. In the following list, the major scientific contributions and structure of the thesis are summarised.

- A cardiorespiratory motion gating approach based on the formation of a novel statistical model of the motion of the CS catheter, using principal component analysis (PCA) of tracked electrode locations from standard monoplane RFA X-ray fluoroscopy images is presented in Chapter 3. The chapter goes on to describe the methodology of how a modification of the technique allows application to very low dose scenarios. Along with cardiorespiratory motion determination, this Tracked-PCA technique is able to track the CS catheter throughout the normal and very low dose X-ray images.

- A novel robust to varying image-content motion gating technique applicable to more types of minimally invasive procedures, such as CRT, where the CS catheter is not present in the X-ray images, is developed. The purpose of the developed technique was to remove the constraint of the presence of the CS catheter in the X-ray images. The technique is based on the hierarchical manifold learning (HML) technique [97], and is also described in Chapter 3. This HML-based technique is able to automatically determine the regions that carry cardiac and respiratory motion information directly from standard monoplane X-ray fluoroscopy images. Unlike most previously developed motion gating techniques, the main novelty of the technique is that it is robust to varying image-content. Thus, it is robust to typical EP X-ray images that can contain a varying number of different types of EP catheters and may include contrast agent injection.

- An additional robust to varying image-content motion gating technique, the Masked-PCA technique, is also developed to increase the cardiac gating accuracy and robustness of the HML-based technique. The PCA statistical method is used in combination with other image processing operations to make the proposed Masked-PCA technique suitable for cardiorespiratory gating. Again, this developed technique does not rely on specific catheters being present in the image data or the localisation of these devices, and makes no assumptions about the nature of the motion present in the images. The technique is described in Chapter 3.

- One major limitation of the above and other model-based approaches is the requirement to build a separate model for each X-ray view. The Tracked-PCA technique is significantly extended to make it X-ray system view-angle independent and therefore much more clinically useful. This approach is based on forming a PCA-based model of the CS catheter in

a first or *training* view and then using this to determine both the cardiac and the respiratory phases prospectively in any arbitrary second or *current* view. For the application, the method uses epipolar constraint and a Euclidean distance/angle-based cost function. Along with cardiorespiratory motion determination, this technique is able to track the CS catheter throughout the X-ray images, again in any arbitrary subsequent view. The technique is described in Chapter 3.

- The application and evaluation of the developed motion gating techniques to phantom datasets, for the purposes of cardiorespiratory gating of X-ray fluoroscopy images at normal and very low dose is demonstrated in Chapter 4. The datasets were acquired using a bespoke beating and breathing left ventricular phantom [98] with an inserted CS catheter. The angulation of the scanner was changed between frames in the acquisition of these phantom images to acquire biplane and rotational X-ray sequences. The application and validation of the proposed techniques to these datasets is demonstrated in this chapter.

- The translation from the application and evaluation of the developed motion gating techniques, from phantom to clinical datasets, is demonstrated in Chapter 5. The developed techniques are validated for motion gating on X-ray imaging sequences from patients undergoing RFA for the treatment of AF. CS catheter tracking was also validated for the Tracked-PCA and the View-angle independent techniques. The HML-based and Masked-PCA techniques are further evaluated on X-ray images from CRT procedures. The CRT procedure is another example of a minimally-invasive procedure that uses a special kind of pacemaker, called a biventricular pacemaker, designed to treat the delay in heart ventricle contractions in heart failure patients. Some of the sequences from the CRT patients were CS angiography sequences that used contrast agent for improved image guidance. The performance of the two robust to varying image-content techniques with and without the presence of contrast agent is compared and illustrated in Chapter 5. Furthermore, comprehensive validation of the View-angle independent gating and CS tracking technique on clinical X-ray sequences was carried out for cases where the angulation of the scanner was changed.

- One way to achieve the 2D-3D registration of 3D cardiac data (CT or MRI) to X-ray fluoroscopy is to align optically opaque objects seen in the images, such as interventional devices and more importantly catheters that are reconstructed in 3D from tracking in gated sequential biplane X-ray images [99]. This is an important clinical application suitable for providing image registration for the guidance of cardiac catheterization procedures or for the off-line fusion of cardiac image data for application in biophysical modelling research, demonstrated in Chapter 6 of this thesis. Additionally, motion gating of 3DRXA for which current methods are limited to breath-holding for respiration and either no gating for cardiac motion or arresting the heart using adenosine or rapid pacing [100] is

demonstrated in Chapter 6. Finally, motion compensation on unseen images taken at any arbitrary projection, by integrating respiratory motion into MRI-derived roadmaps fused with live X-ray fluoroscopy, is also demonstrated in Chapter 6.

Chapter 2

Fundamentals of motion gating/compensation of cardiac catheterisation procedures

Contents

As mentioned in Section 1.5, image guided interventions involve the use of image fusion between high tissue contrast volumetric roadmaps acquired in the pre-procedural phase, with high

temporal resolution X-ray fluoroscopy images acquired during the procedure. The success of the guidance depends on the accurate alignment of the imaging data and the underlying real anatomy that it represents. Ruijters *et al.* [101] investigate the effectiveness, accuracy, robustness and computation times of the described methods for 3D multi modality roadmapping in order to assess their suitability for accurate interventional navigation. A significant limitation of image-guided interventions applied to organs such as the heart is the problem of cardiac and respiratory motion. During breathing, organs such as the heart can undergo motion of up to 25 mm [102]. This causes misalignments between the high-resolution pre-procedure image-derived roadmap and the underlying anatomy. Incorporation of physiological motion into fused roadmaps may increase their utility in guiding diagnostic catheterisation, structural heart interventions, and electrophysiology procedures. Therefore, cardiac and respiratory motion estimation have been proposed as a solution so that the pre-procedure image data can be updated to compensate for the motion or gated to eliminate the motion, thus maintaining the accuracy of the guidance information.

There are essentially three separate processes for cardiorespiratory motion compensation which can be used separately or together in the imaging technique to reduce cardiorespiratory motion artefacts: (i) motion estimation, (ii) gating and (iii) correction. Most cardiorespiratory motion compensation strategies rely on some sort of motion estimation information as input to the gating or correction algorithms. There are a number of ways in which motion estimation can be achieved, such as external monitoring devices, all described later in this chapter. Nevertheless, such techniques alone may be insufficient to adequately compensate for the respiratory motion. This is because they typically only provide relative information about cardiac and respiratory motion, which can be used to determine the cardiac and respiratory phases (systole or diastole and inspiration or expiration for the cardiac and respiratory motions, respectively) but not any absolute motion information, such as displacement, rotation, etc. Therefore, their usefulness for the purpose of cardiorespiratory motion correction is very limited. For cardiorespiratory motion gating, the most commonly used approach is to limit image acquisition to the most quiescent cardiac and respiratory phase, which usually end-diastole for cardiac motion and end-expiration for respiratory motion, and reject data acquired outside of the "cardiorespiratory gating window". Cardiorespiratory motion correction can be either prospective or retrospective, where prospective correction involves estimating the motion before every acquisition of imaging data, using motion estimation techniques, and correcting for it by updating the image acquisition parameters accordingly. Retrospective correction involves correcting for the motion after the imaging is completed.

In this chapter, the different types of motion gating and motion compensation techniques proposed in the literature are reviewed. The aim of this review is to provide a description of the

aims and methodologies regarding those techniques along with an overview of the state-of-the-art on this topic, highlighting the limitations of many current approaches that this thesis seeks to address and emphasising the novelty of the developed methods proposed in Chapters 3, 4 and 5. Non-image based motion gating and motion compensation techniques are reviewed in Section 2.1. Imaged based gating/compensation techniques using imaging modalities besides X-ray fluoroscopy are reviewed in Section 2.2. Image based gating/compensation techniques focussing on X-ray fluoroscopy imaging, which is the target imaging modality behind the work of this thesis, are reviewed in Section 2.3. X-ray image based gating/compensation techniques are subcategorised, with each category representing the classification of each proposed algorithm. These include techniques that are based on anatomical feature detection/tracking, motion modelling, weighted centroid measurements, dimensionality reduction algorithms, the use of the phase correlation algorithm and detection/tracking of interventional devices. The X-ray image based gating/compensation techniques are most relevant to this thesis, as X-ray is the modality targeted here. The non-image based techniques and those using other imaging modalities are less relevant, but they are included to give an overview of all motion gating/compensation techniques. The aim is to illustrate the novelty of the newly developed methods and their ability to address the limitations of previously developed techniques. The review is organized with the more relevant techniques towards the end.

2.1 Non-image based motion gating/compensation techniques

Different approaches have been devised to overcome the problem of cardiac and respiratory motion. The beating motion of the heart is normally compensated for by using a gating-based approach, i.e. by acquiring the images at the same contraction phase, for instance by synchronising image acquisition to the ECG signal [103]. However, this is usually an optional extra when purchasing an X-ray system and, when present, there may be latency between the acquisition of the ECG and the X-ray data that needs to be gated. Any system used for electrophysiology would need to have simultaneous ECG recording. However, during an EP procedure the ablation catheter may disrupt the ECG tracing and thus interfere with an ECG-based gating method.

Respiratory motion is usually handled by using the breath-hold technique that is commonly used during magnetic resonance imaging [104, 105]. Breath holding is also used during external-beam radiotherapy (RT) in an attempt to reduce the dose margins and dose targeting error associated with respiratory motion [106–111]. Although this reduces breathing motion by relatively simple and natural means, it is, nonetheless, restricted by the patient's ability to perform a supervised

breath hold during the treatment. Additionally, breath hold is not practical in the catheter laboratory where patients can be heavily sedated.

As an alternative to breath holding, the breathing cycle can be modified by means of jet ventilation [112], which reduces the lung volume excursions needed to keep the patient oxygenated. Jet ventilation, however, is a procedure performed under general anaesthesia.

Motion-compensated navigation for coronary interventions using magnetic tracking was suggested by Timinger *et al.* [113, 114]. However, this group of techniques requires special catheters equipped with an electromagnetic sensor at increased cost.

Respiratory motion is often handled by the use of markers placed on the patient's body [115]. Gating based on optical measurements of surface markers have been used in radiation therapy [116–122]. MRI and X-ray fluoroscopy images were registered using external fiducial markers, as previously described by George *et al.* [123]. Similar approaches for respiratory gating in cardiac MRI have been investigated, usually using displacement transducers to estimate the breathing phase [124]. Atkinson *et al.* [125] proposed a simple motion model to correct for respiratory motion based on the tracking of a passive marker on the subject's abdomen and correcting superior/inferior translational motion in US images. However, the placement of markers is usually impractical in a clinical setting. Furthermore, it is difficult to set up and prolongs the overall acquisition procedure.

Jiang and Doppke [126] used a spirometer that measures the air flow change of patients, to gate CT acquisition, reconstructing data at three phases of breathing for breast cancer treatment planning, concluding breathing was not a major problem. Giraud *et al.* [127] also used a spirometer to gate CT scans and proposed gating therapy correspondingly. Zhang *et al.* [128] showed the long term drift in spirometer monitoring and developed a calibration technique to overcome this. Van Herk *et al.* [129] used a nasal thermometer to measure the breathing phase and gate CT data. A different approach is sensing of the pressure variation of an elastic thoracic/abdominal belt [130, 131]. However, the correlation between these external surrogates and the motions of the internal anatomy is questionable due to some evidence of hysteresis between the internal movement and external device [132–136]. While implanted radiopaque fiducial markers [137, 138] can provide a more reliable respiratory signal, the invasive implanting process is undesirable and marker migration is also a problem [139, 140]. A summary of published non-imaged based motion gating/compensation methods is given in Table 2.1 detailing the motion gating/compensation technique, the imaging modality employed and the targeted organ. The last column of Table 2.1 reports whether the motion the technique was developed to gate/compensate was cardiac, C, respiratory, R, or both, C/R.

For image gating, detecting the phase using the images should be more reliable and robust compared to cases where an external signal is used. Image-based approaches do not require

any fiducial markers, additional contrast agent or special hardware and do not interfere with the clinical workflow. Their aim is to estimate cardiac and respiratory motion so that the pre-procedure image data can be updated to compensate for the motion or gated to eliminate the motion. The following sections give a comprehensive overview of proposed image based motion gating/compensation approaches.

2.2 Non X-ray image based motion gating/compensation techniques

This section gives a review of cardiac and respiratory motion gating/compensation techniques of imaging modalities that include magnetic resonance imaging (MRI), ultrasound (US), computed tomography (CT), positron emission tomography (PET) and single-photon emission computed tomography (SPECT).

2.2.1 Magnetic resonance imaging

In the study performed by Kellman *et al.* [141], cardiac and respiratory motion was measured using real-time MR images acquired in multiple planes. This allowed the motion of different anatomical structures to be tracked in three-dimensions throughout the cardiac and respiratory cycles. Nonrigid registration was used to compute a retrospective image-based respiratory navigator that was combined with the recorded ECG signal to bin the images according to cardiac and respiratory phase. Weide *et al.* [142] developed an efficient method for tracking intravascular devices in interventional MR images based on tracking paramagnetic markers. The computation for a single image by their method took 0.3 seconds. Moreover, respiratory gating has been implemented using navigator echoes [143, 144] during magnetic resonance image acquisition, which track the position of a high contrast tissue boundary as the diaphragm.

Manifold learning (ML) is a powerful tool for non-linear dimensionality reduction of complex high-dimensional data and various manifold learning algorithms such as locally linear embedding (LLE), Laplacian eigenmaps (LE), or ISOMAP have been proposed. In recent years manifold learning has been shown to be a useful image-based method for cardiac and respiratory phase detection. Wachinger *et al.* [145, 146] used LE for respiratory gating in MRI applications. Bhatia *et al.* [97] proposed a technique called hierarchical manifold learning (HML) which is used to learn the regional correlations in motion within a sequence of time-resolved MR images of the thoracic cavity.

Different strategies cope with the problem of respiratory motion correction by incorporating suitable motion models. In a study by McLeish *et al.* [102], 3D datasets of the whole heart

Table 2.1: Key papers on non-image based motion gating/compensation available in the literature, categorised by the technique applied, modality and organ used and the type of motion being gated/compensated.

Paper	Technique	Modality	Organ	Motion
Nieman *et al.* 2001 [103]	ECG	MSCT*	heart	C
Paling *et al.* 1986 [104]	Breath-hold	MR	upper abdomen	R
Mangeras *et al.* 2004 [105]	Breath-hold	CT	lung	R
Mah *et al.* 2000 [106]	Breath-hold	CT	thorax	R
Rosenzweig *et al.* 2000 [107]	Breath-hold	CT	lung	R
Sixel *et al.* 2001 [108]	Breath-hold	CT	breast	R
Wong *et al.* 1999 [109]	Breath-hold	CT	thorax/abdomen	R
Barnes *et al.* 2001 [110]	Breath-hold	CT	thorax	R
Biancia *et al.* 2005 [111]	Breath-hold	CT	lung	R
Herfarth *et al.* 2001 [112]	Jet ventilation	CT	liver	R
Timinger *et al.* 2004, 2005 [113, 114]	Magnetic tracking	US	heart	R
Khamene *et al.* 2004 [115]	Surface markers	MRI	thorax	R
Kini *et al.* 2000 [116]	Infrared surface markers	CT	moving phantom	R
Ramsey *et al.* 2000 [117]	Reflective surface markers	CT	abdomen	R
Vedam *et al.* 2001 [118]	Reflective surface markers	CCD camera	diaphragm	R
Ford *et al.* 2002 [119]	Reflective surface markers	CT	lung/liver	R
Keall *et al.* 2004 [120]	Surface markers	CT	thorax	R
Nelson *et al.* 2004 [121]	Infrared reflective surface markers	CT	thorax/abdomen	R
Berbeco *et al.* 2005 [122]	Surface markers	CT	thorax/abdomen	R
George *et al.* 2010 [123]	External fiducial markers	XFM**	thorax	R
Ehman *et al.* 1984 [124]	External fiducial markers	MRI	thorax/upped abdomen	R
Atkinson *et al.* 2001 [125]	External fiducial markers	US	abdomen	R
Jiang and Doppke *et al.* 2001 [126]	Spirometer	CT	breast	R
Giraud *et al.* 2000 [127]	Spirometer	CT	thorax	R
Zhang *et al.* 2003 [128]	Spirometer	CT	lung	R
Van Herk *et al.* 2002 [129]	Nasal thermometer	CT	lung	R
Dietrich *et al.* 2006 [130]	Thoracic/abdominal belt	4D CT	abdomen	R
Kleshneva *et al.* 2006 [131]	Thoracic/abdominal belt	4D CT	thorax/abdomen	R
Shirato *et al.* 2003 [138]	Implanted radiopaque fiducial markers	CT	spinal/paraspinal/prostate/liver/lung	R
Kitamura *et al.* 2002 [139]	Implanted fiducial gold markers	CT	liver/prostate	R

*MSCT stands for multi slice computed tomography

**XFM guided interventional procedures are procedures where X-ray is fused with MRI

were acquired at multiple breath-hold levels, and registered using an image intensity based method. Manke *et al.* [147] proposed a patient-specific affine motion model based on a diaphragmatic pencil-beam navigator for prospective respiratory motion correction in coronary MRI. In a follow-up study [148] the authors extended the technique to use multiple navigators at different structures to achieve better correlation particularly for non-translational components of the affine parameter set. An additional subject-specific respiratory motion model that modelled the motion of the heart as an affine transformation has also been applied to motion-correct MRI image acquisitions [149]. With this technique, it is possible to correct for motion prospectively, by modulating the magnetic field gradients and RF fields in order to cancel the effect of motion in the Bloch equations. The main drawback of the method is that it is limited to correcting, at best, affine motion, due to magnetic field gradient systems being linear.

2.2.2 Ultrasound

An approach for retrospective end-diastolic gating of intra coronary ultrasound sequences (ICUS) using feature extraction and classification was proposed by De Winter *et al.* [150]. This method is computationally expensive and requires processing the whole sequence together as some of the features are temporal. Zhu *et al.* [151] propose two techniques to analyse images in the sequence and retrieve the cardiac phase, from intravascular ultrasound (IVUS) images based on average image intensity and absolute difference in pixel intensity between the consecutive frames. However, the robustness of this method was not fairly evaluated as no precise quantified validation of this method was performed. An additional technique for image-based gating in ultrasound specific to detecting the cardiac signal using the centroid algorithm was proposed by Karadayi *et al.* [152]. The generalised Hough transform is a robust technique to detect arbitrary shapes. It was first proposed by Ballard *et al.* [153] and has been used for motion compensation for ICUS catheters [154]. In US applications, Laplacian eigenmaps (LE), a manifold learning algorithm has been used for cardiac gating [155]. However, these techniques are only focussed on cardiac gating/compensation.

Wachinger *et al.* [145] proposed an automatic, image-based respiratory gating method for acquiring 4D breathing data with a wobbler ultrasound probe using LE. They later developed a technique for extraction of respiratory gating navigators from ultrasound images [146]. The method was demonstrated by performing the analysis on various datasets showing different organs and sections, for both 2D and 3D ultrasound data over time.

Motion models have been proposed to correct for motion using US data [156–159]. Peressutti *et al.* [158, 159] proposed a novel framework for motion-correcting the pre-procedural information that combines a probabilistic MRI-derived affine motion model with intra-procedure real-time 3D echocardiography images in a Bayesian framework. The probabilistic model incorporates

a measure of confidence in its motion estimates which enables resolution of the potentially conflicting information supplied by the model and the echo data.

2.2.3 Computed tomography

In Georg *et al.* [160], ISOMAP is used for retrospective reconstruction of respiratory-gated lung computed tomography volumes.

Image similarity measurements between reference images acquired in extreme inhale and exhale positions using normalised cross correlation can be used for motion gating in clinical Cine-CT [161, 162]. Respiratory gating techniques based on projection image intensity measurements of a lung region of interest (ROI) were developed for cone-beam Cine-CT [163–165]. The contrast provided by the diaphragm can also be used for large detector CT. Sonke *et al.* [166] found the axial location of the diaphragm by using filtered 1D projections and used this for phase-gating.

Manzke *et al.* [167] describe a technique that retrospectively selects an optimal gating window based on the correlation between low-resolution 3D cardiac CT data reconstructed at successive temporal frames, to determine the temporal frames where the least motion occurred.

2.2.4 Positron emission tomography/Single-photon emission computed tomography

Many groups compute the centre-of-mass in an ROI and use this as an indicator of motion, mostly of respiration, in PET [168, 169] and cardiac SPECT acquisitions [170]. Additionally, Buther *et al.* [171] used filtering for separation of a respiratory and cardiac signal in cardiac PET. This method needs a high contrast region that can be tracked over time. Visvikis *et al.* [172] placed an ROI over edges of boundaries (using non-attenuation corrected images) and studied the time activity curve. A characteristic frequency was derived via the Fourier transform which then allowed finding amplitude and phase images. This method worked well on phantom data with periodic movement but was not evaluated for patients.

A method for respiratory gating specific to 3D PET, which does not need any ROIs, was developed by He *et al.* [173]. The approach relies on the fact that axial motion will affect the total count rate, due to the axially non-uniform sensitivity in 3D PET. The main advantage of this method is that it is very easy to implement. However, it relies on axial motion and sufficient contrast.

Thielemans *et al.* [174] developed a motion gating technique based on PCA. The hypothesis of the proposed technique was that the motion causes the underlying data to change, and that PCA therefore can detect this change. By using the first basis vectors, or principal components, the

technique automatically suppresses noise. The technique was evaluated on PET and CINE-CT data.

King *et al.* [175] proposed a real-time respiratory motion correction for simultaneous PET-MR using an MR-derived motion model. Later, King *et al.* [176] propose and describe a technique for free-form nonrigid respiratory motion correction in the thorax. The model is based on a principal component analysis of the motion states encountered during different breathing patterns, and is formed from motion estimates made from dynamic 3-D MRI data. Finally, the authors demonstrate a potential application of the technique, which is MRI-based motion correction of real-time PET data for simultaneous PET-MRI acquisition.

A summary of published non X-ray image based motion gating/compensation methods is given in Table 2.2 detailing the motion gating/compensation technique, the organ used and the type of motion the technique was developed to gate/compensate, illustrated with a C for cardiac motion , R for respiratory motion and C/R when the method handles both cardiac and respiratory motion. The techniques are categorised according to the imaging modality employed. These include MR, US, CT and PET/SPECT.

2.3 X-ray image based motion gating/compensation techniques

Several X-ray image-based approaches have been developed in which motion is extracted purely from the X-ray images, which are then processed to correct for the motion. In this section the aims and methodologies regarding more recent X-ray image-based techniques are described. The section is categorised into anatomical feature detection/tracking based, motion modelling based, weighted centroid measurement based, dimensionality reduction based, phase correlation based and interventional device detection/tracking based techniques.

2.3.1 Anatomical feature detection/tracking based techniques

Several motion gating/compensation techniques using tracking of visible anatomical structures in the X-ray images have been developed and proposed. In this section, the key papers are summarised.

Martin-Leung *et al.* [177] propose a method that estimates the respiratory phases from grey-level X-ray fluoroscopic images used for procedure guidance based on their similarity to a pre-procedural recorded angiographic reference frame by applying a mutual information (MI) similarity measure. The MI calculation was performed only on selected ROIs and the results were

TABLE 2.2: Key papers on non X-ray image based motion gating/compensation available in the literature, categorised by the imaging modality employed. The summary details the technique applied, modality used and the type of motion being gated/compensated.

Paper	**Technique**	**Motion**
Magnetic resonance imaging		
Kellman *et al.* 2008 [141]	Image-based navigator	R
Van der Weide *et al.* 2001 [142]	Intravascular device tracking	R
Wang *et al.* 1996 [143]	Navigation echoes for diaphragm tracking	R
Ehman *et al.* 1989 [144]	Navigation echoes for diaphragm tracking	R
Wachinger *et al.* 2010, 2012 [145, 146]	LE	R
Bhatia *et al.* 2012 [97]	HML	C/R
McLeish *et al.* 2002 [102]	Motion models	R
Manke *et al.* 2002, 2003 [147, 148]	Affine motion models	R
Nehrke and Bornert *et al.* 2005 [149]	Affine motion models	R
Ultrasound		
De Winter *et al.* 2003 [150]	Feature extraction/classification	C
Zhu *et al.* 2003 [151]	Image intensity	C
Karadayi *et al.* 2006 [152]	Centroid algorithm	C
Ballard *et al.* 1981 [153]	Generalised Hough transform	C
Van Horn *et al.* 1994 [154]	Generalised Hough transform	C
Wachinger *et al.* 2010,2012 [145, 146]	LE	R
Isguder *et al.* 2010 [155]	LE	R
King *et al.* 2010 [156, 157]	Rigid/affine motion models	R
Peressutti *et al.* 2012, 2013 [158, 159]	Affine motion models/Bayesian estimation	R

Table 2.2 continued from previous page.

Paper	Technique	Motion
Computed tomography		
Georg *et al.* 2008 [160]	Isomap	R
Carnes *et al.* 2009 [161]	Image similarity	R
Eck *et al.* 2005 [162]	Image similarity	R
Chavarrias *et al.* 2008 [163]	Projection image intensity	R
Farncombe *et al.* 2008 [164]	Projection image intensity	R
Hu *et al.* 2004 [165]	Image intensity	R
Sonke *et al.* 2005 [166]	Filtered 1D projections	R
Manzke *et al.* 2004 [167]	Image correlation	C
Positron emission tomography/Single-photon emission computed tomography		
Klein *et al.* 2001 [168]	Centre-of-mass computation	R
Bundschuh *et al.* 2007 [169]	Centre-of-mass computation	R
Bruyant *et al.* 2002 [170]	Centre-of-mass computation	R
Buther *et al.* 2009 [171]	Filtering	C/R
Visvikis *et al.* 2003 [172]	Characteristic frequency using Fourier transform	R
He *et al.* 2008 [173]	Axial motion	R
King *et al.* 2011b [175]	Motion models	R
King *et al.* 2012 [176]	Motion models	R
Thielemans *et al.* 2011 [174]	PCA	C/R

varying depending on the choice of ROIs. This technique was compared to the local correlation technique [178] regarding accuracy and robustness but no quantification of its accuracy was carried out. A similar approach using normalised MI was presented by Moser *et al.* [179]. In this feasibility study, a single image from the entire fluoroscopic sequence was used as a reference out of the series and compared with all other images by calculating the normalised MI and looking for accordance in the respiratory phase. The approach was also extended to inter-modal comparisons between fluoroscopic images and digitally reconstructed radiographs, which offer the additional possibility of considering differences between planning and treatment situations adequately. This technique was validated by comparing the derived signals to a commercially available respiratory gating system (AZ-733V, Anzai Medical, Tokyo, Japan) that consists of a load cell (miniature compression load cell), which is fixed to the patient with a waist belt, and proportionally converts changes in the chest or abdomen diameter during respiration into an analogue electrical signal. However, this method was only tested on one patient data set, thus questioning the validity of the study. Berbeco *et al.* detected the breathing phase information by analysing the fluoroscopic intensity fluctuations in the lung. However, the approach requires the selection of an ROI in a section of the middle of the lung that does not contain the tumor [180].

Ma *et al.* [95, 96] developed and clinically evaluated a motion gating method for respiratory motion compensation based on diaphragm tracking. This method tracks the image intensity within a manually defined rectangular ROI that lies across the diaphragm. The diaphragm motion of subsequent X-ray images is determined by computing the 1D translation (along the long axis of the rectangle) that minimised the mean sum of squared differences between the intensities in the current image and the reference image within the ROI. To compensate for the respiratory motion, the 3D heart roadmap was translated along the head-to-foot vector of the patient by the 1D displacement of the diaphragm and evaluated using the lasso catheter tip electrode in the X-ray data as a reference structure. However, this method requires a motion correction factor (0.6) which may not be valid for all patients. Additionally, it requires a manually defined ROI which is free of other features such as guide wires or catheters. The ROI may have to be changed often due to C-arm rotation, changing contrast and features moving into the ROI.

Condurache *et al.* [181] proposed a different method to extract the respiration information by detecting and tracking the diaphragm in X-ray projection images of the chest. For this method the diaphragm is described using the boundary of its projection, which was assumed to be approximately circular in shape. Diaphragm detection is then based on edge detection followed by a Hough transform for circles. To avoid misleading effects from vessel and shutter edges, morphological filtering in the image and minimum intensity projection in the edge map have been applied, respectively to eliminate them. To restrict the search in the Hough parameter space and thus provide real time capabilities to the algorithm, prior anatomical knowledge about

position and size of the diaphragm was considered. In subsequent frames, diaphragm position and size are predicted from previous detection and tracking results.

A common problem for these approaches is that the diaphragm is not always visible in cardiac X-ray images due to collimation to reduce radiation dose. Additionally, the diaphragm is not often in the field of view, especially when considering the case of obese patients. An alternative to diaphragm tracking is to use heart border tracking. Ma *et al.* [95, 96] proposed a method based on tracking the heart border using the image intensity in a ROI, similar to their diaphragm tracking method. However, heart border tracking can be influenced by cardiac cycle motion. This method also requires manual initialisation of the defined ROI that will be tracked.

A different method was developed by Ma *et al.* [95, 96] that detects the trachea bifurcation using the generalised Hough transform (GHT). This feature was chosen as it is located immediately above the left atrium and moves in a similar way to the left atrium during respiratory motion. It is also clearly visible in cardiac X-ray fluoroscopic images, making it a good choice as an anatomic surrogate for motion correction. Nevertheless, this method becomes less robust and accurate when it is used for low dose X-ray images. This is because low dose X-ray images have fewer strong edges for the tracheal bifurcation and this causes the GHT method to detect the wrong object. The trachea detection method requires a 3D model to generate the 2D GHT contour model. In this study, it was found that the pre-operative 3D MRI image data was not ideal for generating the 3D tracheal model because of the low contrast of the tracheal bifurcation in the MR images yielding a noisy and truncated model of the trachea.

2.3.2 Motion modelling based techniques

Motion modelling techniques have been proposed to estimate and compensate for cardiac and respiratory motion in image acquisitions and image guided interventions. A motion model can be defined as a process that takes some surrogate data as input and produces a motion estimate as output. In this section various motion modelling techniques that have been proposed in the literature as a solution to the problem of cardiac and respiratory motion of the heart during X-ray fluoroscopy image guided cardiac catheterisation interventions are reviewed.

Different motion models including translation, rigid body and affine transformations as well as statistical models have been investigated by several studies to characterise the effect of respiration on the heart and coronary arteries. Respiratory phase determination by diaphragm tracking was demonstrated by Shechter *et al.* [182], in which a cardiac respiratory parametric model (CRPM) of the motion of the coronary arteries was constructed from biplane contrast-enhanced X-ray image sequences. By tracking the displacement of the diaphragm in the angiograms, a respiratory signal was obtained. Later, the same CRPM was used to retrospectively and prospectively correct images acquired at any cardiac/respiratory phase combination [183]. However, forming

the model from X-ray images under contrast injection means that it will be constructed from a limited amount of data. Similarly to various anatomical feature detection/tracking based techniques, the main drawbacks of these approaches are that they require manual landmark selection for diaphragm tracking and the use of the contrast agent. As mentioned previously, the diaphragm is not always in the X-ray field of view, particularly for obese patients.

Schneider *et al.* [184] proposed and validated a PCA-based respiratory motion model, again from contrast-enhanced X-ray images, for motion compensation during image-guided cardiac interventions. In building the respiratory motion model, PCA is applied on samples obtained from rigid 2D/3D registration of a preoperative 3D segmentation of the coronary arteries. The PCA model is subsequently used to constrain re-registrations performed during interventions.

Models have been proposed that are formed from MR imaging [94]. King *et al.* [94, 185] developed MRI models of respiratory motion incorporated into roadmaps to guide electrophysiology procedures. Respiratory motion was extracted from a single MRI volume acquired at end-expiration registered to 2D or 3D dynamic acquisitions at various respiratory phases. An affine motion model for the heart was computed, and the affine parameters were fitted to polynomial functions of the diaphragm position. The model was applied by tracking the diaphragm position in the X-ray fluoroscopy imaging and updating the roadmap accordingly. Because the model was only valid at end-diastole, the X-ray images were ECG-gated.

Zhu *et al.* [186] proposed a temporally compositional motion model for respiratory motion compensation for coronary roadmapping in fluoroscopic images. The model is used to deal with large image motion incurred by deep breathing. Specifically, an extended Lucas-Kanade algorithm involving a weighted sum-of-squared-difference measure is proposed to estimate the soft tissue motion in the presence of static structures.

Faranesh *et al.* [187] proposed a motion compensation technique to incorporate both cardiac and respiratory motion into dynamic, motion-corrected 3D roadmaps to guide cardiac interventional procedures. Real-time MR images acquired in several planes were used to construct affine models for the individual cardiac structures of interest, to capture variation in motion between different parts of the heart. These models were then used to drive the motion of 3D roadmaps fused onto live X-ray fluoroscopy.

As highlighted in McClelland *et al.* [188], most of the motion modeling work proposed to date remains as research proposals. The only respiratory motion model currently in use in the clinic is embedded in the cyberknife system for RT treatment [189]. One reason for this lack of clinical translation lies in the lack of accuracy or robustness of many current motion-modelling techniques. Furthermore, according to King *et al.* [94], the majority of the motion of the heart caused by the respiratory motion is translational motion and the majority of the translational motion of the heart is in the superior-inferior (SI) direction (head-to-foot direction). Although

1D motion models or 2D translational motion models are less accurate than more comprehensive motion models such as patient specific affine motion models, they do not require additional patient specific data and lengthy computation and can be used in any EP procedure. In the sections below, motion compensation is accomplished using 1D motion or 2D translational motion of the heart in the SI direction.

2.3.3 Weighted centroid measurement based techniques

Lehmann *et al.* [190] proposed a technique capable of measuring coronary motion from the 2D projection images acquired during rotational angiography, with the aim of developing an image-based cardiac gating strategy specifically for 3D coronary angiography. The image-based technique is based on the weighted centroid of the opacified coronary arteries. The 1D vector component of the centroid that is parallel to the axis of rotation is chosen as the image-based metric of motion. In coronary angiography the patient's SI axis is roughly aligned with the detector's axis of rotation, therefore the image-based metric of motion is the SI component of the weighted centroid (SIC), and this is used to track vessel motion. However, the 1D vector component of the centroid that is parallel to the axis of rotation is independent of the angular position of the detector. Therefore, this technique has the advantage of being view-angle independent, and therefore much more clinically useful than other motion gating/compensation algorithms. Nevertheless, the technique's robustness as a function of angle is not fully tested as the authors analysed data from only two views. Clinically, where small field of view (FOV) X-ray image intensifier detectors are used in coronary angiography, the background structures may move in and out of the FOV and it is important that their effect on the SIC measurement be minimised. An additional drawback of this technique is that it can only gate the cardiac motion of the heart. The utility of the technique in 3D coronary angiography has been demonstrated in an animal study. The success of the animal experiment is encouraging, but further analysis of 3D clinical angiograms is necessary.

2.3.4 Dimensionality reduction based techniques

Fischer *et al.* [191] presented a method to extract a respiratory signal using incremental ISOMAP from live X-ray sequences in real-time. Incremental ISOMAP updates the embedding without recomputing unchanged information. The eigendecomposition is not computed from scratch, but updated from the previous solution, assuming that the new point does not change the manifold and thus the eigenvectors and eigenvalues drastically. As the relative importance of the eigenvectors is not important for this application, the embedding is not weighted by the eigenvalues as in standard ISOMAP. Instead, the eigenvectors are normalised to length N, the

number of points in the manifold, to avoid shrinkage of the eigenvector components due to newly arriving samples.

However, at least one full breathing cycle must be observed in a training phase of T images at the beginning of the procedure before the mapping can give correct results. Another drawback of this method is that a change of the C-arm angulation or the table position invalidates the mapping. Therefore, it must be relearned after each system movement. Additionally, this technique was only validated on animal data and cannot be used to extract cardiac motion information.

2.3.5 Phase correlation based techniques

One method for automatic image-based motion gating is to calculate the cumulated phase shift in the spectral domain from X-ray coronary angiography images as a measure of the net motion of objects in the scene [192].

The main drawback of the phase correlation algorithm is that it finds the global translation in the image plane; it assumes that objects in the scene exhibit only translations. This limitation is illustrated by Wachinger *et al.* [146] by producing synthetic images which show periodic motion. The first scenario consisted of a rectangle moving up and down. For the second scenario, a fixed rectangle was added, and for the third a rectangle that grows and shrinks was added. The three scenarios are illustrated in blue, red and green colours, respectively in Figure 2.1a. The corresponding energy curves of the phase correlation technique have been plotted in Figure 2.1b. For the first scenario (blue) the signal is correct. The addition of a fixed object (red) already leads to a slight distortion, while the addition of the shrinking/growing object (green), leads to an extraction of a false motion signal. Since the addition of the shrinking/growing object prevents the extraction of the correct motion, it is likely that this approach is not best suited for motion estimation in EP images where the organ motion is not necessarily in-plane, and consequently, there is no uniform global translation. To further validate this assumption the phase correlation algorithm is applied to EP images and the motion is extracted and validated. This is illustrated in Chapter 5.

Specifically, in the case of clinical data, the energy change could be caused by the motion of catheters or contrast agent injection. As the method uses the overall motion of moving objects, the cardiac and respiratory cycle motions detected by this method could be incorrect when the clinician manipulates the catheters or injects contrast agent.

Motion gating methods based on catheter motion detection have also been proposed in the literature. These applications require fast, accurate, and robust image-based catheter detection methods. However, to design such methods and use them during EP procedures is a challenging

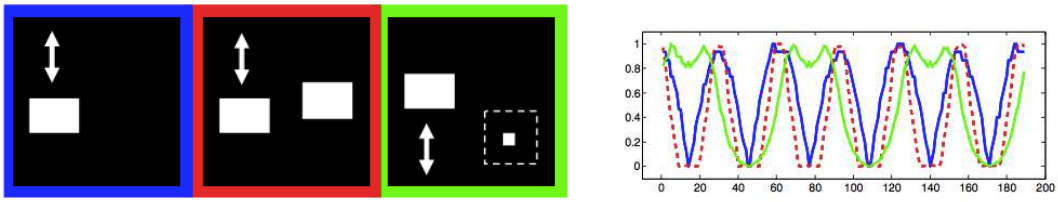

(a) (b)

FIGURE 2.1: Analysis of the phase correlation technique for synthetic images. (a) The three different motion scenarios are illustrated, with (b) their corresponding energy (gating) curves. Reproduced with permission from [146]. Copyright Elsevier B.V.

task. Motion gating/compensation techniques based on interventional device tracking available in the literature are presented and reviewed in the following section.

2.3.6 Interventional device detection/tracking based techniques

Meijering *et al.* [193] gave a review of techniques to track objects and structures within user-defined ROIs in X-ray images. Various techniques rely on guidewire tracking [194, 195] to locate a coronary artery in fluoroscopic images. In recent research practice, the medical imaging community has refocused its efforts to detect catheters directly in X-ray images. Many different types of catheters are used during EP procedures, each having specific configurations of electrodes (e.g. size, shape). These electrodes are used for the measurement of electrical signals within the heart and also for the delivery of radiofrequency energy during treatment. Accurate and robust localisation of catheters in the X-ray images can provide enhanced functionality during procedures for guidance and also for post-procedural analysis. Electrode detection methods must be robust enough to be used routinely during clinical procedures. The most relevant works on EP catheter tracking in the literature are reviewed, emphasising the key contribution of each work.

A technique for tracking catheters in X-ray images was first proposed by Franken *et al.* [196]. The method uses a steerable tensor voting in combination with a catheter-specific multi-step extraction algorithm. This method is tested on noisy fluoroscopy images, by adding Poisson noise to the images. The success rates for extraction of the catheter tip and extraction of the entire catheter are low, especially in noisy images ($43\% - 57\%$). The computational cost was relatively high making the method not applicable in clinic. Implementation on a graphical processing unit was suggested.

A crucial application of catheter localisation is to record the position of the ablation catheter-tip in X-ray and map it onto the 3D roadmap during ablation therapies. Fallavollita *et al.* [197]

developed a catheter tip detection algorithm based on thresholds of the fluoroscopic images. However, this technique failed in low contrast images.

Wu *et al.* [198] proposed an approach to automatically build the CS catheter model by analysing the catheter shape and electrode number from user initialisation, by marking the electrodes in the order from the tip to the proximal electrode in the first frame. Novelly designed hypotheses generated by a number of learning-based detectors were fused to automatically detect and track the catheter in fluoroscopy. Robust hypothesis matching through a Bayesian framework was then used to select the best hypothesis for each frame.

A proposed method for addressing multiple catheter tip-detection was presented by Yatziv *et al.* [199]. Here the authors require user interaction for their detections using a geodesic framework. Furthermore, Milletari *et al.* [200] proposed a method to perform automatic detection of EP catheters in fluoroscopic sequences. This approach does not need any initialisation, is completely automatic, and can detect an arbitrary number of catheters at the same time. The method is based on the use of blob detectors and clustering in order to detect all catheter electrodes, overlapping or not, within the X-ray images.

The motion and deformation of catheters that lie inside cardiac structures can provide valuable information about the motion of the heart. Hence, detection and tracking of EP catheters can potentially be used for motion gating and/or motion compensation. Eliminating and/or compensating for the motion results in improved guidance information, a significant factor for a successful procedure outcome. The above detection and tracking techniques could potentially be used for motion gating/compensation. Nevertheless, no such application and validation was provided. Various successful approaches where tracking of the EP catheters can be used for motion gating/compensation are available in the literature [201–209]. A thorough review of these techniques is presented below.

2.3.6.1 CFM catheter tracking techniques

Brost *et al.* [201, 202] proposed an image-based respiratory motion correction technique, performed by tracking the 3D position of a lasso catheter, or in other words the CFM or mapping catheter, from biplane X-ray images, illustrated in Figure 2.2. Firstly, a 3D model of the CFM catheter was reconstructed from two views. Secondly, the reconstructed catheter model was tracked by 2D/3D image registration to estimate the respiratory motion at the site of ablation.

The algorithm is based on the assumption that the perspective projection of a lasso catheter, when fit to the pulmonary veins, can be approximated as a 2D ellipse. The lasso catheter is reconstructed in 3D from biplane X-ray projections that are taken simultaneously using a calibrated biplane C-arm X-ray system. The assumption that the lasso catheter can be approximated as

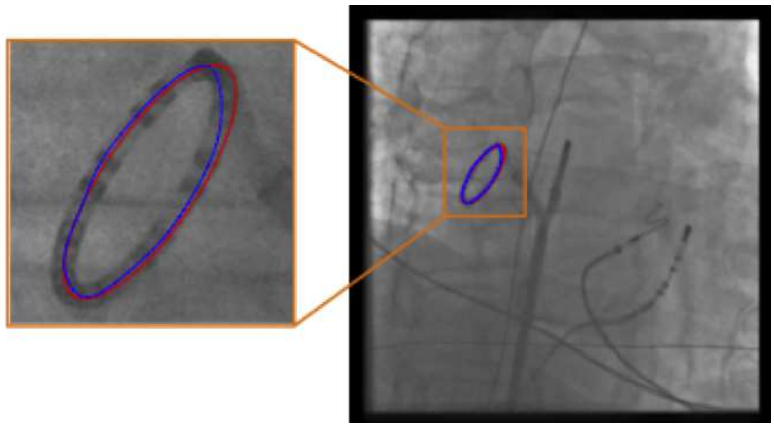

FIGURE 2.2: Lasso catheter tracking technique. Reproduced with permission from [201]. Copyright Springer.

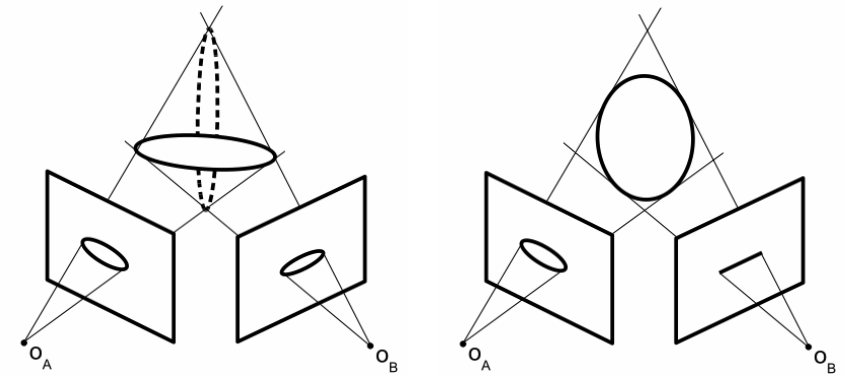

(a) (b)

FIGURE 2.3: The figure illustrates the two scenarios when reconstructing a 3D model of a CFM catheter from two views. (a) This case shows two possible solutions when reconstructing a 3D ellipse from biplane 2D ellipses. The correct solution can be found by using prior knowledge, e.g., of the diameter of the circumferential mapping catheter. (b) This special case reconstructs a 3D ellipse from one 2D ellipse in one X-ray view and a line in the other. Reproduced with permission from [202]. Copyright Elsevier B.V.

an ellipse in 3D was taken because a 3D elliptical object remains elliptical when perspective projected onto a 2D imaging plane. Under some special view orientations, the ellipse can, however, collapse to a line. As a consequence, the algorithm is designed to reconstruct a 3D lasso model either from 2D ellipses extracted from biplane X-ray views, or from one ellipse and one line. The two cases are illustrated in Figure 2.3a and b, respectively.

After the 3D model of the CFM catheter has been generated from the first frame of the fluoroscopic sequence, it is tracked in 3D throughout the remainder of the biplane sequence by performing 2D/3D registration on pre-processed X-ray images. The reconstructed 3D catheter model is first rotated and then translated in 3D by the transformation matrices, R and T, respectively. Then it is projected onto the two imaging planes of the biplane C-arm system. The average distance between the projected points and the closest feature point (i.e. the circumferential mapping catheter) in the fluoroscopic images is efficiently calculated using a distance map.

The average instance is used to optimise the registration transformation.

A disadvantage of this method is that a biplane system is less common than a monoplane system in the clinical setting due to its much higher cost, and involves increased radiation exposure for both the patient and the clinician. Additionally, cases exist where the algorithm fails to accommodate catheters of different size or detects wrong structures in the presence of high background clutter.

Later, Brost *et al.* developed a similar respiratory motion correction method that requires only monoplane fluoroscopy and therefore works in 2D [203]. The 2D ellipses are calculated, and then CFM catheter is tracked throughout the sequence [201, 202] to perform motion estimation.

To avoid the possible cases where the previous algorithm failed to accommodate catheters of different size or the possibility of detecting wrong structures in the presence of high background clutter, a learning-based segmentation was introduced to replace the previously proposed filter-based one [204]. This approach requires a training phase for the segmentation of the catheter. After the 3D model is reconstructed, a combination of Haar-like features [210] and a cascade of boosted classifiers is used to segment the CFM catheter. This learning-based algorithm avoids enhancing unwanted structures. After the learning based segmentation is achieved the 3D motion at the site of ablation is estimated by tracking the reconstructed model in 3D from biplane fluoroscopy, similarly to the filtered-based technique described previously [201, 202].

Later, a learning-based method that relied only on monoplane fluoroscopy to perform 2D motion compensation was presented by the authors. Specifically, in this technique the CFM catheter is tracked by a combination of learning-based catheter classification and then model-based 2D/2D registration [206].

Following this work, an additional approach was proposed that facilitates full 3D motion compensation even if only monoplane X-ray views are available [207]. In EP labs equipped with biplane C-arm systems, often only one imaging plane is used at a time to reduce the dose to the patient. In this case, the methods suggested in [201, 202, 204] are not applicable. The 2D methods described in [203, 206], which require only monoplane fluoroscopy, are not ideal either as they require re-initialisation of the catheter model as soon as the C-arm view direction changes. Consequently, to perform motion compensation using a 3D catheter model, a constrained 2D/3D registration was proposed using only a single biplane shot for the generation of a 3D catheter model. The registration restricts the search directions in 3D to be parallel to the imaging plane. No search is performed perpendicular to the optical plane, i.e., along the optical axis.

However, this method assumes that shifts along the optical axis merely result in size changes of the motion-compensated fluoroscopic overlay. For the method to be successful the mismatch in

depth between the 3D overlay and the live fluoroscopic images should result in no changes of the left atria size for augmented fluoroscopy applications in clinical practice.

In Brost *et al.* [205], the CS catheter was used as a point of reference to detect when the CFM catheter had been moved from one PV to another, while the motion estimate for adapting the fluoroscopic overlay was derived by localising the CFM catheter. The motion compensation approach involved tracking of the CFM catheter as well as tracking of a virtual electrode (VE) placed on the CS catheter. The absolute distance between the centre of the CFM catheter and the VE is used to identify whether the CFM has been moved from one PV to another. The VE was a reference point set by clicking on an arbitrary position along the catheter sheath that has to be more proximal than the most proximal real electrode. Similar to the CFM catheter, manual interaction is used to generate the initial CS catheter model in the first frame in a fluoroscopic sequence. Using a tracking framework combined with a geodesic constraint, the VE is tracked throughout the remaining sequence. For this approach the authors assumed that the absolute distance between CS catheter and CFM catheter remains sufficiently stable to classify whether the CFM catheter has been moved away from a PV ostium. Both catheters were tracked at the same time and the absolute 2D distance between the VE and the CFM catheter loop's centre between two consecutive frames was compared. If the distance changed by more than a certain percentage, then it was assumed that the CFM catheter had been moved from one PV to another. In this case, no motion compensation was applied to the fluoroscopic images until another stable CFM position had been reached.

However, the maximum frame rate of the lasso catheter tracking was only 3 frames per second (fps) in the biplane X-ray system and 10 fps in the monoplane X-ray system. To overcome this problem, the previously proposed method by Brost *et al.* [207] was altered to reduce computation time. The new method proposed the application of the distance transform to the pixels classified as catheter and not to the pixels identified as background [208]. Specifically, the distance transform is only calculated for those pixels segmented as catheter, and the highest values of the distance transform are found along the centreline of the catheter. As a result, the processing speed increases to 20 fps, but at the same time, the method becomes less accurate.

Nevertheless, all the above techniques proposed by Brost *et al.* rely on tracking a CFM catheter when it is in firm contact with a PV during ablation for atrial fibrillation. The lasso catheter is not universally present in EP procedures. As a result the methods are not generally applicable to other interventional procedures. For the methods to be successful the assumption that the CFM catheter remains anchored at the PV being ablated needs to be made. This might not always be the case as its position is frequently changed within the heart by the cardiologist. An additional disadvantage is that all the tracking methods required manual initialisation. Specifically, the projection of the mapping catheter on the imaging plane should be first extracted by manual clicking followed by fast marching in one frame of the fluoroscopy sequence.

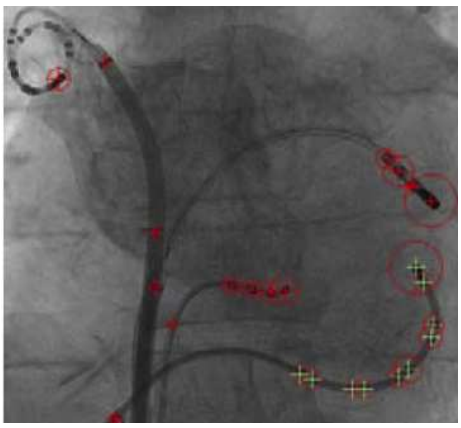

FIGURE 2.4: CS catheter tracking technique. Reproduced with permission from [209]. Copyright Springer.

2.3.6.2 CS catheter tracking techniques

Ma *et al.* [95, 96, 209] proposed a different method to correct for respiratory motion using real-time image-based CS catheter tracking, illustrated in Figure 2.4. The technique works by first using a fast multi-scale blob detection method to detect all possible electrode-like objects in the X-ray image. Then a cost function is computed to select the CS catheter from all catheter-like objects in the image. This technique is then applied to correct for respiratory motion by applying a low pass filter to the 2D motion of the CS catheter and updating the 3D roadmap using this filtered motion.

In practice, Ma *et al.* pre-compute the masks of these Gaussian derivatives, convolve with the input image and calculate the determinant of the Hessian matrix. Blobs are defined as local extrema of the determinant of the Hessian matrix and the strength of the blob as the normalised value of the determinant of the Hessian matrix. The next step involves deciding which combination of blobs represents the CS catheter. Based on the shape model of the 10-electrode CS catheter a unified cost function was designed to estimate the likelihood of candidate catheter-like objects.

Finally, the CS detection method was used to correct for respiratory motion in 2D fluoroscopic image sequences during cardiac EP procedures. This approach tracks the position of the proximal electrode of the 10-electrode CS catheter to use for respiratory motion correction. The reason for choosing this electrode is that the proximal electrode has less cardiac cycle motion and has lower tracking errors than the distal electrode (catheter tip). For a monoplane X-ray system, a low pass filter to the 2D translational motion of the proximal electrode was first applied to reduce cardiac motion further and then the filtered 2D translational motion was applied directly to the 3D roadmap.

Authors claim that the proposed CS catheter detection method is accurate and robust even in lower dose fluoroscopy images as CS catheter electrodes remain highly visible. In this paper, normal dose refers to X-ray sequences of kVp range from 77-82kVp and peak X-ray current from 736-989mA. The frame rate of normal dose X-ray sequences is ±7.5 fps. Low dose refers to X-ray sequences with a frame rate of 3 fps, a kVp range from 81–96kVp and peak X-ray current from 2–4mA. A sub-millimeter accuracy of the CS catheter detection method was achieved. Updating the 3D roadmap by the filtered 2D motion of the CS catheter significantly improved the accuracy of fluoroscopy overlays for cardiac EP procedures. This method was used to detect respiratory motion, but since it is real-time, achieving a frame rate of 21 fps, it could potentially also be applied to the detection of the much faster cardiac cycle motion. Additionally, it does not require any user interaction and can detect the CS catheter position without defining a ROI in the X-ray image. However, the presence of cardiac cycle motion in the CS catheter is a potential disadvantage for respiratory motion correction.

Later, Ma *et al.* [211] developed an automatic image-based ablation point tagging system for AF ablation procedures, based on real-time simultaneous detection of the CS catheter and the ablation catheter. This method facilitates full 3D motion compensation even if only monoplane X-ray views are available. The first step of the method is the tracking of the two catheters. After tracking the two catheters, the CS catheter was used for motion gating. This method was designed to find a pair of images in similar respiratory and cardiac cycle motion phases from two short X-ray fluoroscopic image sequences, which were acquired from two different angle-views, anteroposterior (AP) and left/right anterior oblique (LAO/RAO) view, using a monoplane X-ray system when both the ablation catheter and CS catheter remain stationary. To find the pair of images, the CS catheter was tracked in every frame of the two sequences. For each possible pair of images from two views, the 3D position of the proximal electrode of the 10-electrode CS catheter was reconstructed using the epipolar constraint and the 3D point was the mid-point of the shortest line segment connecting two epipolar lines. After computing the 3D position of the proximal electrode, the 3D point was projected back to the two image planes to obtain two 2D projected points. A 2D error was defined as the distance between the projected point and the original 2D position of the proximal electrode in one X-ray image view. The reconstruction error of the 3D point was defined as the maximum of the two 2D errors. An error matrix was computed as reconstruction errors among all possible pairs of X-ray images. Finally, the motion gating was achieved by selecting a pair of images with a minimum reconstruction error. The 3D position of the ablation catheter tip head was computed from this pair of images and mapped onto the surface of the 3D roadmap and the 3D roadmap was constantly moved with the motion of the proximal electrode of the CS catheter.

Finally, Ma *et al.* [212] extended their basic CS catheter detection method by developing a unified framework that can be adapted to detect any of the three most common types of EP catheter

(CS, ablation and lasso). This generalised computational framework for catheter detection and tracking includes fast blob detection, shape-constrained searching, model-based detection, and template-based tracking. This method could potentially be used for respiratory motion correction for 3D anatomical overlay guided EP interventions. However, no such application was demonstrated in that study. An important drawback of this technique is that the method is unsuccessful at X-ray doses where the CS catheter electrodes are not highly visible throughout the X-ray images.

Kaeppler *et al.* [213] proposed a different method to achieve motion compensation for fluoroscopy guided cardiac ablation procedures by localising the CS catheter. The movement of the CS catheter during the cardiac cycle is captured using a feature set based on the positions of the electrodes of the CS catheter. These features, computed for all images in a training set, include information on relative positions and angles between catheter electrodes, and are used to capture CS catheter rotations and deformations which are typical for cardiac motion. Based on this information the position of the CFM catheter is estimated. To correlate the motion of both catheters, this method includes a training phase in which both catheters are tracked together using the method proposed by Wu *et al.* [198]. The acquired data is then used to set up an estimation model for the position of the mapping catheter. After that, the model can be used to estimate the cardiac and respiratory motion of the left atrium by observing the CS catheter only. This method assumes that both the CS and the mapping catheter are equally affected by respiratory movement while heart beat related motion patterns of the two catheters usually differ.

Similarly to the work developed by Brost *et al.*, the limitation that the lasso catheter is not universally present in EP procedures exists. As a result the proposed method is not generally applicable to other interventional procedures. Additionally, the CFM and the CS catheter tracking require manual initialisation. This method is only applied to normal dose images. The effectiveness of this method in lower dose images is not demonstrated. Since EP procedures result in substantial patient and staff radiation doses due to the long fluoroscopy duration and radiation exposure, which might result in acute radiation-induced skin injuries or radiation-induced cancer, it is necessary to minimise patient dose in order to outweigh the radiation risk by the benefit of the interventional procedure. Therefore, developing a robust-to-noise gating technique can potentially minimise patient exposure to radiation by allowing the use of lower dose fluoroscopy. This thesis is devoted to developing such motion gating techniques and their successful application to X-ray images with low dose. Application with the dose reduced by more than 50 times, where the CS catheter electrodes might not be visible to the human eye, is demonstrated.

2.3.7 Review

Key papers on X-ray image-based motion gating/compensation available in the literature are summarised in Table 2.3 detailing the motion gating/compensation technique used, purpose, study and motion. "Technique" is included to reveal essential information about the method proposed, i.e. whether it is a learning/filter-based, model, tracking-based approach etc. Included in this column is the anatomical structure/interventional device used for the development of the technique. "Purpose" states whether the developed technique demonstrates motion gating and/or motion compensation of cardiac catheterisation procedures. This are illustrated as G, for motion gating, C, for motion compensation and N/A if the technique is developed to be potentially useful for motion gating/compensation but no such validation is illustrated by the authors. "Study" states whether the proposed technique was validated on clinical and/or phantom data. The last column of Table 2.3 reports whether the motion the technique was developed to gate/-compensate was cardiac, C, respiratory, R, or both, C/R. This table is categorised according to the classification of each proposed algorithm. These include anatomical feature detection/-tracking based, motion modelling based, weighted centroid measurement based, dimensionality reduction based, phase correlation based and interventional device detection/tracking based techniques. Quantitative comparison of the methods, for example in terms of accuracy and variability, is difficult because of the different ways in which the approaches have been validated, the different ways in which experimental results have been reported and the different datasets used by each approach. However, such a comparison is given in Table 2.4, as an attempt to emphasise the limitations of the techniques proposed to date that this thesis seeks to overcome. Nevertheless. in Table 2.4, the X-ray image based techniques most relevant to the work behind this thesis are summarised. Included in this table are # sequences/patients/frames, accuracy, speed, success rate, tracking error, average M_{rec}, image acquisition, model, X-ray image dose, gold standard correlation and RMS. "Accuracy" is given in terms of a mean 2D- or 3D- target registration error (TRE), if available. TREs need to be compared to a standard reference technique. This reference can be found by manual alignment by a clinical or imaging expert, using static fiducial markers, based on a pre-calibration of the system, or by some other proven technique. Robustness is measured in terms of a percentage "success rate", with success defined as achieving accuracy within a clinical tolerance of 2 mm for most targets in the heart, or being deemed successful by a clinical expert. For the methods proposed by Ma *et al.* and King *et al.*, the success is defined as achieving accuracy within 5 mm. The percentage of the motion recovered, M_{rec}, is calculated as

$$M_{rec} = \frac{100(TRE_{before} - TRE_{after})}{TRE_{before}} \tag{2.1}$$

where TRE_{before} and TRE_{after} are the average TREs over all validation frames before and after the respiratory motion correction.

"Image acquisition" illustrates whether the technique is applicable to monoplane, biplane systems, or rotational angiography. "Model", refers to whether motion compensation was done using 1D, 2D, 3D translation, affine models, etc. "RMS" refers to the root mean square error of the developed model, a statistical measure of the magnitude of a varying quantity. Only papers proposing and validating motion gating/compensation are considered, leaving techniques that could potentially be used for motion gating/compensation out of the review table. Additionally, to allow direct comparison to the techniques developed throughout this thesis the table reviews only image-based techniques that are used for X-ray fluoroscopic image acquisitions, targeting the anatomical region of the heart in cardiac catheterisation procedures.

2.4 Discussion

Incorporating cardiac and respiratory motion into fused roadmaps for increasing suitability and accuracy in guiding diagnostic catheterisation, structural heart interventions, and electrophysiology procedures has been attempted using the plethora of methods that are outlined in this review chapter.

Regarding the non-image based motion gating/compensation techniques, as can be noted in Section 2.1, some considerable progress over time can be observed. As already noted in this chapter, non-image based techniques require fiducial markers, additional contrast agent, special hardware which interferes with the clinical workflow or possible hysteresis between the internal movement and external device. Consequently, the necessity to improve the motion estimation accuracy and its clinical application has led to the investigation and proposal of more sophisticated techniques that are able to detect the cardiorespiratory phases using the images themselves.

X-ray image-based motion gating/compensation techniques have been proposed based on tracking anatomical ROIs, such as the diaphragm, regions in the lung, the heart border or the trachea bifurcation. A common problem for these approaches is that they require manual initialisation of the defined ROIs that will be tracked which should be free of other features such as guidewires or catheters. Additionally, ROIs may have to be changed, due to C-arm rotation, changing contrast or features moving into the ROI. As shown in McClelland *et al.* [188], respiratory motion modelling, an alternative way to estimate and correct for respiratory motion, is an emerging field, but to date the clinical uptake has been very limited due to a lack of accuracy and robustness, and the interruptions that this typically introduces into the clinical workflow. A motion gating algorithm based on the calculation of the cumulated phase shift in the spectral domain from X-ray coronary angiography images has reported very successful results for the extraction of cardiac and respiratory motion. However, this technique finds the global translation in the image plane, and it assumes that objects in the scene exhibit only translations. Consequently,

TABLE 2.3: Key papers on X-ray image based motion gating/compensation available in the literature, categorised by the classification of each algorithm. The summary details the technique applied, purpose, study and the type of motion being gated/compensated.

Paper	Technique	Purpose	Study	Motion
Anatomical feature tracking based techniques				
Martin-Leung *et al.* 2003 [177]	Mutual information (MI) similarity measure	G	clinical	R
Moser *et al.* 2008 [179]	Normalised MI	G	phantom	R
Berbeco *et al.* 2005 [180]	Fluoroscopic intensity fluctuations	G	clinical	R
Ma[1] *et al.* 2011b, 2012 [95, 96]	Diaphragm tracking (track intensity differences)	C	clinical	R
Ma[2] *et al.* 2011b, 2012 [95, 96]	Heart border tracking (track intensity differences)	C	clinical	R
Ma[3] *et al.* 2011b, 2012 [95, 96]	Trachea tracking (generalized Hough transform)	C	clinical	R
Condurache *et al.* 2005 [181]	Diaphragm tracking (Hough transform)	G	clinical	R
Motion modelling based techniques				
Shechter *et al.* 2004, 2005 [182, 183]	CRPM*	C	clinical	C/R
Schneider *et al.* 2010 [184]	PCA based motion model	C	clinical/phantom	R
King *et al.* 2009a, 2009b [94, 185]	Affine motion models	C	clinical	R
Zhu *et al.* 2010 [186]	Motion model based on Lucas-Kanade algorithm	C	clinical/phantom	R
Faranesh *et al.* 2013 [187]	Affine motion models	C	clinical	C/R
Weighted centroid measurement based techniques				
Lehmann *et al.* 2006 [190]	Weighted centroid of coronary arteries	G	clinical/animal	C
Dimensionality reduction based techniques				
Fischer *et al.* 2014 [191]	Incremental ISOMAP	G	animal	R
Phase correlation based techniques				
Sundar *et al.* 2009 [192]	Computation of cumulated phase shift in the spectral domain	G	clinical	C/R

*CRPM stands for cardiac respiratory parametric model, formulated and used to decompose the deformation field into cardiac and respiratory components.

Table 2.3 continued from previous page.

Paper	Technique	Purpose	Study	Motion
Interventional device tracking based techniques				
Baert *et al.* 2003 [194]	Guidewire tracking	NA	clinical	-
Wang *et al.* 2009 [195]	Guidewire tracking	NA	clinical	-
Franken *et al.* 2006 [196]	Catheter tracking	NA	clinical	-
Fallavollita *et al.* 2004 [197]	Ablation catheter tip detection	NA	clinical	-
Wu *et al.* 2011 [198]	CS catheter detection/tracking	NA	clinical	-
Yatziv *et al.* 2012 [199]	Multiple catheter tip-detection	NA	clinical	-
Milletari *et al.* 2013	Automatic detection of EP catheters	NA	clinical	-
Brost *et al.* 2009, 2010a [201, 203]	3D filter-based detection/tracking of CFM catheter	C	clinical	C/R
Brost *et al.* 2010b [203]	3D learning-based detection/tracking of CFM catheter	C	clinical	C/R
Brost *et al.* 2010c [204]	2D filter-based detection/tracking of CFM catheter	C	clinical	C/R
Brost *et al.* 2011a [205]	CS/CFM detection/tracking	C	clinical	C/R
Brost *et al.* 2011b [206]	2D learning-based detection/tracking of CFM catheter	C	clinical	C/R
Brost *et al.* 2011c [207]	Unconstrained learning-based detection/tracking of CFM catheter	C	clinical	C/R
Brost *et al.* 2012 [208]	Unconstrained learning-based detection/tracking of CFM catheter	C	clinical	C/R
Ma *et al.* 2010, 2011b, 2012 [95, 96, 209]	CS catheter tracking	C	clinical	C/R
Ma *et al.* 2011a [211]	CS/ablation catheter detection/tracking	G/C	clinical	C/R
Ma *et al.* 2013 [212]	CS/ablation/CFM catheter detection/tracking	NA	clinical	-
Kaeppler *et al.* 2012 [213]	CS/CFM catheter detection/tracking	G/C	clinical	C/R

The blue colour in C/R highlights the fact that although the authors claim to compensate for both cardiac and respiratory motion, decoupling the cardiac from the respiratory motion wasn't part of their experimental method.

TABLE 2.4: Key papers on X-ray image-based motion gating/compensation available in the literature, categorised by # sequences/patients/frames, accuracy, speed, success rate, tracking error, average motion recovered, image acquisition, model, X-ray image dose, gold standard correlation and RMS.

Paper	# sequences/patients/frames Tracking	Comp./Gating	Accuracy (mm) 2D/3D	Speed(fps)	Success rate (%) 2D/3D	Tracking error (mm) 2D/3D
Ma[1] *et al.* 2011b, 2012 [95, 96]	25/18/782	-/8/418	1.6 ± 0.8/-	>30	100 /-	0.4 ± 0.3 /-
Ma[2] *et al.* 2011b, 2012 [95, 96]	25/18/1073	-/8/418	1.7 ± 0.9/-	>30	100 /-	0.4 ± 0.3 /-
Ma[3] *et al.* 2011b, 2012 [95, 96]	20/18/954	-/8/418	1.9 ± 1.0/-	3	96.7 /-	0.7 ± 0.2 /-
Shechter *et al.* 2004 [182]	-/10/-	-/10/-	- / -	-	- /-	- /-
Shechter *et al.* 2005 [183]	-/5/500	-/5/500	- / -	-	- /-	- /-
Schneider *et al.* 2010 [184]	-	13/-/>90	- / <2	-	- /-	- /-
King *et al.* 2009a [94]	volunteers: -	-/4/126	3-4 / 2-4	>30	97.6 /-	- /-
	patients: -	-/3/-	2.2-3.9 / 1.9-3	>30	97.6 /-	- /-
King *et al.* 2009b [185]	volunteers: -	-/7/-	2-4 / 1.0?2.8	>30	- /-	- /-
	patients: -	-/1/-	0.63-1.73 / 1.0?2.8	>30	- /-	- /-
Zhu *et al.* 2010 [186]	-	-/7/106	1.14 ± 1.38 / -	-	- /-	- /-
Faranesh *et al.* 2013 [187]	-	-/4/-	- / -	-	- /-	1.1 ± 1.0 /-
Lehmann *et al.* 2006 [190]	-	-/-/61	- / -	0.20	- /-	- /-
Sundar *et al.* 2009 [192]	-	-/-/132	- / -	60	- /-	- /-
Fischer *et al.* 2014 [191]	-	48/-/>3552	- / -	>20	- /-	- /-
Brost *et al.* 2009, 2010a [201, 202]	46/16/1288	46/16/1288	- /-	3	95.56 / 89.84	0.90 ± 0.61 / 1.16 ± 0.93
Brost *et al.* 2010b [203]	46/16/1288	46/16/1288	- /-	1	99.05 / 85.71	0.84 ± 0.33 / 1.29 ± 0.72
Brost *et al.* 2010c [204]	46/16/1288	46/16/1288	/ -	10	97.78 /-	0.65 ± 0.44 /-
Brost *et al.* 2011b [206]	46/16/1288	46/16/1288	- / -	10	100.00 /-	0.59 ± 0.61 /-
Brost *et al.* 2011c [207]	46/16/1288	46/16/1288	- / -	10	99.52 / 41.11	0.78 ± 0.30 / 2.44 ± 1.24
Brost *et al.* 2012 [208]	46/16/1288	46/16/1288	- / -	10	- /-	0.61 ± 0.45 / 2.10 ± 1.26
Kaeppler *et al.* 2012 [213]	1/1/30	13/958	1.98 ± 1.30 / -	20	- /-	1.99 ± 1.20 /-
Ma *et al.* 2010 [209]	25/18/1048	-/8/418	1.8 ± 0.9 / -	21	99.3/-	0.4 ± 0.2 /-
Ma *et al.* 2011a [211]	57/16/1083	57/16/1083	1.4 ± 0.7 / -	15	97.5 /-	0.5 ± 0.3 /-

Table 2.4 continued from previous page.

Paper	Average M_{rec} (%)	Image acquisition	Model	X-ray image dose	Gold standard corr. cardiac/respiratory	RMS (mm)
Ma[1] *et al.* 2011b, 2012 [95, 96]	45-75	M	1D trans.	normal/low	- / -	-
Ma[2] *et al.* 2011b, 2012 [95, 96]	41-74	M	1D trans.	normal/low	- / -	-
Ma[3] *et al.* 2011b, 2012 [95, 96]	39-71	M	1D trans.	normal	- / -	-
Shechter *et al.* 2004 [182]	-	B	3D trans./rigid/affine	normal	- /-	<1
Shechter *et al.* 2005 [183]	48-63	B	3D trans./rigid/affine	normal	- /-	1.5-13.6pixels
Schneider *et al.* 2010 [184]	-	B/M	3D trans.	-	- / -	-
King *et al.* 2009a [94]	30-50	B	affine	normal/low	- / -	<1
	23.5-78.9	B	affine	normal/low	- /-	<3
King *et al.* 2009b [185]	-	B	affine	normal/low	- / -	2.8
	-	B	affine	normal/low	- /-	2.8
Zhu *et al.* 2010 [186]	-	M	affine	-	- / -	-
Faranesh *et al.* 2013 [187]	-	B	affine	normal	- / -	-
Lehmann *et al.* 2006 [190]	-	rotational ang.	2D trans.	normal	-/ mean diff. $14 \pm 80ms$	-
Sundar *et al.* 2009 [192]	-	B	2D trans.	normal	0.92/0.88	-
Fischer *et al.* 2014 [191]	-	B	2D trans.	normal	- /0.97 ± 0.02	-
Brost *et al.* 2009, 2010a [201, 202]	-	B	2D trans.	-	- / -	-
Brost *et al.* 2010b [203]	-	B	2D trans.	-	- / -	-
Brost *et al.* 2010c [204]	-	M	2D trans.	-	- / -	-
Brost *et al.* 2011b [206]	-	M	2D trans.	-	- /-	-
Brost *et al.* 2011c [207]	-	M	2D trans.	-	- /-	-
Brost *et al.* 2012 [208]	-	M	2D trans.	-	- / -	-
Kaeppler *et al.* 2012 [213]	-	M	2D trans.	-	- /-	-
Ma *et al.* 2010 [209]	37-72	M	2D trans.	normal/low	- / -	-
Ma *et al.* 2011a [211]	-	M	2D trans.	normal/low	- / -	-

this approach is not best suited for motion estimation in EP images where the organ motion is not necessarily in-plane, and consequently there is no uniform global translation. View-angle independent algorithms are much more clinically useful, especially in 3D rotational angiography procedures because of their applicability in cases where the anglulation of the scanner is changed between frames. The technique proposed by Lehmann *et al.* [190] is the only technique that has yet exploited this potential. Nevertheless, the technique's clinical robustness as a function of angle is not fully tested as the authors analysed data from only two views. Dimensionality reduction algorithms have also been proposed to extract motion. However, most of the proposed methods only handle respiratory motion. Gating both cardiac and respiratory motion is essential for the precise guidance of cardiac catheterisation procedures. Dimensionality reduction techniques that gate both types of motion [174, 214] have been developed for PET/CT and MR imaging acquisitions, which are not the targeted acquisition behind the work of this thesis.

To overcome most of the above limitations, motion gating/compensation techniques based on detection and tracking of interventional devices have been proposed. Capturing intracardiac catheter movement and deformation can provide valuable information about cardiac motion. Hence, accurate and robust localisation of catheters in the X-ray images is necessary to eliminate and compensate for the motion, providing enhanced functionality during procedures for guidance and post-procedural analysis. As shown in Tables 2.3 and 2.4 motion gating/compensation based on detection/tracking of interventional devices is an emerging field with successful works recently proposed. Nevertheless, the proposed techniques have various drawbacks that compromise their effectiveness. Motion compensation by detection/tracking of the CFM catheter, as proposed by Brost *et al.* and Kaeppler *et al.*, requires the CFM catheter to remain anchored at the PV being ablated. This might not always be the case as its position is frequently changed within the heart by the cardiologist. Moreover, the more robust and accurate developed techniques proposed by Brost *et al.* require acquisition using a biplane system. Such a system is less common than a monoplane system in the clinical setting due to its much higher cost. Additionally, when present and used, it involves increased radiation exposure for both the patient and the clinician. Furthermore, these proposed techniques require manual initialisation, an essential limitation for their clinical application. Despite the great advantage that the CS catheter is commonly present in cardiac catheterisation procedures and its position is not routinely altered, limitations of the techniques proposed by Ma *et al.*, where the CS catheter is used for motion compensation, currently exists. An important drawback of the techniques proposed by Ma *et al.* and almost all existing motion gating/compensation techniques is that they remain unsuccessful at lower doses where, for example the catheter electrodes are not highly visible throughout the X-ray images. Furthermore, decoupling the cardiac from the respiratory motion can be challenging.

The scope of this work was to devise methods to address these limitations and foster the clinical translation of motion gating/compensation techniques. In order to illustrate whether this was

successful, the techniques that could be applied using the datasets used in this thesis where implemented and compared in Chapter 5. One of the major limitations of X-ray imaging is that it uses ionising radiation, associated with a small but definite stochastic risk of inducing a malignant disease to the patient and the clinical personnel [215]. Furthermore, there is a deterministic risk of skin damage both to the patient and the operator, as well as a small risk of eye injury to the operator [216–218]. X-ray radiation dose is of particular importance in very long procedures such as EP studies. Therefore, it is important to develop robust-to-noise gating/compensation techniques that produce sufficient benefit to the exposed individual to offset the radiation risk it causes. With the heightened awareness of cancer potential from cumulative exposure, this work has stepped up efforts to minimise the risk, by the development of four robust-to-noise novel motion gating techniques presented in Chapter 3 and evaluated in both phantom and clinical datasets in Chapters 4 and 5, respectively. The application of the developed techniques to ultra low dose X-ray images where the dose is reduced by more than 50 times, is also demonstrated in Chapters 4 and 5.

The first proposed technique, Tracked-PCA, is based on the formation of a novel statistical model of the motion of the CS catheter based on the statistical technique of PCA of tracked electrode locations from X-ray fluoroscopy images. To drop the constraint of the presence of the CS catheter in the images, two robust to varying image-content techniques have been developed, the HML-based and Masked-PCA techniques. The techniques are robust to typical EP X-ray images that contain a varying number of different types of EP catheters and may include contrast agent injection. HML and PCA statistical methods are used in combination with other image processing operations to make these techniques suitable for cardiorespiratory motion gating. Finally, an X-ray system view-angle independent technique was developed based on learning CS catheter motion using PCA and then applying the derived motion model to unseen images taken at arbitrary projections. In Chapter 6 applications of the gating technique spanning from basic research to clinical tasks are demonstrated. These include catheter reconstruction in 3D from catheter tracking in gated sequential biplane X-ray images that can effectively achieve 2D/3D registration of 3D cardiac data (CT or MRI) to X-ray fluoroscopy, motion gating of 3D rotational X-ray angiography sequences where the angulation of the scanner is changed between frames, and motion compensation on unseen images taken at any arbitrary projection, by integrating cardiorespiratory motion into MRI-derived roadmaps fused with live X-ray fluoroscopy.

Chapter 3

Developed methods

Contents

This chapter provides a description of the aims and methodologies of the four developed cardiorespiratory motion gating techniques. Details of the materials used to validate them are provided in Chapters 4 and 5, for phantom and clinical procedures, respectively.

3.1 Tracked-PCA technique

3.1.1 Introduction

The motion and deformation of catheters that lie inside cardiac structures can provide valuable information about the motion of the heart. In this Section 3.1, the formation of a novel statistical

model of the motion of a CS catheter based on principal component analysis of tracked electrode locations from standard monoplane X-ray fluoroscopy images is described. The CS catheter is routinely used during EP procedures and provides reference information to the cardiologist throughout the procedure. The reason for choosing the CS catheter instead of other catheters is because the CS catheter remains in place throughout the procedure, its position is not routinely altered and it is rarely overlapped by other catheters in the X-ray projections that are commonly used during EP procedures, i.e. PA and LAO (left anterior oblique) 30°. This is due to the positioning of the main part of the CS along the border of the mitral valve annulus. Additionally, since the main part of the CS is a curved structure, it has similar foreshortening in all routinely used X-ray projections, which makes it an ideal choice for derivation of motion.

A preliminary version of this technique is described in Panayiotou *et al.* [219], which is an extension of the work presented in Panayiotou *et al.* [220].

3.1.2 Methods

In this section the formation of the statistical model of catheter motion (Section 3.1.2.1) is first described, then its application to retrospective gating in normal dose images (Section 3.1.2.2) and finally how a modification of the technique allows application to gating in very low dose images (Section 3.1.2.3).

3.1.2.1 Statistical model formation

The formation of the statistical model comprises two main steps. Firstly, the technique described by Ma *et al.* [209] is used to track the electrodes of the CS catheter throughout the X-ray sequence. Secondly, PCA is applied to the coordinates of the tracked electrodes. Initially, independent component analysis (ICA) was applied to the dominant modes of variation obtained after the application of PCA in an attempt to produce more meaningful independent signals. However, the results were not improved as the two motion signals were sufficiently separated by PCA. ICA was therefore not used as part of the methodology. The steps are described below and a block diagram of the proposed method for cardiac and respiratory gating is shown in Figure 3.1.

Coronary sinus catheter detection. The CS catheter used in this work is composed of ten electrodes, distributed in pairs along the catheter. The CS tracking technique [209] uses a fast multi-scale blob detection method [221] to detect all electrode-like objects in an X-ray image and a cost function to discriminate the CS catheter from other catheters.

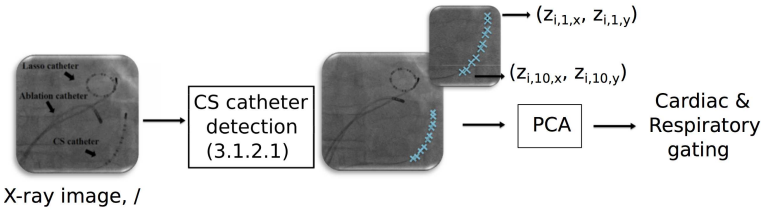

FIGURE 3.1: Block diagram of the proposed Tracked-PCA method for cardiac and respiratory gating

The multi-scale blob detection method is based on the determinant of the Hessian matrix [221].

$$\text{detH}(L(x,y;t)) = L_{xx}L_{yy} - L_{xy}^2. \tag{3.1}$$

where $L_{x,y;t} = I(x,y)*g(x,y;t)$ is the scale-space representation of the image $I(x,y)$ with the scale factor t and $g(x,y;t)$ is a Gaussian filter. $t = \sigma^2$, with σ being the standard deviation of the Gaussian function. t is calculated as $t = (\frac{(s-1)}{3})^2$ where s is the blob size, set to 6 and 3 pixels for the catheter tip electrode and the smaller electrodes, respectively. $L_{xx} = I(x,y)*g_{xx}$, where * is the convolution operator and $g_{xx}(x,y;t) = -\frac{1}{2\pi t^2}(1 - \frac{x^2}{t})e^{-(x^2+y^2)/2t}$. L_{yy} and L_{xy} are defined similarly.

Blobs are defined as local extrema of the determinant of the Hessian matrix and the strength of the blob as the normalised value of the determinant of the Hessian matrix.

The next step involves deciding which combination of blobs represents the CS catheter. Based on the shape model of the 10-electrode CS catheter a unified cost function was designed to estimate the likelihood of candidate catheter-like objects. The cost function is unified to include two possible variations of the arrangement of the CS electrodes: evenly distributed and paired.

$$CSCathCost = \frac{\sum_{i=1}^{N-2} |\cos\theta_i - \overline{\cos\theta}|}{N-2} + \frac{\sum_{i=1}^{N-1} |\text{Blob}_i - \overline{\text{Blob}}|}{N-1} \tag{3.2}$$

where $\overline{\cos\theta}$ is the mean of cosines of all deviation angles between line segments joining CS catheter electrode blobs and $\overline{\text{Blob}}$ is the mean of blob strengths of the 9 electrodes (excluding the catheter tip electrode). Blob_i is normalized to a range of zero to one which is the same value range as $\cos\theta_i$. N is the total number of electrodes, $N = 10$ in this case. $\cos\theta_i$ can be computed efficiently using $\cos\theta_i = \frac{\overrightarrow{V_i}\cdot\overrightarrow{V_{i+1}}}{\|\overrightarrow{V_i}\|\|\overrightarrow{V_{i+1}}\|}$. $\overrightarrow{V_i}$ and $\overrightarrow{V_{i+1}}$ are consecutive blobs on the catheter, shown in Figure 3.2.

Two constraints were introduced to quickly remove unwanted candidates. The first constraint is the maximum electrode gap. This is defined as twice the length of the maximum distance Max_{dist} between two neighbouring CS catheter electrodes, obtained by physical measurement of a CS catheter. 10-electrode CS catheters have two variations of electrode distributions and

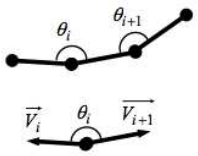

FIGURE 3.2: The definition and calculation of the deviation angle, θ [95].

whichever maximum distance between two neighbouring electrodes is larger was chosen. The second constraint is the minimum deviation angle which must be larger than 90° as catheters in human vessels cannot have sharp turns. This condition can be translated into $\overrightarrow{V_i} \cdot \overrightarrow{V_{i+1}} < 0$.

In the current work, manual localisation was performed in cases where the technique failed to accurately detect the CS catheter electrodes. This was done by manually localising the centre of any misdetected electrode of the CS catheter. After application of the tracking algorithm, the x and y positions of each of the ten electrodes in the identified catheter were concatenated into a single column vector for each time point. Hence, the data generated by the tracking process consisted of:

$$\mathbf{s}_i = (z_{i,1,x}, z_{i,1,y}, \ldots z_{i,10,x}, z_{i,10,y})^T, 1 \leq i \leq N \tag{3.3}$$

where $z_{i,e,x}$ and $z_{i,e,y}$ represent the x and y coordinates of the e^{th} electrode in the i^{th} frame. $e = 1$ corresponds to the distal electrode, and N is the number of frames. $\mathbf{s}_i \in \mathbb{R}^{20\times 1}$ is the i^{th} column of matrix $\mathbf{s} \in \mathbb{R}^{20\times N}$.

Principal component analysis. PCA transforms a multivariate dataset of possibly correlated variables into a new dataset of a smaller number of uncorrelated variables called principal components (PCs), without any loss of information [222]. Here, PCA is applied to estimate the dominant modes of variation in the electrodes' motion as the catheter moves and deforms during respiratory and cardiac cycle motion.

Firstly, the mean vector is computed:

$$\overline{\mathbf{s}} = \frac{1}{N}\sum_{i=1}^{N} \mathbf{s}_i \tag{3.4}$$

and the covariance matrix:

$$\mathbf{S} = (\mathbf{s} - \overline{\mathbf{s}})(\mathbf{s} - \overline{\mathbf{s}})^T \tag{3.5}$$

where $(\mathbf{s} - \overline{\mathbf{s}}) \in \mathbb{R}^{20\times N}$ represents $\overline{\mathbf{s}} \in \mathbb{R}^{20\times 1}$ subtracted from each column of $\mathbf{s}$, according to the standard PCA technique. The eigenvectors $\mathbf{v}_m \in \mathbb{R}^{20\times 1}$, $1 \leq m \leq M$ of $\mathbf{S}$ represent the PCs, where M is the total number of eigenvectors, and the corresponding eigenvalues $\mathbf{d}_m \in \mathbb{R}^{1\times 1}$, $1 \leq m \leq M$ represent the variance of the data along the direction of the eigenvectors. For this specific application $M = 20$, since the $\mathbf{s}_i$ are of length 20, although at most $N - 1$ of these

eigenvectors will have non-zero eigenvalues. Next, to estimate the contribution of each of the PCs to the variation in the electrode positions, the scalar projection between the original data and each of the PC vectors is computed:

$$P_{m,i} = \mathbf{v}_m^T \cdot (\mathbf{s_i} - \overline{\mathbf{s}}), 1 \leq m \leq M, 1 \leq i \leq N \tag{3.6}$$

The hypothesis is that the PCA will extract the cardiac and respiratory modes and that $P_{m,i}$ will therefore represent cardiac/respiratory signals that can be used for gating. It was found by visual inspection that the variation of the first PC was dominated by cardiac motion and that the variation of the second PC was dominated by respiratory motion for all subjects. The underlying cause of this is the fact that the CS catheter is located around the mitral value annulus and therefore the motion of this catheter is dominated by cardiac motion as opposed to respiratory motion, irrespective of the X-ray projection. For all ten data sets being processed the peaks of the variation of the first PC corresponded to systole with the troughs corresponding to diastole and the peaks of the variation of the second PC corresponded to end-inspiration (EI) with the troughs corresponding to end-expiration (EX). Although it cannot be guaranteed that this will always be the case it would be possible to manually check this and change the signs of the projections if necessary. This would cause minimal interruption to the clinical workflow.

3.1.2.2 Retrospective gating in normal dose images

For retrospective gating using normal dose images the task is to gate the same images that were used for forming the statistical model. The scalar projections from Eq. (3.6) were used for this purpose.

Cardiac gating. The first PC is used to detect systolic frames of the image sequences which are represented by the peaks of the variation of the first PC with frame number,

$$\Omega_{sys} = \{i \mid P_{1,i-1} < P_{1,i} > P_{1,i+1}\} \tag{3.7}$$

where Ω_{sys} is the set of all frame numbers that are identified as systole.

Respiratory gating. The second PC relates to the respiratory motion. However, some cardiac motion remains. To compensate for the cardiac motion the variation of the second PC is gated using the peaks of the variation of the first PC. Even though in two independent signals like cardiac/respiratory motion their peaks can never be guaranteed to coincide, the aim is to find the closest point on the respiratory signal that represents a peak on the cardiac signal.

Hence, EI and EX are represented by:

$$\Omega_{sys,EI} = \{i \mid P_{2,j} < P_{2,i} > P_{2,k}\ i,j,k\ \in\ \Omega_{sys}, j < i < k\} \tag{3.8}$$

$$\Omega_{sys,EX} = \{i \mid P_{2,j} > P_{2,i} < P_{2,k}\ i,j,k\ \in\ \Omega_{sys}, j < i < k\} \tag{3.9}$$

respectively, where j, i and k are temporally consecutive systolic frames.

3.1.2.3 Gating in very low dose images

For very low dose images the task is to gate previously unseen frames based on a statistical model formed from normal dose images during a calibration phase. The technique could be used for either retrospective or prospective gating in very low dose X-ray fluoroscopy images. In this section its use for prospective gating is demonstrated. The gating is prospective in the sense that there is no need to collect the whole sequence before processing. However, the gating technique would suffer from a time lag of 1 sample interval because of the need to identify peaks/troughs in the extracted signals. Consequently, the gating is almost prospective, but because of the phase lag it will be called 'near real-time gating'. The gating uses the same blob detection algorithm that was used during model formation. The idea is that, after the calibration phase, the subsequent X-ray images can be acquired with a much lower dose since the model will provide sufficient constraints on the electrode locations to enable tracking to be successful even in low dose X-ray.

Blob detection in corrupted X-ray images. The fast multi-scale blob detector was used to detect all possible electrode-like objects in the noise-corrupted X-ray images. The x and y positions of all detected blobs in the image were concatenated into a blob list, **BL**.

CS catheter position estimation. The result of the PCA on catheter locations in normal dose images gives possible CS catheter positions throughout the X-ray sequence. Only the variation of the first and second PCs are of interest, as they correspond to the largest percentage of variation. The tracking works by determining the weights for the first two PCs that give a catheter position most similar to the detected blobs. The PCA model outlined in Section 3.1.2.1 can produce a new set of electrode locations, $\hat{s}$ according to

$$\hat{s} = \overline{\mathbf{s}} + \sum_{m} w_m \mathbf{v}_m \tag{3.10}$$

where $w_m (m \in \{1,2\})$ are the weights of the first two PCs. The catheter shape at an arbitrary cardiac/respiratory phase is denoted by weights w_1 and w_2, which define the electrode locations

$\hat{s}_{w_1 w_2}$. The task of the tracking process is to find, for each frame, the weights $\hat{w_1}$ and $\hat{w_2}$ that represent the cardiac/respiratory phases of that frame. These are estimated according to

$$\hat{w_1}, \hat{w_2} = \underset{w_1 w_2}{\operatorname{argmin}} D(\hat{s}_{w_1 w_2}, \mathbf{BL}) \tag{3.11}$$

where $D(\hat{s}_{w_1 w_2}, \mathbf{BL})$ is a function that computes the sum of the minimum Euclidean distances between the electrode locations contained in $\hat{s}_{w_1 w_2}$ and the nearest corresponding blobs from the blob list, **BL**. In a plane, computing the Euclidean distance is the most appropriate measure of real distance.

Motivated by the 3σ rule, that states that for a normal distribution, nearly all (99.73%) of the values lie within 3 standard deviations of the mean, the search space for the weights varies from $-3\sqrt{d}_m$ to $+3\sqrt{d}_m$, where d_m is the m^{th} eigenvalue, and $1 \leq m \leq 2$. An exhaustive search, with the number of steps in each direction chosen so that the distal electrode moved by not more that 7 pixels in each step, is used to solve the optimisation. The function is minimised using this coarse-scale exhaustive search followed by an iterative optimisation using Matlab's lsqnonlin function with the trust-region-reflective algorithm (MATLAB Release 2013a, The MathWorks, Inc., Natick, Massachusetts, USA). This method is appropriate for an unconstrained, overdetermined system.

Cardiac gating. $\hat{w_1}$ is used to detect systolic frames, Ω_{sys}, of the image sequence. These are represented by the peaks of the variation of $\hat{w_1}$ with frame number.

$$\Omega_{sys} = \{i \mid w_{1,i-1} < w_{1,i} > w_{1,i+1}\} \tag{3.12}$$

where $w_{1,i}$ is the value of the 1^{st} weight obtained in the i^{th} frame.

Respiratory gating. The peaks of the variation of $\hat{w_2}$ over time represent (EI) respiratory frames, Ω_{EI}, while the troughs represent (EX) respiratory frames, Ω_{EX}.

$$\Omega_{EI} = \{i \mid w_{2,i-1} < w_{2,i} > w_{2,i+1}\} \tag{3.13}$$

$$\Omega_{EX} = \{i \mid w_{2,i-1} > w_{2,i} < w_{2,i+1}\} \tag{3.14}$$

where $w_{2,i}$ is the value of the 2^{nd} weight obtained in the i^{th} frame.

3.2 Hierarchical manifold learning-based technique

3.2.1 Introduction

As already mentioned in Chapter 2, numerous motion compensation techniques have been developed to cope with cardiorespiratory motion [95, 181–183, 201–209, 219, 223]. These techniques largely rely on detection and tracking of specific features in the images, such as interventional devices. The dependence on specific features in the images, such as the diaphragm, heart border, CFM or CS catheters, introduces possible drawbacks. For instance, the diaphragm is not always visible in cardiac X-ray images due to collimation to reduce radiation dose. The heart border might be influenced by cardiac motion. The CFM catheter is not universally present in EP procedures and its position is frequently changed within the heart by the cardiologist. Furthermore, these tracking methods required manual initialisation. Additionally, the CS catheter detection method might fail when some of the electrodes on the CS catheter move out of the FOV.

A novel and clinically useful method is presented in this section to automatically determine the regions that carry cardiac and respiratory motion information directly from standard monoplane X-ray fluoroscopy images. The application of the method for the purposes of retrospective cardiac and respiratory gating of phantom and clinical X-ray fluoroscopy images at normal and very low dose will be demonstrated in Chapters 4 and 5, respectively.

Similarly to the HML-based technique, the objective of the development of the previously described algorithm, the Tracked-PCA, was cardiorespiratory motion gating at normal and low dose X-ray images. The method involved the formation of a statistical model of the motion of a CS catheter based on PCA of tracked electrode locations from standard monoplane X-ray fluoroscopy images. The gating relied on the CS catheter being present in the X-ray images. The main novelty of the current proposed motion gating approach is that it is robust to varying image-content. Therefore, it does not rely on specific catheters being present in the image data or the localisation of these devices. Besides being applicable to RFA procedures, the technique is also applicable to CRT procedures where the CS catheter is not present in the X-ray images.

As pointed out in Chapter 2, Bhatia *et al.* [97] proposed a technique called HML which is used to learn the regional correlations in motion within a sequence of time-resolved MR images of the thoracic cavity. This non-linear dimensionality reduction technique is used as part of the current proposed technique.

The proposed technique has been presented in Panayiotou *et al.* [224]. Details on each part of the proposed framework are provided in the following sections.

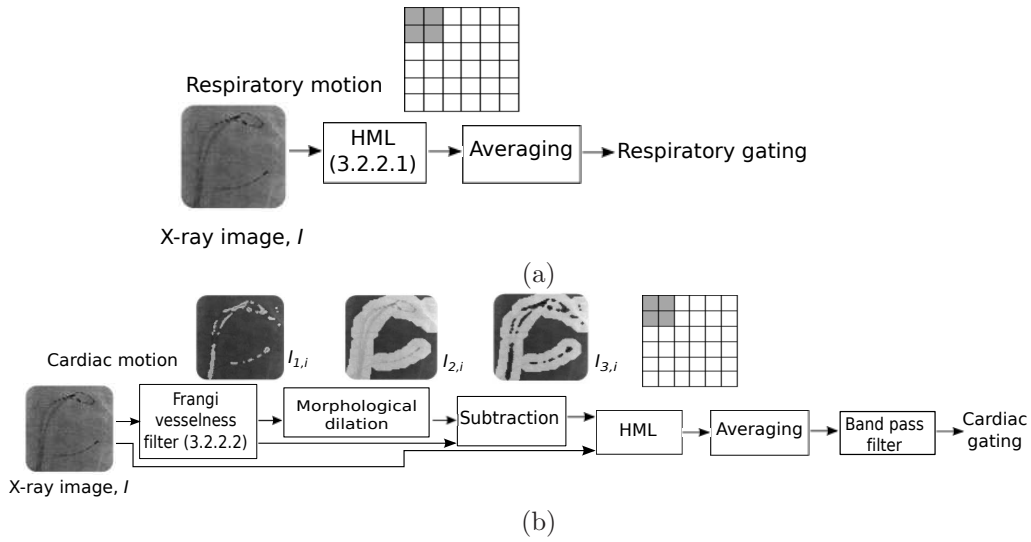

FIGURE 3.3: Block diagram of the proposed HML-based method (a) for respiratory gating; (b) for cardiac gating

3.2.2 Methods

A block diagram of the proposed method for cardiac and respiratory gating is shown in Figure 3.3. First, the respiratory gating approach is described and then the expansion of this technique with a number of other image processing operations to make it suitable for cardiac motion gating is outlined.

3.2.2.1 Respiratory gating

Hierarchical manifold learning. Manifold Learning (ML) is a non-linear dimensionality reduction technique, which aims to embed data that originally lies in a high dimensional (high-D) space into a lower dimensional (low-D) space, while preserving characteristic properties. Laplacian eigenmaps (LE) is a particular ML technique, which is often chosen for medical imaging applications [225]. One of the disadvantages of applying conventional ML techniques to medical images is that the whole of the image is embedded into the low-D space even though not all the image contains relevant information. To prevent this weakness HML is used, a recently proposed technique [97]. To avoid the need to pre-define regions of interest, the images are separated into regular patches, of size 2^2 pixels each, finding a manifold embedding for each image patch. The methodology is based on the idea of manifold alignment [226]. Given a first level embedding $\overline{\mathbf{x}}$ of the full image, the image can then be recursively subdivided into equal smaller parts. As each subdivision is contained within the current level, embeddings at successive levels are expected to be similar in some way. The new embedding x of one of these sub-parts is obtained by amending the LE cost function such that the new embedding is also close to the embedding obtained at the previous level, that is, the new embedding is aligned to its "parent" embedding $\overline{\mathbf{x}}$. The idea

is to align each patch embedding to several parent manifolds, with the strength of the aligning constraint dependent on the distance to parent patch centres. For a 2D image, it would seem natural to constrain a new patch to be close to its four nearest (in terms of distance) parent patches [97]. Consequently, in this technique, four (2D) parent patches are used. As the aim is to recover both the cardiac and respiratory motions, the data is reduced to 2 dimensions. By using a manifold embedding dimensionality of 2, each patch in each time frame is represented by a 2D coordinate. The values in each dimension are treated separately. It was found by correlation with the gold standard traces that the coordinates of the 1^{st} dimension represent the respiratory motion while the coordinates of the 2^{nd} dimension represent the cardiac motion. The output of the HML process is denoted by P_1 and P_2, for the 1^{st} and 2^{nd} dimension, respectively. As the whole sequence should be collected before the HML technique is applied, the technique is used retrospectively.

Gating. HML is applied to the 2^2 size patches of the X-ray images, denoted I. Eq. (3.15) is then used to obtain the respiratory phase for each frame, i.

$$\overline{P}_{1,i} = \sum_{j \in I} \frac{P_{1,j,i}}{G_I} \tag{3.15}$$

where $P_{1,j,i}$ is the 1^{st} dimension of the HML result at patch j, frame i and G_I is the total number of patches in I. The peaks of the plots at each time frame represent EI respiratory frames, Ω_{EI}, while the troughs represent EX respiratory frames, Ω_{EX}.

$$\Omega_{EI} = \{i \mid \overline{P}_{1,i-1} < \overline{P}_{1,i} > \overline{P}_{1,i+1}\} \tag{3.16}$$

$$\Omega_{EX} = \{i \mid \overline{P}_{1,i-1} > \overline{P}_{1,i} < \overline{P}_{1,i+1}\} \tag{3.17}$$

3.2.2.2 Cardiac gating

The embedding coordinates of the 2^{nd} dimension, P_2, of each patch relate to the cardiac motion. However, this is significantly affected by respiratory motion. To compensate for the respiratory motion several additional steps are applied to the X-ray images: a Frangi vesselness (FV) filter [227] followed by morphological opening, morphological dilation and a Butterworth filter.

Frangi vesselness filter. The FV filter is applied to all X-ray images in the sequence. This technique identifies tubular structures in the X-ray images, such as catheters and pacing leads, which are expected to carry useful cardiac motion information, using Hessian eigenvalues. The responses of the FV filter are binarised by applying a threshold. To remove the noise present while preserving the shape and size of the detected structures, morphological opening is applied

to the binarised responses. The results of this opening process are denoted by $I_{1,i}$, where i is the X-ray frame number.

Morphological dilation. The previous step is followed by the application of morphological dilation. This operation adds patches to the boundaries of detected structures, which produces $I_{2,i}$. In morphological dilation the value of the output patches is the maximum value of all the patches in the input patches' neighbourhood. Computing $I_{3,i} = I_{2,i} - I_{1,i}$ the image patches around the detected tubular structures are identified. The HML is applied to these patches only. These patches were found to be more useful for extracting cardiac motion information than using the tubular structures themselves. Although the tubular structures are expected to carry useful cardiac motion information, the necessity for the clinician to manipulate the catheters throughout the interventional procedures adversely affects the accuracy of the systolic peaks. For cardiac motion, Eq. (3.18) is used

$$\overline{P}_{2,i} = \sum_{j \in I_{3,i}} \frac{P_{2,j,i}}{G_{I_{3,i}}} \tag{3.18}$$

where is $P_{2,j,i}$ the 2^{nd} dimension of the HML results at patch j in frame i and $G_{I_{3,i}}$ is the total number of patches in $I_{3,i}$.

Band pass filter and gating. To remove residual respiratory motion, a 2^{nd} order Butterworth band pass filter is applied to the obtained plots using Matlab's filtfilt function. The function performs zero-phase digital filtering by processing the input data in both the forward and reverse directions. A zero-phase filter was chosen because it helps preserve features in a filtered time waveform exactly where they occur in the unfiltered signal. The peaks of the plots represent systolic frames.

$$\Omega_{sys} = \{i \mid \overline{P}_{2,i-1} < \overline{P}_{2,i} > \overline{P}_{2,i+1}\} \tag{3.19}$$

Unlike the Tracked-PCA technique, for this technique the variation of the 1^{st} dimension corresponds to respiratory motion instead of cardiac. This may be because HML is applied to the whole image where respiratory motion is more dominant than cardiac motion. The variation of the 1^{st} dimension of the HML result corresponds directly with respiratory motion. Therefore, the respiratory signal does not need to be cardiac gated as previously required for the Tracked-PCA technique. Although for the Tracked-PCA technique the first 2 PCs largely represent cardiac and respiratory motion, the variation of the 1^{st} and 2^{nd} PCs extracted do not correspond directly with cardiac and respiratory motion since some cardiac motion remains in the 2^{nd} PC. This may be due to the data not being jointly normal as required for the PCA. Since the HML-technique is a non-linear dimensionality reduction technique, it completely removes the cardiac motion from the 1^{st} dimension.

To build the algorithm, appropriate values have to be chosen for the four parameters involved in extracting the cardiac phases. These parameters include: a threshold level on the normalised output, 0 to 1, of the FV filter, the number of morphological dilations of the identified structures, and the pass band and stop band frequencies (normalised from 0 to 1) of the Butterworth band pass filter. The values are determined by optimising on training data. Details of the optimisation are given in Chapter 4, Section 4.3.3.

3.3 Masked-PCA based technique

3.3.1 Introduction

In this section, a novel and clinically useful technique, the Masked-PCA technique, is proposed for automated image-based cardiorespiratory motion gating of monoplane X-ray fluoroscopy images. The PCA statistical method is used in combination with other image processing operations to make the proposed Masked-PCA technique suitable for cardiorespiratory gating. The technique is robust to varying image-content, thus it does not require specific catheters or any other optically opaque structures to be visible. Therefore, it works without any knowledge of catheter geometry. The application of the technique for the purposes of retrospective cardiorespiratory gating of normal and very low dose phantom and clinical X-ray fluoroscopy images is demonstrated in Chapters 4 and 5, respectively.

A cardiorespiratory motion gating technique for cardiac image-guided interventions also applicable to typical EP X-ray images that can contain a varying number of different types of EP catheters and may include contrast agent injection was presented in Section 3.2. The purpose of the development of the currently proposed Masked-PCA technique is the improvement of the accuracy and robustness of the extraction of cardiac phases, which are particularly important in facilitating the clinical workflow. The clinical translation of cardiorespiratory motion gating techniques is usually hindered by their lack of accuracy/robustness [188]. The higher the accuracy/robustness of the technique the more efficient will be its translation into clinical practice, achieving safer and more successful procedure outcomes.

The work presented for this technique is described in Panayiotou *et al.* [228]. The proposed framework of the Masked-PCA technique is provided below.

3.3.2 Methods

A block diagram of the proposed Masked-PCA method is shown in Figure 3.4, giving an outline of how the gating approach becomes suitable for cardiorespiratory motion gating.

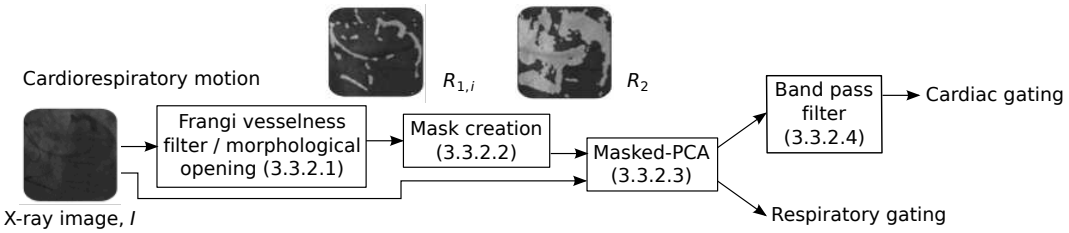

FIGURE 3.4: Block diagram of the proposed cardiorespiratory motion gating Masked-PCA technique.

3.3.2.1 Frangi vesselness filter and morphological operations

The FV filter, a vessel enhancement filter, is applied to all X-ray images in the sequence. Applying a threshold binarises the responses of the FV filter. To remove the noise present while preserving the shape and size of the detected structures morphological opening is then applied to the binarised responses. The previous step is followed by the application of morphological dilation. The FV filter along with the morphological operations is applied to all X-ray images in the sequence. The results of this process are denoted by $R_{1,i}$, where i is the X-ray frame number. Up to this point, the processing is similar to that applied in the HML-based technique for the extraction of cardiac phases.

3.3.2.2 Mask creation

Any pixels detected by the above image processing operations, in any frame of the X-ray sequence, are used to create a single mask, denoted by R_2. Specifically, the mask R_2 is computed as the union of all detected pixels in the mask of each image, $R_{1,i}$, for $1 \leq i \leq N$, where N is the total number of frames in the sequence. The mask, R_2 is the same for each frame in the sequence. Consequently, since the whole sequence should be collected before processing, the technique is intended for retrospective analysis. The intensities of each of the pixels in the mask were concatenated into a single column vector for each frame. Hence the data generated by this process consisted of:

$$\mathbf{q}_i = (R_{2_{i,1}}, R_{2_{i,2}}, \ldots R_{2_{i,J}})^T, 1 \leq i \leq N \tag{3.20}$$

where $R_{2_{i,j}}$ represents the intensity of the j^{th} pixel of the masked image, R_2, in the i^{th} frame. N is the number of frames and J is the number of pixels in the mask created. $\mathbf{q}_i \in \mathbb{R}^{J\times 1}$ is the i^{th} column of matrix $\mathbf{q} \in \mathbb{R}^{J\times N}$.

3.3.2.3 Principal component analysis

PCA is then applied to estimate the modes of variation of the data vectors, $\mathbf{q}_i$. Firstly, the mean vector is computed:

$$\overline{\mathbf{q}} = \frac{1}{N}\sum_{i=1}^{N}\mathbf{q}_i \tag{3.21}$$

and the covariance matrix:

$$\mathbf{Q} = (\mathbf{q} - \overline{\mathbf{q}})(\mathbf{q} - \overline{\mathbf{q}})^T \tag{3.22}$$

where $(\mathbf{q} - \overline{\mathbf{q}}) \in \mathbb{R}^{J\times N}$ represents $\overline{\mathbf{q}} \in \mathbb{R}^{J\times 1}$ subtracted from each column of $\mathbf{q}$, according to the standard PCA technique. The eigenvectors, $\mathbf{v}_m \in \mathbb{R}^{J\times 1}$, $1 \leq m \leq J$ of $\mathbf{Q}$ represent the PCs, where the total number of eigenvectors is equal to the number of pixels, J, and the corresponding eigenvalues, $\mathbf{d}_m \in \mathbb{R}^{1\times 1}$, $1 \leq m \leq J$ represent the variance of the data along the direction of the eigenvectors.

Note that all eigenvalues of the covariance matrix are zero except those that are nonzero eigenvalues of

$$\mathbf{Q}' = (\mathbf{q} - \overline{\mathbf{q}})^T(\mathbf{q} - \overline{\mathbf{q}}) \tag{3.23}$$

Therefore, to reduce computational time the eigenvectors, $\mathbf{v}'_n \in \mathbb{R}^{N\times 1}$, $1 \leq n \leq N$ and eigenvalues, $\mathbf{d}'_n \in \mathbb{R}^{1\times 1}$, $1 \leq n \leq N$ of $\mathbf{Q}' \in \mathbb{R}^{N\times N}$ were calculated. The corresponding eigenvectors, whose eigenvalues are non-zero, were obtained: $\mathbf{v}_m = (\mathbf{q} - \overline{\mathbf{q}}) \cdot \mathbf{v}'_n$, where $\mathbf{v}_m \in \mathbb{R}^{J\times 1}$, $1 \leq m \leq N$ is an eigenvector of the covariance matrix $\mathbf{Q}$ [229]. For this application although there are J eigenvectors, at most $N-1$ of these will have non-zero eigenvalues. Next, to estimate the contribution of each of the PCs to the variation in the pixel intensities, the scalar projections between the original data and each of the PC vectors were computed:

$$P_{m,i} = \mathbf{v}_m^T \cdot (\mathbf{q_i} - \overline{\mathbf{k}}), 1 \leq m \leq J, 1 \leq i \leq N \tag{3.24}$$

The hypothesis is that the PCA will extract respiratory and cardiac modes and that $P_{m,i}$ will therefore represent respiratory/cardiac signals that can be used for gating. It was found by correlation with the gold standard traces that the variation of the 1^{st} PC was dominated by respiratory motion. To recover the cardiac signal a band pass filter on the variation of the 1^{st} PC, $P_{1,i}$, is required. To recover the respiratory motion the variation of $P_{1,i}$ was cardiac gated using the identified end-systolic frames. Unlike in the Tracked-PCA method, the 2^{nd} PC was not used. Instead, both type of motions have been extracted using only the 1^{st} PC. This may be due to the fact that neither of the motions is dominant in the regions covered by the mask. Therefore, the technique fails to separate them from each other. Nevertheless, as will be outlined in Chapters 4 and 5 the gating performance of this technique is overall superior to the HML-based technique.

3.3.2.4 Band pass filter and cardiac gating

For gating, the task is to gate the same images that were used for forming the statistical model. The scalar projections from Eq. (3.24) were used for this purpose. To recover the cardiac motion, a 2^{nd} order Butterworth band pass filter is applied to the variation of the 1^{st} PC using Matlab's filtfilt function. The peaks of the band pass filtered plots represent end-systolic frames, Ω_{sys}.

$$\Omega_{sys} = \{i \mid P_{1,i-1} < P_{1,i} > P_{1,i+1}\} \tag{3.25}$$

where Ω_{sys} is the set of all frame numbers that are identified as end-systole.

3.3.2.5 Respiratory gating

To recover the respiratory motion, the 1^{st} PC is cardiac gated using the identified end-systolic frames. EI and EX frames are represented, respectively, by the peaks and troughs of the variation of the 1^{st} PC with frame number.

$$\Omega_{sys,EI} = \{i \mid P_{1,j} < P_{1,i} > P_{1,k}\ i,j,k\ \in\ \Omega_{sys}, j < i < k\} \tag{3.26}$$

$$\Omega_{sys,EX} = \{i \mid P_{1,j} > P_{1,i} < P_{1,k}\ i,j,k\ \in\ \Omega_{sys}, j < i < k\} \tag{3.27}$$

where $\Omega_{sys,EI}$ and $\Omega_{sys,EX}$ are the set of all frame numbers that are identified as EI or EX, respectively, and i, j and k are temporally consecutive end-systolic frames.

To build the algorithm, appropriate values have to be chosen for the four parameters involved in extracting the cardiac and respiratory phases. These parameters include: a threshold level on the normalised output, 0 to 1, of the FV filter, the number of morphological dilations of the identified structures, and the pass band and stop band frequencies (normalised from 0 to 1) of the Butterworth band pass filter. The values are determined by optimising on training data. Details of the optimisation are given in Chapter 4, Section 4.3.3.

3.4 View-angle independent technique

3.4.1 Introduction

Earlier in this chapter, techniques for measuring not only the cardiac phase but both cardiac and respiratory motions simultaneously were proposed. These include the HML-based technique (Section 3.2) and the Masked-PCA technique (Section 3.3), which are model-based approaches.

Additionally, another model-based method, the Tracked-PCA technique, for automated image-based near real-time cardiorespiratory motion gating in normal and very low dose X-ray fluoroscopy images, was described. The technique can predictively gate unseen frames based on a statistical model formed from normal dose images during a calibration phase using PCA of the motion of the CS catheter, a particular catheter that is nearly always present in EP procedures. One major limitation of these and other model-based approaches is the requirement to build a separate catheter model for each X-ray view. In this section, the Tracked-PCA approach is significantly extended to make it X-ray system view-angle independent and therefore much more clinically useful. The proposed approach is based on forming a PCA-based model of the CS catheter in a first or *training* view and then using this to determine both the cardiac and the respiratory phases, in near real-time, in any arbitrary second or *current* view. Along with cardiorespiratory motion determination, this technique is able to track the CS catheter throughout the X-ray images, again in any arbitrary subsequent view. Catheter reconstruction in 3D from catheter tracking in gated sequential biplane X-ray images can effectively achieve 2D/3D registration of 3D cardiac data (CT, MRI or 3DRXA) to X-ray fluoroscopy [99], a particularly important application to enhance X-ray fluoroscopy image guidance during cardiac catheterisation procedures.

Similar to all the previously developed techniques described in this chapter, this View-angle independent technique is robust-to-noise. Therefore, it can extract clinically useful cardiorespiratory motion information whilst minimising exposure to ionising radiation. An application of this approach is motion gating of 3DRXA for which current methods are limited to breath-holding for respiration and either no gating for cardiac motion or arresting the heart using adenosine or rapid pacing [100].

Preliminary work was presented in Panayiotou *et al.* [230]. This work has been extended and submitted as a journal paper, which forms the basis of this section.

3.4.2 Methods

In this section, the formation of a statistical model of catheter motion in the *training* view is described (Section 3.4.2.1), following the method described previously in Section 3.1, and then its application on the *current* view (Section 3.4.2.2), which is the novel contribution of this work, is explained.

3.4.2.1 Statistical model formation in the *training* view

The formation of the statistical model comprises two main steps. Firstly, the technique described in Ma *et al.* [209] is used to track the electrodes of the CS catheter throughout the X-ray sequence.

Secondly, PCA is applied to the coordinates of the tracked electrodes. The steps are described below.

CS catheter detection. The CS tracking technique [209] is applied to all frames in the *training* view, θ_1. After the application of the tracking algorithm, the x and y positions of each of the 10 electrodes are concatenated into a single column vector for each time point. Hence, the data generated by the tracking process consists of:

$$\mathbf{s}_i = (z_{i,1,x}, z_{i,1,y}, \dots z_{i,10,x}, z_{i,10,y})^T, 1 \leq i \leq N \tag{3.28}$$

where $z_{i,e,x}$ and $z_{i,e,y}$ represent the x and y coordinates of the e^{th} electrode in the i^{th} frame. $e = 1$ corresponds to the distal electrode, and N is the number of frames. $\mathbf{s}_i \in \mathbb{R}^{20\times 1}$ is the i^{th} column of matrix $\mathbf{s} \in \mathbb{R}^{20\times N}$.

Principal component analysis. As previously described in this chapter (Section 3.1.2.1), the mean vector, $\overline{\mathbf{s}} \in \mathbb{R}^{20\times 1}$, and the covariance matrix, $\mathbf{S} \in \mathbb{R}^{20\times 20}$ are computed, for the purpose of the PCA technique. The eigenvectors $\mathbf{v}_m \in \mathbb{R}^{20\times 1}$, $1 \leq m \leq M$ of $\mathbf{S}$ represent the PCs, where M is the total number of eigenvectors, and the corresponding eigenvalues $\mathbf{d}_m \in \mathbb{R}^{1\times 1}$, $1 \leq m \leq M$ represent the variance of the data along the direction of the eigenvectors. Similar to the Tracked-PCA method $M = 20$ since the $\mathbf{s}_i$ are of length 20 (Section 3.1). The result of the PCA gives possible CS catheter electrode positions in θ_1. It was found, by correlation with the gold standard traces, that the first and second modes of variation represented the cardiac and respiratory motions, respectively (Section 3.1).

3.4.2.2 Application of statistical model on the *current* view

This section describes in detail the framework for determining the position of the CS catheter in the *current* view. For this application, the method uses the epipolar constraint and the fact that the X-ray fluoroscopy imaging modality is assumed to follow the pin-hole camera model [231, 232]. Specifically, with the use of the epipolar geometry, each of the 2D electrode positions obtained when forming the statistical model in the *training* view is backward projected to form a 3D line, which is then forward projected to generate a 2D epipolar line, in the *current* view, that contains the corresponding electrode position.

Pinhole camera model. Epipolar reconstruction allows loss of depth information to be recovered from a 2D projection image if another 2D image is taken of the same target from a different view, assuming the complete camera parameters of the X-ray fluoroscopy projective modality [233–236], are known. The camera parameters include $C = (c_s, l_s, k_1, k_2, \delta_x, \delta_y, \delta_z, \alpha, \beta, \gamma)$.

(c_s, l_s) are the pixel coordinates of the image where the beam is incident to the projection plane. $k_1 = \frac{f}{\Delta_u}$ and $k_2 = \frac{f}{\Delta_v}$, where f is the distance between the source and the projection plane, and Δ_u and Δ_v are the pixel spacing in the (u, v)-axes, respectively on the projection plane. $\delta = (\delta_x, \delta_y, \delta_z)$ and (α, β, γ) are the parameters defining the position and orientation of the camera in 3D space, illustrated in Figure 3.5.

The first four parameters, (c_s, l_s, k_1, k_2) describe the perspective projection and are known as the *intrinsic* parameters of the system. The remaining six, $(\delta_x, \delta_y, \delta_z, \alpha, \beta, \gamma)$ describe the position and orientation of the system in terms of a rigid-body translation and rotation, and are known as the *extrinsic* parameters of the system. These ten parameters can be used to create a perspective projection matrix, $\mathrm{M} \in \mathbb{R}^{3\times4}$. This matrix can be used to project a 3D position in homogeneous world coordinates, i.e. the isocentre coordinate system, $(x, y, z, 1)^T$ to a 2D position in homogeneous fluoroscopy coordinates $(u, v, 1)^T$, as shown in equation Eq. (3.29).

$$\mathbf{M}\begin{bmatrix} x \\ y \\ z \\ 1 \end{bmatrix} = \lambda \left| \begin{matrix} u \\ v \\ 1 \end{matrix} \right] \tag{3.29}$$

where λ is a scaling factor. The matrix $\mathbf{M}(C) = \mathbf{P}(c_s, l_s, k_1, k_2)\mathbf{T}(\delta_x, \delta_y, \delta_z)\mathbf{R}(\alpha, \beta, \gamma)$ can be split up into three separate matrices. These include the perspective matrix, $\mathbf{P} \in \mathbb{R}^{3\times4}$ (Eq. (3.30)), the translational matrix, $\mathbf{T} \in \mathbb{R}^{4\times4}$ (Eq. (3.31)) and the rotational matrix, $\mathbf{R} \in \mathbb{R}^{4\times4}$ (Eq. (3.32)).

$$\mathbf{P} = \begin{bmatrix} c_s & k_1 & 0 & 0 \\ l_s & 0 & -k_2 & 0 \\ 1 & 0 & 0 & 0 \end{bmatrix} \tag{3.30}$$

$$\mathbf{T} = \begin{bmatrix} 1 & 0 & 0 & \delta_x \\ 0 & 1 & 0 & \delta_y \\ 0 & 0 & 1 & \delta_z \\ 0 & 0 & 0 & 1 \end{bmatrix} \tag{3.31}$$

$$\mathbf{R} = \begin{bmatrix} \cos\beta\cos\gamma & \sin\alpha\sin\beta\cos\gamma - \cos\alpha\sin\gamma & \cos\alpha\sin\beta\cos\gamma + \sin\alpha\sin\gamma & 0 \\ \cos\beta\sin\gamma & \sin\alpha\sin\beta\sin\gamma + \cos\alpha\cos\gamma & \cos\alpha\sin\beta\sin\gamma - \sin\alpha\cos\gamma & 0 \\ -\sin\beta & \sin\alpha\cos\beta & \cos\alpha\cos\beta & 0 \\ 0 & 0 & 0 & 1 \end{bmatrix} \tag{3.32}$$

The *intrinsic* and *extrinsic* parameters describe the ideal pin-hole camera model, which can be used to describe the X-ray fluoroscopy imaging modality. This model describes the relationship

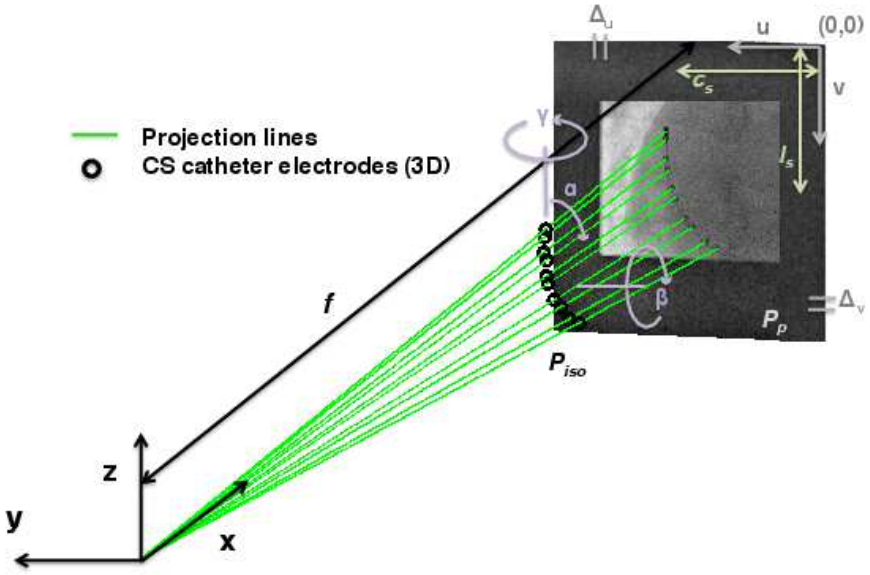

FIGURE 3.5: The relationship between a 3D point, $\mathbf{r}$, and its corresponding 2D projection, $\mathbf{p}$, onto the image plane. A 3D model of the CS catheter electrodes located at the isocentre of the projective imaging system, P_{iso}, is projected onto the projective plane, P_p, using the pinhole camera model. Projection parameters (c_s, l_s, k_1, k_2) define the projection while translations along the coordinate axes $(\delta_x, \delta_y, \delta_z)$ and rotations about the isocentre (α, β, γ) define the view coordinates (x, y, z) in relation to the isocentre.

between the 3D point on the imaging target with position $\mathbf{r} = (x, y, z)^T$, and its corresponding point on the 2D projection plane, with pixel coordinates $\mathbf{p} = (u, v)^T$, illustrated on Figure 3.5.

Projection and backprojection. For points defined in view coordinates Eq. (3.29) becomes

$$\begin{bmatrix} c_s & k_1 & 0 & 0 \\ l_s & 0 & -k_2 & 0 \\ 1 & 0 & 0 & 0 \end{bmatrix} \begin{bmatrix} x \\ y \\ z \\ 1 \end{bmatrix} = \lambda \begin{bmatrix} u \\ v \\ 1 \end{bmatrix} \tag{3.33}$$

Finding the 2D projection, $\mathbf{p}$, of a 3D position, $\mathbf{r}$, is known as forward projection. This is obtained by solving Eq. (3.33) for $\mathbf{p}$,

$$\begin{bmatrix} c_s x + k_1 y \\ l_s x - k_2 z \\ x \end{bmatrix} = \lambda \begin{bmatrix} u \\ v \\ 1 \end{bmatrix} \tag{3.34}$$

$$\begin{bmatrix} u \\ v \end{bmatrix} = \begin{bmatrix} c_s + k_1(\frac{y}{x}) \\ l_s - k_2(\frac{z}{x}) \end{bmatrix} \tag{3.35}$$

Without loss of generality, the optical axis is chosen to be the positive x-axis, as illustrated in Figure 3.5 and the scaling factor is set to x in the last row of Eq. (3.34).

The backward-projection of a 2D point, $\mathbf{p}$, is a line, called the projection line. The parametric equation for projection lines with λ as a parameter can be computed, by solving Eq. (3.33) for $\mathbf{r}$. This is done by applying the Moore-Penrose pseudo-inverse, $\mathbf{P}^+ \in \mathbb{R}^{4\times3}$, of matrix $\mathbf{P}$ to both sides of Eq. (3.33).

$$P^+P\begin{bmatrix} x \\ y \\ z \\ 1 \end{bmatrix} = P^+\begin{bmatrix} u \\ v \\ 1 \end{bmatrix}\lambda \tag{3.36}$$

where $P^+ = \begin{bmatrix} 0 & 0 & 1 \\ \frac{1}{k_1} & 0 & \frac{-c_s}{k_1} \\ 0 & \frac{1}{-k_2} & \frac{l_s}{k_2} \\ 0 & 0 & 0 \end{bmatrix}$ which results in

$$\begin{bmatrix} x \\ y \\ z \\ 0 \end{bmatrix} = \lambda\begin{bmatrix} 1 \\ \frac{(u-c_s)}{k_1} \\ \frac{(l_s-v)}{k_2} \\ 0 \end{bmatrix} \tag{3.37}$$

Camera parameters from DICOM information. Assuming the imaging target is approximately at the isocentre of the fluoroscope, with the isocentre defining the origin of the coordinate system and the X-ray beam is normal to the detector at the centre of the image, the camera matrix, $M(C) \in \mathbb{R}^{3\times4}$ is computed directly from the DICOM header of the X-ray images, as illustrated in Eq. (3.38).

$$M(C) = \begin{bmatrix} \frac{W-1}{2} & \frac{SID}{\Delta_u} & 0 & 0 \\ \frac{H-1}{2} & 0 & \frac{-SID}{\Delta_v} & 0 \\ 1 & 0 & 0 & 0 \end{bmatrix}\begin{bmatrix} \cos(\phi)\cos(\psi) & -\sin(\phi) & \cos(\phi)\sin(\psi) & SOD \\ \sin(\phi)\cos(\psi) & \cos(\phi) & \sin(\phi)\sin(\psi) & 0 \\ -\sin(\psi) & 0 & \cos(\psi) & 0 \\ 0 & 0 & 0 & 1 \end{bmatrix} \tag{3.38}$$

where, $\begin{bmatrix} \cos(\phi)\cos(\psi) & -\sin(\phi) & \cos(\phi)\sin(\psi) \\ \sin(\phi)\cos(\psi) & \cos(\phi) & \sin(\phi)\sin(\psi) \\ -\sin(\psi) & 0 & \cos(\psi) \end{bmatrix}$ is the rotation matrix to describe the orientation of the view coordinates relative to the isocentre, SID is the distance from the source to the detector, SOD is the distance from the source to the isocentre, Δ_u and Δ_v are the imager pixel spacing, ϕ is the positioner primary angle, ψ is the positioner secondary angle, W is the number of rows and H the number of columns in the X-ray image. The positioner primary angle

is defined in the transaxial plane at the isocentre with zero degrees in the direction perpendicular to the patient's chest, $+90°$ at the patient's left hand side (LAO) and $-90°$ at the patient's right hand side (RAO). The positioner secondary angle is defined in the sagittal plane at the isocentre with zero degrees in the direction perpendicular to the patient's chest. $+90°$ corresponds to the caudal direction.

Epipolar line reconstruction. Using epipolar geometry, each of the 2D electrode positions obtained when applying the statistical model in θ_1 is backward projected to form a 3D line, $\mathbf{l}_b$, which is then forward projected to generate a 2D epipolar line, $\mathbf{l}_e$, in the *current* view, θ_2, that contains the corresponding electrode position. Hence, 10 epipolar lines in θ_2 for each frame in the *current* view are generated.

Blob detection and CS catheter position estimation. The position of the CS catheter is now determined in the new image in θ_2 and simultaneously its state of cardiorespiratory motion is determined. This is done by determining the cardiorespiratory state in the PCA model of θ_1 that produces epipolar lines that intersect the catheter electrodes in the new image in θ_2. First, the fast multi-scale blob detector is used to detect all possible electrode-like objects in the new image. The positions of all detected blobs are concatenated into a blob list, **BL**.

Using the PCA model, an instance of the CS catheter, $\hat{\mathbf{s}}$, can be generated in θ_1 according to

$$\hat{\mathbf{s}} = \overline{\mathbf{s}} + \sum_m w_m \mathbf{v_m} \tag{3.39}$$

where w_m are the weights for each eigenvector. If the first two eigenvectors are used then the instance can be represented by $\hat{s}_{w_1 w_2}$. The weights $\hat{w_1}$ and $\hat{w_2}$ that represent the cardiorespiratory phase of the image for θ_2 are then estimated according to

$$\hat{w_1}, \hat{w_2} = \underset{w_1 w_2}{\operatorname{argmin}}[D(\hat{s}_{w_1 w_2}, \mathbf{BL}) + A(\hat{s}_{w_1 w_2})] \tag{3.40}$$

where $D(\hat{s}_{w_1 w_2}, \mathbf{BL})$ is a function that computes the sum of the minimum Euclidean distances between the epipolar lines generated by $\hat{s}_{w_1 w_2}$ and their nearest corresponding blobs from **BL**. Its purpose is to position the epipolar lines so that they pass through the electrodes in the new view. $A(\hat{s}_{w_1 w_2})$ is a function that computes the sum of angles between line segments joining successive blobs, in order for the optimisation to favour a smoothly curving line of blobs representing the electrodes. Similar to the Tracked-PCA technique the function is minimised using a coarse-scale exhaustive search followed by an iterative optimisation using Matlab's lsqnonlin function with the trust-region-reflective algorithm. However, for the technique to run faster, the search space for the weights now varies from $-2\sqrt{d_m}$ to $+2\sqrt{d_m}$, where d_m is the m^{th} eigenvalue, and

$1 \leq m \leq 2$. This does not compromise the performance of the technique since as stated by the 2σ rule, for a normal distribution, about 95% of the values lie within 2 standard deviations of the mean. For the application of the model on rotational sequences (see Chapter 6), where the CS catheter position deviation was larger, the search space for the weights varies from $-3\sqrt{d_m}$ to $+3\sqrt{d_m}$, to solve the optimisation.

The resulting weights indicate the cardiorespiratory phases and the blobs from **BL** nearest to the epipolar lines give the catheter location in the new image.

3.4.2.3 Cardiac and respiratory gating of the *current* view

Similar to the Tracked-PCA technique, the unknown cardiac/respiratory phases are denoted by $\hat{s}_{w_1 w_2}$, which are the electrode locations produced by weights w_1 and w_2. Specifically, $\hat{w}_1$ is used to detect systolic frames, Ω_{sys}, of the image sequence, using Eq. (3.12). These are represented by the peaks of the variation of $\hat{w}_1$ with frame number. The peaks of the variation of $\hat{w}_2$ over time represent (EI) respiratory frames, Ω_{EI}, Eq. (3.13), while the troughs represent EX respiratory frames, Ω_{EX}, Eq. (3.14).

3.4.2.4 Correction of incorrectly annotated electrodes

In addition to generating gating information, the gated electrode positions in the two views were used to reconstruct the 3D position of the CS catheter and then to track the catheter in very low dose X-ray at the new angle. This is useful in EP procedures for relating signals measured at the electrodes to locations on the anatomy. However, it is possible that an electrode is associated with an incorrect blob in the new image. This can happen if the incorrect blob is close to the epipolar line, and these incorrect electrodes must then be corrected.

Each set of CS electrode positions from the two projection planes is back-projected to reconstruct the CS catheter in 3D. The CS catheter's maximum inter-electrode distance is 5mm and incorrectly annotated electrodes are considered the ones that are located more than 9mm away from their neighbouring electrodes. Clusters of more than 2 electrodes located less than 9mm away from their neighbours are considered to be correctly annotated. A smooth spline, $\mathbf{s_r}$, $1 \leq r \leq R$, comprising a total of R points, is computed to fit the correctly annotated electrodes.

In cases where the proximal or the distal electrodes are incorrectly annotated, the two nearest spline points are used to extrapolate a 3D straight line, $\mathbf{l}_r$, passing through them. Taking all vectors as column vectors, the 3D point, $\mathbf{c}$, that minimises the sum of squared errors to $\mathbf{l}_r$ and the back projection line $\mathbf{l}_b$ from the corresponding electrode in θ_1, is found using the 3D line-to-line

distance equation [237],

$$c = ((I - \mathbf{d} \cdot \mathbf{d}^T) + (I - \mathbf{d}_2 \cdot \mathbf{d}_2^T))^{-1} \cdot [(I - \mathbf{d} \cdot \mathbf{d}^T) \cdot \mathbf{r} + (I - \mathbf{d}_2 \cdot \mathbf{d}_2^T) \cdot \mathbf{r}_2] \tag{3.41}$$

I is the identity matrix, $\mathbf{d}$ is the unit direction vector of $\mathbf{l}_r$, $\mathbf{d}_2$ is the unit direction vector of $\mathbf{l}_b$, r is the nearest point on the spline, $\mathbf{r}_2$ is a point on $\mathbf{l}_b$ and $*^T$ represents the transpose. The electrode is then corrected to $\mathbf{r}_{cor}$, the point on line $\mathbf{l}_b$ that is closest to $\mathbf{c}$, and therefore $\mathbf{l}_r$, using Eq. (3.42)

$$\mathbf{r}_{cor} = \mathbf{r}_2 + ((c - \mathbf{r}_2)^T \cdot \mathbf{d}_2)\mathbf{d}_2 \tag{3.42}$$

In cases where an incorrect electrode is found somewhere in the middle of the CS catheter, it is corrected to the point on line $\mathbf{l}_b$ that is closest to one of the points on the spline segment, using Eq. (3.43)

$$\mathbf{r}_{cor} = \mathbf{r}_2 + ((s_r - \mathbf{r}_2)^T \cdot \mathbf{d}_2)\mathbf{d}_2 \tag{3.43}$$

The 10 final 3D electrode points are forward projected to θ_2. Figure 3.6 illustrates a faultless electrode annotation scenario. The backward-projected lines, $\mathbf{l}_b$ reconstructed from each of the 10 electrodes in θ_1, the 3D reconstruction of the CS electrodes and the backward-projected lines from the correctly annotated electrodes in θ_2 are illustrated on the figure. Figures 3.7 and 3.8 illustrate a scenario of correcting incorrectly annotated electrodes at the end and in the middle of the CS catheter, respectively. The backward-projected line reconstructed from the corresponding incorrect electrode in θ_1 along with the backward-projected lines reconstructed from the annotated electrode in θ_2 before and after correction, denoted by $\mathbf{l}_{incorrect}$ and $\mathbf{l}_{correct}$, respectively, are illustrated on the figures.

3.5 Summary

In this chapter the novel frameworks of the developed motion gating techniques were presented. The first proposed technique, Tracked-PCA, is based on the formation of a novel statistical model of the motion of the CS catheter using the statistical technique of PCA of tracked electrode locations from X-ray fluoroscopy images. The model is developed for the purposes of retrospective cardiac and respiratory gating of X-ray fluoroscopy images in normal dose X-ray. A modification of the technique allows application to very low dose scenarios. For the application of the technique to very low dose images the motion gating could be used either retrospectively or in near real-time. In this chapter its use for near real-time gating was proposed. The gating is near real-time in the sense that although there is no need to collect the whole sequence before processing, it will be performed with a phase-lag of 1 sample interval. Along with near real-time cardiorespiratory motion determination, this technique is able to track the CS catheter throughout the X-ray images. The technique relies on the constraint that the CS catheter is present in the X-ray

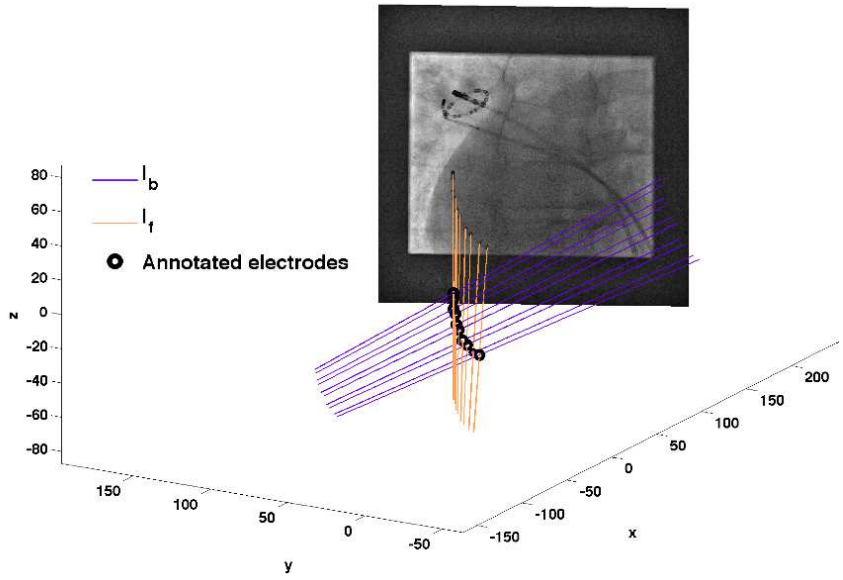

FIGURE 3.6: Graphical representation of a faultless electrode annotation scenario. The backward-projected lines, $\mathbf{l}_b$, reconstructed from each of the 10 electrodes in θ_1, the 3D reconstruction of the CS electrodes and the backward-projected lines from the correctly annotated electrodes in θ_2 are illustrated on the figure.

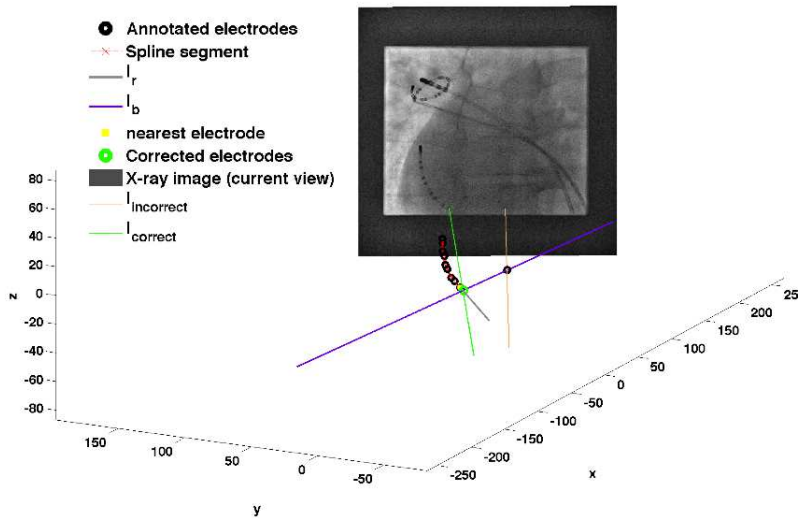

FIGURE 3.7: Graphical representation of a scenario of correcting incorrectly annotated electrodes at the end of the CS catheter. The 3D spline segment, the annotated electrodes, the corrected electrode, the 3D straight line, $\mathbf{l}_r$, extrapolated from the two nearest spline points, the nearest correct electrode, the backward-projected line reconstructed from the corresponding incorrect electrode in θ_1, $\mathbf{l}_b$, and the backward-projected lines reconstructed from the annotated electrode in θ_2 before and after correction, denoted by $\mathbf{l}_{incorrect}$ and $\mathbf{l}_{correct}$, respectively, are illustrated on the figure.

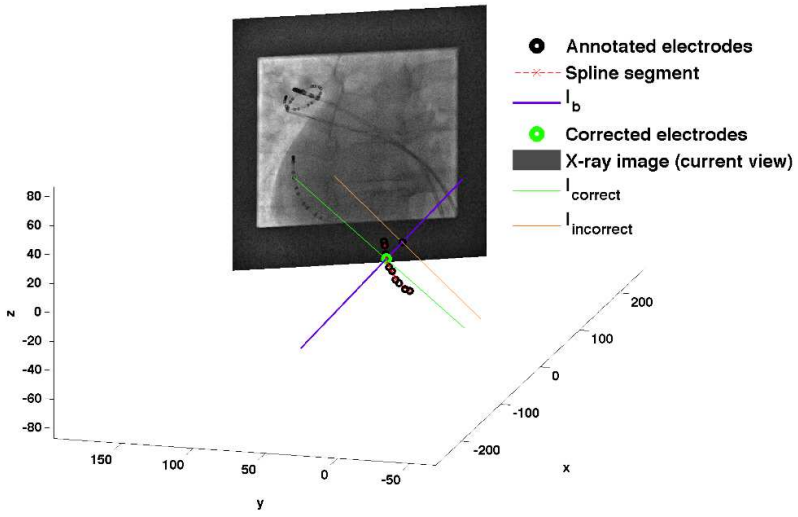

FIGURE 3.8: Graphical representation of a scenario of correcting incorrectly annotated electrodes at the middle of the CS catheter. The 3D spline segment, the annotated electrodes, the corrected electrode, the backward-projected line reconstructed from the corresponding incorrect electrode in θ_1, $\mathbf{l}_b$, and the backward-projected lines reconstructed from the annotated electrode in θ_2 before and after correction, denoted by $\mathbf{l}_{incorrect}$ and $\mathbf{l}_{correct}$, respectively, are illustrated on the figure.

images. To drop the constraint of the presence of the CS catheter in the images, a robust to varying image-content technique has been developed, the HML-based technique. The technique is robust to typical EP X-ray images that contain a varying number of different types of EP catheters and may include contrast agent injection.

An additional robust to varying image-content motion gating technique, the Masked-PCA technique, is later developed with the aim of increasing the cardiac gating performance of the HML-based technique. The PCA statistical method is used in combination with other image processing operations to make the proposed Masked-PCA technique suitable for cardiorespiratory gating. Again, this developed technique does not rely on specific catheters being present in the image data or the localisation of these devices, and makes no assumptions about the nature of the motion present in the images. For the HML-based and Masked-PCA techniques, the whole sequence should be collected before processing. Therefore, the techniques are intended for retrospective analysis. Both techniques are intended to work on low dose images and are therefore robust-to-noise. One major limitation of the above and other model-based approaches is the requirement to build a separate model for each X-ray view. Therefore, the Tracked-PCA technique is significantly extended to make it X-ray system view-angle independent. This approach is based on forming a PCA-based model of the CS catheter in a first or *training* view and then using this to determine both the cardiac and the respiratory phases, in near real-time, in any arbitrary second or *current* view. For this application, the method uses the epipolar constraint and a Euclidean

distance/angle-based cost function. Along with near real-time cardiorespiratory motion determination, this technique is able to track the CS catheter throughout the X-ray images, again in any arbitrary subsequent view. Similar to all other techniques, this View-angle independent technique is robust-to-noise. Therefore, it remains robust and accurate when applied to very low dose X-ray images. It will be shown in the following chapters that the techniques developed in this thesis can extract useful information from interventional X-ray images whilst minimising exposure to ionising radiation.

Chapter 4

Phantom validation

Contents

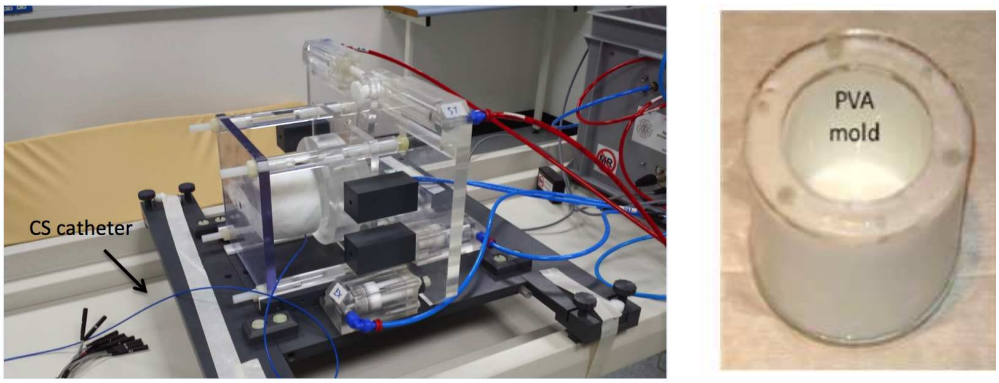

(a) (b)

FIGURE 4.1: (a) Bespoke beating and breathing left ventricular phantom with an inserted CS catheter. (b) PVA cylinder mold.

4.1 Introduction

As described in Chapter 3, in order to provide a comprehensive validation of the proposed frameworks of the motion gating techniques, experiments have been conducted on both phantom and clinical data. In this chapter, the techniques' feasibility, robustness and performance are evaluated in vitro. Applying the algorithms to phantom models of the heart has many benefits that cannot be reproduced in a live clinical environment for reasons of safety and practicality. Firstly, multimodal fiduciary markers may be placed directly on a model of the heart to obtain a gold standard cardiac and respiratory motion which is impractical in a live clinical environment. This gold standard result allows a quantitative assessment of the algorithms' performance. Additionally, multiple catheter trajectories can be tested in a single phantom whereas this would be highly impractical, and potentially dangerous, to practice in a patient. This provides the ability to determine whether the algorithms' robustness is dependent on specific catheter configurations.

Experiments have been performed on a bespoke beating and breathing left ventricular phantom [98] with an inserted CS catheter, designed to emulate the clinical workflow of a typical catheterisation, as illustrated in Figure 4.1a. For this phantom, polyvinyl alcohol (PVA, Lenticats, GeniaLab, Braunschweig, Germany) [238, 239] was used as a tissue-mimicking material, to mimic the heart during cardiac interventions. A cylindrical PVA phantom with an inner radius of 6.6cm, an outer radius of 8.2cm and a length of about 9cm, providing an initial wall thickness about 1.6cm, was generated using one freeze / thaw cycle at $-35°C/+20°C$. The PVA phantom, illustrated in Figure 4.1b, was placed in an MR-compatible air-pressured actuator [113] which compresses and rotates the PVA according to a preset heart rate. Along with the cardiac motion, the phantom actuator can translate the phantom up and down to simulate breathing motion. For the experiments demonstrated in this chapter, the cardiac rate varied between 70 and 100 cycles per minute (cpm), while the respiratory rate varied between 8 and 12 cpm.

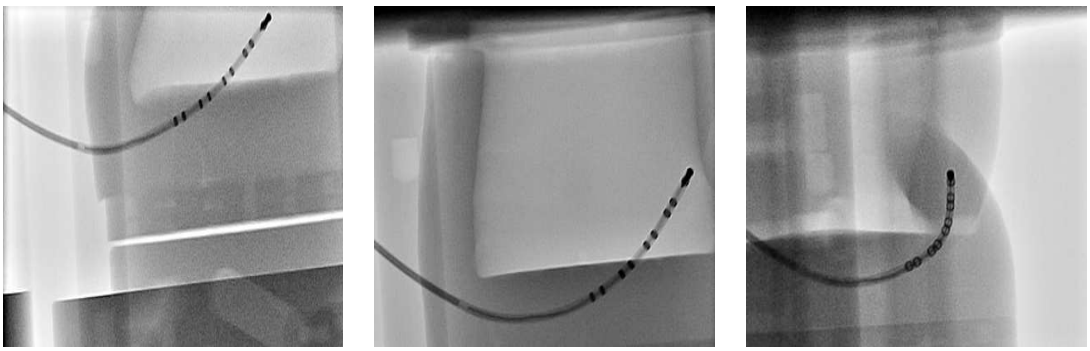

(a) (b) (c)

FIGURE 4.2: The first image of three example X-ray phantom sequences with varying configurations of the inserted CS catheter, where (a) illustrates a smooth CS catheter structure (b) a more curved structure compared to the first image and (c) an even more curved structure.

4.2 Data acquisition

All imaging was carried out using a monoplane 25cm flat panel cardiac X-ray system (Philips Allura Xper FD10, Philips Healthcare, Best, The Netherlands) in one of the catheterisation laboratories at St. Thomas' Hospital, London. As stated previously, phantom images were acquired using a bespoke beating and breathing left ventricular phantom with an inserted CS catheter. Two sequential multiplane (one biplane and one triplane) phantom X-ray sequences were acquired, comprising a total of 1741 frames, 5 runs in total, running from a minimum of 9.8 to a maximum of 22.7 seconds, covering at least two respiratory cycles. The triplane sequences, comprising a total of 767 frames, were acquired using cardiac and respiratory rates of 70 cpm and 12 cpm, respectively, while the biplane sequences, comprising a total of 974 frames, were acquired using 100 cpm and 8 cpm, respectively. X-ray imaging was performed at 30 frames per second. The X-ray system settings were 70-100 kVp with the tube current under automatic exposure control. All X-ray images were 1024^2 pixels in resolution, with a pixel to mm ratio, $R_{\text{X-ray}}$, of 0.25. Included in this ratio is the typical magnification factor of the X-ray system.

Figure 4.2 illustrates the first image of three example X-ray sequences that have been processed showing different CS catheter configurations. These catheter configurations depend on the extent of the curved structure of the catheters. The figure is an attempt to show that the proposed algorithms' robustness is not dependent on specific catheter configurations.

4.3 Methods of validation

4.3.1 Ground truth gating and catheter tracking

To validate the proposed techniques, gold standard cardiorespiratory signals were generated along with a gold standard for the electrode positions in each X-ray image. The latter was done only for the Tracked-PCA and View-angle independent technique by the use of the real-time CS tracking technique [209]. Manual tracking was performed in cases where the technique failed to accurately detect electrodes. This was done by manually localising the centre of any misdetected electrode of the CS catheter. To generate the gold standard cardiorespiratory signals, two different regions of interest moving independently with cardiac and respiratory motion were automatically tracked. This was done by using the diaphragm/heart border tracking technique [95]. For additional verification of the gold standard accuracy, two metal ball bearings were attached to the phantom and tracked to obtain cardiac and respiratory motion signals. Tracking of these ball bearings was done manually by localising their centres, in the same way as the CS catheter electrodes were located when the automatic tracking technique failed. This was done for two example phantom sequences. Results were compared and found to be identical to the gold standard results from the diaphragm/heart border tracking.

An example image of one processed X-ray sequence is shown in Figure 4.3a, with the CS catheter, the PVA phantom, the attached metal ball bearings and the ROIs used to obtain the cardiac and respiratory gold standards indicated. The first image of the same example processed X-ray sequence at normal dose is shown in Figure 4.3b, where electrodes identified as CS catheter electrodes are shown by green and white crosses, detected by the algorithm proposed by Ma *et al.* [209]. Manual tracking was performed in cases where the algorithm failed to accurately detect electrodes. 0.2% of the total 17410 electrode detections were carried out manually.

4.3.2 Training and testing data

To apply the techniques retrospectively, all frames of the sequence were used for both training and testing the model. There was no separation between training and testing data because the technique is intended for retrospective analysis. On the other hand, for the techniques applied in near real time (the Tracked-PCA technique in low dose X-ray images and the View-angle independent technique) the model was formed from training data and tested on a separate testing sequence.

For the low dose analysis of the Tracked-PCA technique the leave-one-out cross-validation (LOOCV) approach was used [240]. To use this approach, training and testing data were taken from the same sequence. This involved using a single frame from the original X-ray sequence

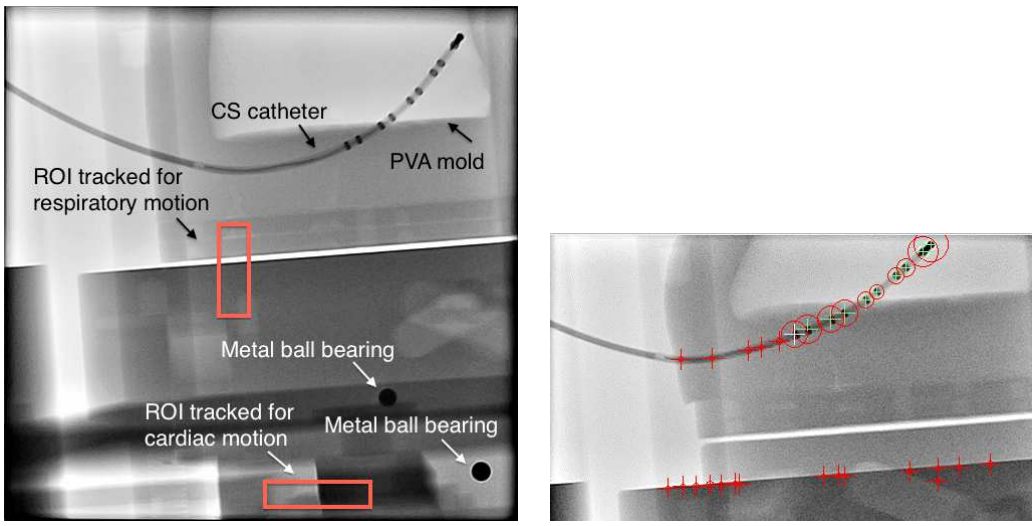

(a) (b)

FIGURE 4.3: (a) Case 1: example X-ray image of the phantom showing the inserted CS catheter, the PVA phantom, the attached metal ball bearings and the ROIs tracked to obtain cardiac and respiratory gold standard results. (b) Electrodes identified as CS catheter electrodes are shown in green crosses, detected by the algorithm proposed by Ma *et al.* [209]. The white cross illustrates the proximal electrode of the CS catheter. Red circles illustrate the strength of the detected blobs.

as the validation data, and the remaining frames as the training data, for each of the frames in turn. The model was trained on noise-free images but the validation frame had various levels of noise added. Separate PCA models were formed for each X-ray sequence and each model was tested on every frame of the sequence, both uncorrupted and at all different levels of SNR. A total of 13928 tests were performed.

The View-angle independent technique was validated on the 2 sequential multiplane (one biplane and one triplane) phantom X-ray sequences. The PCA model was formed for each sequence individually (training data) and the method run on each possible combination of sequence pairs (testing data), giving a total of 8 phantom experiments.

4.3.3 Optimisation of parameters

The HML-based and Masked-PCA algorithms have four parameters that must be set. This was done using the LOOCV approach [240]. This involved using 4 of the phantom sequences as the training data and the remaining sequence as the validation data. To build the algorithm, the four parameters involved in extracting the cardiac phases were optimised. These parameters are: a threshold level on the normalised output, 0 to 1, of the FV filter, the size of the structuring element in the morphological dilation of the identified structures, and the pass band and stop band frequencies (normalised from 0 to 1) of the band pass filter. The optimisation was done by an iterative approach, applied separately for each set of 4 training data. Initially, the first

two parameters (FV filter threshold and number of morphological dilations) were optimised by exhaustively searching within the ranges 0.01 to 0.99 in steps of 0.001 and 1 to 40 in steps of 1, respectively. The other two parameters (pass and stop band frequencies) were initially set to 0.25 and 0.75 in the normalised range 0 to 1. Optimum values for the first two parameters were determined by comparing to the gold standard results. Following this, the other two parameters were optimised in a similar way, keeping the first two fixed at their optimum values, and varying both the pass and stop bands in the normalised range 0.01 to 0.99 in steps of 0.001. These two exhaustive searches were applied alternately a number of times until the four values had converged. The optimization was done in this way because it is faster than a 4D exhaustive search.

The parameters were optimised to be > 0.02, 27–33, 0.54–0.62 and 0.96–0.98, respectively, for the HML-based technique applied on the phantom X-ray sequences. The parameters were optimised to be > 0.02, 1, 0.54–0.62 and 0.96–0.98, respectively, for the Masked-PCA technique.

4.3.4 Application in normal dose images

4.3.4.1 Gating validation

To validate the motion gating techniques the signals obtained using the gold standard methods were compared to the signals obtained using the automatic methods. For both cardiac and respiratory gating, the absolute frame difference was computed between the automatic techniques and the gold standard techniques. Specifically, end-systolic, end-inspiration (EI) and end-expiration (EX) peaks were recorded from the automatic and gold standard methods and their corresponding absolute frame differences were computed. Faultless gating results are signified when the absolute frame difference is zero. Since at the ends of the cycle the phantom stopped moving for a few frames, the trace does not have single frames defining the peaks. Instead, for the phantom data only, the frame difference at a peak was defined as the worst of the two differences between the start and end points of the stationary period. Zero frame difference corresponded to cases where both the start and end of the stationary period matched exactly. Even though the whole cycle is detected, as illustrated in Section 4.4.2.1, for evaluation, only the start and end points of the peaks and troughs were used, since the gold standard is well-defined at these points.

4.3.4.2 Frame rate dependency validation

To further investigate the algorithms' performance on varying frame rates, each sequence, initially acquired at a frame rate of 30 f/s, was resampled to alter its frame rate. This resulted in obtaining additional sequences of 10f/s, 5f/s and 3f/s. The techniques were applied to the

obtained sequences to investigate the algorithms' robustness and accuracy on sequences acquired with different frame rates. For these experiments, once the frames were removed the ground truth was adjusted by moving the ground truth peaks to the nearest remaining frame.

4.3.5 Application in very low dose images

4.3.5.1 Application of Poisson noise

In X-ray imaging, the image intensities correspond to the number of transmitted photons per pixel. Consequently, to simulate the noise in low dose X-ray images, the images were corrupted by applying Poisson noise. Input pixel values in an image are interpreted as scaled to the display range of the X-ray system. Poisson noise is added after unscaling to an original signal level. The chosen scaling determined the SNR. The final image is then obtained by scaling the noisy image back to the display range. The magnitude of the noise varies across the image, as it depends on the local image intensity. The image noise is therefore specified in terms of the median value of the Poisson mean. Higher median values produce images with higher signal to noise ratio (SNR). SNR values of $\sqrt{50}$, $\sqrt{10}$, $\sqrt{8}$, $\sqrt{6}$, $\sqrt{5}$, $\sqrt{2}$ and $\sqrt{1}$ were used. These values were chosen by initially applying the CS catheter tracking algorithm on low noise levels that are almost indistinguishable from the noise-free image, and then gradually increasing the noise level until the algorithm started failing, i.e. the success rate became less than 90%.

Figure 4.4 illustrates the results of the application of Poisson noise on the first image of an example phantom X-ray sequence. In Figure 4.4, the first image of an uncorrupted example phantom X-ray sequence is displayed, along with the simulated noisy images with SNRs ranging from $\sqrt{50}$ to $\sqrt{1}$.

4.3.5.2 Catheter tracking validation

To validate the performance of the CS catheter tracking, median errors per electrode for the uncorrupted and the different SNR X-ray sequences were calculated. Errors were calculated with respect to the gold standard detection. Since the technique is designed return tracking locations for each of the 10 CS catheter electrodes, errors were calculated for each of them independently. Success rates were also calculated. For the proposed technique to be acceptable in clinical practice, failure cases were considered to be the ones where individual errors per electrode were above 2 mm [93].

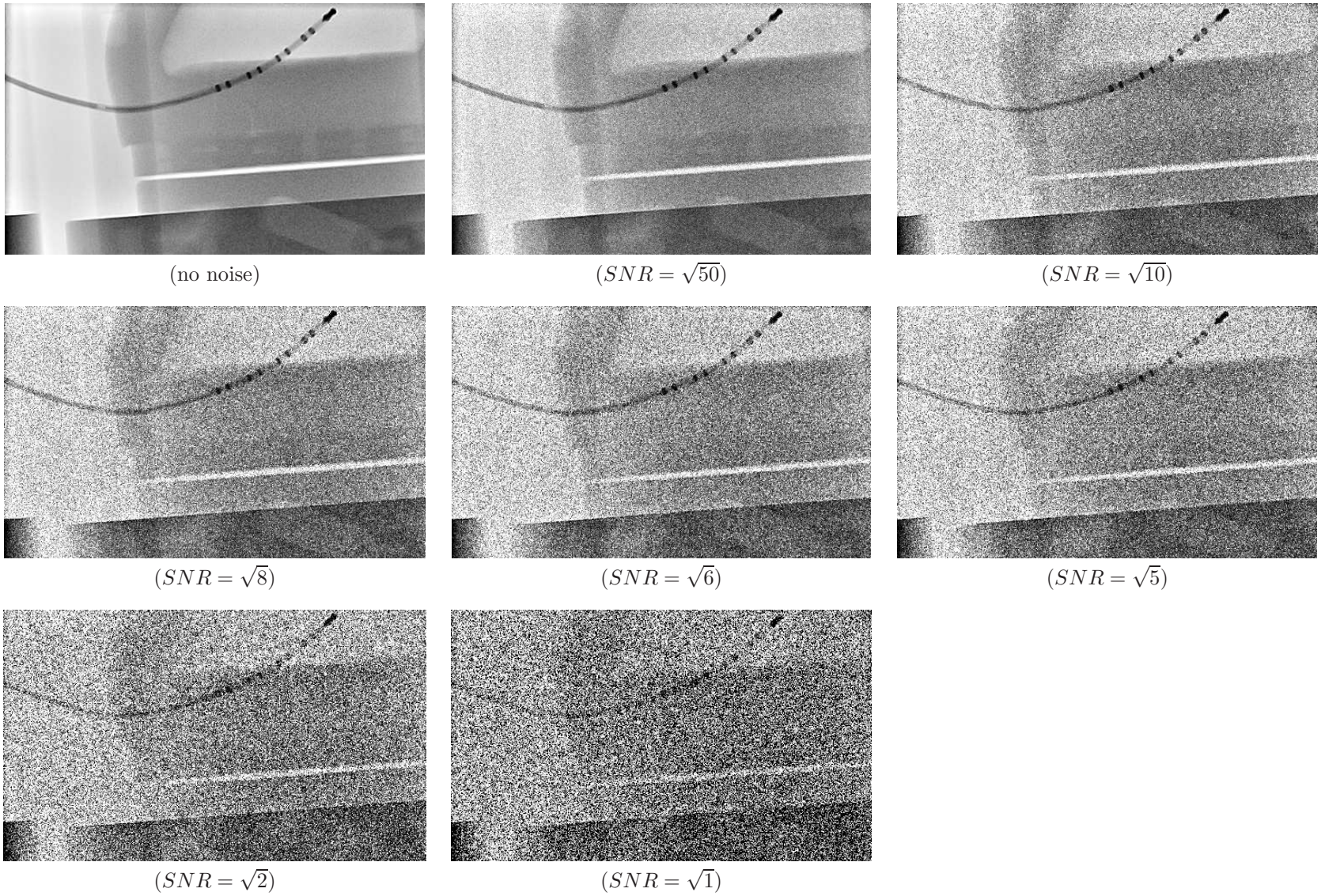

FIGURE 4.4: Case1: example of an uncorrupted phantom X-ray image and the same X-ray image corrupted with different levels of Poisson noise.

4.3.5.3 Gating validation

Similar to the gating validation on normal dose images, for both cardiac and respiratory gating, the absolute frame difference was computed between the automatic techniques and the gold standard techniques. For the validation on low dose images absolute frame differences were computed for all noise levels. A comparison of the Tracked-PCA, HML-based and Masked-PCA techniques was included to show the effect of the extra step of developing a robust to varying image-content method that does not rely on any specific catheters being present in the images. Also the comparison shows the effect of the development of the Masked-PCA technique to increase the cardiac gating performance of the HML-based technique. Furthermore, a comparison of the View-angle independent technique with the proposed single view Tracked-PCA technique was included to show the effect of the extra step of changing view-angle.

4.4 Experimental results

4.4.1 Gold standard validation

It is important to investigate the accuracy and precision of the chosen gold standard methods. In this section, an experimental quantitative validation of the gold standard used for the validation of the developed techniques on phantom sequences is performed. In particular, this section states the accuracy, precision and robustness of the gold standards. Gold standard methods include: the automatic diaphragm/heart border tracking technique [95], used as the ground truth for motion gating by tracking two different regions of interest moving independently with cardiac and respiratory motion, the real-time tracking technique and the manual detection of the CS catheter electrodes performed in cases where the real-time CS catheter tracking technique failed. These last two were used in combination as a gold standard for the validation of the CS catheter tracking.

As already mentioned in Section 4.3.1, the accuracy and robustness of the diaphragm/heart border tracking technique [95], was validated by manual tracking of ball bearings attached to the phantom. This was done by localising their centres in every frame of the sequence. Two example phantom sequences, comprising a total of 1050 frames and a total of 68 peaks/troughs, were used. The peaks/troughs of the obtained results were compared and found to be identical to the gold standard results from the diaphragm/heart border tracking.

Regarding the real-time tracking technique's accuracy, CS catheter detection errors were evaluated in Ma *et. al* [95]. To test the accuracy of the CS detection, two clinical experts were asked to manually pick the centre of all electrodes of the CS catheter on 1048 X-ray images, comprising a total of 10480 CS catheter electrodes. The 2D distance was calculated between the manually

TABLE 4.1: Average and standard deviation of the difference between the results of the two observers per electrode over all frames of a randomly chosen phantom sequence, starting from the proximal (el.1) and moving to the distal (el.10) electrode.

Difference between observers (mm)		
Electrode number	Average	Standard deviation
1	0.40	0.90
2	0.42	1.06
3	0.49	1.11
4	0.45	1.02
5	0.41	0.98
6	0.49	2.07
7	0.45	1.18
8	0.48	1.13
9	0.52	1.65
10	0.53	1.95

defined centres and the centres detected by the automated method for all 10 electrodes. Overall, a 2D detection error of 0.39 ± 0.22 mm was achieved for all electrodes in all images.

Regarding the manual electrode detection gold standard method, manual localisation of the electrodes was done by two independent observers. Inter-observer variability for electrode detection was assessed by computing the average Euclidean distances between the manually defined electrode positions detected by Observer 1 and Observer 2 over all frames in the test sequence. The purpose of the validation was to assess the precision of manual CS catheter detection considered as the ground truth for the validation of the CS catheter tracking performed in cases where the real-time CS catheter tracking technique failed. This was done for one phantom sequence comprising a total of 330 frames. Consequently, a total of 3300 electrode detections were performed by both observers and their detection accuracy was evaluated. Results were computed for each of the 10 electrodes individually and illustrated in Table 4.1. The results were initially computed in pixels and converted to mm using the pixel to mm ratio, $R_{\text{X-ray}}$ (Section 4.2).

4.4.2 Tracked-PCA technique

4.4.2.1 Retrospective method in normal dose images

Example of cardiac and respiratory traces. A graphical representation of cardiac phases obtained after applying the Tracked-PCA method (dashed-dot black line) for one example X-ray sequence is illustrated in Figure 4.5a. The gold standard cardiac trace is also shown in a solid black line. The respiratory traces obtained after applying the Tracked-PCA method are illustrated in Figure 4.5b in a dashed-dot black line, for the same phantom case. The gold standard respiratory trace is also shown in a solid black line.

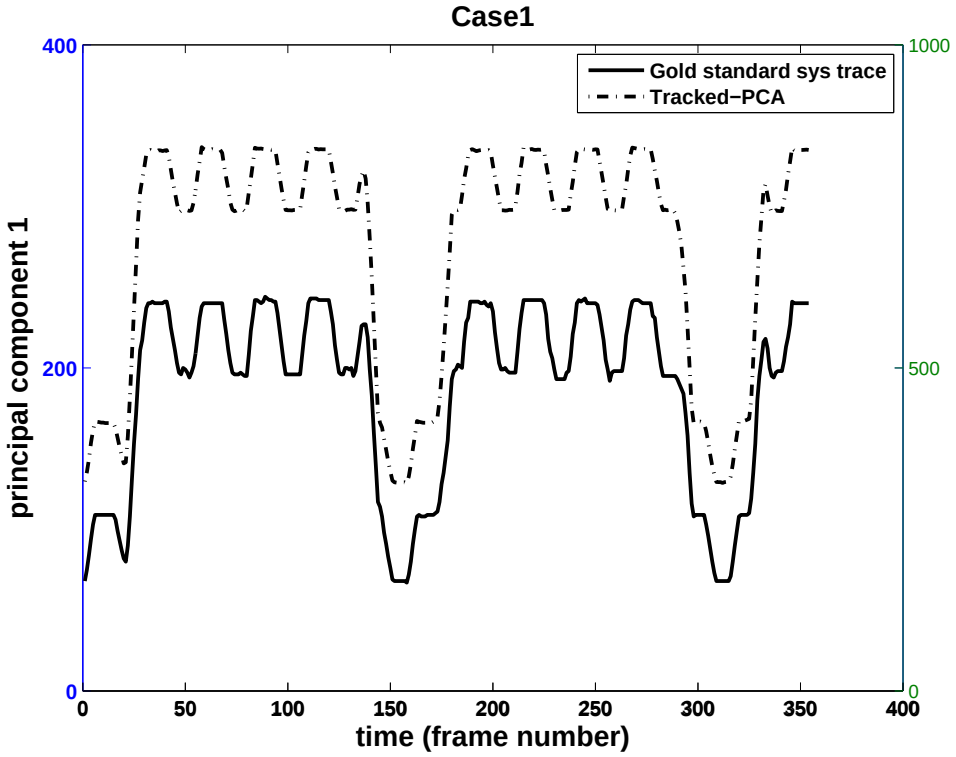

(a)

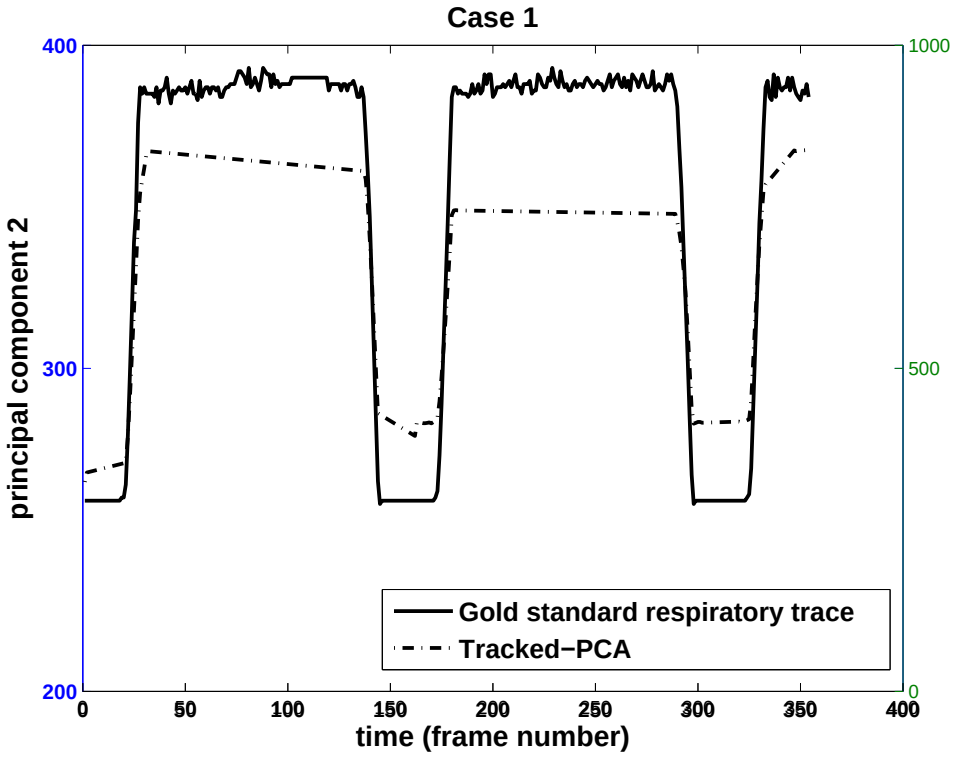

(b)

FIGURE 4.5: (a) The cardiac trace obtained after applying the Tracked-PCA method is illustrated in a dashed-dot black line for an example phantom case, Case 1. The gold standard cardiac signal is also shown in a solid black line. (b) The respiratory trace obtained after applying the Tracked-PCA method is illustrated in a dashed-dot black line for the same phantom case. The gold standard respiratory signal is also shown as a solid black line. In both graphs the blue y-axis scale corresponds to the gold standard trace while the green one corresponds to the trace obtained using the automatic technique.

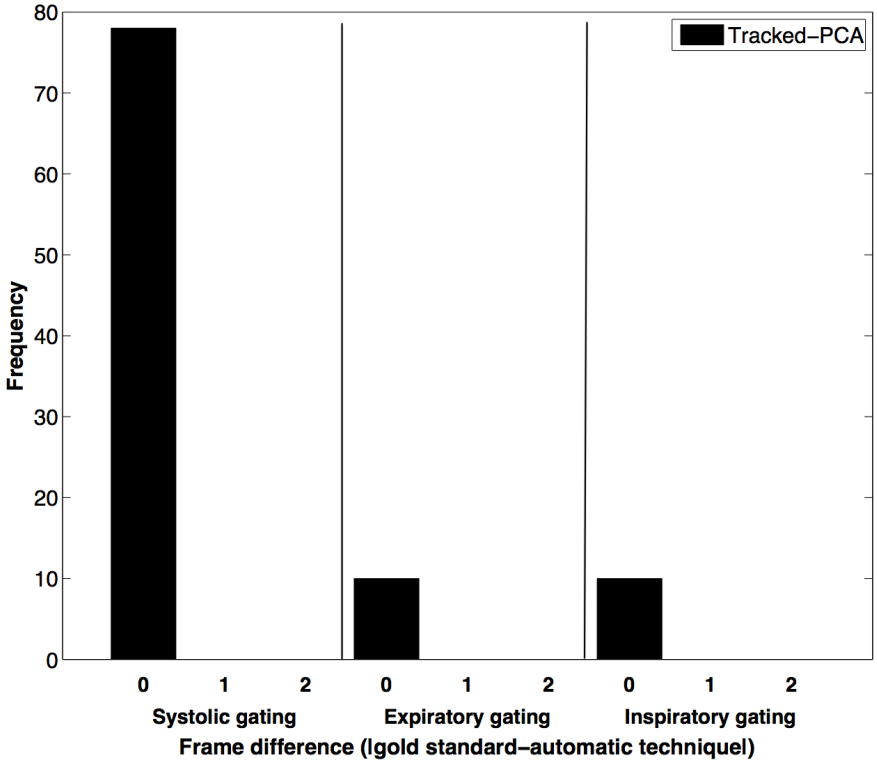

FIGURE 4.6: Frequency distributions of frame difference errors for cardiac (end-systolic), EX and EI gating using the Tracked-PCA technique.

TABLE 4.2: Percentage success rates for different frame rates. Success rate is defined as the percentage of gold standard gating frames that exactly match their corresponding automatically detected gating frames.

	Success rates (%)		
Frame rate	end-systolic gating	EX gating	EI gating
30 f/s	100	100	100
10 f/s	100	100	100
5 f/s	100	100	100
3 f/s	100	100	100

Quantitative validation. The gating results can be seen in the frequency distribution bar charts in Figure 4.6, for end-systolic, EI and EX gating. Specifically, Figure 4.6 illustrates the frame difference errors in histogram plots, i.e. the number of peaks or troughs with 0, 1 or 2 frames separation from the gold standard for the phantom sequences, for all gating tasks. The results illustrate that the proposed Tracked-PCA technique is faultless in the extraction of cardiac and respiratory motion information of the X-ray phantom sequences. Table 4.2 displays the percentage success rates over all sequences at different frame rates. Percentage success rates were computed using the equation $\frac{100x}{x_{total}}$, where x corresponds to the number of gold standard and automatic-gating frames that are matched within the allowable gating error and x_{total} corresponds to the total number of gold standard gating frames. Percentage success rates were computed for end-systolic, EX and EI gating for all sequences at different frame rates.

4.4.2.2 Near-real-time method in very low dose images

Blob detection method on noisy X-ray images. Figure 4.10 illustrates the results of applying the fast multi-scale blob detector to detect all possible electrode-like objects. In Figure 4.10, an uncorrupted phantom X-ray image is shown, along with the noisy X-ray images with SNRs ranging from $\sqrt{50}$ to $\sqrt{1}$. Electrodes identified as CS catheter electrodes are shown in green crosses. The white crosses illustrate the proximal electrode of the CS catheter, while the red circles illustrate the strength of the detected blobs, with larger circles indicating stronger blobs.

PCA-based CS catheter tracking. The results of the Tracked-PCA CS catheter tracking technique are displayed in Figure 4.11, in yellow crosses. Figure 4.11 demonstrates the CS catheter position on the first phantom image of the uncorrupted example X-ray sequence along with the CS catheter detection on the noisy phantom X-ray images with ranging SNRs from $\sqrt{50}$ to $\sqrt{1}$.

CS catheter tracking quantitative validation. In preliminary experiments, median errors per electrode were computed when using different numbers of PCs to predict the catheter position. Results confirmed that only the first two PCs contained useful information and the rest were dominated by noise. Hence, only the first and second PCs were used in this study. Figure 4.7a illustrates median errors per electrode for the Tracked-PCA CS catheter tracking on the uncorrupted and the seven different SNR X-ray images. Errors are calculated with respect to the gold standard detection. Since the technique is designed to track each of the ten CS catheter electrodes separately, errors are calculated and displayed for each of them independently in different grey scale colours, starting from the proximal (black colour) and moving to the distal (white colour) electrode. Success rates were also calculated. For the proposed technique to be acceptable in clinical practice, failure cases were considered to be the ones where individual errors per electrode were above 2 mm [93]. In Figure 4.7b, median errors were calculated and are shown only for the successfully tracked CS catheter electrodes. Figure 4.8, shows the range of the values in terms of the 25^{th} percentile, median and 75^{th} percentile, over all electrodes, and for successfully tracked electrodes, for each noise level. In particular, the values are not computed for each electrode individually but over all electrodes in each noise level. Percentage success rate (%) results are illustrated in Figure 4.9. Outcomes show that the proposed method for tracking the CS catheter on low dose X-ray images performs exceptionally well, with 100% success rates for the normal dose phantom images and the images of SNR values of $\sqrt{50}$, $\sqrt{10}$ and $\sqrt{8}$.

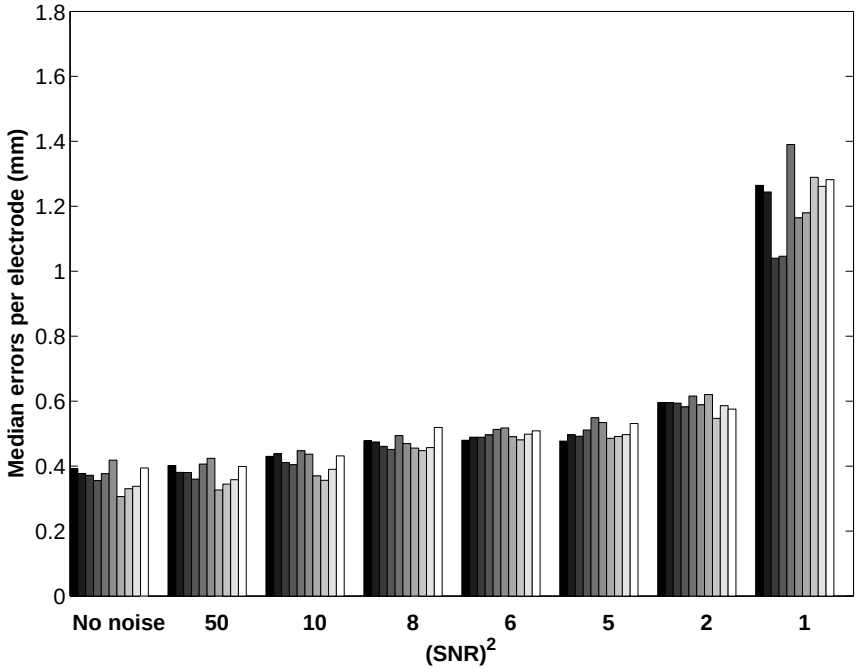

(a)

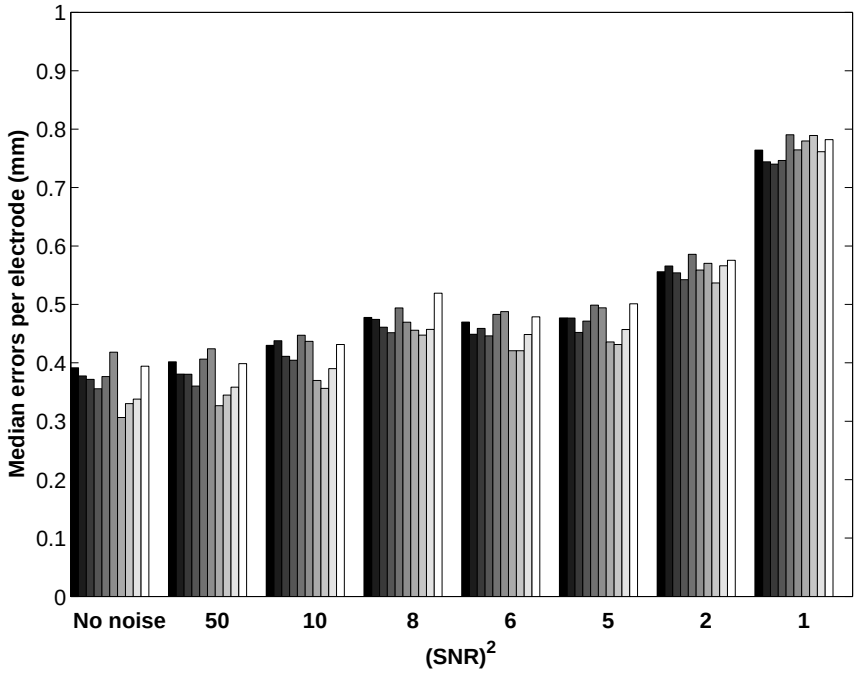

(b)

FIGURE 4.7: Median errors per electrode, at different SNR levels, with respect to the gold standard for (a) all tracked CS electrodes (b) only for the successfully tracked CS electrodes using the Tracked-PCA technique. These are the ones tracked with less than 2mm accuracy. Different grey scale colour bars are used to distinguish the CS catheter electrodes, starting from the proximal (black colour) and moving to the distal electrode (white colour).

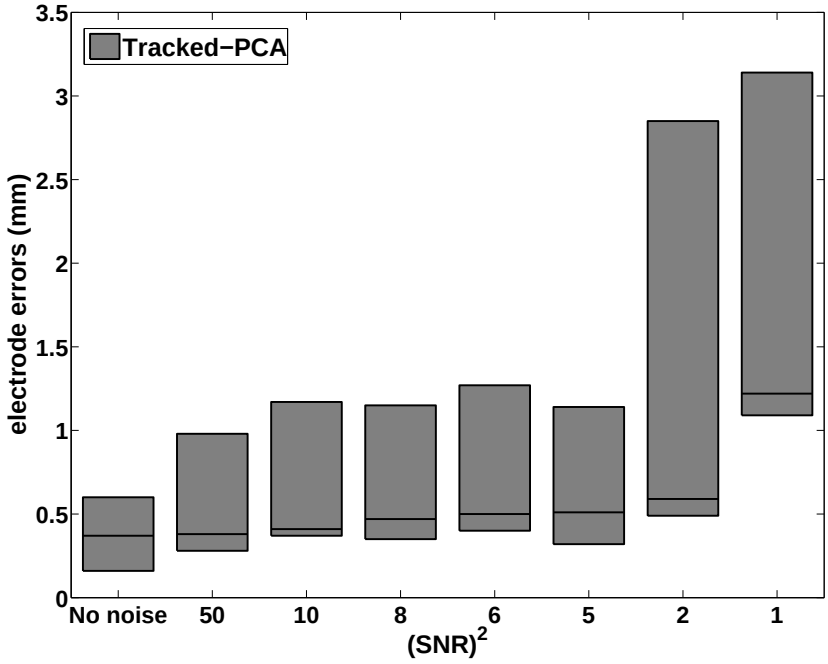

(a)

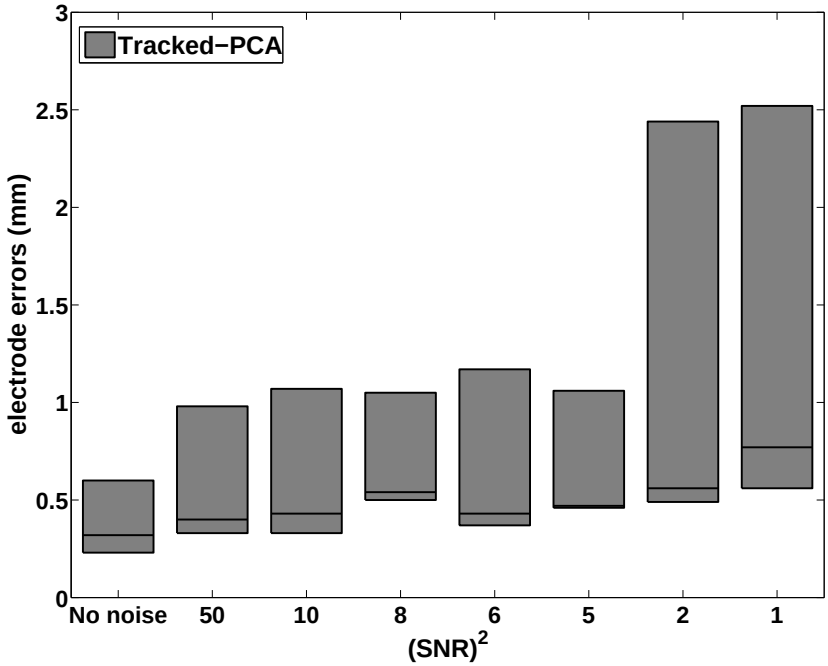

(b)

FIGURE 4.8: Illustration of the 25^{th} percentile, median and 75^{th} percentile, values over (a) all CS catheter electrodes in the data sets (b) only successfully tracked CS catheter electrodes, for each noise level using the Tracked-PCA technique on phantom datasets.

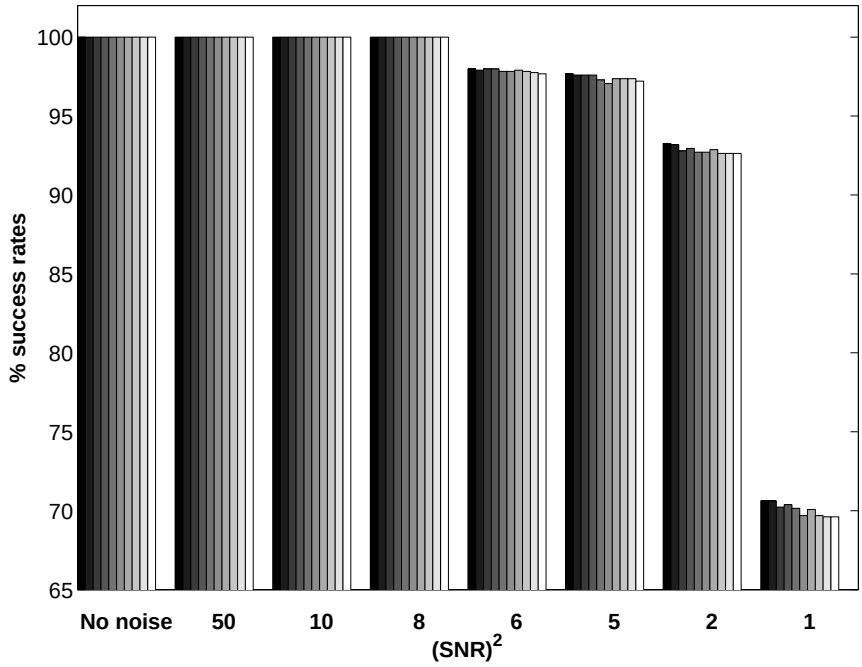

FIGURE 4.9: Tracked-PCA CS catheter tracking technique percentage success rates (%). Success cases are considered to be the ones where the individual errors per electrode are below 2 mm.

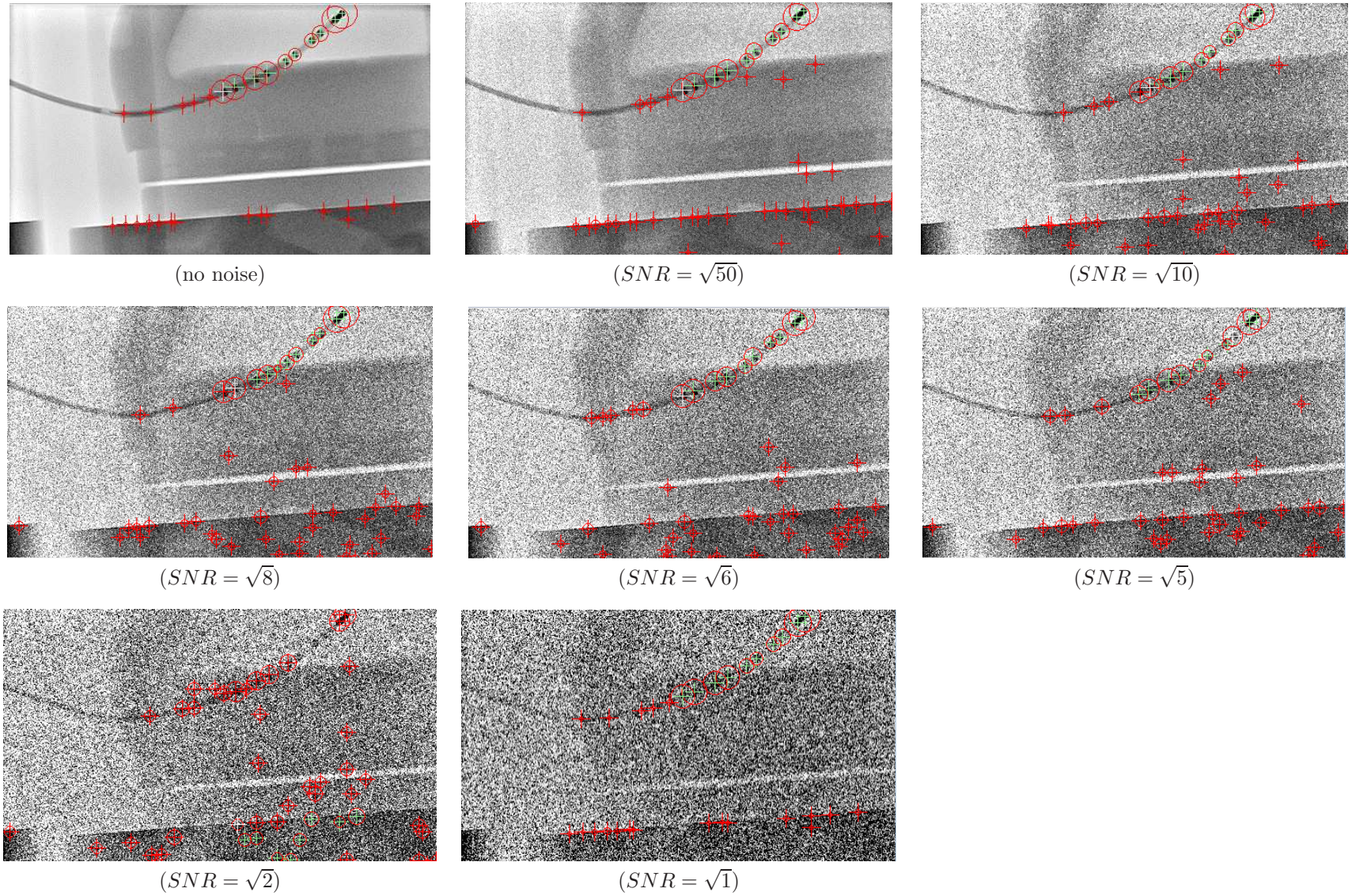

FIGURE 4.10: Case 1: example results of the blob detection method on an uncorrupted phantom X-ray image and the noisy images having different levels of Poisson noise. Electrodes identified as CS catheter electrodes are shown in green crosses. White crosses are the positions of the proximal electrode of the CS catheter. Red crosses are the positions of other detected blobs.

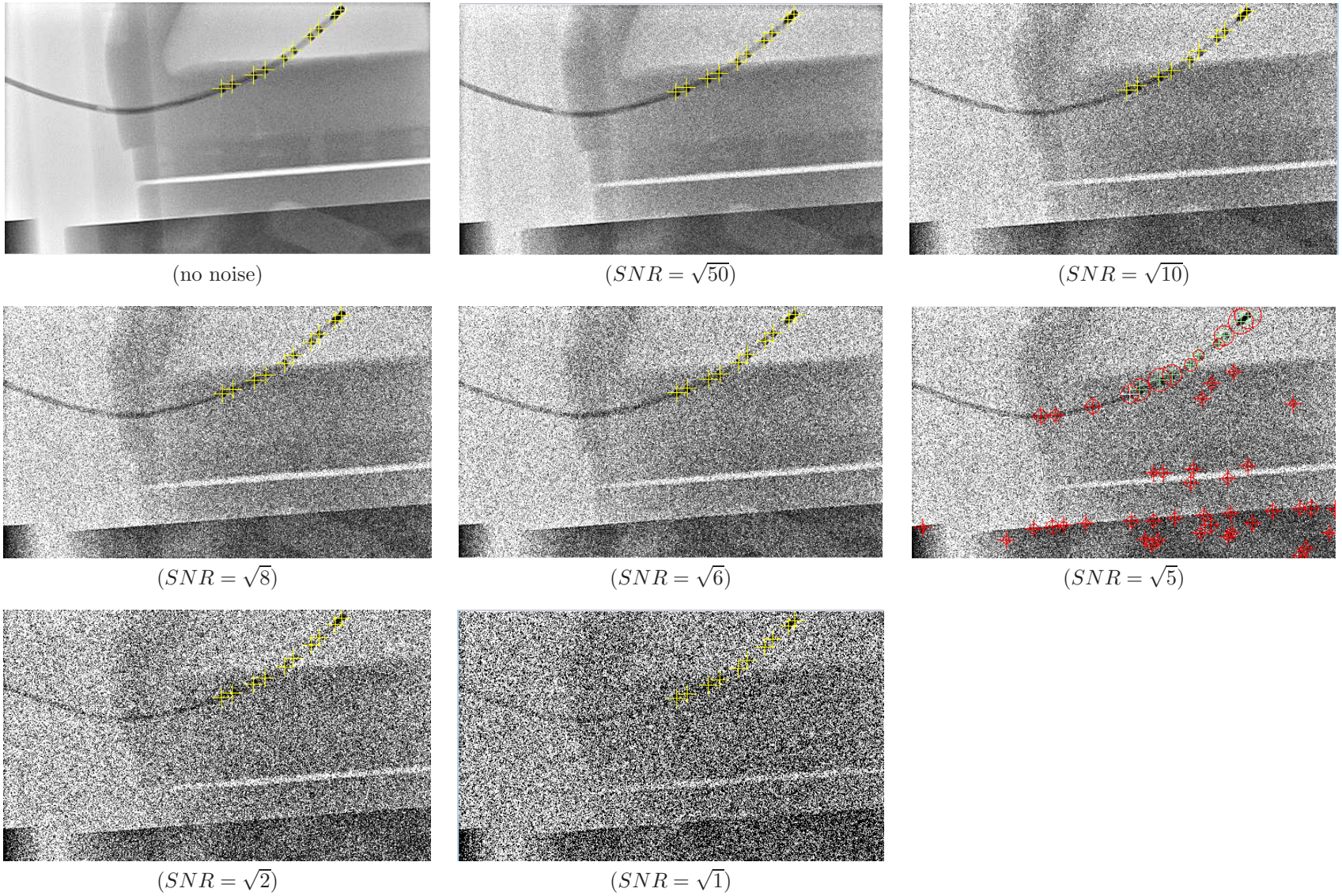

FIGURE 4.11: Case 1: representation of the CS catheter predicted position using the Tracked-PCA technique on (a) an uncorrupted example phantom X-ray image and (b–h) CS catheter predicted position on the same X-ray image simulated to have different levels of SNR.

Cardiac and respiratory motion gating. For both cardiac and respiratory gating, the frame difference was computed between the Tracked-PCA method and the gold standard methods. This was tested on all X-ray sequences at normal dose and the 7 different SNR levels. The results are illustrated in Figure 4.12.

Execution time. Regarding the algorithm's performance, the execution time for the retrospective experiments was around 0.0038 seconds per frame and for the experiments in near-real time, depending on the step size, the execution time was between 0.08 and 0.1 seconds per frame, all running in Matlab on Windows 7 with a 3.4 GHz Intel Core i7 CPU and 8 GB of RAM. For the clinical translation of the technique, it is essential that the algorithm operate in real time. In the current implementation this requirement is not met. However, this was not the focus of this work and the algorithm would need to be optimized for clinical use.

4.4.3 Hierarchical manifold learning-based technique

4.4.3.1 Retrospective method in normal dose images

FV Filter and morphological dilation output images. Figure 4.13a gives an illustration of the output of the thresholded FV filter response of the first frame, $I_{1,1}$, of one example phantom X-ray sequence after the application of the threshold level and the morphological opening, overlaid with the corresponding X-ray image. Figure 4.13b illustrates the image output, $I_{3,1}$, overlaid with the corresponding X-ray image for the same example case, Case 2.

Example of cardiac and respiratory traces. For respiratory gating validation, a plot of the respiratory trace obtained using the HML-based technique for Case 2 is illustrated in Figure 4.14a as a dashed-dot black line. The gold standard respiratory trace is also shown in a solid black line. The cardiac traces obtained are illustrated in a dashed-dot black line in Figure 4.14b, for the same phantom case. The gold standard cardiac trace is also shown in a solid black line.

Quantitative validation. The gating results can be seen in the frequency distribution bar charts in Figure 4.15, for end-systolic, EI and EX gating. The results illustrate that the proposed HML-based technique is faultless in the extraction of cardiac and respiratory motion information from the X-ray phantom sequences. Table 4.3 displays the percentage success rates over all sequences at different frame rates, with success defined, as for the Tracked-PCA method, as the proportion of gated frames in the gold standard that are exactly matched by an automatically gated frame. Percentage success rates were computed for end-systolic, EX and EI gating.

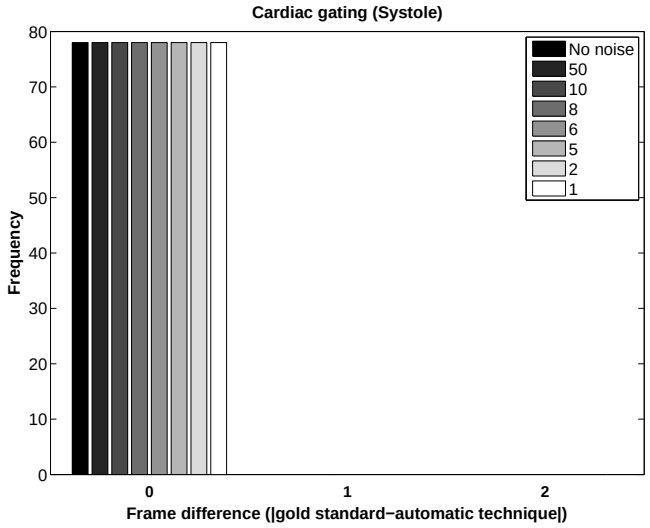

(a)

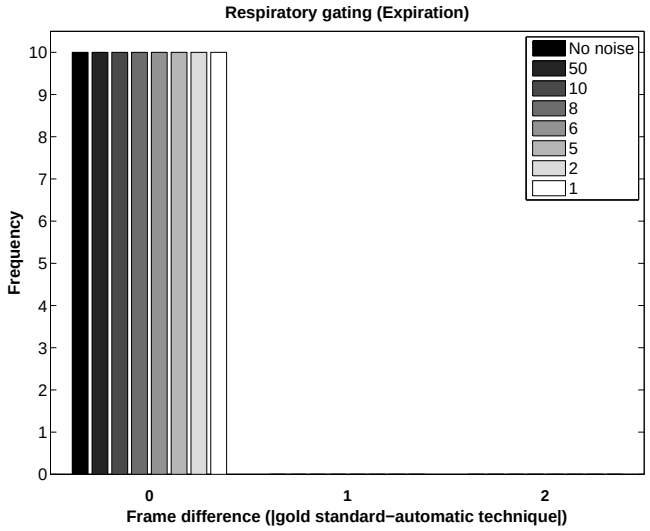

(b)

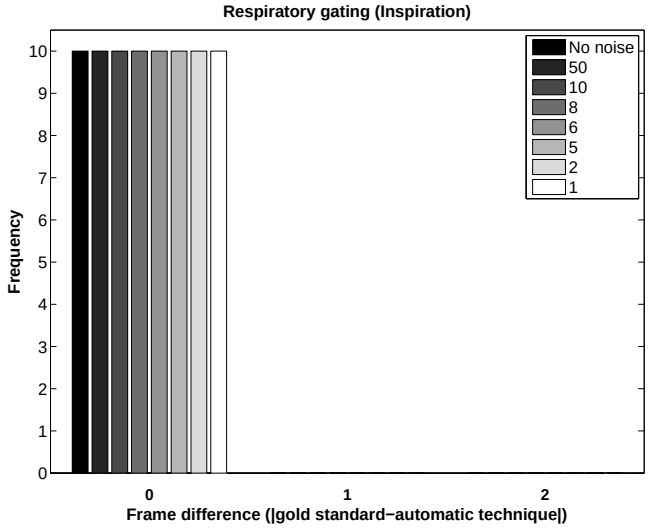

(c)

FIGURE 4.12: Frequency distributions of frame difference errors for (a) end-systolic, (b) EX and (c) EI gating at normal dose and the seven different SNR^2 levels using the Tracked-PCA method.

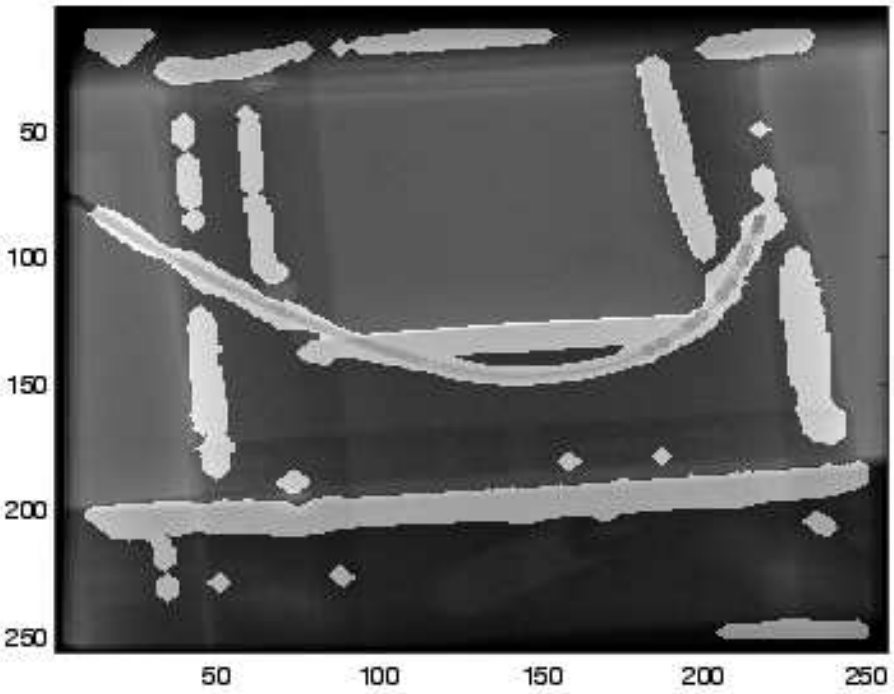

(a)

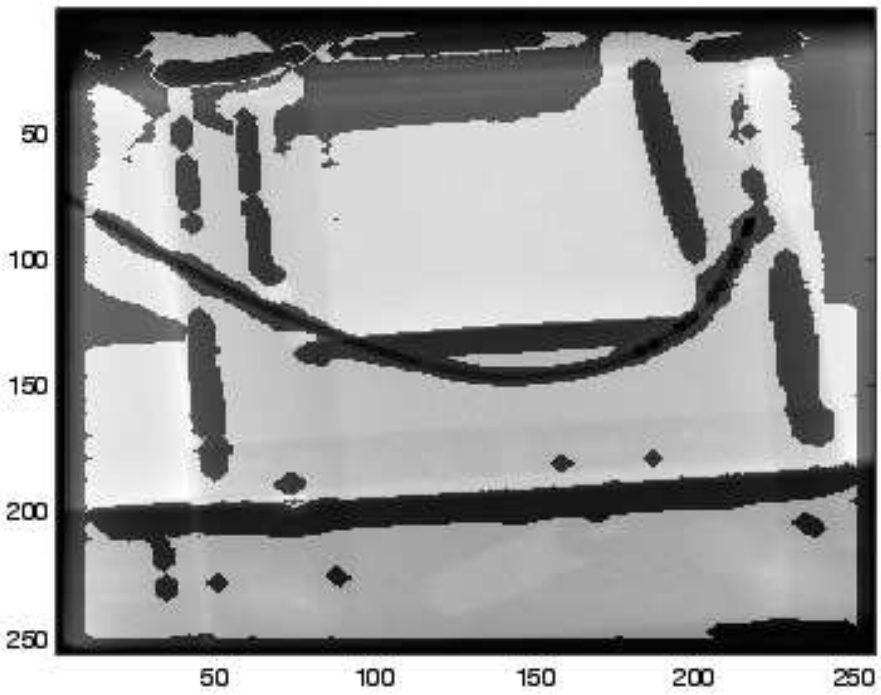

(b)

FIGURE 4.13: (a) Image output of the FV filter followed by morphological opening, $I_{1,1}$, overlaid with the corresponding X-ray image for Case 2. (b) Image output, $I_{3,1}$, overlaid with the corresponding X-ray image for Case 2.

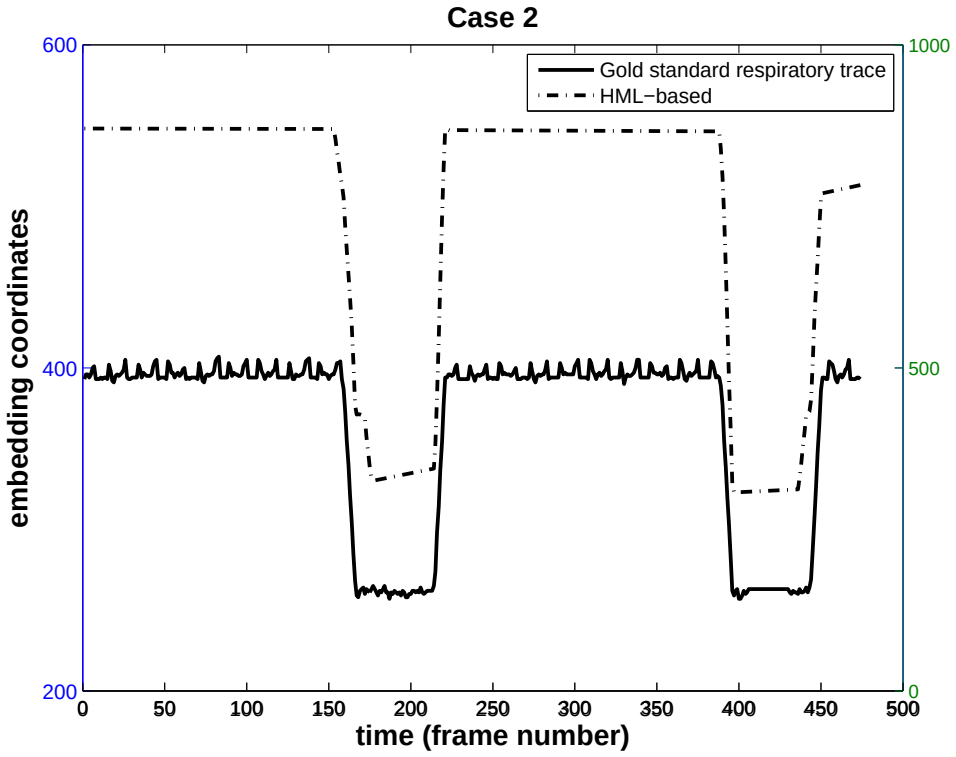

(a)

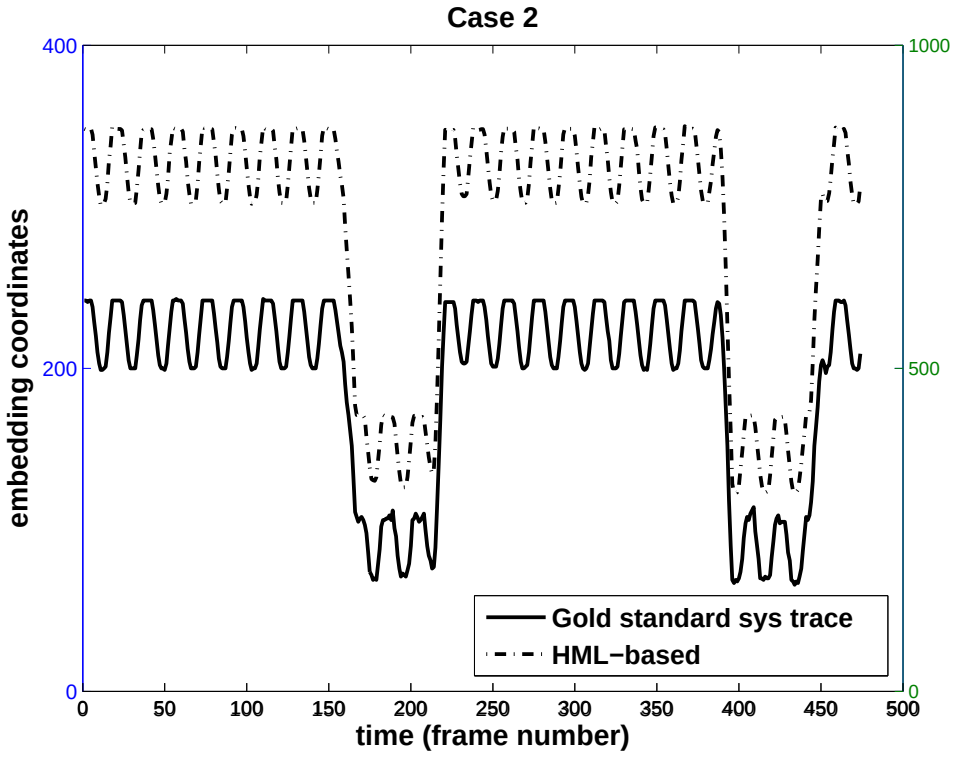

(b)

FIGURE 4.14: (a) Graphical representation of the average of the 1^{st} dimension of the 2D manifold embedding in the low-D Euclidean space for the 2^2 size pixel patches with X-ray frame number, for an example phantom case, Case 2 (dashed-dot black line). The gold standard trace is shown as a solid black line. (b) The HML-based method cardiac trace obtained using the average of the 2^{nd} dimension of the 2D manifold embedding of the identified patches with X-ray frame number, is illustrated for the same example case (dashed-dot black line). The gold standard cardiac trace is illustrated in a solid black line. In both graphs the blue y-axis scale corresponds to the gold standard trace while the green one corresponds to the trace obtained using the automatic technique.

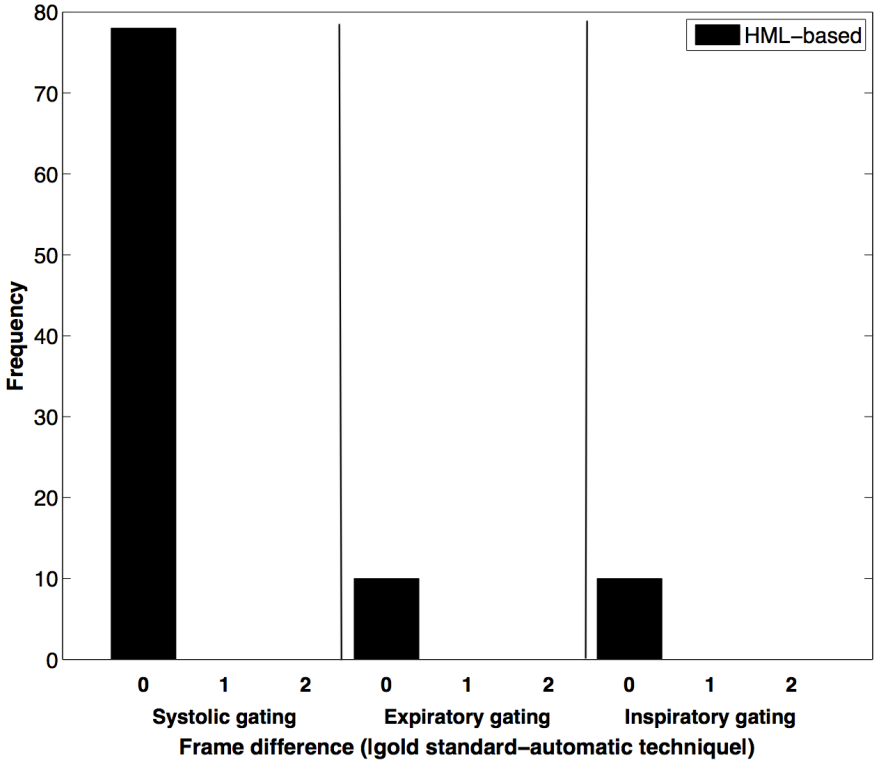

FIGURE 4.15: Frequency distributions of frame difference errors for end-systolic, EX and EI gating using the HML-based technique.

TABLE 4.3: Percentage success rates for all frame rates using the HML-based technique. Success is defined as the percentage of gold standard gating frames that exactly match their corresponding automatically detected gating frames.

	Success rates (%)		
Frame rate	end-systolic gating	EX gating	EI gating
30 f/s	100	100	100
10 f/s	100	100	100
5 f/s	100	100	100
3 f/s	100	100	100

4.4.3.2 Retrospective method in very low dose images

The results are illustrated in Figures 4.16a–c, for end-systolic, EX and EI gating, respectively. The results demonstrate that the automatic method is robust and accurate even on the lowest SNR simulated X-ray sequences. Specifically, for the low SNR values of $\sqrt{1}$, end-systolic, EX and EI success rates of 100% were achieved.

Execution time. Regarding the algorithm's performance, the execution time was 1.1 seconds per frame running in Matlab on Windows 7 with a 3.4 GHz Intel Core i7 CPU and 8 GB of RAM.

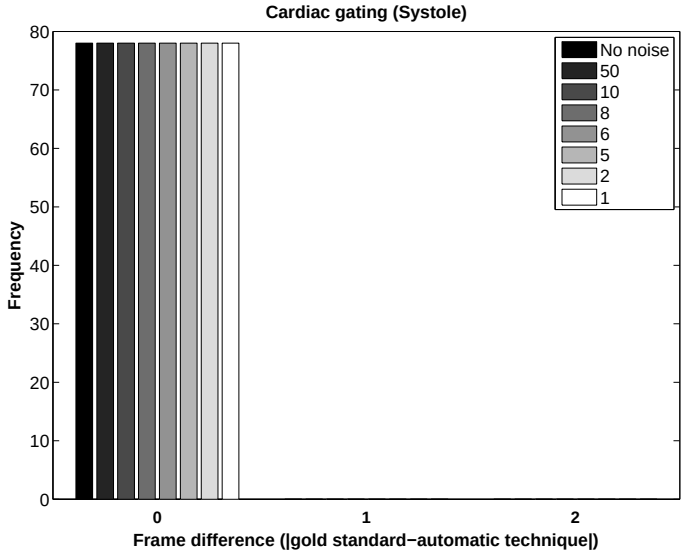

(a)

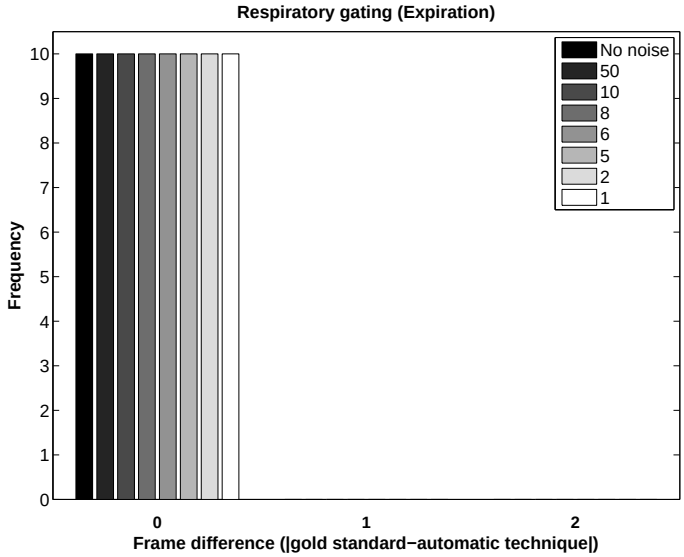

(b)

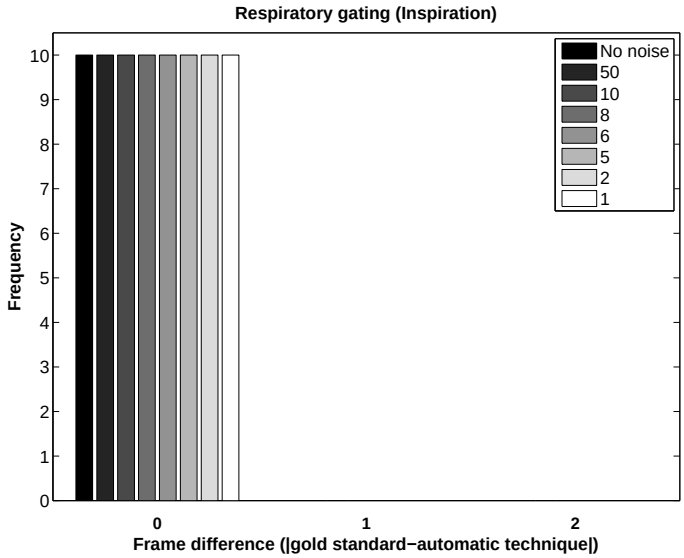

(c)

FIGURE 4.16: Frequency distributions of frame difference errors for end-systolic, EX and EI gating using the HML-based technique for the normal dose and each of the 7 different SNR^2-level X-ray sequences.

TABLE 4.4: Percentage success rates at different frame rates using the Masked-PCA technique. Success is defined as the percentage of gold standard gating frames that exactly match their corresponding automatically detected gating frames.

	Success rates (%)		
Frame rate	end-systolic gating	EX gating	EI gating
30 f/s	100	100	100
10 f/s	100	100	100
5 f/s	100	100	100
3 f/s	100	100	100

4.4.4 Masked-PCA technique

4.4.4.1 Retrospective method in normal dose images

FV filter and mask output. Figure 4.17a gives an illustration of the output of the thresholded FV filter response, $R_{1,1}$, of the first frame of one example phantom X-ray sequence, Case 3, after the application of the threshold level and the morphological operations, overlaid with the corresponding X-ray image. Figure 4.17b illustrates the mask, R_2, overlaid with the corresponding X-ray image for the first frame of the same example case (Section 3.3.2.2).

Example of cardiac and respiratory traces. The results of the cardiac gating validation are shown in Figure 4.18a as a dashed-dot black line, for one example case, Case 3, for the first 300 out of the 680 frames of the sequence. The gold standard cardiac trace is also shown in a solid black line. The respiratory traces obtained are illustrated in a dashed-dot black line in Figure 4.18b, for the same phantom case, for the first 300 frames. The gold standard respiratory trace is also shown in a solid black line.

Quantitative validation. The gating results can be seen in the frequency distribution bar charts in Figure 4.19 for end-systolic, EI and EX gating, respectively over all 5 phantom X-ray sequences. The results illustrate that the proposed Masked-PCA technique is faultless in the extraction of cardiac and respiratory motion information of the X-ray phantom sequences. Table 4.4 displays the percentage success rates over all sequences at different frame rates, with success defined as the proportion of gold standard gated frames with an exactly matching automatically gated frame. Percentage success rates were computed for end-systolic, EX and EI gating for all different frame rate sequences.

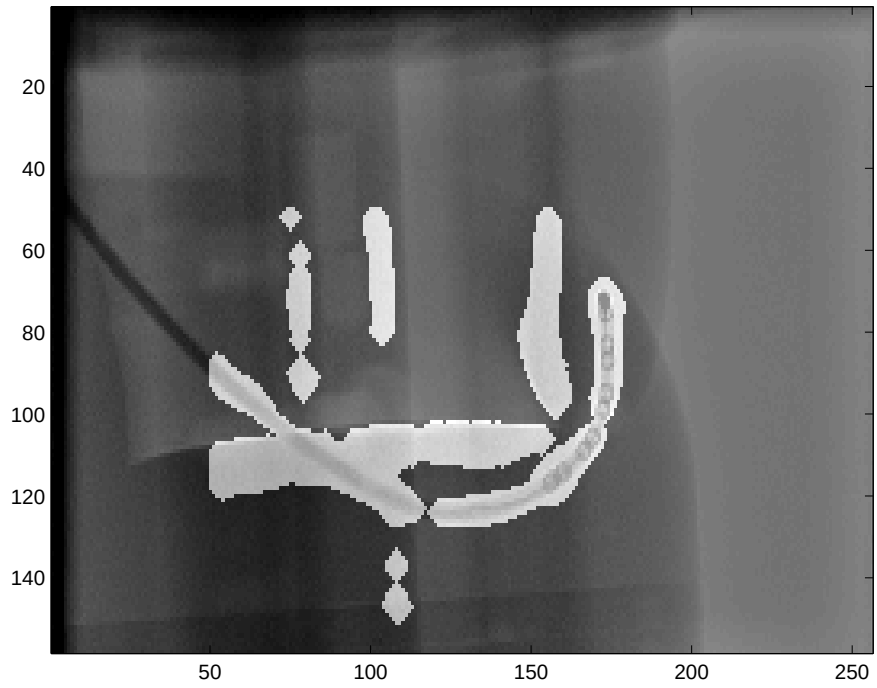

(a)

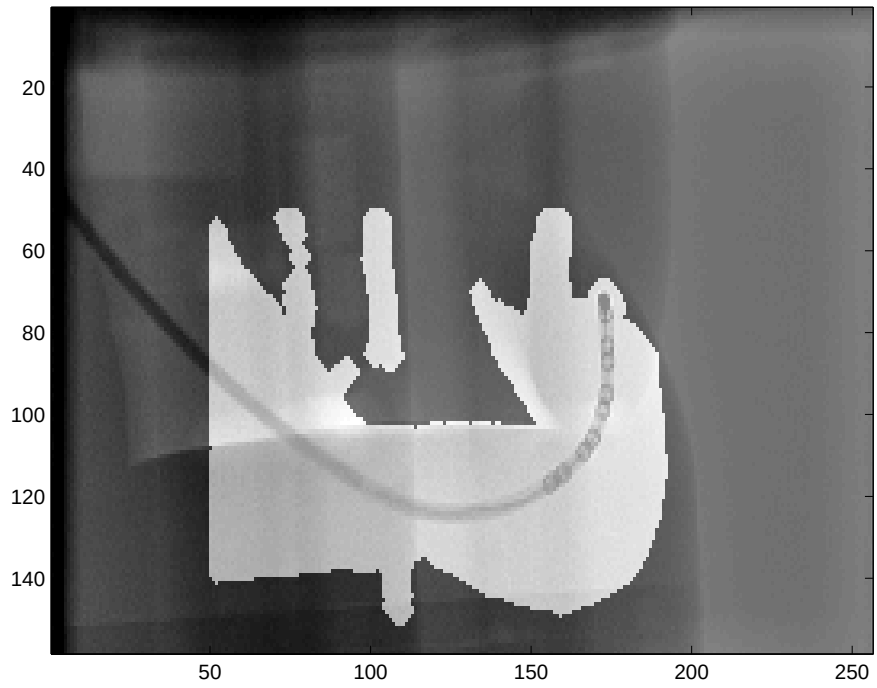

(b)

FIGURE 4.17: (a) Thresholded output of the FV filter followed by morphological operations, $R_{1,1}$, overlaid with the corresponding X-ray image for one example phantom case. (b) Mask output, R_2, overlaid with the corresponding X-ray image for the same example case.

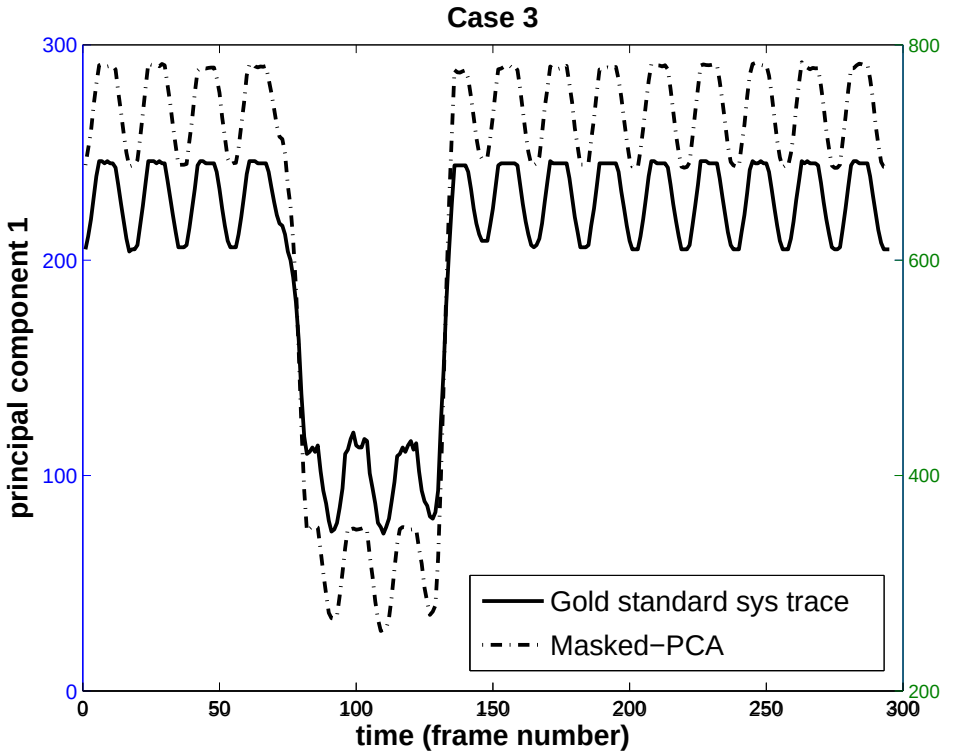

(a)

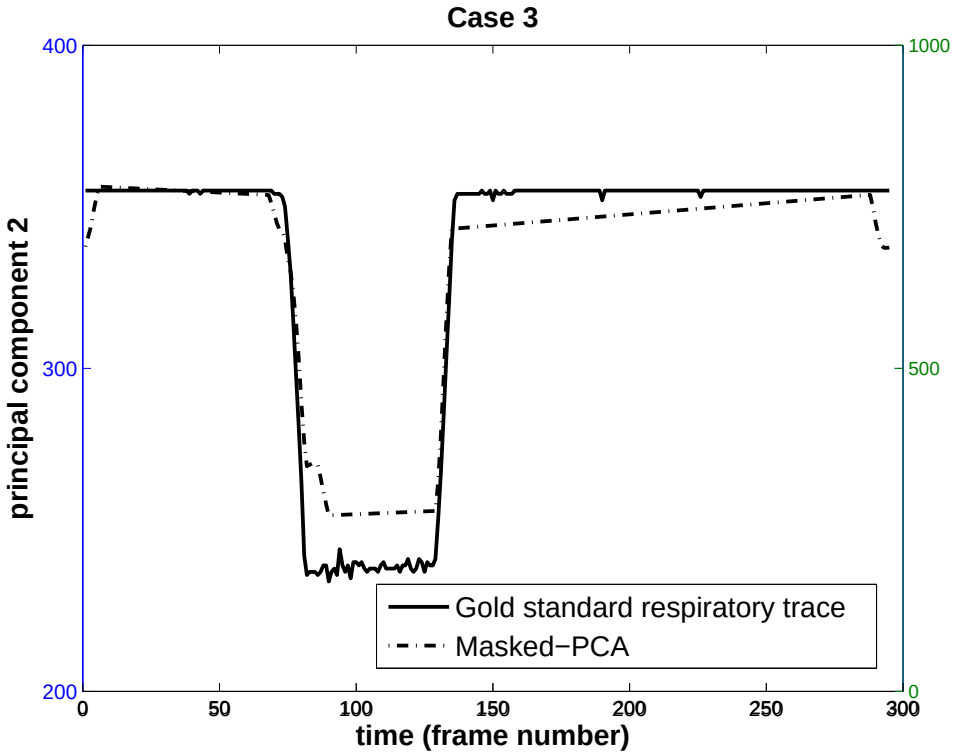

(b)

FIGURE 4.18: (a) Graphical representation of the obtained cardiac trace from the Masked-PCA method with X-ray frame number for an example phantom case, Case 3, in a dashed-dot black line. The gold standard trace is shown as a solid black line. (b) The obtained respiratory trace is illustrated for the same example case. The gold standard cardiac trace is illustrated in a solid black line. In both graphs the blue y-axis scale corresponds to the gold standard trace while the green one corresponds to the trace obtained using the automatic technique.

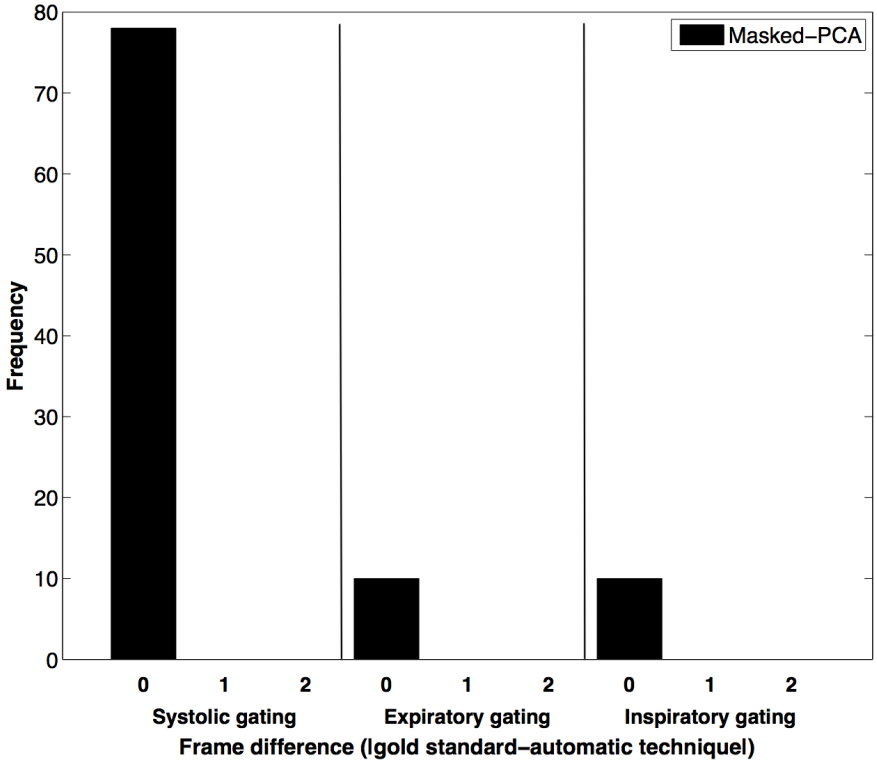

FIGURE 4.19: Frequency distributions of frame difference errors for end-systolic, EI and EX gating using the Masked-PCA technique.

4.4.4.2 Retrospective method in very low dose images

Cardiorespiratory gating was performed using the Masked-PCA technique for the very low dose X-ray image sequences. For both cardiac and respiratory gating, the frame difference was computed between the Masked-PCA method and the gold standard methods. The results are illustrated in Figure 4.20a–c, for end-systolic, EX and EI gating, respectively. The results demonstrate that the automatic method is robust and accurate even on the lowest SNR simulated X-ray sequences. Specifically, for the low SNR values of $\sqrt{1}$, end-systolic, EX and EI success rates of 100% were achieved.

Execution time. Regarding the algorithm's performance, the execution time was around 0.0048 seconds per frame running in Matlab on Windows 7 with a 3.4 GHz Intel Core i7 CPU and 8 GB of RAM.

4.4.4.3 Comparative quantitative validation

To comparatively validate the Masked-PCA technique to the previous techniques, the Tracked-PCA and HML-based, percentage (%) gating success rates were computed for all the techniques

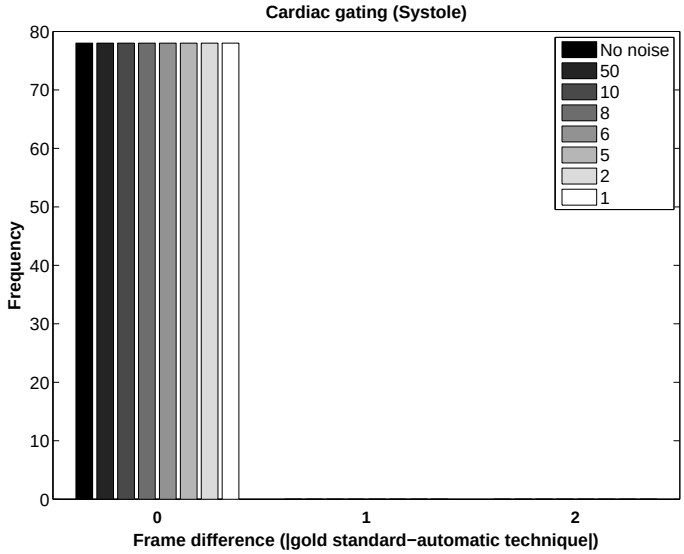

(a)

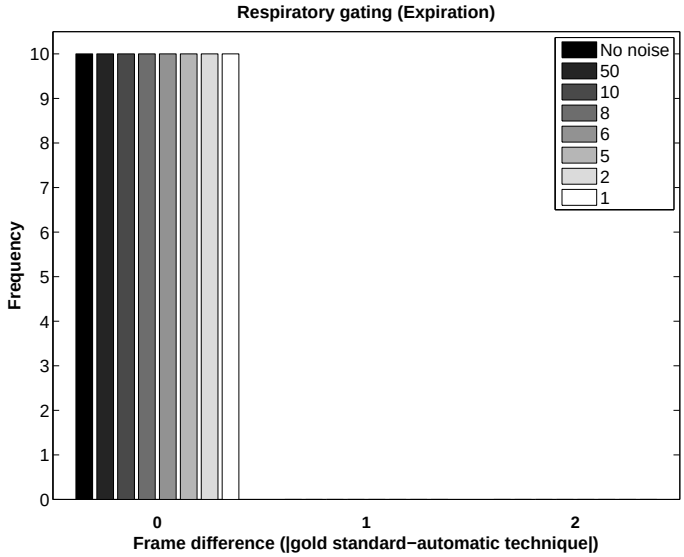

(b)

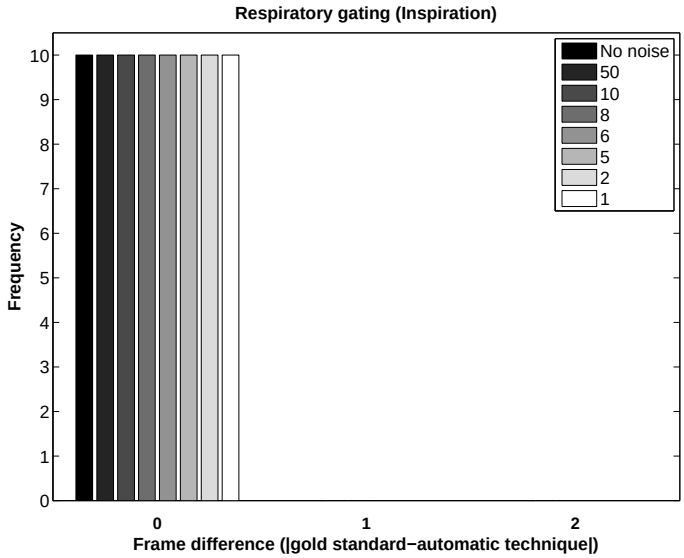

(c)

FIGURE 4.20: Frequency distributions of frame difference errors for end-systolic, EX and EI gating using the Masked-PCA technique for the normal dose and each of the 7 different SNR^2 level X-ray sequences.

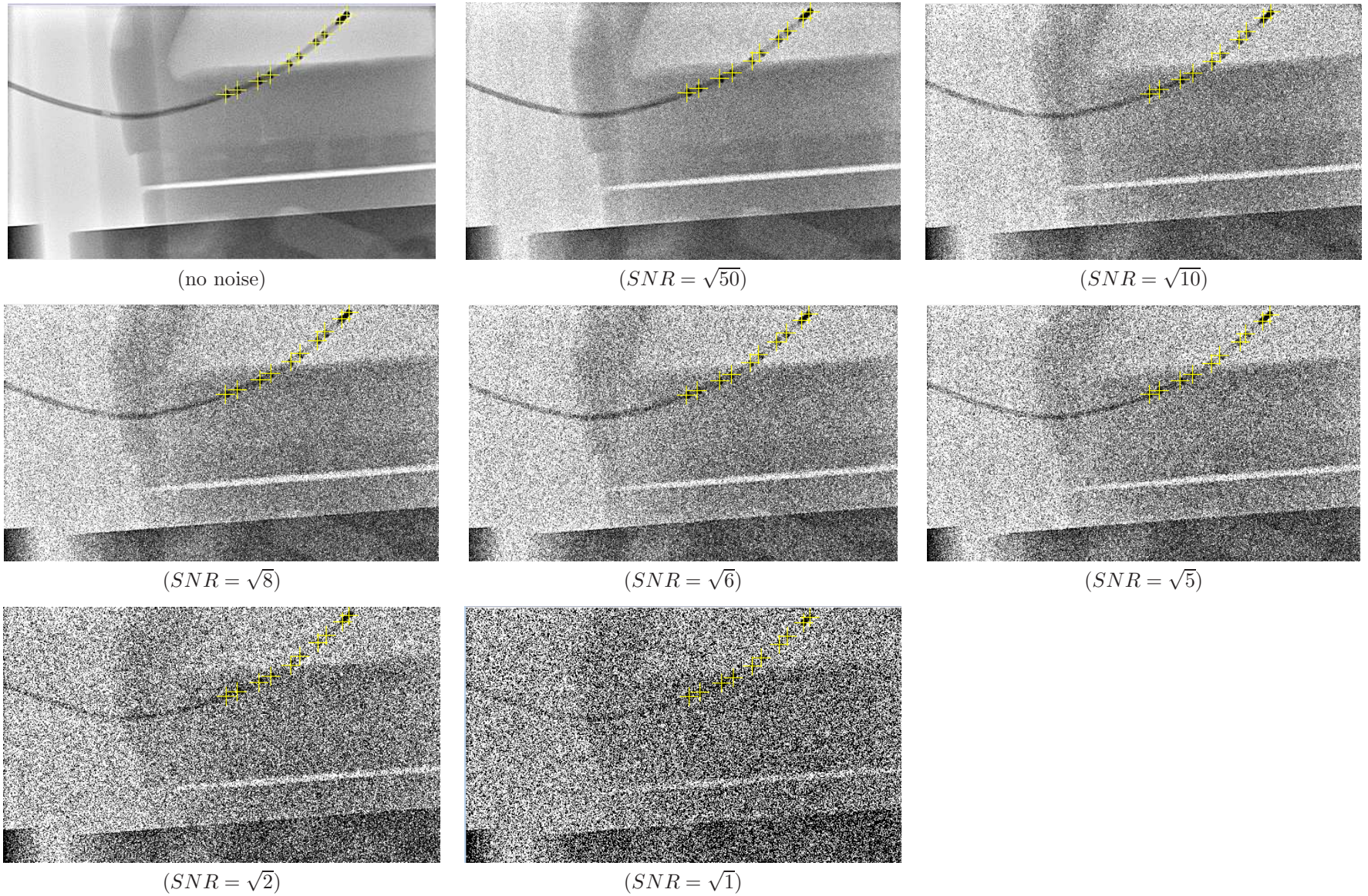

FIGURE 4.21: The View-angle independent CS catheter tracking technique is illustrated in yellow crosses on an uncorrupted phantom X-ray image and on the same X-ray image corrupted with different levels of Poisson noise.

for their application on the phantom sequences.. Percentage success rates were computed for end-systolic, EX and EI gating for all the seven different noise levels and were computed to be 100%, in all cases. Consequently, outcomes show that the three techniques are robust and accurate in motion extraction even at the lowest SNR values of $\sqrt{1}$ for the application on phantom sequences.

4.4.5 View-angle independent technique

4.4.5.1 Application to multiplane sequence pairs at normal & low dose

Example of CS catheter tracking. Figure 4.21 illustrates the results of the CS catheter tracking technique on the 1^{st} image of an uncorrupted example phantom X-ray sequence, Case 1 (as also illustrated in Section 4.4.2), and the simulated noisy images, with SNR values of $\sqrt{50}$, $\sqrt{10}$, $\sqrt{8}$, $\sqrt{6}$, $\sqrt{5}$, $\sqrt{2}$ and $\sqrt{1}$, respectively, after the formation of the model on a different X-ray sequence.

Quantitative validation of CS catheter tracking. Figure 4.22a illustrates the CS catheter tracking median errors per electrode for the uncorrupted phantom X-ray images and the corrupted X-ray images having SNR values of $\sqrt{50}$, $\sqrt{10}$, $\sqrt{8}$, $\sqrt{6}$, $\sqrt{5}$, $\sqrt{2}$ and $\sqrt{1}$. Errors were calculated for each electrode and are shown in different grey scale colours, starting from the proximal (black colour) and moving to the distal (white colour) electrode. For the technique to be acceptable in clinical practice, failure cases were considered to be the ones where errors per electrode were above 2mm [93]. In Figure 4.22b, median errors were calculated and are shown only for the successfully tracked CS catheter electrodes. Figure 4.23, shows the range of the values in terms of the 25^{th} percentile, median and 75^{th} percentile, for all electrodes, and for successfully tracked electrodes, for each noise level. Success rates were also calculated and are shown as percentages (%) in Figure 4.24 for the phantom images.

Quantitative validation of cardiorespiratory motion gating. Figure 4.25 illustrates the frame difference errors in frequency distribution bar charts for the phantom biplane sequences, for all gating tasks and noise levels. Specifically, Figure 4.25 illustrates the frame difference errors in histogram plots, i.e. the number of peaks or troughs with 0, 1 or 2 frames separation from the gold standard for the phantom sequences, for all gating tasks. Cases where no peaks are detected using the automatic technique are also illustrated on the figure. These are the cases where the start and end points of the stationary period are not clearly defined.

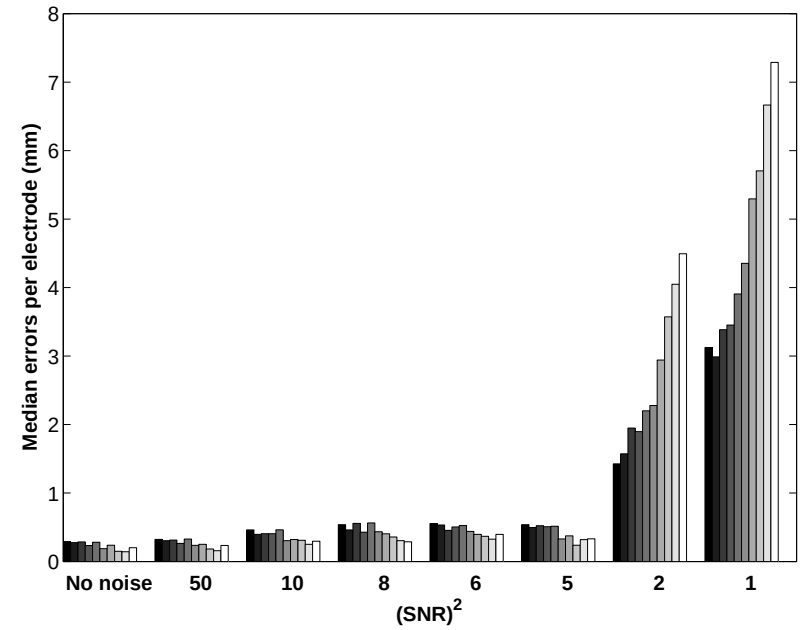

(a)

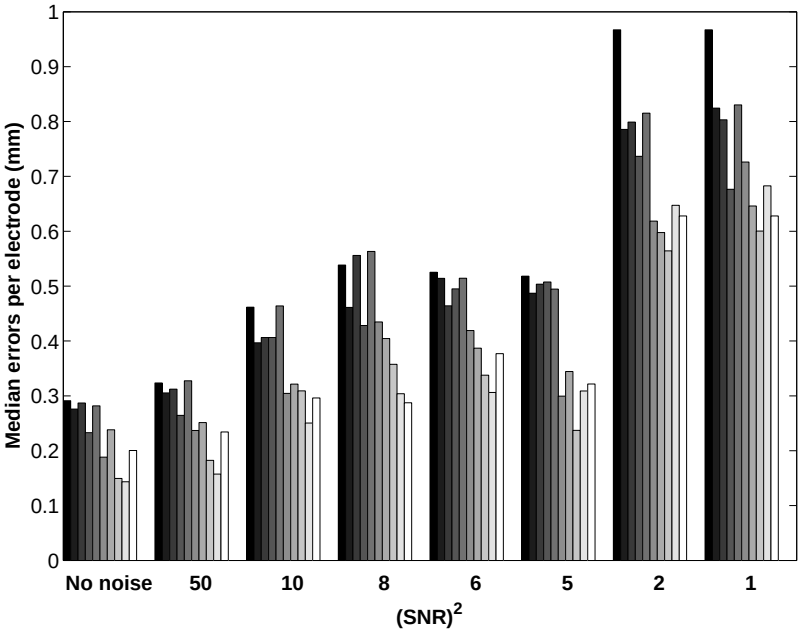

(b)

FIGURE 4.22: Median errors per electrode with respect to the gold standard, for phantom X-ray sequences for the uncorrupted and the 7 levels of SNR (a) for all tracked CS electrodes (b) only for the successfully tracked CS electrodes using the View-angle independent technique. These are the ones tracked with less than 2mm accuracy. Different grey scale colour bars are used to distinguish the CS catheter electrodes, starting from the proximal (black colour) and moving to the distal electrode (white colour)

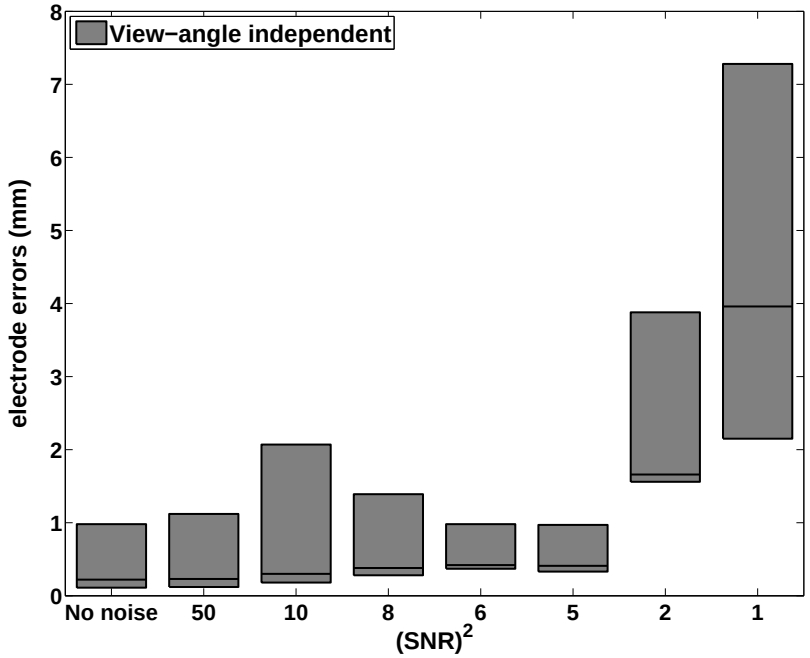

(a)

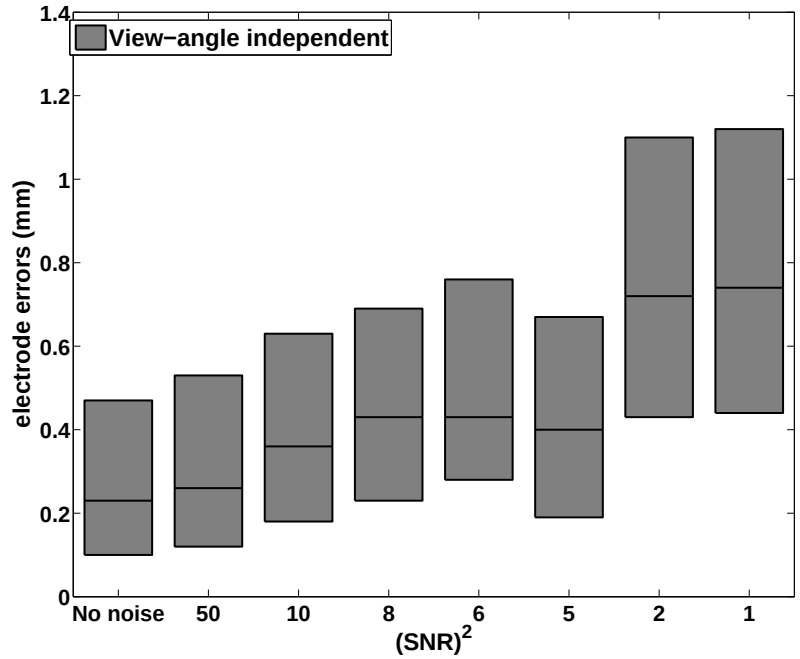

(b)

FIGURE 4.23: Illustration of the 25^{th} percentile, median and 75^{th} percentile, values over (a) all CS catheter electrodes in the data sets (b) only successfully tracked CS catheter electrodes for each noise level using the View-angle independent technique on phantom datasets.

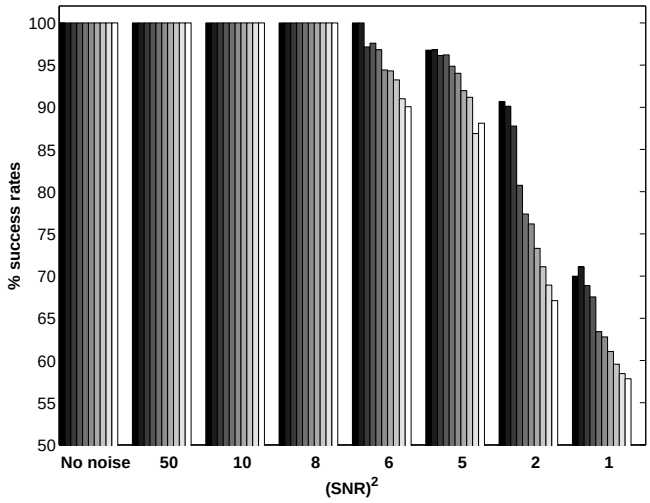

FIGURE 4.24: CS catheter tracking technique percentage success rates (%), for phantom X-ray sequences for the uncorrupted images and the images corrupted with the 7 different levels of SNR using the View-angle independent technique. Success cases are considered to be the ones where the errors per electrode are below 2mm.

Execution time. Regarding the algorithm's performance on the different experiments, depending on the step size, the execution time was between 0.44 and 1.73 seconds per frame running in Matlab on Windows 7 with a 3.4 GHz Intel Core i7 CPU and 8 GB of RAM.

4.4.5.2 Comparative quantitative validation

To comparatively validate the technique to the Tracked-PCA technique (Section 4.4.2) percentage (%) gating success rates and % success rates for CS catheter tracking for both techniques for the same sequences were calculated and are shown in Figure 4.26. For the illustration of the the CS catheter tracking success rates, the 10 CS catheter electrodes were not treated individually. Instead, for each of the noise levels the % success rates were computed as an average over the success rates of each of the CS catheter electrodes. In the Tracked-PCA method, the statistical model was formed from normal dose images during a calibration phase and applied to low dose images acquired from the same view-angle, whereas the View-angle independent technique applies the model to a different view-angle. There are no false positives or negatives (i.e. extra/fewer detected peaks/troughs) over the processed sequences at SNR down to $\sqrt{1}$ for the Tracked-PCA, but the View-angle independent technique has some undetected cardiac peaks at an SNR of $\sqrt{2}$ or lower. These outcomes show that the View-angle independent technique is robust and accurate in both CS catheter tracking and motion extraction even at the lowest SNR values of $\sqrt{1}$.

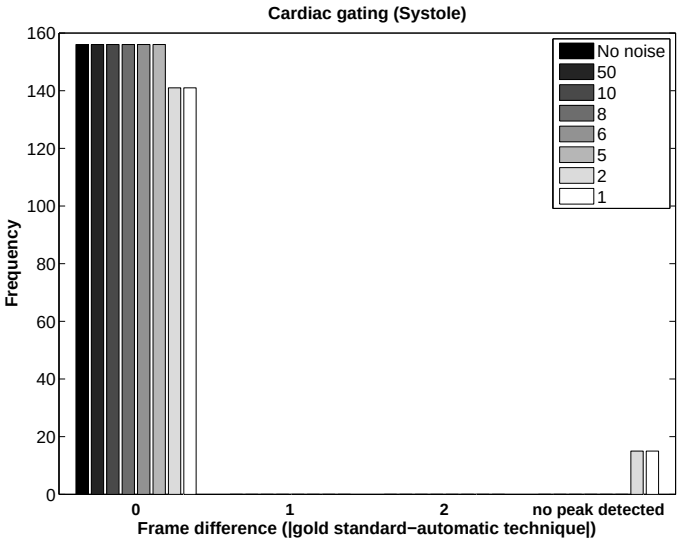

(a)

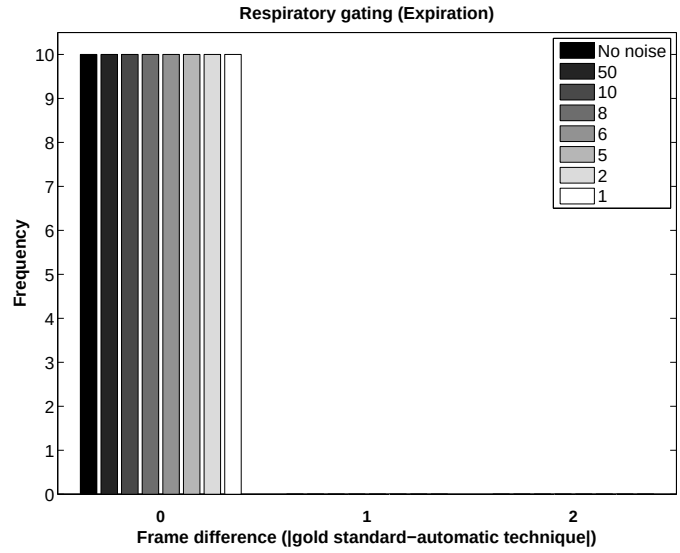

(b)

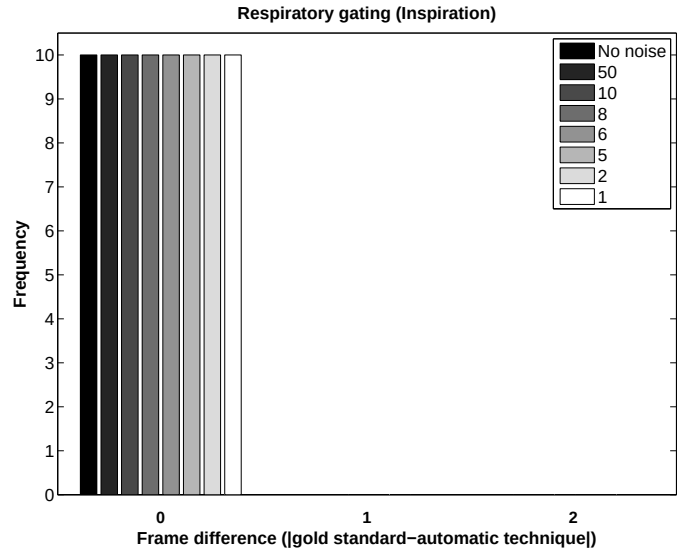

(c)

FIGURE 4.25: Frequency distributions of frame difference errors for (a) end-systolic, (b) EX, and (c) EI gating for the uncorrupted and all noise corrupted X-ray sequences using the View-angle independent technique on phantom sequences. SNR^2 values of the level of noise added are shown. Cases where no peak is detected, as shown in (a) are the cases where the start and end points of the stationary period are not clearly defined.

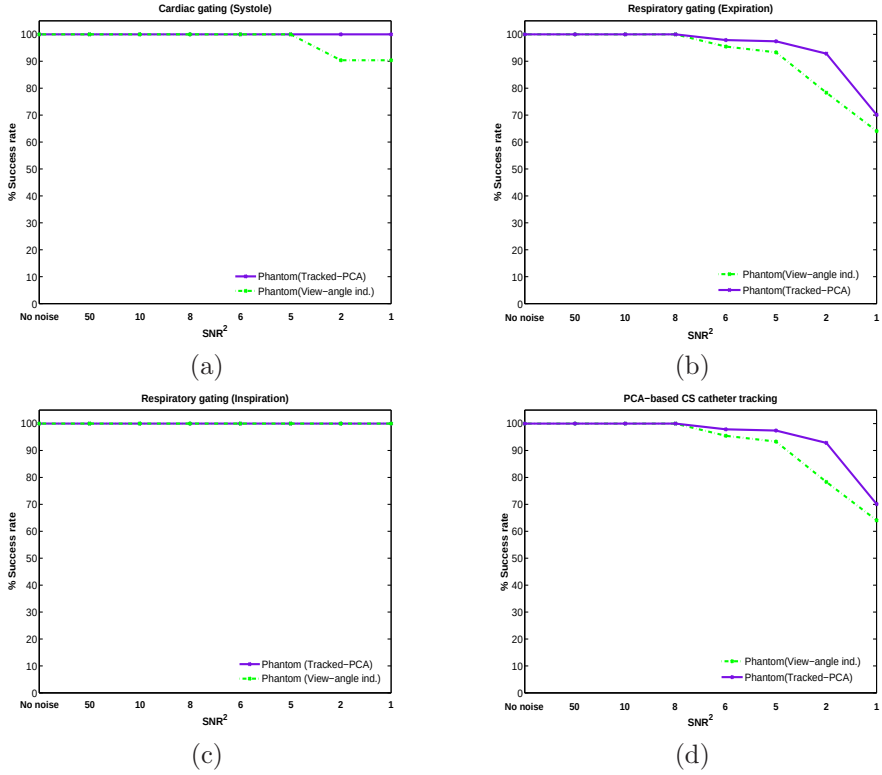

FIGURE 4.26: Percentage success rates for (a) end-systolic, (b) EX (c) EI gating and (d) CS electrode tracking for the uncorrupted and all noise corrupted X-ray sequences computed for the application of the View-angle independent and the Tracked-PCA technique on phantom sequences. In (a) the lines overlap at No noise and at $SNRs$ $\sqrt{50}$ to $\sqrt{5}$, in (b and d) the lines overlap at No noise and at $SNRs$ $\sqrt{50}$ to $\sqrt{8}$ and in (c) the lines overlap at all noise levels.

4.5 Discussion

In this chapter, the novel techniques previously presented in Chapter 3 were applied and validated on phantom X-ray fluoroscopy datasets. The experiments were designed to emulate the clinical workflow of typical cardiac catheterisation procedures. The datasets were acquired using a bespoke beating and breathing left ventricular phantom [98] with an inserted CS catheter. In particular, the experimental validation of the techniques is demonstrated for the purposes of automatic gating in normal and very low dose X-ray fluoroscopy phantom images. Additionally, the performance of the techniques on different frame rates was evaluated. Along with cardiorespiratory motion gating, the novel frameworks of the Tracked-PCA and View-angle independent techniques were employed to track the CS catheter throughout the X-ray sequences. The validation of the techniques for catheter tracking was demonstrated in this chapter. The techniques have been applied on two sequential multiplane phantom X-ray sequences (one biplane and one triplane, 1741 frames, 5 runs in total) and success rates for end-systolic cardiac gating, EI and EX respiratory gating were computed. Additionally, for the techniques designed to track the CS catheter, median errors per electrode with respect to the gold standard electrode positions have been established.

4.5.1 Tracked-PCA technique

The novel framework of the developed Tracked-PCA technique for robust cardiorespiratory motion gating was validated in this chapter. For the proposed framework a novel statistical model of the motion of the CS catheter based on PCA of tracked electrode positions from standard monoplane X-ray images is formed. Using the statistical model on unmodified fluoroscopy images the performance of the technique is demonstrated for retrospective image-based gating, and it was shown that the method is able to detect cardiac and respiratory phases from these phantom X-ray fluoroscopy images. Computed success rates for end-systolic cardiac gating, EI and EX respiratory gating were all 100%. These results indicate a faultless cardiorespiratory motion extraction. Furthermore, cardiac and respiratory motions have been extracted from the corrupted sequences. Figure 4.12 illustrates that this method is robust even when the motion is estimated from the very low dose rate X-ray sequences. When the gating technique is applied on cases with SNR values of $\sqrt{1}$, end-systolic, EI and EX gating have been established with success rates of 100%, for all gating tasks. Therefore, motion-gating accuracy is within 0.1s even at the lowest noise levels, achieving the minimum clinical accuracy objective set in this thesis, which is based on the three targeted clinical applications that this thesis seeks to address.

This accurate and robust method is able to detect the CS catheter in every frame of the X-ray sequences with a few millimetres accuracy. Even in cases with the lowest SNR values, median errors per electrode did not exceed 0.9 mm for the successfully tracked CS electrodes. For the technique to be acceptable in clinical practice, failure cases were considered the ones where individual errors (mm) per electrode were above 2 mm. Even when the computation of median errors included all CS electrodes irrespective of whether they were unsuccessfully tracked or not, the median errors per electrode did not exceed 1.6mm.

As mentioned in Section 1.6, the tracking algorithms should be able to achieve these accuracies within this tolerance at least 90% of the time. The phantom experiments conducted in this chapter show that the Tracked-PCA technique can meet the accuracy objective up until the 2^{nd} highest application of Poisson noise, i.e. at the SNR level of $\sqrt{2}$. Within the constraints of these objectives, the dose reduction factor for this technique should be somewhere between $\frac{1}{25}$ and $\frac{1}{50}$ of the normal dose images, indicating the potentially valuable clinical robustness of the technique to noise. Consequently, since at the SNR values below $\sqrt{2}$ there are frames where the CS catheter tracking fails, there is no reason to go lower than $\sqrt{1}$ for application of the technique to motion gating.

Although the novel technique is fully automatic, approximately 0.2% of the total 17410 blobs detected by the real-time tracking technique [209] were failures and had to be manually corrected. These failures usually happen on the second electrode. This is because the second electrode is very close to the catheter tip (the distal electrode) and it can be detected together with the

catheter tip as a single large blob. Furthermore, the real-time tracking technique may fail when some of the electrodes on the CS catheter move out of the field of view so that the complete CS catheter body is not visible throughout the procedure. This may be caused by the use of the zoom-in function or collimation of the X-ray system.

The variation of the first and second PCs extracted by applying PCA do not correspond directly with cardiac and respiratory motion since some cardiac motion remains in the second PC and needs to be removed by cardiac gating. This may be due to the data not being jointly normal as required for the PCA. However, the success of the technique suggests that the first 2 PCs largely represent cardiac and respiratory motion.

In phantom data the number of non-electrode blobs largely increases with increasing noise. Fortunately, this does not significantly affect the accuracy of the technique as the model provides sufficient constraints on the electrode locations to enable catheter tracking to be successful even in low dose X-ray, and this is expected to also be the case with clinical data.

4.5.2 HML-based technique

Experimental validation of the application of the HML-based retrospective image-based motion gating technique was demonstrated in this chapter, on normal and very low dose X-ray fluoroscopy phantom images. This method is able to detect cardiac and respiratory phase directly from X-ray images. For the application of the technique to normal dose X-ray images, success rates were computed to be 100%, for all gating tasks. Furthermore, the technique is robust even when the motion is extracted from the very low dose X-ray sequences, i.e. where (SNR^2) was 1. As illustrated in Figure 4.16, end-systolic, EX and EI success rates of 100% were achieved for all gating tasks. Similar to the previous technique, the motion-gating accuracy of the HML-based technique is within 0.1s. It therefore meets the motion-gating accuracy objective set in this thesis for all three clinical applications that this thesis seeks to address.

Unlike the Tracked-PCA technique, the variation of the 1^{st} dimension of the HML result corresponds more directly with respiratory motion. Therefore, the respiratory signal does not need to be cardiac gated as previously required for the Tracked-PCA technique. This might be due to the fact that the HML technique is a non-linear dimensionality reduction technique. Therefore, it does not require the data to be jointly normal and it may be that it can better remove the cardiac motion from the 1^{st} dimension.

Investigations show that the reason the end-systolic gating is best on the specified patches is because of the inclusion of the heart border, a structure that carries significant cardiac motion information. More focus should be given on modifying the technique by giving more emphasis to the importance of the heart border structure. Furthermore, the additional step of computing

$I_{3,i} = I_{2,i} - I_{1,i}$ to detect the image patches around the detected tubular structures gave better results than detecting the tubular structures themselves. This could be due to the fact that cardiac gating could be affected when the clinician manipulates the catheters, pacing leads or injects contrast agent in the vessels.

The previously proposed work on motion gating (Section 4.4.2) described the formation of a statistical model of the motion of a CS catheter based on PCA of tracked electrode locations from X-ray images. Faultless gating is achieved for the application of the technique even on the highest SNR value of $\sqrt{1}$. However, the Tracked-PCA technique requires the CS catheter to be present in the images. The HML-based technique does not rely on tracking the CS catheter and may work with no catheter in the images. Instead, the method is robust to varying image-content. Translating this method to clinical data, it could potentially be applied to more procedures than RFA, such as cardiac resynchronisation therapy (ventricular pacing) procedures where no catheters are present, just pacing leads, and which may or may not use contrast agent injection.

4.5.3 Masked-PCA technique

The Masked-PCA technique is based on the use of the PCA statistical method in combination with other image processing operations to make the technique suitable for cardiorespiratory gating. Similar to the validation of the previously described techniques the application of the Masked-PCA technique in normal and very low dose phantom X-ray fluoroscopy sequences was demonstrated in this chapter. End-systolic, EX and EI success rates of 100%, for all five phantom X-ray sequences, have been established at normal dose.

For the application of the technique to images corrupted by applying Poisson noise, cardiac and respiratory motion was also extracted and results are illustrated in Figure 4.20. Outcomes demonstrate that the technique is robust even when the motion is extracted from the very low dose rate X-ray sequences, i.e. where (SNR^2) was 1. End-systolic, EX and EI success rates of 100% were achieved using the Masked-PCA technique, achieving the motion gating accuracy objective set in this thesis.

Unlike most previously developed motion gating techniques, the main novelty of the technique, similar to the HML-based technique, is that it is robust to varying image-content. Thus, it is expected to be robust to typical EP X-ray images that can contain a varying number of different types of EP catheters and may include contrast agent injection. As the technique is not dependent on any particular catheter being present in the procedure, it has the potential for application in more types of cardiac catheterisation procedures than just RFA.

4.5.4 View-angle independent technique

The experimental validation on phantom images of the novel View-angle independent technique was presented in Section 4.4.5. The technique was developed for the determination of cardiorespiratory motion gating of unseen frames using a PCA-based model of CS catheter motion that can be applied to a secondary X-ray view. The technique was experimentally validated on phantom imaging sequences in normal and very low dose scenarios. Using the model on unmodified images for cardiorespiratory motion gating on unseen frames, end-systolic, EI and EX gating success rates of 100% were established. For very low dose applications, the technique established gating success rates of more than 90%, even at the low SNR value of $\sqrt{1}$. Results demonstrate that the performance of the technique in terms of motion gating accuracy in the secondary view are exceptionally good, even with the application of the technique on the noisiest images. The algorithm is capable of achieving motion gating in any arbitrary view, without the need to build a separate PCA-model for each X-ray view. However, for the very low dose scenarios, where the SNR values are less than $\sqrt{2}$, the constraints of the designed cost function were shown to be insufficient to obtain the correct set of epipolar lines in the *current* view, and therefore in at most 10% of the cases the technique fails to achieve the motion gating accuracy objective set in this thesis.

As illustrated in Figure 4.22a with high noise, the distal electrode has larger errors than the proximal. This happens because an error in the weights has more effect on the epipolar lines at the distal than at the proximal end, and consequently the distal electrodes tend to have larger errors. This is explained by the motion of the CS catheter throughout the sequence. In most frames the proximal end is moving mostly side to side, in which case the epipolar lines wouldn't change much with incorrect weights, whereas the distal end has more up and down movement as the weights vary.

The technique is able to gate CS catheter electrode positions in the two views to reconstruct the 3D position of the CS catheter and then to track the catheter in very low dose X-ray images at the new angle. Gating information is extracted by the estimated weights, w_1 and w_2, that represent cardiac and respiratory motion information, respectively, as outlined in Section 3.4.2.2. In the case of accurate estimation of the weights, this corresponds to obtaining the correct set of epipolar lines in the *current* view. Although this guarantees the accurate extraction of cardiorespiratory motion information it does not guarantee the correct annotation of catheter electrodes. In very low dose applications there are cases where an electrode is incorrectly annotated, as a noise blob might be closer to the epipolar line than the actual catheter blob. As outlined in Section 3.4.2.4 the algorithm is able to correct for this incorrect electrode annotation. Although correcting for these cases does not alter the gating accuracy, correct CS electrode annotation is clinically useful in EP procedures for relating signals measured at the electrodes to locations on

the anatomy. Additionally, for clinical application to rotational acquisitions, the electrodes can be removed by replacing with adjacent background prior to 3D reconstruction in an attempt to reduce motion artefacts. The algorithm was able to detect the CS catheter with median errors of successfully annotated electrodes not exceeding 1mm per electrode, well below the acceptable value in clinical practice which is 2mm [93]. The algorithm is able to achieve these accuracies, with the pre-decided tolerance of at least 90% of the time that allows at most one of the ten electrodes to be misdetected in each frame, even when applied to images with the low SNR value of $\sqrt{5}$. Consequently, the dose reduction factor for this technique is around $\frac{1}{10}$ of the normal dose images. The main reason for the algorithm's failures is the ineffectiveness of the blob detection algorithm at very low doses and at view-angles that distort the solid circular shape of the CS catheter electrodes, resulting in their misdetection.

4.5.5 Comparison of techniques

In this chapter, motion gating results indicate a faultless cardiorespiratory motion extraction using the model-based Tracked-PCA, HML-based and Masked-PCA techniques even when the images were corrupted with the lowest SNR value of $\sqrt{1}$. Additionally, a faultless gating is demonstrated in sequences where the angulation of the scanner is changed between frames with the use of the View-angle independent technique on images corrupted with SNR values down to $\sqrt{5}$. Although the accuracy of the motion gating is reduced at the lowest SNR values of $\sqrt{2}$ and $\sqrt{1}$, the performance of the technique does not fall below 90%. Although such accuracy and robustness is not guaranteed in the clinical scenario, the obtained results are promising, and high accuracy and robustness is expected.

For the applications of rotational gating and phase matching for 3D reconstruction, it is expected that both applications will always use the diastolic phase. Therefore, to validate the motion gating accuracy of the techniques for these applications, validation of diastolic gating should be performed. Although in this chapter the validation is done on systolic gating only, systolic and diastolic gating performances are expected to be the same in the phantom data, such that the systolic results are indicative of the results in diastolic gating.

Furthermore, it was demonstrated that the developed techniques are not affected by changes in frame rates, as the performances of the techniques are not compromised with their application on sequences of 3f/s, 5f/s, 10f/s or 30f/s.

The PCA-based CS catheter detection methods, Tracked-PCA and View-angle independent methods, can detect the CS catheter position without defining a ROI in the X-ray image. These novel CS catheter detection algorithms have been validated on phantom experiments and have been demonstrated to achieve accuracies within the 2mm clinical tolerance, a criterion for suitability for deployment in the clinical workflow.

The Tracked-PCA technique in low dose images and the View-angle independent technique, as already mentioned in Chapter 3, could be used for 'real-time' gating, but would suffer from a time lag of 1 sample interval because of the need to identify peaks/troughs in the extracted signals. Consequently, the techniques perform motion gating in 'near-real time'. In terms of clinical application, the techniques can potentially be used for performing 2D-3D registration of 3D cardiac data (CT or MRI) to X-ray fluoroscopy, using catheters that are reconstructed in 3D from sequential biplane X-ray images. The techniques will be suitable for providing image registration for 3D dynamic compensation. In particular, they will be suitable for the updating of 3D roadmaps to significantly improve the accuracy of fluoroscopy overlays for cardiac procedures or for the off-line fusion of cardiac image data for application in biophysical modelling research.

A significant advantage of the Tracked-PCA technique on low dose images is that it can operate within a few seconds per image sequence. Specifically, the technique is implemented with execution time between 0.08 and 0.1 seconds per frame, depending on the step size. Although the application of the technique to motion gating suffers from a time lag of 1 sample interval, this will not be the case for its application to 3D dynamic compensation, because there is no need to identify peaks/troughs in the extracted signals. Therefore, the technique is fast enough to be potentially applied for real-time 3D dynamic compensation. On the other hand, the View-angle independent technique is implemented with execution time between 0.44 and 1.73 seconds per frame. Therefore, real-time motion compensation is not currently feasible. However, code optimisation was not the focus of this work and would need to be considered for real-time clinical application.

For the validation of the experiments presented in this Chapter gold standard methods were chosen and compared to the obtained results. The diaphragm/heart border gold-standard tracking technique [95] was validated by manual tracking of ball bearings attached to the phantom, which gave identical results to those of the diaphragm/heart border tracking. The separate validation of the gating using ball bearings verifies that the diaphragm/heart border tracking technique is faultless and hence most reliable. Regarding the real-time catheter tracking technique's accuracy, CS catheter detection errors were evaluated and an overall 2D detection error of 0.39 ± 0.22 mm was achieved for all electrodes in all images. Regarding the manual electrode detection gold standard method, inter-observer variability for electrode detection was assessed, and the average Euclidean distances between the manually defined electrode positions detected by Observer 1 and Observer 2 over all frames in the test sequence over all ten electrodes of the CS catheter were found to be 0.46mm. Additionally, for the electrode detection the maximum value of the measured precision was found to be 0.56mm, which is around 2 times less than the radius of the smallest CS catheter electrode [209]. Hence, the ground truth is sufficient for the computed experiments.

The techniques developed and validated throughout this thesis are workflow-friendly and do not require any fiducial markers or contrast agent. They will be particularly useful for registration and overlay of pre-procedural images with X-ray fluoroscopy for guidance and biophysical modelling. Most importantly, the techniques are robust-to-noise. Therefore, they have the potential to greatly reduce radiation dose in image-guided cardiac catheter procedures and outweigh the radiation risk by the benefit of the interventional procedure. As a consequence, radiation to patients and staff will decrease significantly, accomplishing the main objective behind the work of this thesis, which is to address the problem of acute radiation risks introduced with X-ray fluoroscopic image guidance.

4.5.6 Conclusion

Applying the algorithms to phantom models of the heart has many benefits that cannot be reproduced in a live clinical environment for reasons of safety and practicality. Firstly, using rigid phantoms that have well-controlled imaging properties can provide a ground truth reference. For instance, multi-modal fiduciary markers may be placed directly on a model of the heart to obtain a gold standard for motion gating which is impractical in a live clinical environment. This gold standard would allow a quantitative assessment of the algorithms' performance. In particular, in this chapter tracking of the ball bearings attached on the phantom allowed evaluation of the performance of the diaphragm/heart border tracking technique, something that could not be evaluated using clinical data. Additionally, multiple catheter trajectories can be tested in a single phantom whereas this would be highly impractical, and potentially dangerous, to practice in a patient. This enables evaluation of different catheter configurations. Specifically, the algorithms' validation regarding variability in catheter shape is tested in this chapter. Results demonstrated that the methods do not rely on catheter configuration.

On the other hand, clinical applications introduce uncertainties that are affected by: the imaging field of view, the anatomical region of interest, variations in image quality due to the patient's anatomy, the presence of non-rigid structures in the field of view, and other factors that are outside the control of a phantom-based assessment. The Tracked-PCA and View-angle independent algorithms relied on the CS catheter being present in the images and remaining there throughout the procedure. Nevertheless, in patient images some of the electrodes on the CS catheter might move out of the field of view so that the complete CS catheter body is not visible throughout the procedure. This is expected to compromise the accuracy and precision of the CS catheter detection algorithms when applied to clinical data. However, this will never be the case for phantom images, hence results might demonstrate accuracies and robustness that are not translated when used clinically.

Additionally, images from patient data differ from phantom data in more ways with the most significant being the non-rigid nature of the heart throughout the cardiorespiratory cycle. The motion of the heart might not be repetitive as in phantom images and therefore, the regulation of the motion might be unrealistic. Additionally, this might introduce motion artefacts and potential phase mismatch issues between images of the heart compromising the ability of the techniques for performing 2D-3D registration of 3D cardiac data (CT or MRI) to X-ray fluoroscopy, using catheters that are reconstructed in 3D from sequential biplane X-ray images, a potential significant clinical application of the proposed algorithms. Furthermore, patient images usually have lower contrast than images of phantoms and so imaging of the heart often involves the injection and perfusion of contrast agent into the blood stream for better vessel and chamber visibility. However, the rapid transportation of blood disperses the contrast agent non-uniformly throughout the vessels and chambers, resulting in cardiac images where some regions of interest have little or no contrast at all. With patient data, it is possible that the blob detection method would have even worse performance in low doses resulting in detection of many noise blobs that could compromise the performance of the developed techniques.

All in all, although the algorithms developed in this thesis proved to be robust, accurate and precise when applied to phantom data, their clinical translation cannot be guaranteed. In particular, motion gating techniques that meet stringent commissioning and acceptance criteria for accuracy and precision will not necessarily deliver the same level of accuracy and precision in clinical practice. Therefore, for a more comprehensive validation of the algorithms' robustness, accuracy and precision, their application and validation in clinical patient data is demonstrated in Chapter 5. Generally, though, obtaining a ground truth for patient procedures is particularly challenging and it is therefore difficult to know the actual clinical accuracy of a motion gating technique.

Chapter 5

Clinical validation

Contents

5.1 Introduction

In this chapter, the techniques' feasibility, robustness, accuracy and precision are demonstrated by validating them on clinical patient data. Images from patient data differ from images from phantom data in several ways with the most significant being the non-repeatable motion of the heart throughout the cardiorespiratory cycle of the clinical sequences compared to the phantom sequences. This introduces motion artefacts and potential phase mismatches between images of the heart. Additionally, patient images usually have lower contrast than images of phantoms and so imaging of the heart usually involves the injection and perfusion of contrast agent into the blood stream for better vessel and chamber visibility. However, the rapid transportation of blood disperses the contrast agent non-uniformly throughout the vessels and chambers, resulting in cardiac images where some regions of interest have little or no contrast at all.

To deal with the uncertainties introduced when gating or motion correction algorithms are applied on patient data, the algorithms are usually augmented with a number of additional image processing techniques. These techniques may include morphological operations, skeletonisation, restricting the region of interest, histogram equalisation, etc. Since the techniques proposed in this thesis are developed to be robust-to-noise, no such modifications are required for the application and validation of the techniques in clinical data. Instead, they are applied as described in Chapter 3.

5.2 Data acquisition

All patient procedures were carried out using a monoplane 25cm-flat-panel cardiac X-ray system (Philips Allura Xper FD10, Philips Healthcare, Best, The Netherlands) in one of the catheterisation laboratories at St. Thomas' Hospital, London, U.K. This study was approved by Guy's and St Thomas' Hospitals Local Ethics Committee. 10 different clinical fluoroscopy monoplane sequences, comprising a total of 660 frames, running from a minimum of 16.3 to a maximum of 25 seconds, covering at least 2 respiratory cycles, were acquired from 10 patients who underwent RFA procedures for the treatment of AF. An additional 3 sequential biplane clinical sequences, from three different patients who underwent RFA procedures for the treatment of AF, comprising a total of 244 frames, running from a minimum of 8.0 to a maximum of 19.3 seconds, covering at least 2 respiratory cycles were used. No contrast agent was used in these sequences. In addition, 12 different clinical fluoroscopy monoplane sequences (1070 frames) and 3 sequential biplane sequences (438 frames) were acquired, running from a minimum of 11.6 to a maximum of 36 seconds, covering at least 2 respiratory cycles, from 9 patients undergoing CRT (bi-ventricular pacing) procedures. 9 of the total of 18 sequences from the CRT patients, comprising 777 frames, were CS angiography sequences. Contrast agent was used in these 9

TABLE 5.1: Details of the datasets employed in this chapter. The columns denote the procedure employed, whether the sequences were monoplane (M) or sequential biplane (SB), the number of frames in the sequence, the number of patients, the frame rate of the sequences, whether contrast agent was used, and which algorithms were tested with each dataset.

	Data acquisition					
Procedure	Acquisition M/SB	No. of frames	No. of patients	Frame rate (f/s)	Contrast Yes/No	Algorithm tested
RFA	M	660	10	3	No	Tracked-PCA HML-based Masked-PCA
RFA	SB	244	3	3	No	View-angle independent
CRT	M	526	3	3	No	HML-based Masked-PCA
CRT	M	205	1	15	No	HML-based Masked-PCA
CRT	M	339	2	15	Yes	HML-based Masked-PCA
CRT	SB	342	2	15	Yes	HML-based Masked-PCA
CRT	SB	96	1	7.5	Yes	HML-based Masked-PCA

sequences, but not in the other 9. Specifically, the iodinated agent, lopamidol, was used at a strength of 300 $\frac{mg}{ml}$, undiluted. A total of 2412 X-ray images were processed.

X-ray imaging was performed at 3 frames per second (f/s) for 16 patients, 7.5 f/s for one patient and 15 f/s for five patients. The X-ray system settings were 70–100 kVp with the tube current under automatic exposure control. All X-ray images were 512^2 pixels in resolution, with a pixel size, $R_{\text{X-ray}}$, of 0.25 mm/pixel. Included in this ratio is the typical magnification factor of the X-ray system.

The 10 RFA monoplane clinical sequences were used for the validation of the Tracked-PCA, HML and Masked-PCA techniques. The 18 biplane and monoplane CRT clinical sequences were used for the validation of the HML and Masked-PCA techniques. The additional RFA biplane clinical sequences were used for the validation of the View-angle independent technique. The Tracked-PCA and View-angle independent techniques were not tested on sequences acquired from CRT procedures as the CS catheter was not present in the images. For the sake of clarity, Table 5.1 summarises the datasets used to evaluate the methods proposed in this thesis.

5.3 Methods of validation

Certain methods of validation included in this section are similar to the ones used for validating the techniques on phantom images, which are described in detail in Chapter 4. Specifically, these are the details of the training and testing data, optimisation of parameters, and the application

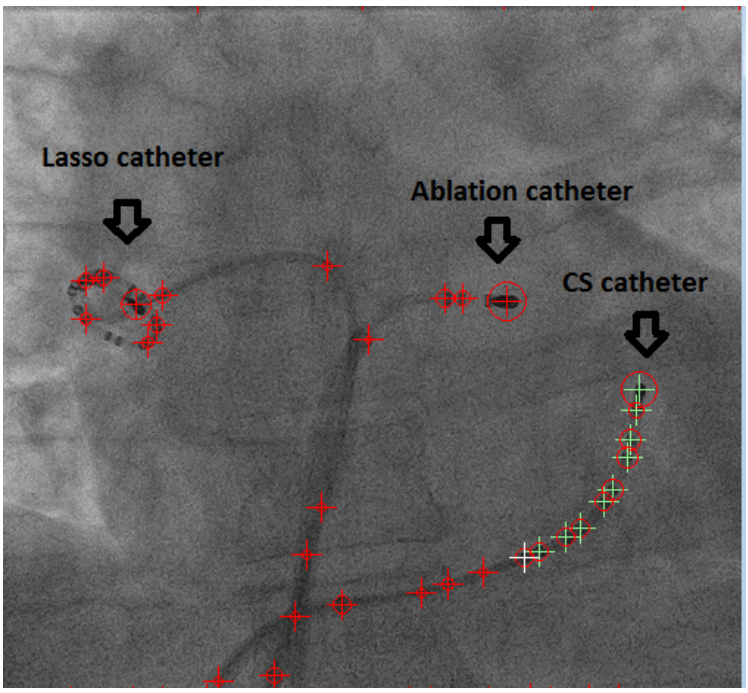

FIGURE 5.1: An example X-ray image showing the different types of EP catheters during the ablation stage of a procedure to treat AF. The CS catheter electrodes have been differentially detected, in green crosses, by the algorithm in [209]. Red crosses are the positions of other catheter electrodes.

in normal and in low dose images. Hence, in this chapter they are summarised only briefly. Only the parts that are different to the previous chapter are described in more detail.

5.3.1 Ground truth gating and catheter tracking

To validate the proposed techniques, gold standard cardiorespiratory signals were generated along with a gold standard for the electrode positions in each X-ray image. Similar to the phantom validation, the latter was done only for the Tracked-PCA and View-angle independent technique by the use of the real-time CS tracking technique [209], with manual correction of any misdetected electrodes. 0.7% of the total 6600 electrode detections were carried out manually. The first image of a processed example X-ray sequence is shown in Figure 5.1, where the CS catheter electrodes have been differentially detected, in green crosses. Red crosses are the positions of other catheter electrodes.

Manual gating of the cardiac cycle at end-systole was performed by an experienced observer, by visually detecting the end of contraction of the left ventricle from the fluoroscopic left heart border shadow. Manual gating of the cardiac cycle at end-systole was further validated by additional observers who were trained to identify the end-systolic frames throughout the X-ray sequences. Systole was chosen as opposed to diastole for validation since the manual ground truth is more reliable for end-systole where rapid motion can be used as the visual cue.

The respiratory gating was validated using either diaphragm or heart border tracking as described in [95] for the ground truth. The choice of ground truth was determined by which structure was visible in the X-ray images. The respiratory signal obtained from diaphragm/heart border tracking was cardiac gated using the manually identified end-systolic frames.

5.3.2 Training and testing data

The training and testing data for each algorithm were arranged with the same approach as in Chapter 4. The available clinical data allowed 4880 catheter tracking tests for the low dose analysis of the Tracked-PCA technique. The View-angle independent technique was validated on the 3 sequential biplane RFA clinical sequences, comprising a total of 244 frames, and therefore giving a total of 6 clinical experiments. For the HML-based and Masked-PCA techniques training and testing data were not separated because the techniques are intended for retrospective analysis. Rather, all frames were used for both training and testing the model.

5.3.3 Optimisation of parameters

The parameters were optimised separately for the clinical data, using the method described in Chapter 4. The parameters are: a threshold level on the normalised output, 0 to 1, of the FV filter, the size of the structuring element in the morphological dilation of the identified structures, and the pass band and stop band frequencies (normalised from 0 to 1) of the band pass filter, and were found to be > 0.02, 27–33, 0.54–0.62 and 0.96–0.98, respectively, for the HML-based technique applied on the clinical X-ray sequences. The parameters were optimised to be > 0.02, 1, 0.54-0.62 and 0.96-0.98, respectively, for the Masked-PCA technique.

5.3.4 Application in normal dose images

5.3.4.1 Gating validation

The motion gating validation of the techniques was done with the same approach as described in Chapter 4, with the only difference being the evaluation of the frame differences between the automatic and gold standard techniques. Unlike the phantom experiments where the trace had peaks/troughs covering several frames, in clinical data the phases are well described with single frames defining the peaks/troughs. Hence the corresponding absolute frame differences are easily computed by comparing the peaks/troughs directly.

5.3.4.2 Comparative quantitative validation

This section describes different comparative quantitative methods of validation between the developed techniques, and other published techniques, on RFA and/or CRT procedures.

Tracked-PCA technique. It is important to investigate whether the new Tracked-PCA technique is superior to simply using the Cartesian coordinates of the electrode positions alone. Therefore, as a comparative technique, the tracking data for the proximal and distal electrodes of the CS catheter were employed using the same gating technique. Specifically, for the proximal electrode the x coordinate, $z_{i,1,x}$ was used in place of $P_{1,i}$ and the y-coordinate, $z_{i,1,y}$ was used in place of $P_{2,i}$. Similarly, for the distal electrode the x-coordinate, $z_{i,10,x}$ was used in place of $P_{1,i}$ and the y-coordinate, $z_{i,10,y}$ was used in place of $P_{2,i}$. This enabled validation of the contribution of the PCA to this technique.

The performance of the Tracked-PCA technique was also compared to other dimensionality reduction techniques. Such techniques include the non-linear dimensionality reduction manifold learning techniques Laplacian eigenmaps [225] and ISOMAP [241] and the linear dimensionality reduction technique Independent component analysis (ICA) [242].

Finally, as an alternative to dimensionality reduction techniques, the performance of the phase correlation technique [192] for EP images containing high-contrast catheters was also examined and compared to the Tracked-PCA technique. According to the phase correlation technique, the Fourier transform of $I_t(x, y)$ is represented by $F(\xi, \eta)$, where $I_t(x, y)$ represents the image at time t of a scene changing with time. Assuming that the objects in the scene exhibit only translations then for $I_{t+1}(x, y) = I_t(x - x_t, y - y_t)$, the Fourier transform is $F_{t+1}(\xi, \eta) = \exp(-j2\pi(\xi x_t + \eta y_t))F_t(\xi, \eta)$. By inverse transforming the ratio of the cross-power spectrum of I_{t+1} and I_t to its magnitude, represented by $\frac{F_{t+1}{F_t}^*}{||F_{t+1}{F_t}^*||} = exp(-j2\pi(\xi x_t + \eta y_t))$, a peak at (x_t, y_t) is obtained. A translation applied to the image produces a phase shift in the spectrum.

This method assumes that image features are a combination of signals at different frequencies, and that calculating the phase shift of the different frequencies in an image amounts to measuring the motion of image features corresponding to those frequencies. The phase shift can be calculated in the Fourier domain. The overall change in the energy within the object being imaged can be estimated by integrating over the phase shift by analysing consecutive frames using Eq. (5.1).

$$E = \int \frac{F(I_t)^* \cdot F(I_{t+1})}{|F(I_t)^*| \cdot |F(I_{t+1})|} \mathrm{d}f \tag{5.1}$$

where $F(I_t)$ represents the Fourier transform of the image I at time t.

The obtained energy, E, is used as an estimate of the current phase of the organ. The extrema of this signal detect definite phase of the cardiac and the respiratory cycle. To obtain separate

cardiac and respiratory signals a Butterworth band pass filter centred at 1Hz is used to recover the cardiac signal, whereas a fourth-order Butterworth low pass filter with normalized cutoff frequency of 0.5, will recover the respiratory signal. The choice of cutoff frequencies was based on the fact that cardiac phase is expected to be around 1Hz, while respiratory phase is expected to be less than that.

CS catheters are often used as diagnostic catheters and one of the most commonly used CS catheters is the 10-electrode decapolar catheter. The arrangement of electrodes has two variations. One is evenly distributed and the other is paired. The presence of 10 electrodes is the unique feature which is used to separate the CS catheter from other catheters, instruments and ECG leads, which is an additional reason for choosing that catheter for the development of the Tracked-PCA technique. For validation of the technique the 10-electrode decapolar catheter with the electrodes distributed in pairs is used. However, the CS catheter sometimes has a different configuration, having only 4-electrodes distributed in pairs, known as a quadripolar CS catheter. To validate the performance of the proposed technique in clinical cases where the quadripolar CS catheter is used, the tracking data, s_i, was truncated to have only the x and y positions of the distal 4 electrodes. This was then compared to the 10-electrode results.

The above comparative approaches were applied on the same ten clinical fluoroscopy sequences that were used for testing and validation of the Tracked-PCA method.

HML-based technique. The cardiorespiratory gating performance of the proposed HML-based technique was compared to the Tracked-PCA technique to show the effect of the extra step of developing a robust to varying image-content technique. This was done only on RFA procedures, as the Tracked-PCA technique requires that the CS catheter is present in the X-ray images.

Masked-PCA technique. The cardiorespiratory gating performance of the proposed Masked-PCA technique was compared to the previously developed robust to varying image-content HML-based gating technique, and to phase correlation technique [192]. The HML-based technique and phase correlation approaches were applied on the same 28 clinical fluoroscopy sequences that were used for testing and validation of the Masked-PCA method.

5.3.5 Application in very low dose images

5.3.5.1 Application of Poisson noise

The X-ray images were corrupted by applying Poisson noise as described in Section 4.3.5.1. SNR values of $\sqrt{50}$, $\sqrt{10}$, $\sqrt{8}$, $\sqrt{6}$, $\sqrt{5}$, $\sqrt{2}$ and $\sqrt{1}$ were used for the Tracked-PCA, HML-based

and Masked-PCA techniques while SNR values of $\sqrt{50}$, $\sqrt{10}$, $\sqrt{8}$, $\sqrt{6}$ and $\sqrt{5}$ were used for the View-angle independent technique. The ranges used here are based on the results of Chapter 4, which indicate a failure of the View-angle independent algorithm on SNR levels of $\sqrt{2}$ and $\sqrt{1}$.

Figure 5.2 illustrates the results of the application of Poisson noise on the first image of an example patient X-ray sequence. The uncorrupted example is displayed, along with simulated noisy images having a SNR of $\sqrt{50}$, $\sqrt{10}$, $\sqrt{8}$, $\sqrt{6}$, $\sqrt{5}$, $\sqrt{2}$ and $\sqrt{1}$, respectively.

5.3.5.2 Catheter tracking validation

Similar to the phantom validation, to validate the performance of the CS catheter tracking, median errors per electrode for the uncorrupted and the different SNR X-ray sequences were calculated. Tracking failures were considered to be those cases where the electrode error was above 2 mm [93]. In this chapter, to further investigate the robustness of the Tracked-PCA CS catheter tracking, it was compared to the results of the real-time tracking technique developed by Ma *et al.* [209] in both normal and very low dose scenarios.

5.3.5.3 Gating validation

Similar to the gating validation on normal dose images, for both cardiac and respiratory gating, the absolute frame difference was computed between the automatic techniques and the gold standard techniques. For the validation on low dose images absolute frame differences were computed for all noise levels. A comparison of the Tracked-PCA, HML-based and Masked-PCA techniques was included to show the effect of the extra step of developing a robust to varying image-content method that does not rely on any specific catheters being present in the images. Also the comparison shows the effect of the development of the Masked-PCA technique to increase the cardiac gating performance of the HML-based technique. Furthermore, a comparison of the application of the View-angle independent technique with the proposed single view Tracked-PCA technique on multiplane patient sequence pairs and previously used phantom images (Chapters 4) was included to show the effect of the extra step of changing view-angle.

5.4 Experimental results

5.4.1 Gold standard validation

This section reports the accuracy, precision and robustness of the gold standards used in clinical data. The gold standard methods include: the automatic diaphragm/heart border tracking technique [95], used as the ground truth for respiratory motion gating, the manual identification

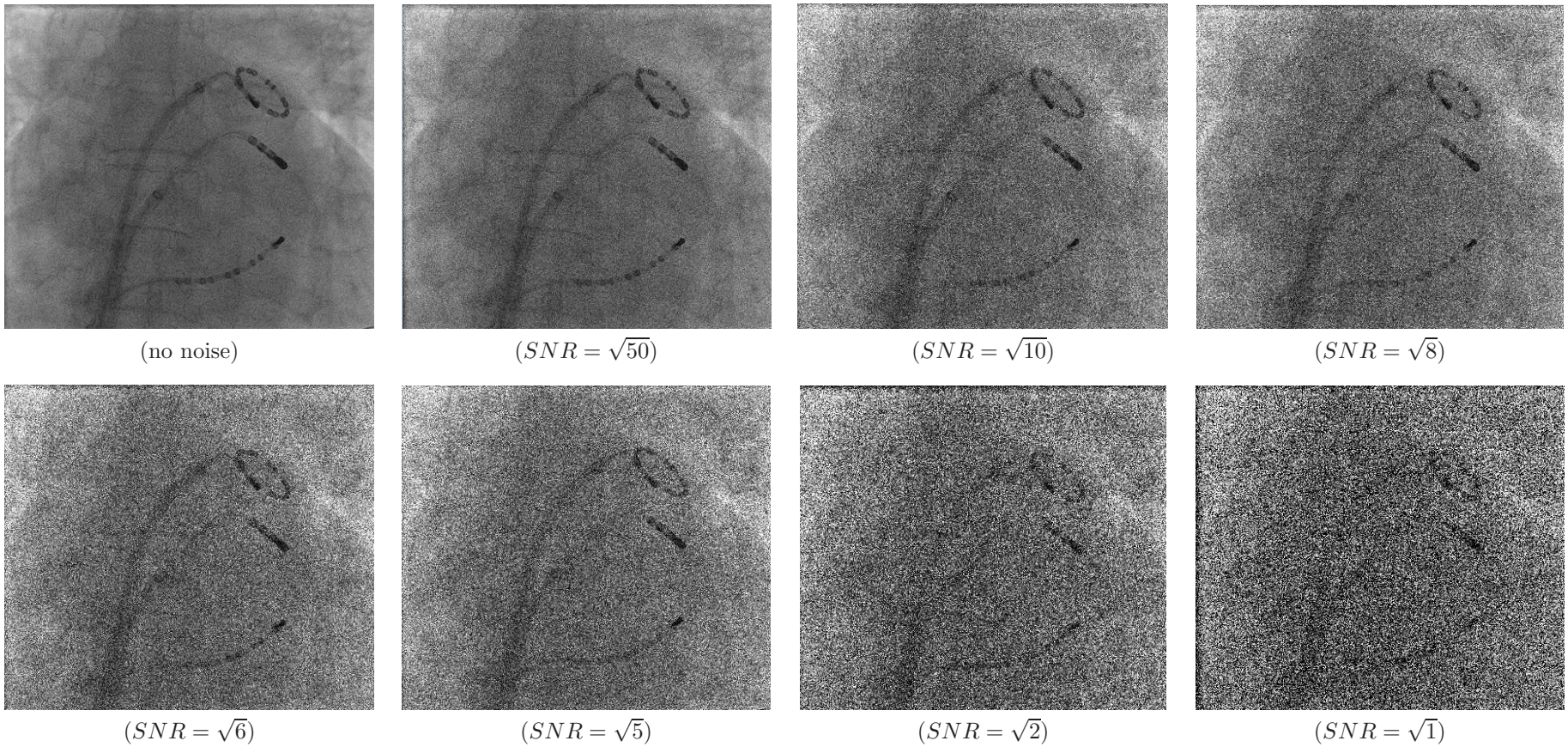

FIGURE 5.2: (a) Case 1: Example of an uncorrupted RFA clinical X-ray image; (b–h) the same X-ray image corrupted with different levels of Poisson noise.

TABLE 5.2: Average and standard deviation of the difference between the results of the two observers per electrode over all frames of a clinical sequence, starting from the proximal (el.1) and moving to the distal (el.10) electrode.

Difference between observers (mm)		
Electrode number	Average	Standard deviation
1	0.28	0.68
2	0.30	0.76
3	0.33	0.79
4	0.28	0.67
5	0.40	0.80
6	0.28	0.64
7	0.40	0.80
8	0.33	0.77
9	0.40	0.88
10	0.46	1.01

of systolic frames, used as the ground truth for cardiac motion gating, the real-time tracking technique and the manual detection of the CS catheter electrodes performed in cases where the real-time CS catheter tracking technique failed. These last two were used in combination as a gold standard for the validation of the CS catheter tracking.

The accuracy and robustness of the diaphragm/heart border tracking technique [95] has already been validated in the previous chapter, Section 4.3.1, by manual tracking of ball bearings attached to the phantom. The peaks/troughs of the obtained results were compared and found to be identical to the gold standard results from the diaphragm/heart border tracking. Similarly, the real-time tracking technique's accuracy for CS catheter detection was evaluated in Ma *et. al* [95] and results were given in Section 4.3.1.

Regarding the manual electrode detection gold standard method, this was separately evaluated on clinical data using the same approach as in Chapter 4, using two observers. One clinical sequence was used, comprising a total of 122 frames. This was a rotational sequence and was chosen because it was one of the more difficult sequences for electrode detection due to the range of catheter views. Consequently, a total of 1220 electrode detections were performed by both observers and their detection precision was evaluated. Results were computed for each of the 10 electrodes individually and are shown in Table 5.2. The results were initially computed in pixels and converted to mm using the pixel to mm ratio, $R_{\text{X-ray}}$ (Section 5.2).

Regarding the manual cardiac gating gold standard method, manual detection of systolic frames was performed by different observers and the average inter observer standard deviation was computed as a proportion of the cardiac cycle, assuming 1s per heartbeat. For the RFA and CRT procedures, four and three experienced observers were used, respectively, to manually detect systolic frames. Results are shown in Table 5.3.

TABLE 5.3: Average inter observer standard deviation as a proportion of the cardiac cycle.

Average standard deviation (s)		
Procedure type	Systolic peaks	Average variation
RFA	183	0
CRT	699	1.91×10^{-4}

The non-zero value for the CRT procedures in Table 5.3 was caused by 7 peaks of 1 frame difference.

5.4.2 Tracked-PCA technique

5.4.2.1 Retrospective method in normal dose images

The percentages of catheter motion in PCs 1 and 2 for each patient were calculated to vary between 78.9%–95.6% for the first PC and between 3.2%–20.5% for the second PC.

Example cardiac and respiratory traces. For cardiac gating validation, a plot of the data with respect to the first PC for the first 30 frames of the X-ray sequence is illustrated in a dashed-dot black line in Figure 5.3a. The plotted vertical black lines correspond to the gold standard end-systolic frames. The results of respiratory gating validation are shown in Figure 5.3b for the same example patient case. The Tracked-PCA technique is shown in a solid black line. The diaphragm tracking (gold standard) is shown in a dashed-dot black line.

Quantitative validation. The results can be seen in the frequency distribution bar charts, i.e. the number of peaks or troughs with 0, 1, 2, 3, 4, 5 or 6 frames separation from the gold standard, in Figures 5.4a, 5.4b and 5.4c for end-systolic, end-expiration (EX) and end-inspiration (EI) gating, respectively. Results illustrate that the Tracked-PCA technique outperforms both of the alternative electrode position-based techniques and the phase correlation technique for all three gating tasks. The phase correlation approach performs the worst.

Table 5.4 summarises the number of false positives and false negatives (i.e. extra/fewer detected peaks/troughs) over all processed sequences for all techniques. Table 5.5 displays the percentage success rates. Percentage success rates were computed based on the motion accuracy objectives set in this thesis, which were determined based on the targeted clinical applications. Two different objectives were set, one for the motion compensation application and one for 3D catheter reconstruction and motion gating of 3D rotational X-ray angiography sequences. For motion compensation, the maximum allowable gating error is 1 second. For the rotational gating and the phase matching for 3D reconstruction the motion gating accuracy objective was set to 0.1s. For a complete set of results, percentage success rates were computed individually for the two objectives

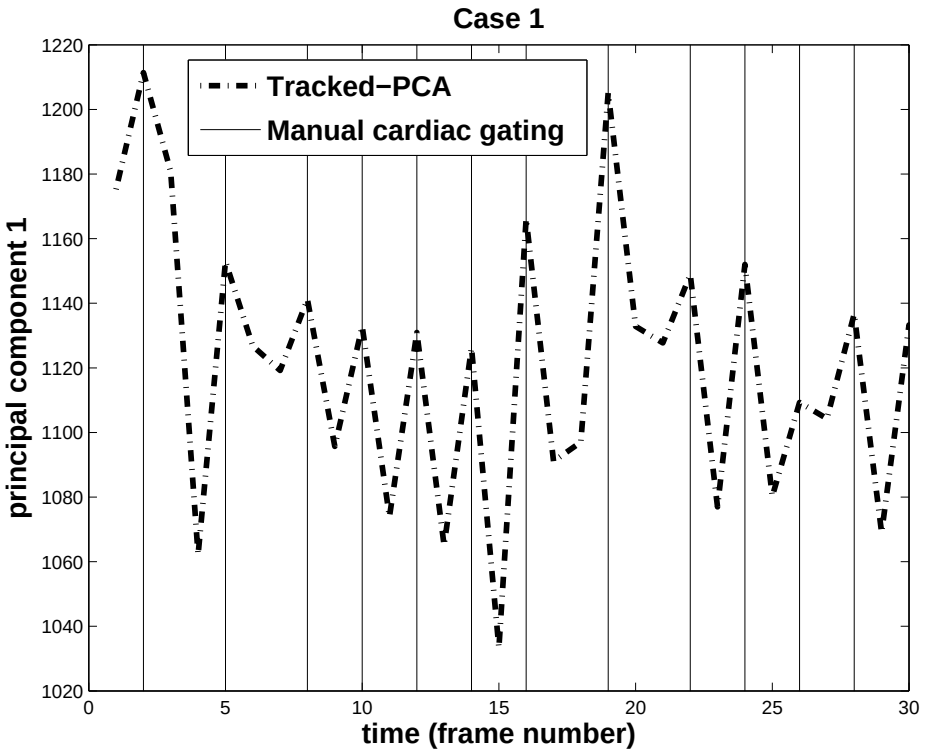

(a)

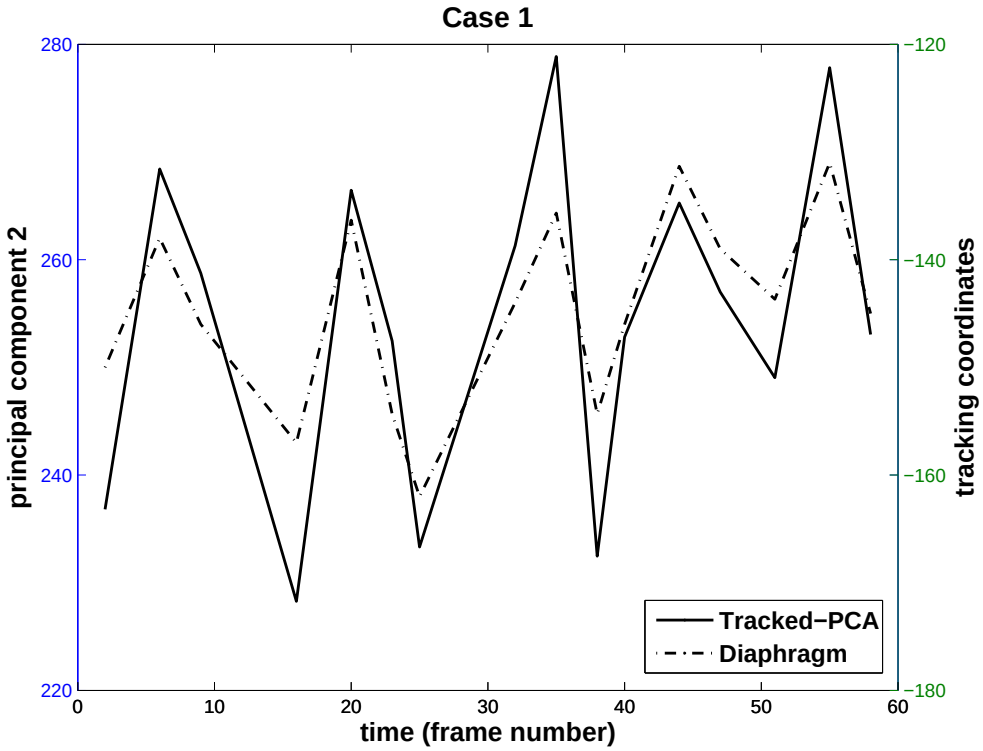

(b)

FIGURE 5.3: (a) Case 1: Graphical representation of the variation of the first PC with X-ray frame number for the Tracked-PCA method. The vertical black lines are the gold standard identification of end-systolic frames. (b) The respiratory traces obtained are illustrated for the same example case in a solid black line. The diaphragm tracking (gold standard) is also shown in a dashed-dot black line. In (b) the green y-axis scale corresponds to the gold standard trace while the blue one corresponds to the trace obtained using the automatic technique.

TABLE 5.4: Misdetection of peaks/troughs. Number of extra/fewer detected gating frames for all automatic techniques (Tracked-PCA technique using a decapolar CS catheter, tracking data for the proximal and distal electrodes of the CS catheter, where gated x is for end-systolic gating and gated y for EX and EI gating, Phase correlation method, Tracked-PCA technique using a quadripolar CS catheter, ICA, Laplacian eigenmaps and ISOMAP) over all gating tasks (end-systolic gating, EX, EI).

Overall extra/fewer peaks or troughs for ten clinical sequences			
Automatic technique	End-systolic gating	EX gating	EI gating
Tracked-PCA (decapolar)	0/0	0/0	0/0
Gated x,y proximal el	11/0	6/0	5/3
Gated x,y, distal el	9/0	6/0	5/3
Phase correlation	13/18	5/9	8/4
Tracked-PCA (quadripolar)	0/0	0/0	0/0
ICA	0/0	1/0	2/1
Laplacian eigenmaps	2/0	0/0	0/0
ISOMAP	4/1	1/0	2/2

and were matched within 0.1s and 1s, respectively. Percentage success rates were computed using the equation $\frac{100x}{x_{total}}$, where x corresponds to the number of gold standard and automatic-gating frames that are matched within the allowable gating error and x_{total} corresponds to the total number of gold standard gating frames. Percentage success rates were computed for end-systolic, EX and EI gating for all automatic-gating techniques. Table 5.6 presents the mean/standard deviations of the frame differences of the three techniques. An f-test was conducted under the null hypothesis that there was no difference in the techniques. The f-test was done on the frame differences of each of the techniques and was conducted for end-systolic, EX and EI, only including peaks/troughs that were detected by all four methods. In all cases the proposed Tracked-PCA technique was found to have significantly lower errors than the alternative techniques ($p < 0.05$). The results confirm the accuracy and robustness of the Tracked-PCA gating method.

Additionally, for both cardiac and respiratory gating, the absolute frame difference was computed for all dimensionality reduction techniques and for the Tracked-PCA technique in clinical cases, with respect to the gold standard methods. These are illustrated in a separate figure for clarity. The Tracked-PCA was tested with both the decapolar and the quadripolar CS catheter. The results can be seen in the frequency distribution bar charts, i.e. the number of peaks or troughs with 0, 1, 2, 3, 4, 5 or 6 frames separation from the gold standard, in Figures 5.5a, 5.5b and 5.5c for cardiac, EX and EI gating, respectively. The results illustrate that the Tracked-PCA technique outperforms all of the alternative dimensionality reduction techniques for all three gating tasks. Additionally, the results demonstrate that the performance of the Tracked-PCA technique is not affected in cases where the quadripolar CS catheter is used. Hence, the method is still applicable if a 4-electrode catheter is used throughout the procedure.

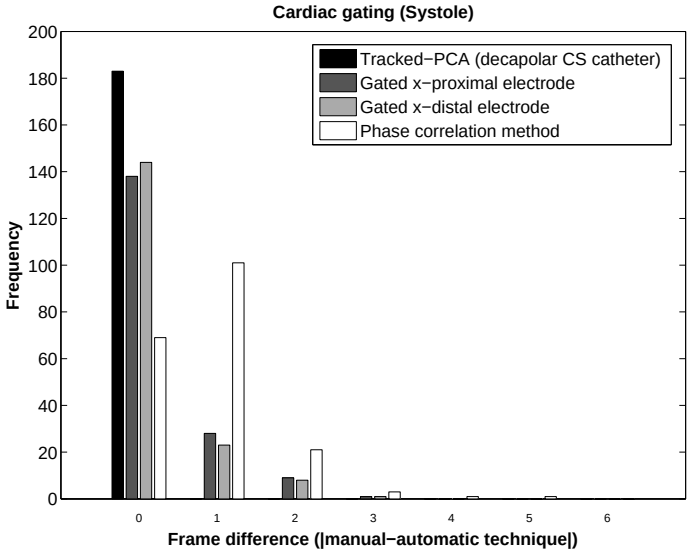

(a)

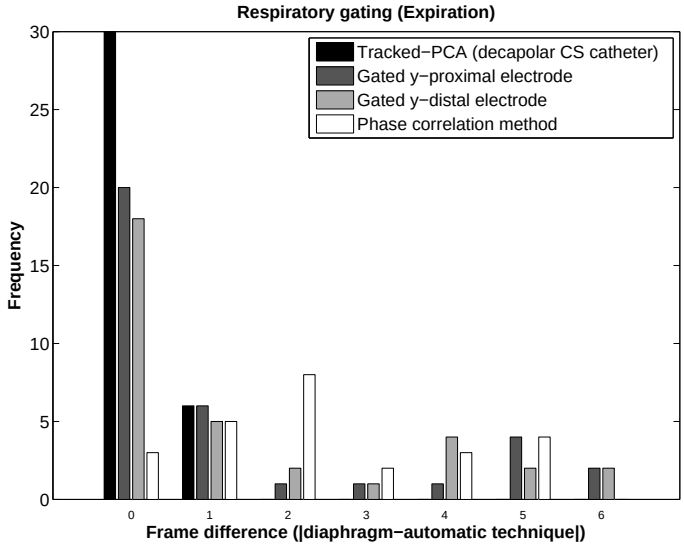

(b)

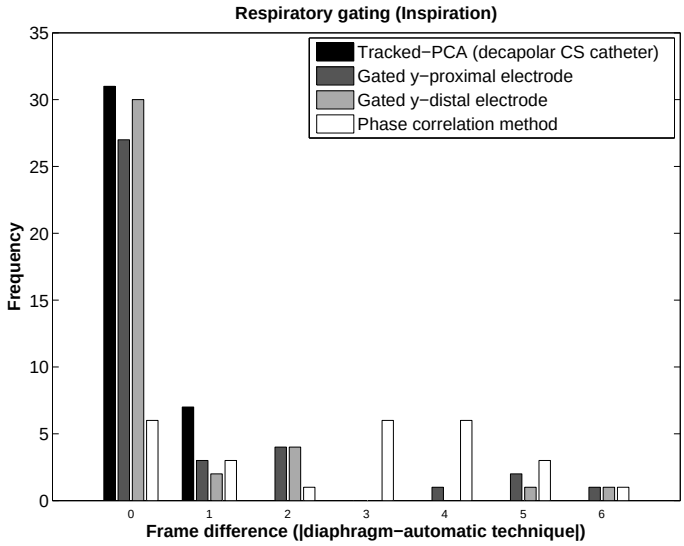

(c)

FIGURE 5.4: Frequency distributions of frame difference errors for (a) cardiac gating, (b) EX gating, and (c) EI gating. Results are illustrated for Tracked-PCA using a decapolar CS catheter, gated proximal electrode tracking data, gated distal electrode tracking data and Phase correlation automatic methods.

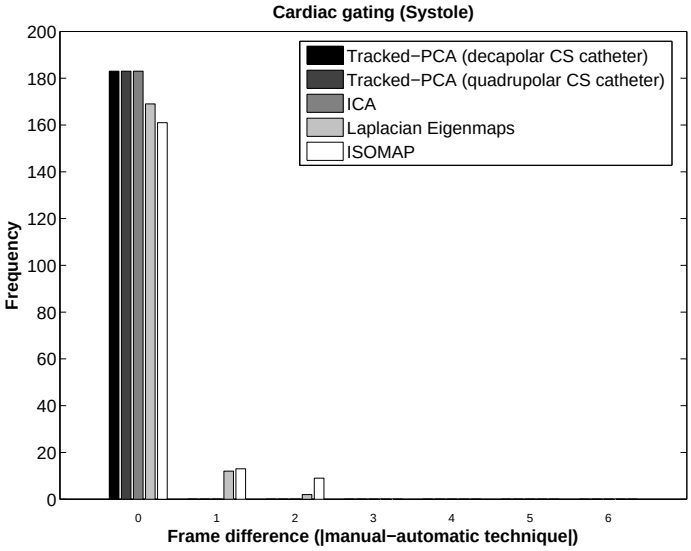

(a)

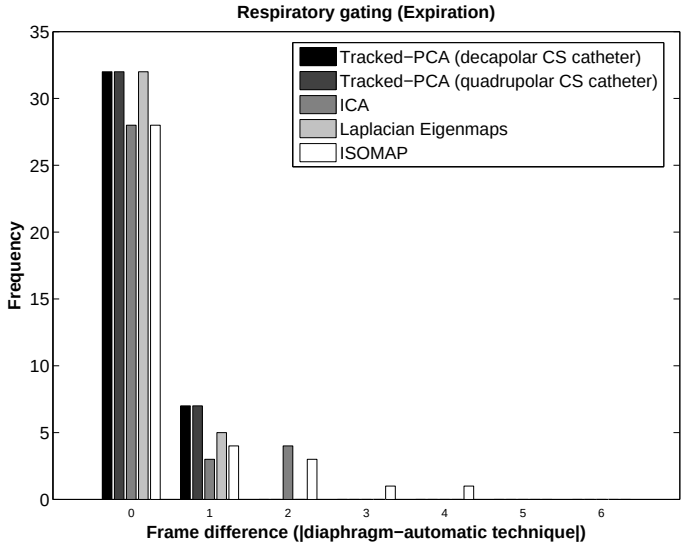

(b)

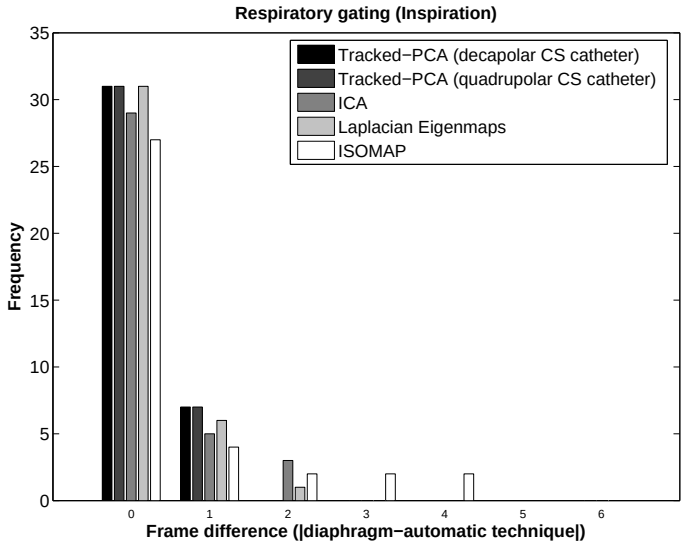

(c)

FIGURE 5.5: Frequency distributions of frame difference errors for (a) cardiac gating (b) EX gating (c) EI gating. Results are illustrated for Tracked-PCA when the decapolar CS catheter is used, Tracked-PCA when the quadripolar CS catheter is used, ICA, Laplacian eigenmaps and ISOMAP methods.

TABLE 5.5: Percentage success rates for all automatic-gating techniques based on their potential clinical application to 3D catheter reconstruction and motion gating of 3D rotational X-ray angiography sequences/ to motion compensation. Percentage success is defined as the proportion of gold standard gating frames that are matched within the allowable gating error by their corresponding automatically-detected gating frames. Systolic gating results for the application of the techniques to motion compensation are not included, because motion compensation is only concerned with respiratory motion.

Success rates (%)			
Automatic technique	End-systolic gating	EX gating	EI gating
Tracked-PCA (decapolar)	100.0./-	86.9/100.0	92.1/100.0
Gated x,y proximal el	78.4/-	54.1/100.0	71.0/100.0
Gated x,y, distal el	81.8/-	48.7/100.0	78.9/100.0
Phase correlation	35.2/-	10.7/100.0	20.7/100.0
Tracked-PCA (quadripolar)	100.0/-	86.9/100.0	92.1/100.0
ICA	100.0/-	71.8/100.0	76.3/100.0
Laplacian eigenmaps	92.3/-	84.6/100.0	84.2/100.0
ISOMAP	88.0/-	71.8/100.0	73.0/100.0

TABLE 5.6: Mean and standard deviation of gating errors in seconds for automatic-gating techniques.

Mean/standard deviation gating errors			
Automatic technique	End-Systolic gating	EX gating	EI gating
PCA	0/0	0.14/0.36	0.07/0.27
Gated x,y proximal el	0.09/0.19	0.48/0.69	0.27/0.53
Gated x,y, distal el	0.08/0.18	0.49/0.66	0.18/0.44
Phase correlation	0.27/0.23	0.78/0.53	0.87/0.60
Tracked-PCA (quadripolar)	0/0	0.14/0.36	0.07/0.27
ICA	0/0	0.10/0.22	0.10/0.20
Laplacian eigenmaps	0.03/0.12	0.04/0.10	0.05/0.11
ISOMAP	0.06/0.16	0.15/0.32	0.20/0.40

Diastolic gating validation. As already mentioned in Section 1.6, for the rotational gating and the phase matching for 3D reconstruction, both applications will use the diastolic phase. Since the heart will be relatively stationary in the diastolic phase for a period of about 0.3s, the motion gating accuracy objective is set to 0.1s. In this chapter cardiac gating validation was performed on systolic frames where the gold standard is most reliable. However, the actual application would need diastolic frames. In this section experiments based on diastolic validation were performed to determine whether the method is just as accurate on diastolic frames, so that the systolic results are valid for the applications. Manual gating of the cardiac cycle at end-diastole was performed by three experienced observers, by visually detecting the end of relaxation of the left ventricle from the fluoroscopic left heart border shadow. No variation between the multiple observers was found. For both systolic and diastolic gating, the absolute frame difference was computed between the Tracked-PCA method and the gold standard methods on the normal dose images. The results can be seen in Figure 5.6 in the frequency distribution bar charts, i.e. the number of peaks or troughs with 0, 1 or 2 frames separation from the gold standard. The results illustrate that the method is just as accurate on diastolic frames, and consequently the systolic results are valid for the applications.

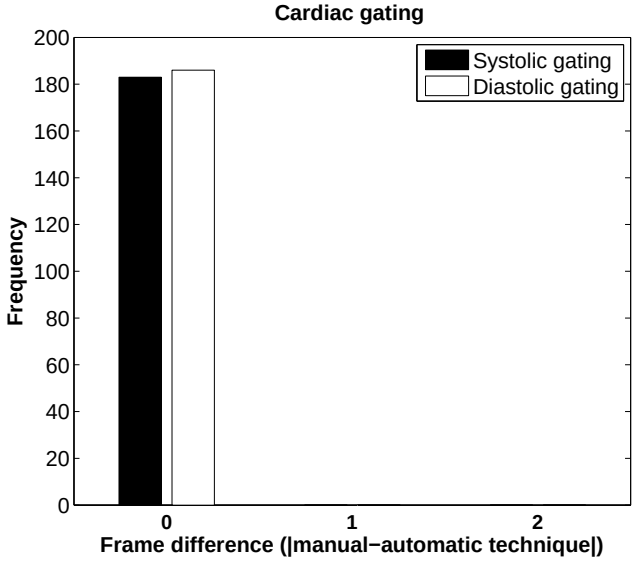

FIGURE 5.6: Frequency distributions of frame difference errors for cardiac gating of both systolic and diastolic frames using the Tracked-PCA method.

5.4.2.2 Near-real-time method in very low dose images

The method is validated on the same ten clinical fluoroscopy sequences from ten patients who underwent RFA procedures for the treatment of AF.

Blob detection method on noisy X-ray images. Figure 5.7 illustrates the results of applying the fast multi-scale blob detector to detect all possible electrode-like objects on an uncorrupted patient X-ray image, and the noisy X-ray images having SNRs of $\sqrt{50}$, $\sqrt{10}$, $\sqrt{8}$, $\sqrt{6}$, $\sqrt{5}$, $\sqrt{2}$ and $\sqrt{1}$, respectively. The CS catheter electrodes have been differentially detected, in green crosses. The white crosses illustrate the proximal electrode of the CS catheter, while the red circles illustrate the strength of the detected blobs.

PCA-based CS catheter tracking. The results of the Tracked-PCA CS catheter tracking technique are displayed in Figure 5.8, in green crosses. The CS catheter position is shown on the first patient image of the uncorrupted example X-ray sequence and on the noisy patient X-ray images at the seven different SNR levels.

CS catheter tracking quantitative validation. Figure 5.9a illustrates the Tracked-PCA CS catheter tracking median errors per electrode for the uncorrupted and seven different SNR X-ray images. Errors are calculated with respect to the gold standard detection. Since the technique is designed to track each of the ten CS catheter electrodes, errors are calculated and displayed for each of them independently. To distinguish errors of each electrode, error bars per

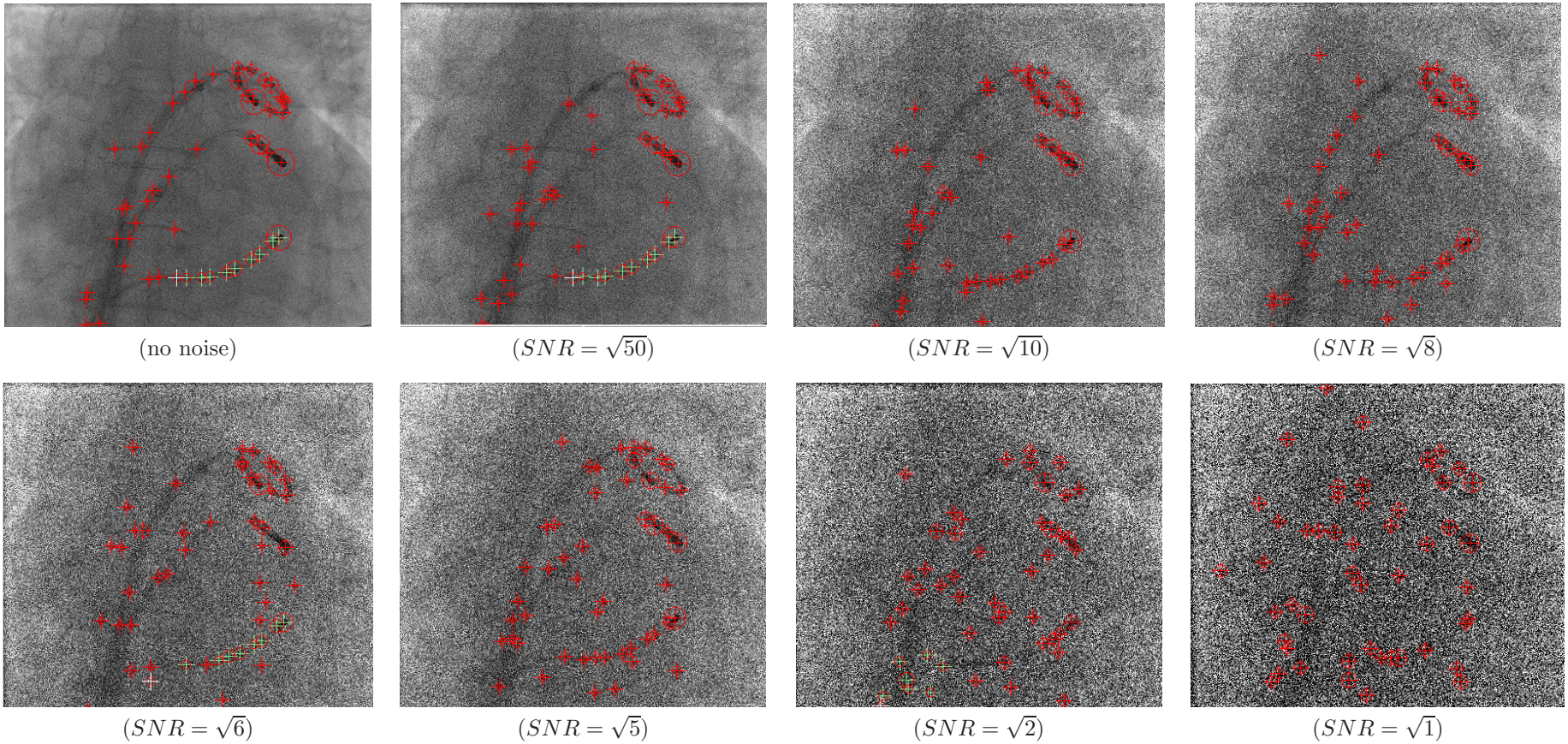

FIGURE 5.7: Case 1: example results from the blob detection method of an uncorrupted clinical X-ray image and the same X-ray image corrupted with different levels of Poisson noise. The CS catheter electrodes have been differentially detected, in green crosses. Red crosses are the positions of other catheter electrodes. White crosses are the positions of the proximal electrode of the CS catheter.

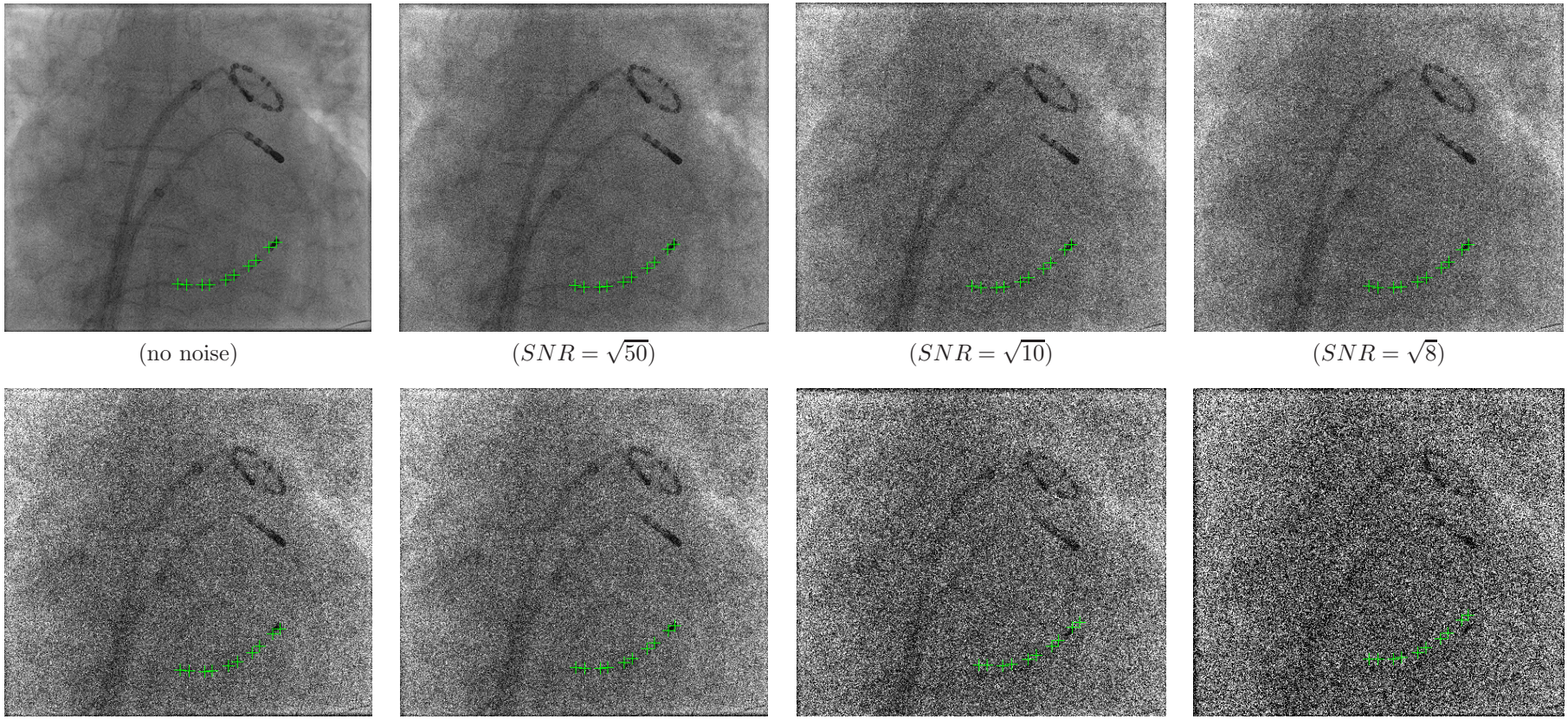

FIGURE 5.8: Case 1: representation of the CS catheter predicted position using the Tracked-PCA technique on an uncorrupted example clinical X-ray image; and CS catheter predicted position on the same X-ray image simulated to have different SNR levels.

electrode are displayed in different grey scale colours, starting from the proximal (black colour) and moving to the distal one (white colour). Initially, median errors per electrode were computed when using different numbers of PCs. Results confirmed that, as with phantom data, only the first two PCs contained useful information and the rest were dominated by noise. Hence, in this study only the first and second PCs are used.

To further investigate the robustness of the technique it was compared to the results of the real-time CS catheter tracking technique [209] on X-ray images at all different levels of SNR X-ray. Median errors per frame per electrode were also computed with respect to the gold standard. Results where an electrode was not detected by this method were excluded from the error calculation for that electrode. Results are illustrated in Figure 5.9b. To allow comparisons with the errors of the Tracked-PCA CS catheter tracking technique a portion of the graph axis scale was zoomed in (Figure 5.9c). Results that fall outside the x-axis scale, SNR X-ray sequences of $\sqrt{2}$ and $\sqrt{1}$, are not displayed on this figure. For the technique to be acceptable in clinical practice, failure cases were considered to be the ones where median errors per electrode were above 2 mm [93]. Consequently, for a more comprehensive validation median errors are illustrated in Figure 5.10 only for the successfully tracked CS electrodes. These are the ones tracked with less than 2mm accuracy. In Figures 5.10a, and 5.10b the median errors per successful electrode detected using the Tracked-PCA technique and Real-time tracking techniques, respectively are demonstrated.

Success rates were also calculated for both methods. Percentage success rate (%) results are illustrated in Figure 5.11a for the Tracked-PCA CS catheter tracking method and in Figure 5.11b for the real-time tracking method. Outcomes show that the Tracked-PCA method for tracking the CS catheter on low dose X-ray images outperforms the real-time tracking technique for noise-corrupted X-ray images. Figure 5.12, shows the range of the values in terms of the 25^{th} percentile, median and 75^{th} percentile, over all electrodes, and for successfully tracked electrodes, for each noise level. In this table, the values are not computed for each electrode individually but over all electrodes in each noise level.

Cardiac and respiratory motion gating. For both cardiac and respiratory gating, the frame difference was computed between the Tracked-PCA method and the gold standard methods. This was tested on the 10 monoplane RFA X-ray sequences for the normal dose and each of the seven different SNR X-ray sequences, comprising of a total of 5280 experiments. The results are illustrated in Figure 5.13. Table 5.7 summarises the number of false positives and false negatives (i.e. extra/fewer detected peaks/troughs) over all processed sequences for the seven different SNR X-ray sequences for all gating techniques.

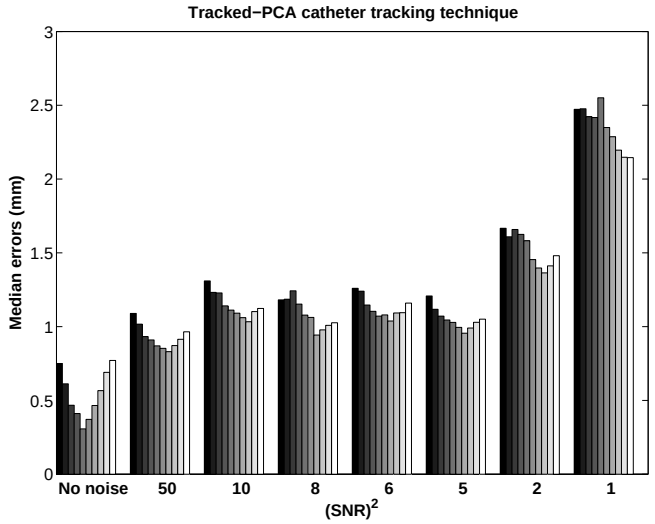

(a)

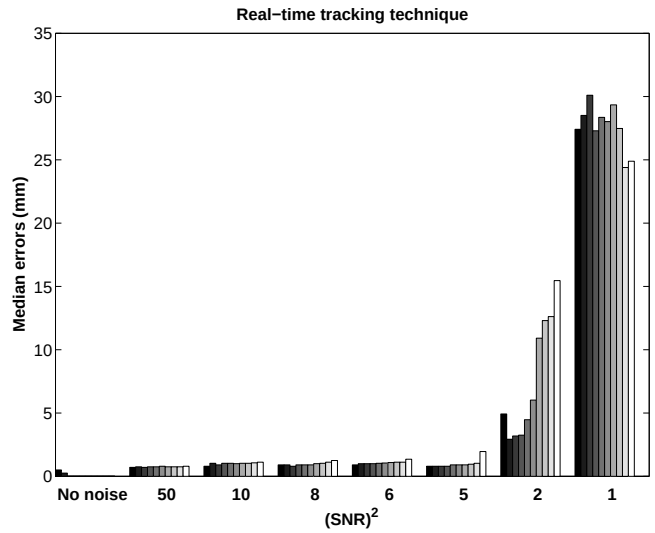

(b)

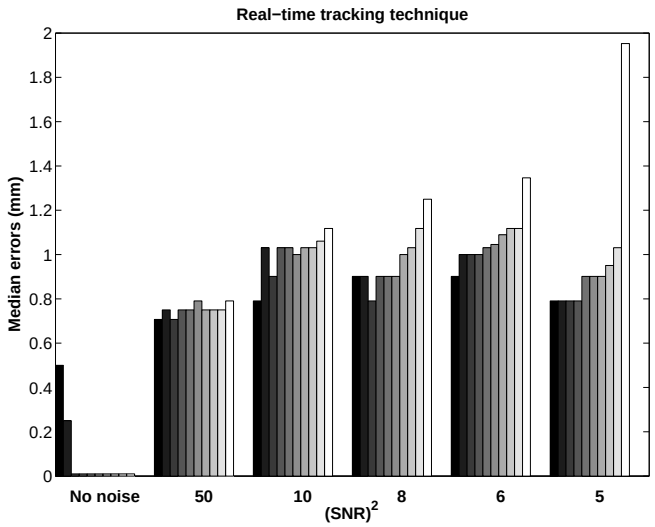

(c)

FIGURE 5.9: (a) Tracked-PCA method median errors per electrode, with respect to the gold standard. (b) Real-time tracking technique median errors per electrode, with respect to the gold standard. (c) Zoomed portion of Figure (b) axis scale. Results that fall outside the axis scale, SNR X-ray sequences of $\sqrt{2}$ and $\sqrt{1}$, are not displayed on this figure. Different grey scale colour bars are used to distinguish the CS catheter electrodes, starting from the proximal (black colour) and moving to the distal electrode (white colour).

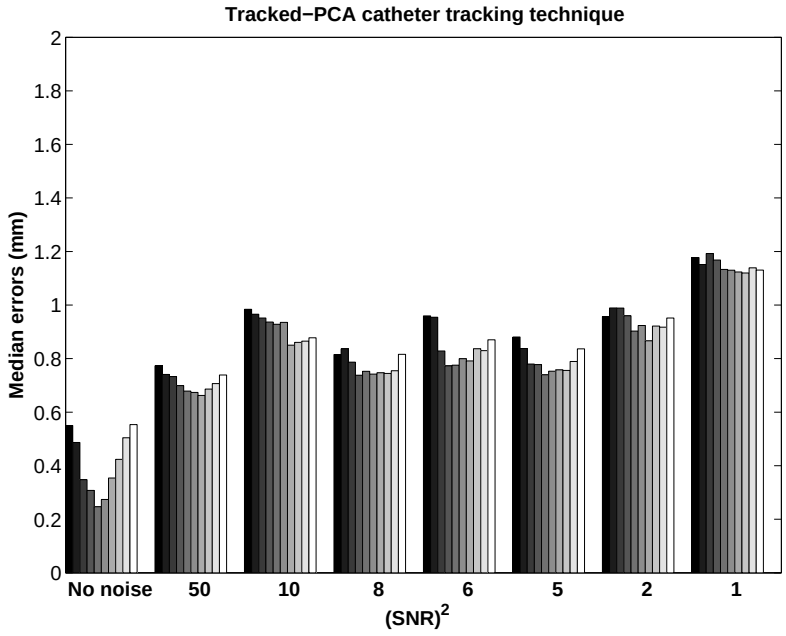

(a)

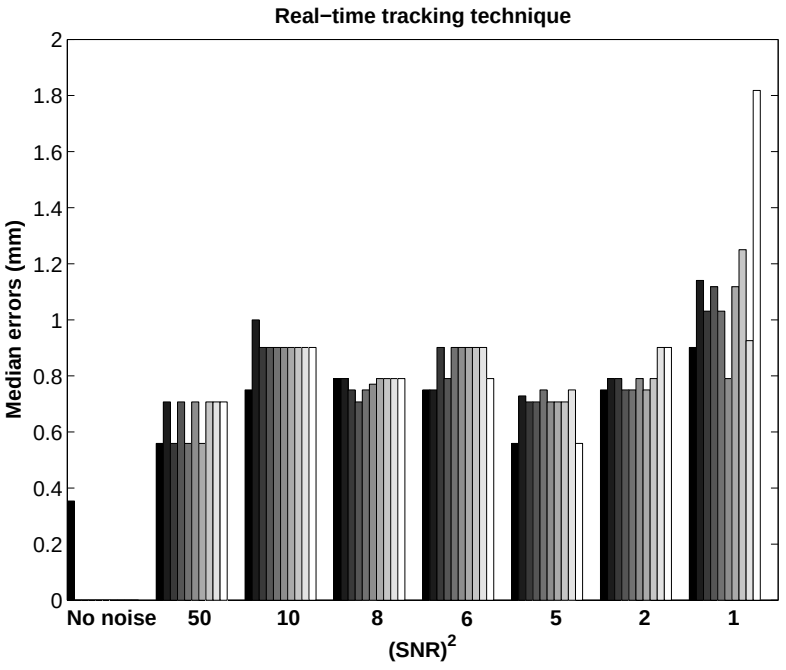

(b)

FIGURE 5.10: Median errors per electrode with respect to the gold standard, for clinical X-ray sequences for the uncorrupted and the seven levels of SNR. Median errors are illustrated only for the successfully tracked CS electrodes, using (a) the Tracked-PCA technique and (b) the Real-time tracking technique. Successfully tracked electrodes are those with less than 2mm accuracy. Different grey scale colour bars are used to distinguish the CS catheter electrodes, starting from the proximal (black colour) and moving to the distal electrode (white colour).

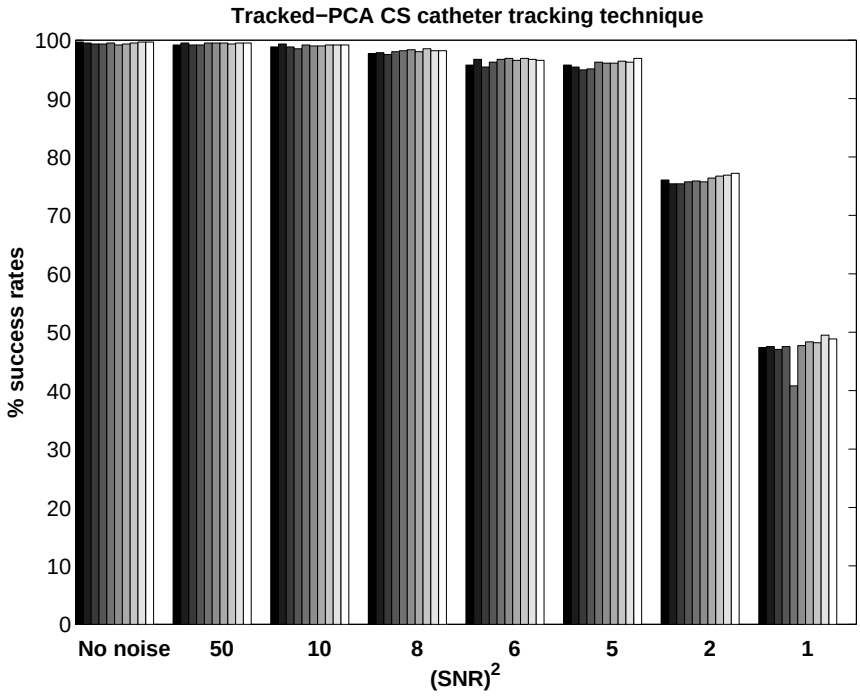

(a)

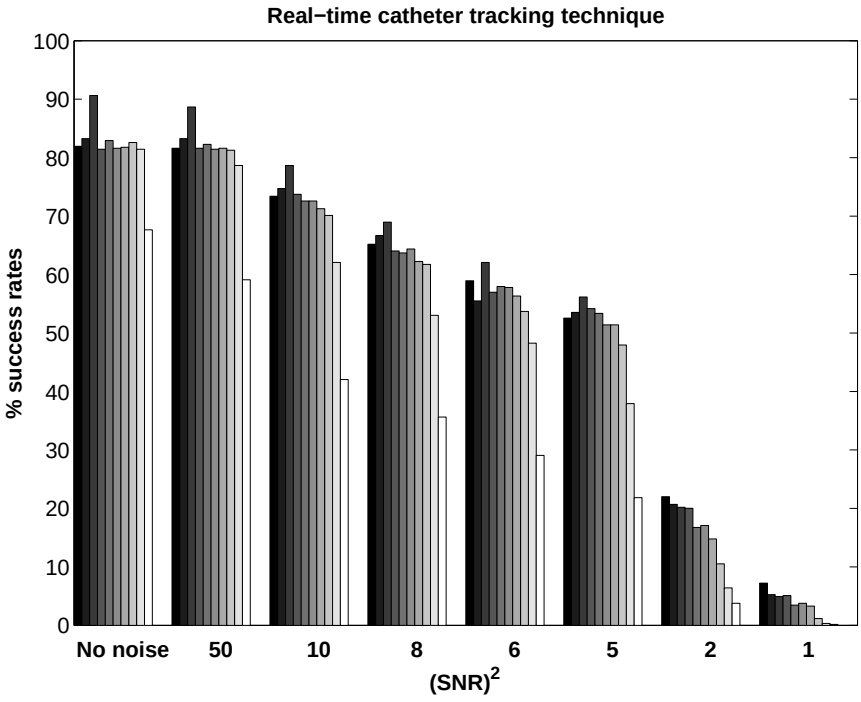

(b)

FIGURE 5.11: (a) Tracked-PCA CS catheter tracking technique percentage success rates (%). (b) Real-time tracking technique percentage success rates (%) for the eight different levels of SNR. Success cases are considered the ones where the median error per electrode is below 2 mm.

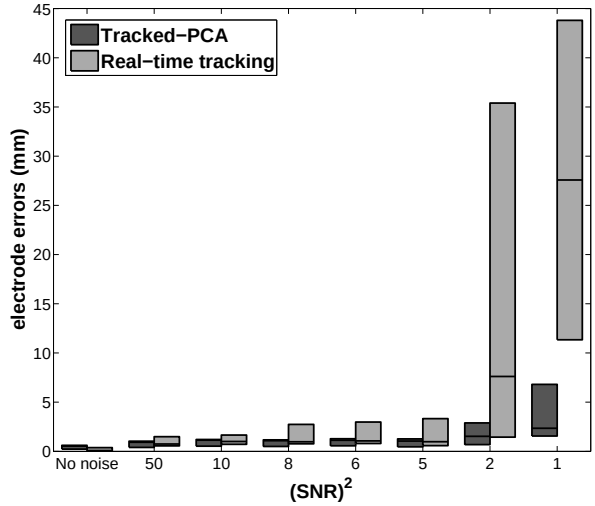

(a)

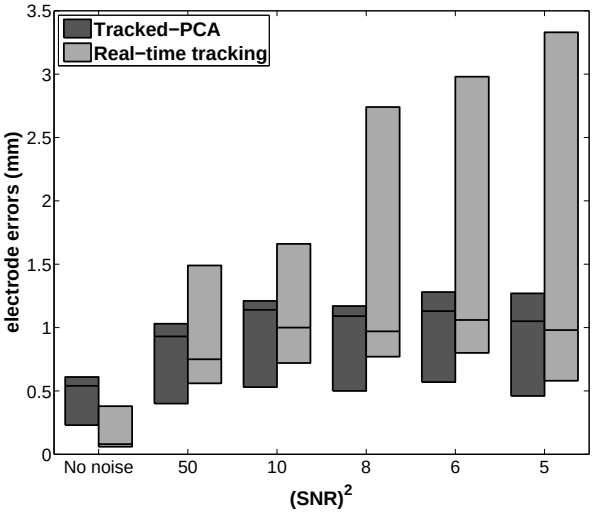

(b)

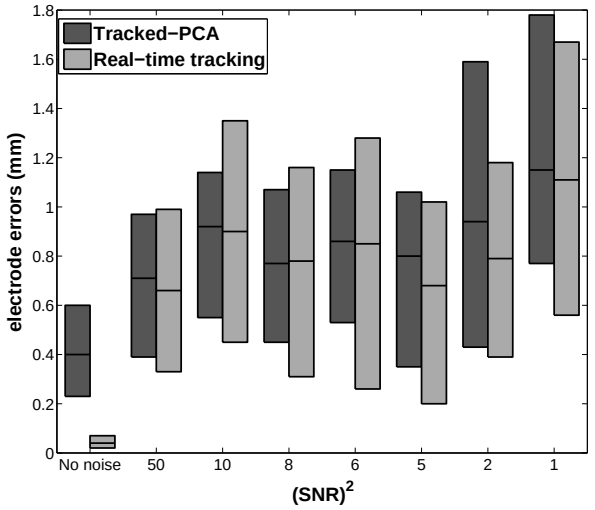

(c)

FIGURE 5.12: Illustration of the 25^{th} percentile, median and 75^{th} percentile values for the Tracked-PCA and Real-time tracking techniques over (a) all CS catheter electrodes in the data sets for each noise level, (b) all CS catheter electrodes in the data sets for noise levels up to SNR values of $\sqrt{5}$ and (c) only successfully tracked CS catheter electrodes, for each noise level. The purpose of (b) was to exclude larger errors in the graphs, allowing better illustration of the results.

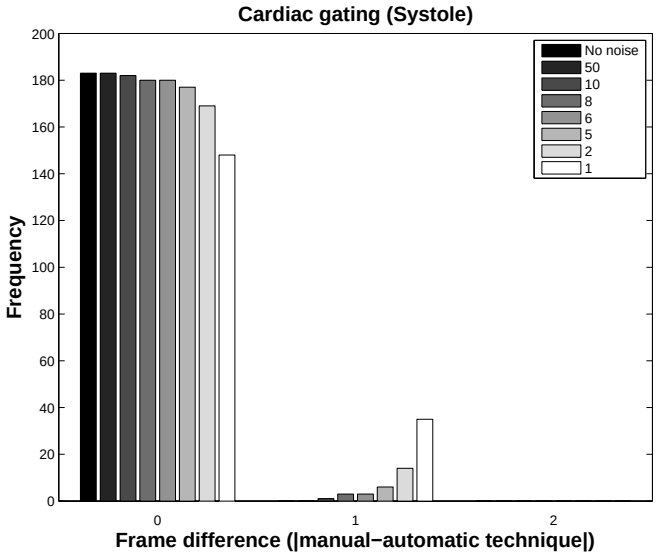

(a)

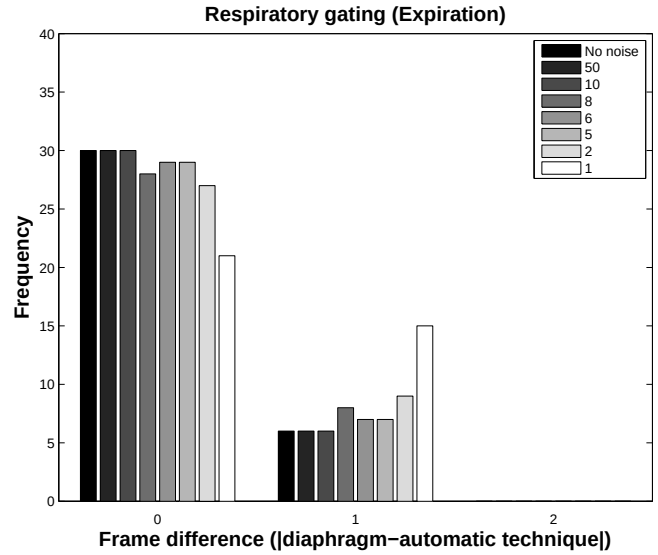

(b)

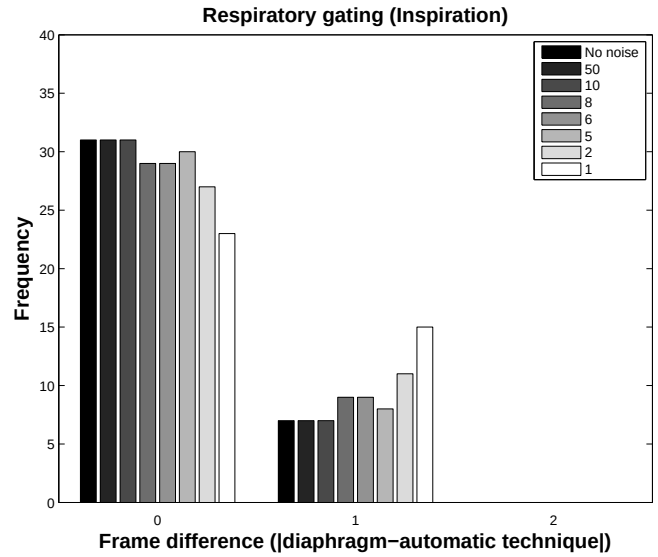

(c)

FIGURE 5.13: Frequency distributions of frame difference errors for (a) cardiac gating, (b) EX gating, and (c) EI gating for the uncorrupted and all seven different SNR^2 X-ray images using the Tracked-PCA method.

TABLE 5.7: Misdetection of peaks/troughs. Number of extra/fewer detected gating frames for all automatic techniques over all gating tasks (end-systolic gating, EX, EI).

Overall extra/fewer peaks or troughs for five clinical sequences			
	Tracked-PCA technique		
SNR	End-systolic gating	EX gating	EI gating
$\sqrt{50}$	0/0	0/0	0/0
$\sqrt{10}$	0/0	0/0	0/0
$\sqrt{8}$	0/0	0/0	0/0
$\sqrt{6}$	0/0	0/0	0/0
$\sqrt{5}$	0/0	0/0	0/0
$\sqrt{2}$	0/0	0/0	0/0
$\sqrt{1}$	0/0	0/1	0/1

Execution time. Regarding the algorithm's performance, the execution time for the retrospective experiments was around 0.0033 seconds per frame and for the experiments in near-real time, depending on the step size, the execution time was between 0.06 and 0.1 seconds per frame, all running in Matlab on Windows 7 with a 3.4 GHz Intel Core i7 CPU and 8 GB of RAM.

5.4.3 Hierarchical manifold learning-based technique

5.4.3.1 Retrospective method in normal dose images

FV filter and morphological dilation output images. Figure 5.14a gives an illustration of the output of the thresholded FV filter response, $I_{1,1}$, of the first frame of one example X-ray sequence, Case 2, after the application of the threshold level and the morphological opening, overlaid with the corresponding X-ray image. Figure 5.14b illustrates the image output, $I_{3,1}$, overlaid with the corresponding X-ray image for the first frame of the same example case.

Example of cardiac and respiratory traces. For respiratory gating validation, a plot of the respiratory trace obtained using the HML-based method for Case 2 is illustrated in Figure 5.15a as a solid black line. The diaphragm/heart border tracking is shown as a dashed-dot black line. The results of the cardiac gating validation are shown in a dashed-dot black line in Figure 5.15b for the first 30 frames for the same case. The plotted vertical black lines correspond to the gold standard end-systolic frames.

Comparative quantitative validation. It is important to investigate whether the new HML-based technique is superior to the previously presented retrospective Tracked-PCA gating approach (Section 5.4.2). Therefore, for both cardiac and respiratory gating, the absolute frame difference was computed between the HML-based method and the gold standard methods on the normal dose images. Specifically, end-systolic, EX and EI frames were recorded from the

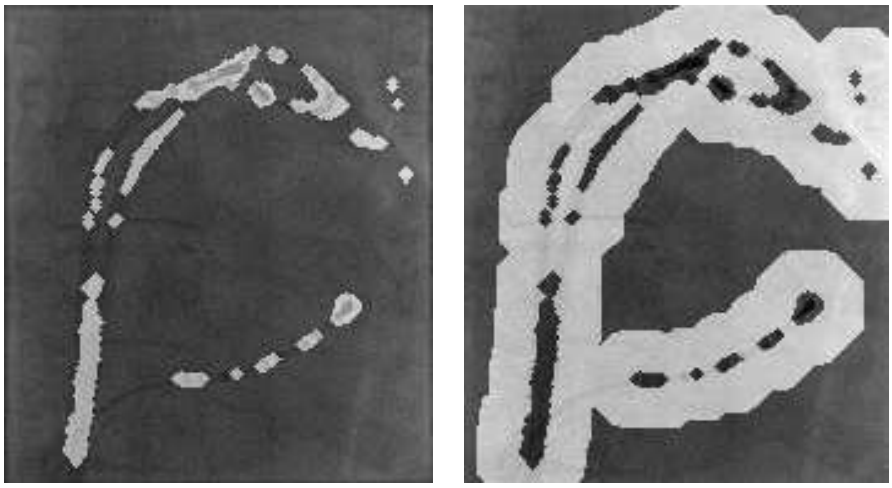

(a) (b)

FIGURE 5.14: (a) Image output of the FV filter followed by morphological opening, $I_{1,1}$, overlaid with the corresponding X-ray image for Case 2. (b) Image output, $I_{3,1}$, overlaid with the corresponding X-ray image for Case 2.

TABLE 5.8: Misdetection of peaks/troughs. Number of extra/fewer detected gating frames for all automatic techniques (HML-based technique and Tracked-PCA technique) over all gating tasks (end-systolic, EX, EI gating).

Overall extra/fewer peaks or troughs for ten clinical sequences			
Automatic technique	End-systolic gating	EX gating	EI gating
HML-based	3/2	0/0	0/0
Tracked-PCA	0/0	0/0	0/0

HML-based and gold standard methods and their corresponding absolute frame differences were computed.

The results can be seen in the frequency distribution bar charts, i.e. the number of peaks or troughs with 0, 1 or 2 frames separation from the gold standard, in Figures 5.16a, 5.16b and 5.16c for EX, EI and end-systolic gating, respectively. The Tracked-PCA results are also shown on the figures for comparison. Results illustrate that the HML-based method is faultless in EX and EI gating and outperforms the Tracked-PCA technique. While the Tracked-PCA technique outperforms the HML-based technique in cardiac gating, it relies on the tracking of a specific catheter, the CS catheter. The proposed HML-based technique does not depend on any particular catheter being present in the X-ray images and requires no knowledge of catheter geometry.

Table 5.8 summarises the number of false positives and false negatives (i.e. extra/fewer detected peaks/troughs) over all processed sequences for both techniques. Table 5.9 displays the percentage success rates. Percentage success rates were computed for end-systolic, EX and EI gating for both automatic-gating techniques.

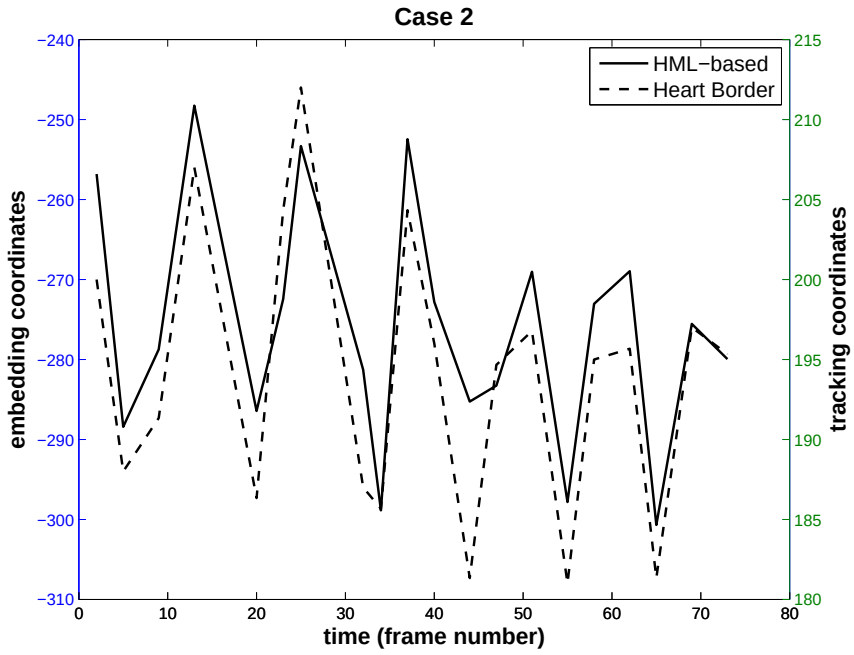

(a)

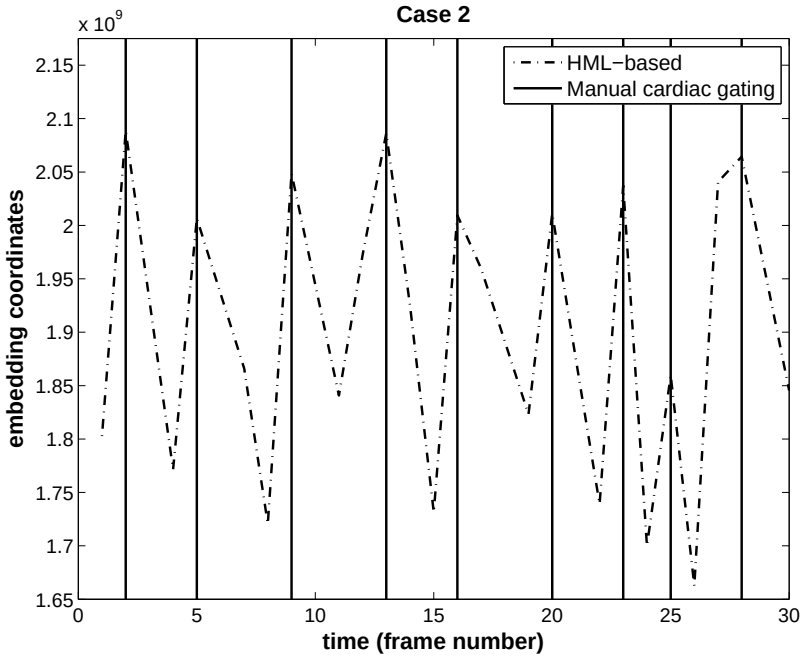

(b)

FIGURE 5.15: (a) Graphical representation of the obtained respiratory trace with X-ray frame number for the HML-based method, illustrated in a solid black line. The heart border tracking (gold standard) is shown in a dashed-dot black line. The green y-axis scale corresponds to the gold standard trace while the blue one corresponds to the trace obtained using the automatic technique. (b) The cardiac trace obtained is illustrated for the same example case. The vertical black lines are the gold standard identification of end-systole.

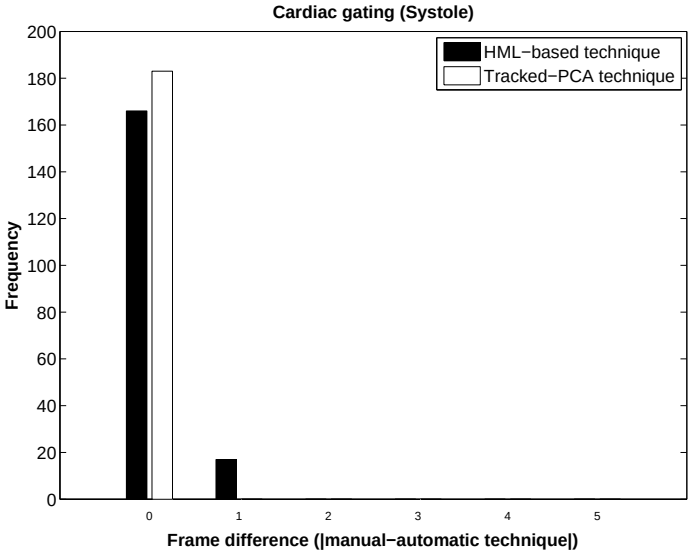

(a)

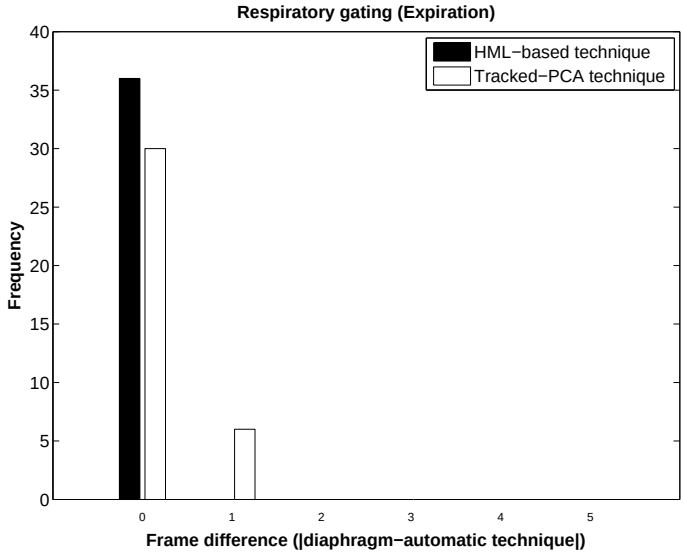

(b)

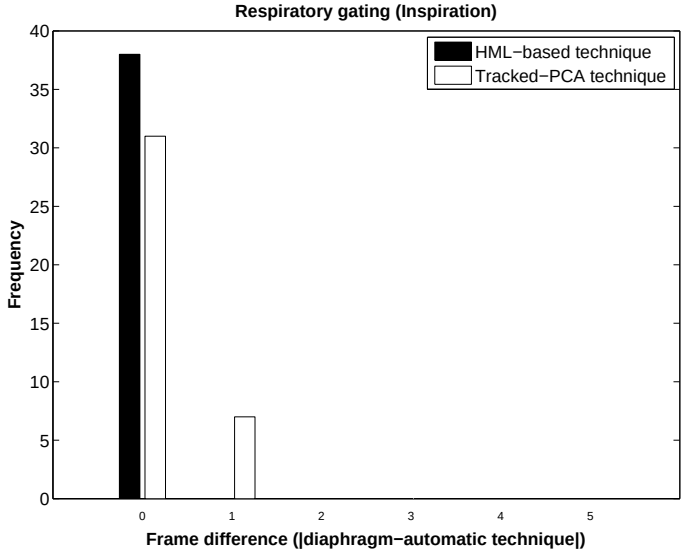

(c)

FIGURE 5.16: Frequency distributions of frame difference errors for (a) end-systolic (b) EX, (c) EI gating and gating. Results are illustrated for the HML-based method and the Tracked-PCA method.

TABLE 5.9: Percentage success rates for all automatic-gating techniques based on their potential clinical application to 3D catheter reconstruction and motion gating of 3D rotational X-ray angiography sequences/ to motion compensation. Percentage success is defined as the proportion of gold standard gating frames that are matched within the allowable gating error by their corresponding automatically detected gating frames.

Success rates (%)			
Automatic technique	End-systolic gating	EX gating	EI gating
HML-based	90.7/-	100.0/100.0	100.0/100.0
Tracked-PCA	100.0/-	86.9/100.0	92.1/100.0

TABLE 5.10: Misdetection of peaks/troughs. Number of extra/fewer detected gating frames for all automatic techniques over all gating tasks (end-systolic, EX, EI gating).

Overall extra/fewer peaks or troughs for ten clinical sequences			
HML-based technique			
SNR	End-systolic gating	EX gating	EI gating
$\sqrt{50}$	3/2	0/0	0/0
$\sqrt{10}$	3/2	0/0	0/0
$\sqrt{8}$	3/3	0/0	0/0
$\sqrt{6}$	3/4	0/0	0/0
$\sqrt{5}$	4/5	0/0	0/0
$\sqrt{2}$	4/6	0/0	0/0
$\sqrt{1}$	8/8	0/0	0/0

5.4.3.2 Retrospective method in very low dose images

For both cardiac and respiratory gating, the frame difference was computed between the HML-based method and the gold standard methods. This was tested on the 10 monoplane RFA X-ray sequences for the normal dose and each of the 7 different SNR X-ray sequences, comprising a total of 5280 experiments. The results are illustrated in Figure 5.17. Table 5.10 summarises the number of false positives and false negatives (i.e. extra/fewer detected peaks/troughs) over all the processed sequences for the seven different SNR X-ray sequences for all gating techniques.

Execution time. Regarding the algorithm's performance, the execution time was 1.1 seconds per frame running in Matlab on Windows 7 with a 3.4 GHz Intel Core i7 CPU and 8 GB of RAM.

5.4.4 Masked-PCA technique

5.4.4.1 Retrospective method in normal dose images

FV filter and mask output. Figure 5.18a gives an illustration of the output of the thresholded FV filter response, $R_{1,1}$, of the first frame of one example X-ray sequence, after the

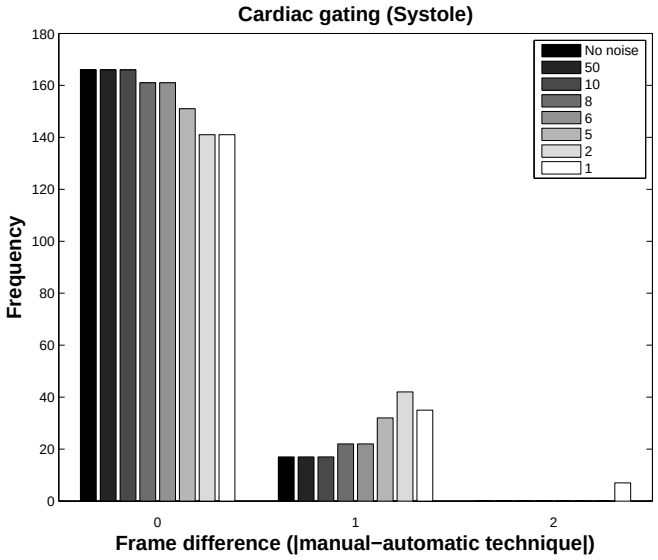

(a)

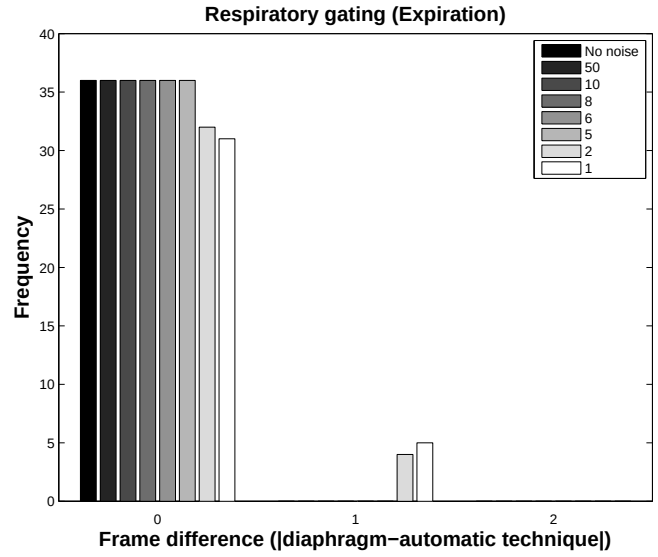

(b)

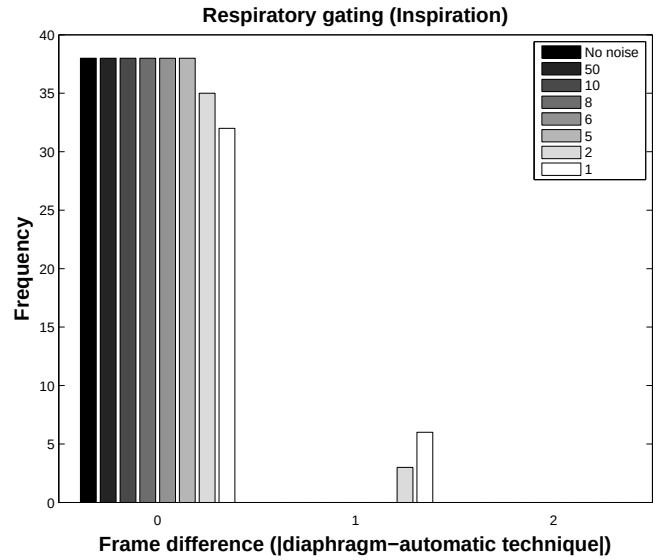

(c)

FIGURE 5.17: Frequency distributions of frame difference errors for (a) cardiac gating, (b) EX gating and (c) EI gating for the uncorrupted and all seven different SNR^2 X-ray images using the HML-based method.

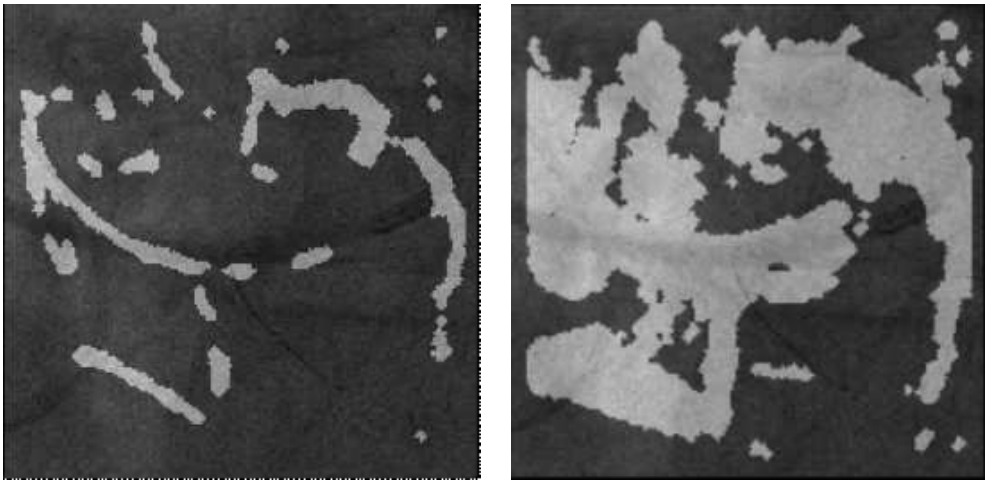

(a) (b)

FIGURE 5.18: (a) Thresholded output of the FV filter followed by morphological operations, $R_{1,1}$, overlaid with the corresponding X-ray image for one example CRT case. (b) Mask output, R_2, overlaid with the corresponding X-ray image of the same example case.

application of the threshold level and the morphological operations, overlaid with the corresponding X-ray image (Section 3.3.2.1). Figure 5.18b illustrates the mask, R_2, overlaid with the corresponding X-ray image for the first frame of the same example case (Section 3.3.2.2).

Example of cardiac and respiratory traces. Three example results of the cardiac gating validation are shown in Figures 5.19a, 5.20a and 5.21a for the first 30 frames of three different patient cases. The Masked-PCA results are shown in dashed-dot black lines. The plotted vertical black lines correspond to the gold standard end-systolic frames. Respiratory gating examples are shown in Figures 5.19b, 5.20b and 5.21b for the same patient cases. The Masked-PCA results are shown in solid black lines. The diaphragm/heart border tracking (gold standard) results are shown in dashed-dot black lines.

Comparative quantitative validation. For both cardiac and respiratory gating, the absolute frame difference was computed between the Masked-PCA method and the gold standard methods. The results can be seen in the frequency distribution bar charts, i.e. the number of peaks or troughs with 0, 1, 2, 3, 4 or 5 frames separation from the gold standard, in Figures 5.22a–c for end-systolic, EX and EI gating, respectively over all 28 X-ray sequences. The results of the HML-based method and the phase correlation method are also illustrated to allow comparison. The results illustrate that the proposed Masked-PCA technique outperforms the phase correlation technique for all three gating tasks, and the previously developed HML-based technique for the cardiac gating task. The HML technique outperforms by one frame the Masked-PCA technique for the EX and EI gating tasks.

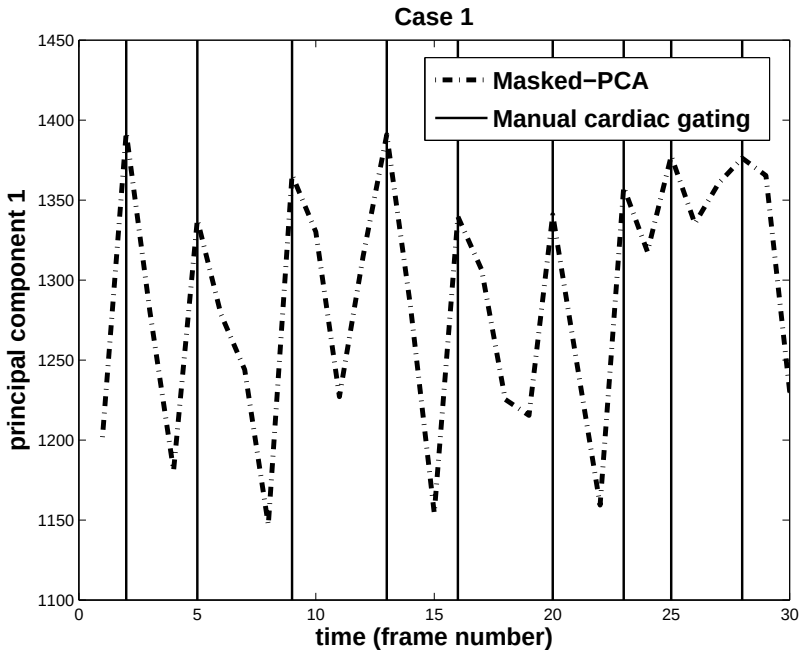

(a)

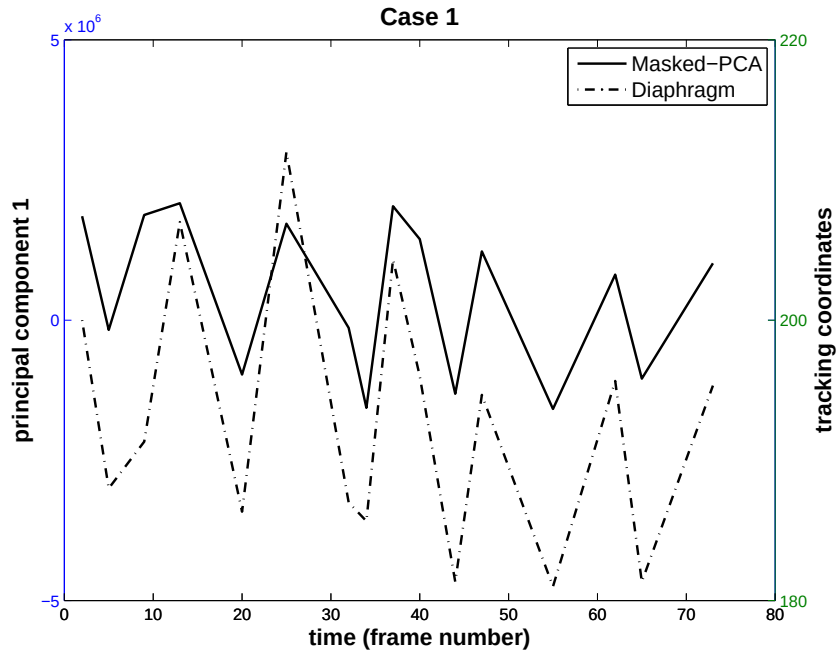

(b)

FIGURE 5.19: (a) Graphical representation of cardiac phase obtained after applying the Masked-PCA method (dashed-dot black line) for the first 30 frames for patient Case 1. The vertical black lines are the gold standard identification of end-systole. (b) The respiratory trace obtained after applying the Masked-PCA method is illustrated in a solid black line for the same patient case. The diaphragm tracking (gold standard) is also shown in a dashed-dot black line. In (b) the green y-axis scale corresponds to the gold standard trace while the blue one corresponds to the trace obtained using the automatic technique.

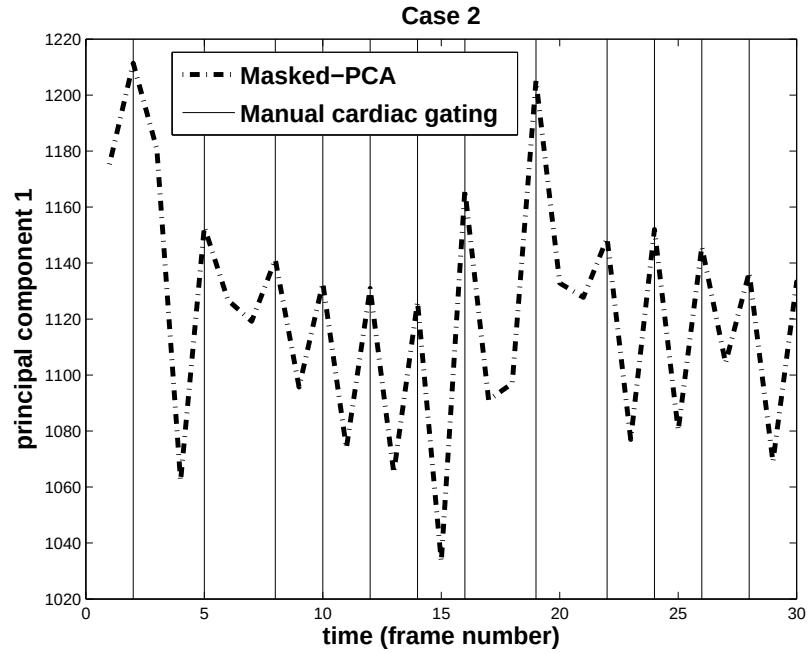

(a)

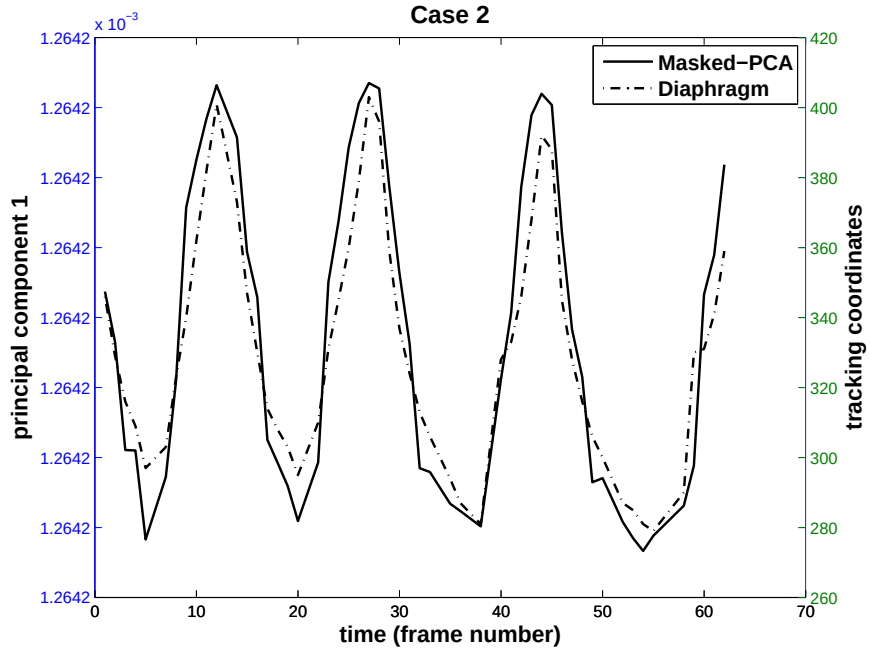

(b)

FIGURE 5.20: Graphical representations of cardiac and respiratory phases for Case 2. The meaning of the figures is as in the caption to Figure 5.19.

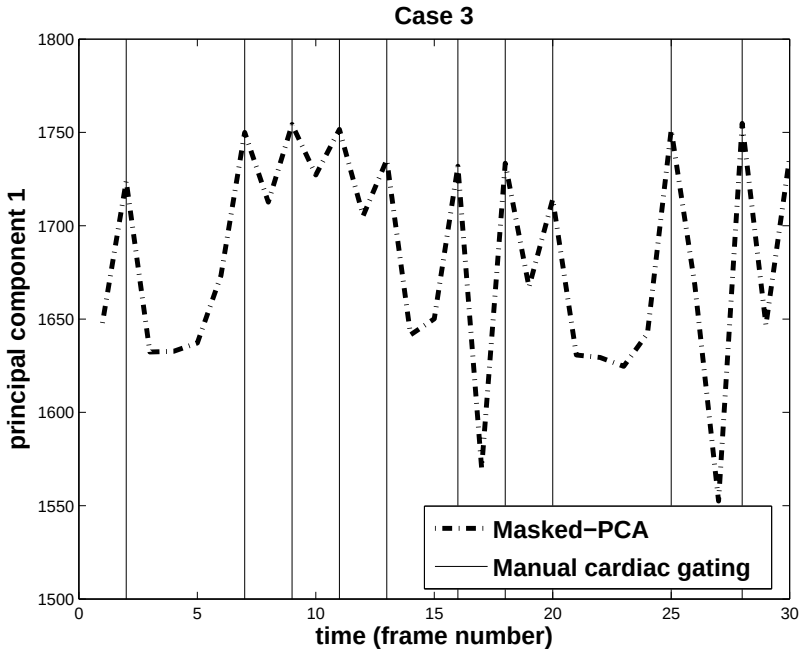

(a)

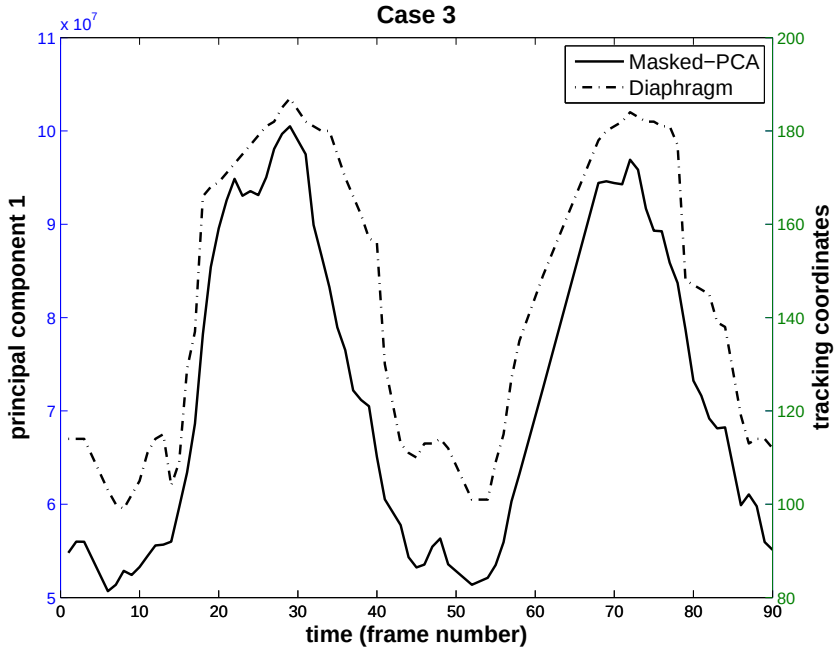

(b)

FIGURE 5.21: Graphical representations of cardiac and respiratory phases for Case 3. The meaning of the figures is as in the caption to Figure 5.19.

TABLE 5.11: Misdetection of peaks/troughs. Number of extra/fewer detected gating frames for three automatic techniques (Masked-PCA technique, HML technique and Phase correlation method) over all gating tasks (end-systolic, EX and EI gating).

Overall extra/fewer peaks or troughs			
Automatic technique	end-systolic gating	EX gating	EI gating
Masked-PCA	11/0	0/0	1/0
HML	19/0	0/0	1/0
Phase correlation	84/18	5/9	8/4

TABLE 5.12: Percentage success rates for all automatic-gating techniques based on their potential clinical application to 3D catheter reconstruction and motion gating of 3D rotational X-ray angiography sequences/ to motion compensation. Percentage success is defined as the proportion of gold standard gating frames that are matched within the allowable gating error by their corresponding automatically detected gating frames.

Success rates (%)			
Automatic technique	end-systolic gating	EX gating	EI gating
Masked-PCA	99.6/-	97.9/100.0	97.0/100.0
HML	94.0/-	100.0/100.0	97.9/100.0
Phase correlation	22.3/-	40.9/100.0	27.9/100.0

TABLE 5.13: Percentage success rates computed individually for each type of procedure based on their potential clinical application to 3D catheter reconstruction and motion gating of 3D rotational X-ray angiography sequences.

Success rates (%) using the Masked-PCA/HML-based techniques			
Type of procedure	end-systolic gating	EX gating	EI gating
RFA ablation/no contrast agent	98.3/90.7	97.0/100.0	97.5/96.7
CRT (pacing)/no contrast agent	100.0/94.6	100.0/100.0	96.6/100.0
CRT (CS ang.)/contrast agent	100.0/96.7	96.7/100.0	96.9/97.0

Table 5.11 summarises the number of false positives and false negatives (i.e. extra/fewer detected peaks/troughs) over all processed sequences for all techniques. Table 5.12 displays the percentage success rates. Percentage success rates were computed for end-systolic, EX and EI gating for all automatic-gating techniques. To illustrate the performance of the Masked-PCA technique with and without the presence of contrast agent, % success rates were computed individually for the RFA ablation procedures, where contrast agent was not used, the 9 CRT (pacing) sequences, where again contrast agent was not used, and the 9 CRT (CS angiography) sequences, where contrast agent was used. The results are given in Table 5.13. In the same table, the performance of the HML-based technique with and without the presence of contrast agent is also shown for comparison. The performance of the techniques is based on their potential clinical application to 3D catheter reconstruction and motion gating of 3D rotational X-ray angiography sequences. The performance of the techniques to motion compensation is not illustrated as results are 100.0% for all methods and all gating tasks in all procedure types.

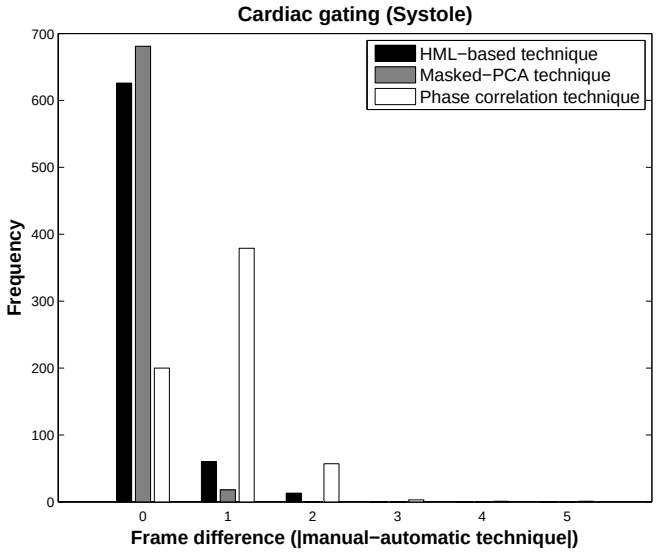

(a)

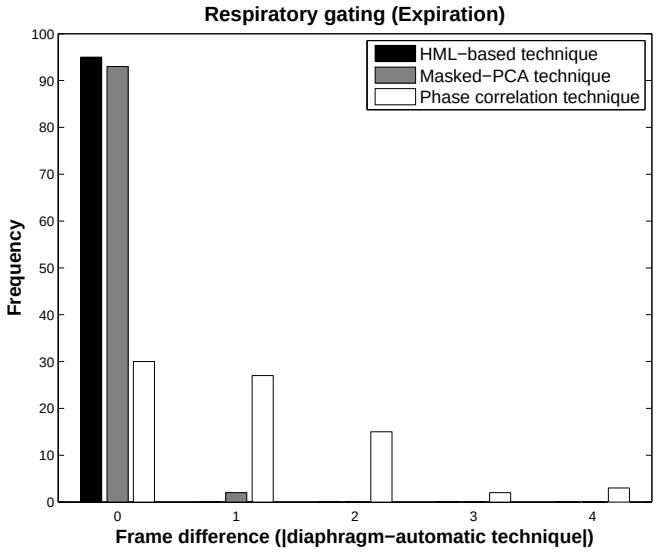

(b)

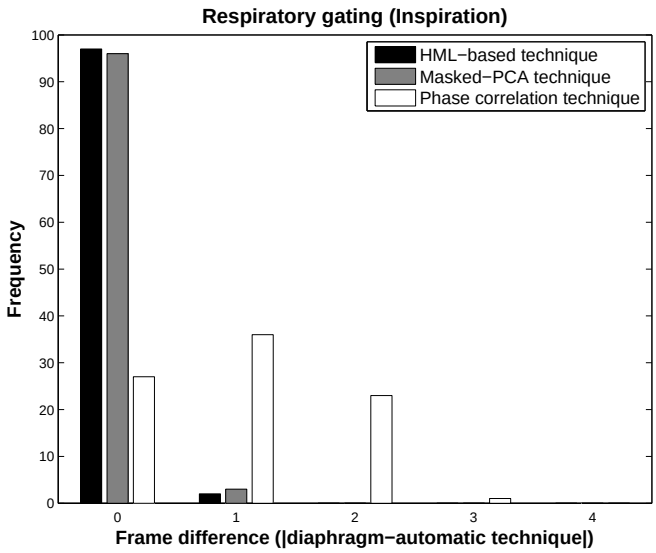

(c)

FIGURE 5.22: Frequency distributions of frame difference errors for (a) end-systolic, (b) EX and (c) EI gating of the 28 EP procedures. Results are illustrated for Masked-PCA (grey colour), HML (black colour) and Phase correlation (white colour).

Statistical significance. An f-test was conducted under the null hypothesis that there was no difference between the currently proposed Masked-PCA technique and the previous HML-based technique. The f-test was done on the frame differences of each of the techniques and was conducted for end-systolic, EX and EI, including only the peaks/troughs that were detected by both methods. For cardiac gating the proposed Masked-PCA technique was found to have significantly lower errors than the HML technique ($p < 0.05$). For EX and EI, the p-values were 0.32 and 0.16, respectively. This means that there is no statistically significant difference between the HML-based technique and Masked-PCA technique for respiratory gating.

5.4.4.2 Retrospective method in very low dose images

Comparative quantitative validation. The Masked-PCA gating technique was validated on 10 EP clinical fluoroscopy sequences from patients who underwent RFA procedures for the treatment of AF. Cardiorespiratory gating was performed on the simulated low dose X-ray sequences. As comparative techniques, cardiorespiratory gating was also performed using both the previously evaluated HML-based technique (Section 5.4.3) and the Tracked-PCA (Section 5.4.2) technique. Comparison with the Tracked-PCA technique is now possible because the evaluation is restricted to the images containing the CS catheter.

The results are illustrated in Figures 5.23a–c for the Tracked-PCA, HML-based and Masked-PCA techniques, respectively. Table 5.14 summarises the number of false positives and false negatives (i.e. extra/fewer detected peaks or troughs) over the same 10 processed sequences for the 7 different SNR X-ray sequences for all gating techniques. Figure 5.24 displays the percentage success rates using the 3D reconstruction and rotational gating objective (<0.1s gating error). The results demonstrate that the automatic methods are robust and accurate even on the lowest SNR simulated X-ray sequences. Specifically, for the low SNR values of $\sqrt{2}$, end-systolic, EX and EI success rates of 89.1%, 88.8% and 86.8%, respectively, were achieved using the Masked-PCA method. Similarly, gating success rates were computed and found to be 77.0%, 88.8% and 92.1% using the HML-based and 92.9%, 73.7% and 71.8%, using the Tracked-PCA technique, for end-systolic, EX and EI gating, respectively. Success rates using the motion compensation objective (<1s gating error) were all 100% at all noise levels.

Execution time. Regarding the algorithm's performance, the execution time was around 0.0048 seconds per frame running in Matlab on Windows 7 with a 3.4 GHz Intel Core i7 CPU and 8 GB of RAM.

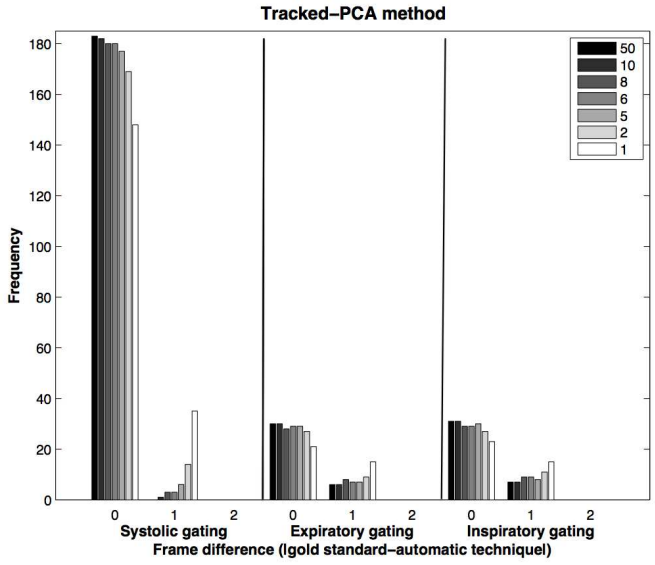

(a)

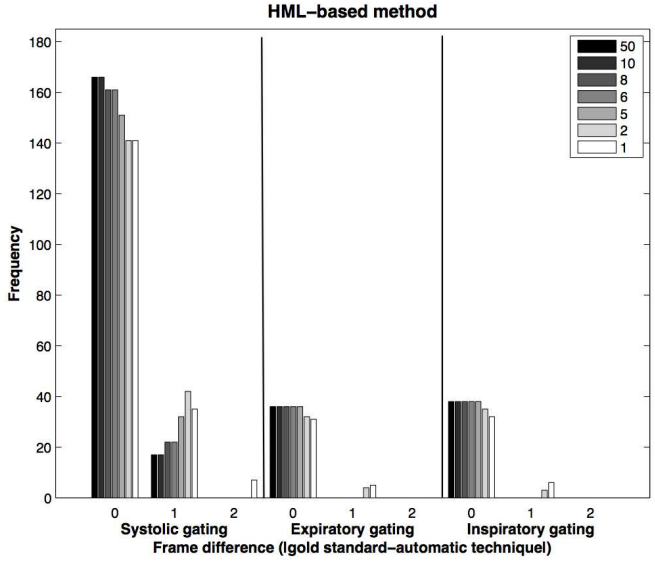

(b)

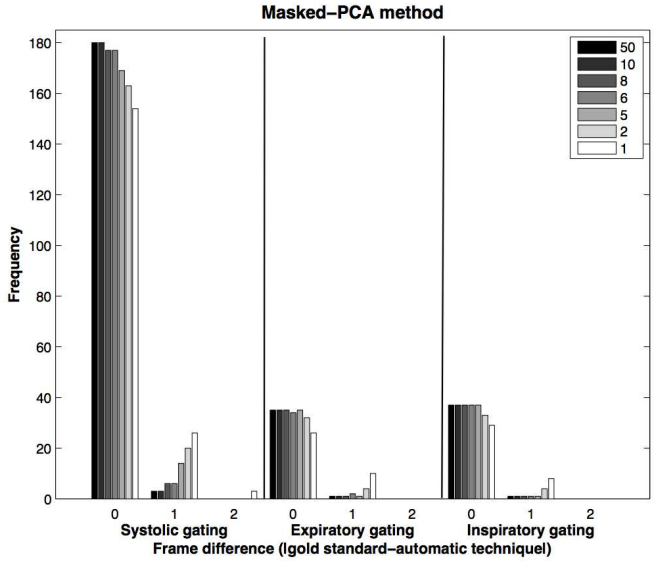

(c)

FIGURE 5.23: Frequency distributions of frame difference errors for end-systolic, EX and EI gating using (a) Tracked-PCA, (b) HML-based and (c) Masked-PCA techniques for each of the 7 different SNR^2 RFA X-ray sequences.

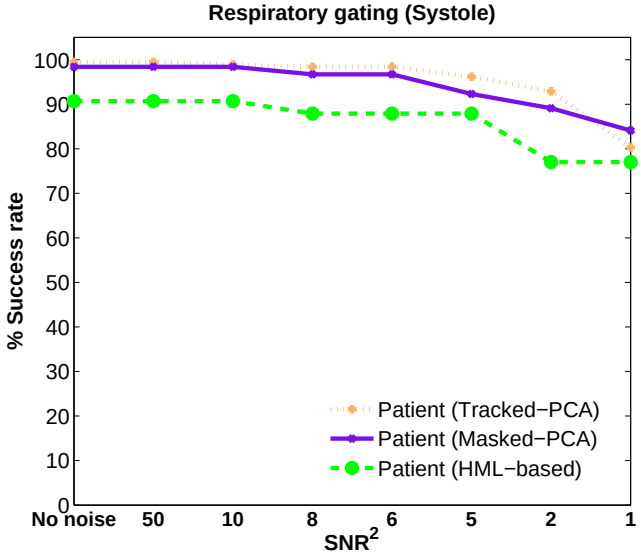

(a)

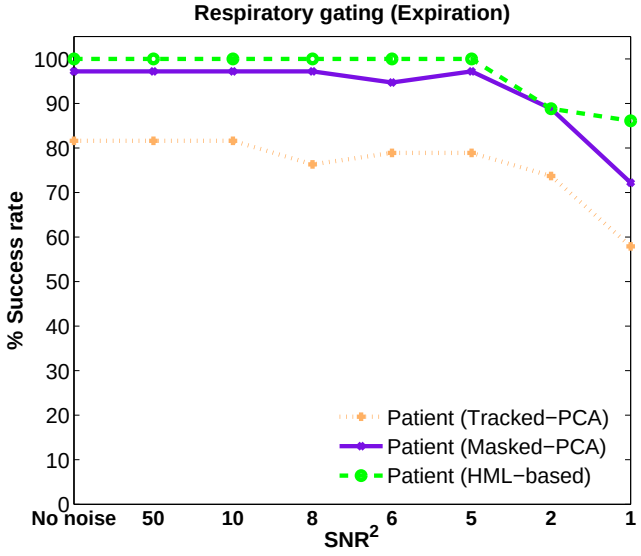

(b)

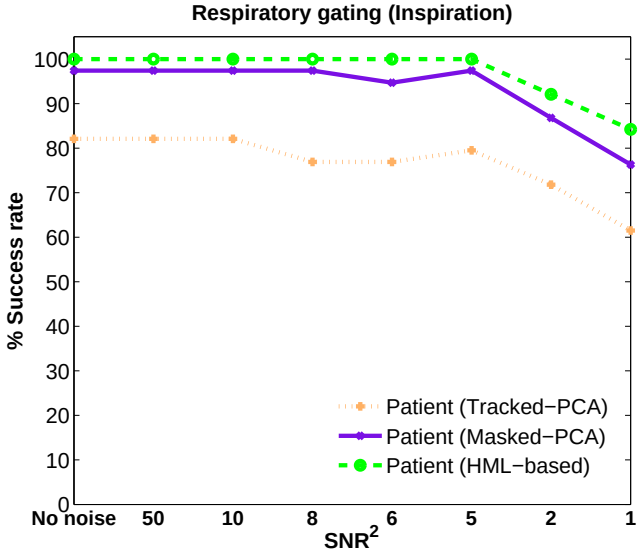

(c)

FIGURE 5.24: (a) End-systolic, (b) EX and (c) EI gating % success rates over all automatic techniques for all noise levels.

TABLE 5.14: Misdetection of peaks/troughs. Number of extra/fewer detected gating frames for all automatic techniques over all gating tasks (end-systolic, EX, EI gating).

	Overall extra/fewer peaks or troughs for 10 clinical sequences		
	Tracked-PCA	Masked-PCA	HML-based
SNR	End-systolic gating/ EX gating/ EI gating		
$\sqrt{50}$	0;0/0;0/0;0	0;0/0;0/0;0	3;2/0;0/0;0
$\sqrt{10}$	0;0/0;0/0;0	0;0/0;0/0;0	3;2/0;0/0;0
$\sqrt{8}$	0;0/0;0/0;0	0;0/0;0/0;0	3;3/0;0/0;0
$\sqrt{6}$	0;0/0;0/0;0	0;0/0;0/0;0	3;4/0;0/0;0
$\sqrt{5}$	0;1/0;1/0;1	0;2/1;1/1;0	4;5/0;0/0;0
$\sqrt{2}$	0;3/0;1/0;1	0;5/0;1/0;0	4;6/0;0/0;0
$\sqrt{1}$	0;7/1;1/1;1	0;9/1;2/1;1	8;8/0;0/0;0

5.4.5 View-angle independent technique

5.4.5.1 Application to multiplane sequence pairs at normal and low dose

Example of catheter tracking. Figure 5.30 illustrates the results of the CS catheter tracking technique on the 1^{st} image of (a) an uncorrupted example X-ray sequence and (b–f) the simulated low dose images, with SNR values of $\sqrt{50}$, $\sqrt{10}$, $\sqrt{8}$, $\sqrt{6}$ and $\sqrt{5}$, respectively.

Quantitative validation of CS catheter tracking. Figure 5.25a illustrates the CS catheter tracking median errors per electrode for patient X-ray images at normal dose and for the 5 SNR values. Errors were calculated for each electrode and are shown in different grey scale colours, starting from the proximal (black colour) and moving to the distal (white colour) electrode. For the technique to be acceptable in clinical practice, failure cases were considered to be the ones where median errors per electrode were above 2mm [93]. For a more comprehensive validation, in Figure 5.25b, median errors were calculated and are shown only for the successfully tracked CS catheter electrodes. Figure 5.26 shows the range of the values in terms of the 25^{th} percentile, median and 75^{th} percentile, over all electrodes, and for successfully tracked electrodes, for each noise level. Success rates were also calculated and are shown as percentages (%) in Figure 5.27.

Quantitative validation of cardiorespiratory motion gating. Figure 5.28 illustrates the frame difference errors in frequency distribution bar charts, i.e. the number of peaks or troughs with 0, 1 or 2 frames separation from the gold standard for the patient biplane sequences, for all gating tasks and noise levels. For a more comprehensive comparison, percentage (%) success rates for end-systolic, EX and EI gating were also calculated and are shown in Figure 5.29 for both the previously used phantom images and currently used clinical images. Using the model on unmodified clinical images for near-real time cardiorespiratory motion gating, end-systolic, EX and EI gating success rates of 100.0%, 85.7% and 92.3%, respectively, were established. Additionally, gating success rates of 80.3%, 71.4% and 69.2% were established, even at the

low SNR value of $\sqrt{5}$. To comparatively validate the technique to the Tracked-PCA method (Section 5.4.2), where the statistical model was formed from normal dose images during a calibration phase and applied to low dose images acquired from the same view-angle, % success rates from both techniques for the same sequences are illustrated on the figure. No false positives or negatives (i.e. extra/fewer detected peaks/troughs) over the processed sequences were found. Outcomes show that the technique is robust and accurate in both CS catheter tracking and motion extraction even at the lowest SNR values of $\sqrt{5}$.

Execution time. Regarding the algorithm's performance on the different experiments, depending on the step size of the optimisation, the execution time was between 0.41 and 1.43 seconds per frame running in Matlab on Windows 7 with a 3.4 GHz Intel Core i7 CPU and 8 GB of RAM.

5.5 Discussion

This chapter demonstrates the validation of the four proposed frameworks, developed and described in this thesis, on clinical datasets. The performance of the four techniques was validated for the purposes of automatic cardiorespiratory motion gating in normal and very low dose X-ray fluoroscopy images, and success rates for end-systolic cardiac gating, EI and EX respiratory gating were computed. Along with cardiorespiratory motion gating, the novel frameworks of the Tracked-PCA and View-angle independent techniques were employed to track the CS catheter throughout the X-ray sequences. The validation of the techniques for catheter tracking was also demonstrated in this chapter. For the validation of the techniques to catheter tracking, median errors per electrode with respect to the gold standard electrode positions have been established. Additionally, comparison of the techniques to other published methods, such as the phase correlation method, and dimensionality reduction methods including ICA, Laplacian eigenmaps and ISOMAP, was illustrated in this chapter. The performance of the techniques was validated on datasets acquired from patients undergoing RFA and CRT procedures. Particularly, 10 RFA monoplane clinical sequences were used for the validation of the Tracked-PCA, HML-based and Masked-PCA techniques, while 18 biplane and monoplane CRT clinical sequences were used for the validation of the HML and Masked-PCA techniques. Three additional RFA biplane clinical sequences were used for the validation of the View-angle independent technique. RFA and CRT procedures result in substantial patient and staff radiation doses due to the long fluoroscopy duration and radiation exposure [73]. Acute radiation-induced skin injuries or radiation-induced cancer are important risks associated with diagnostic and therapeutic procedures that require fluoroscopic imaging. It is necessary to minimise patient dose in order to outweigh the radiation risk by the benefit of the interventional procedure. Therefore, developing a robust-to-noise

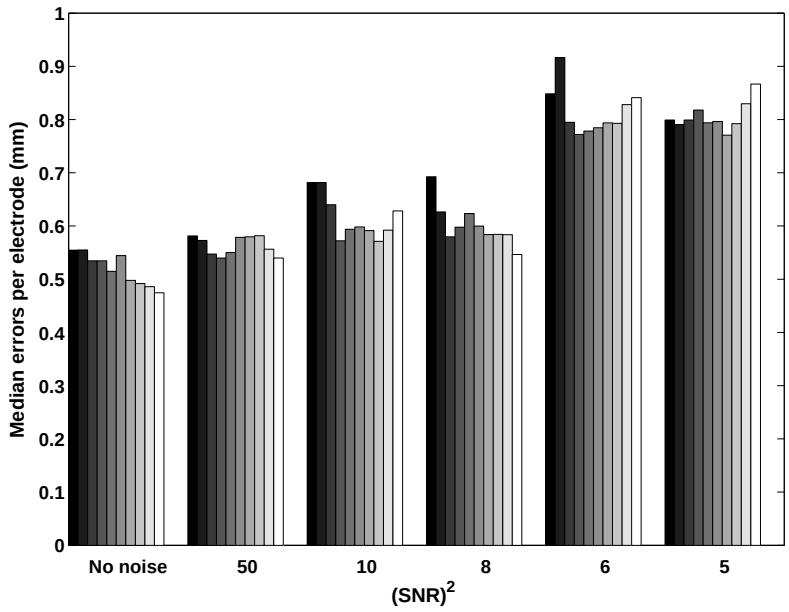

(a)

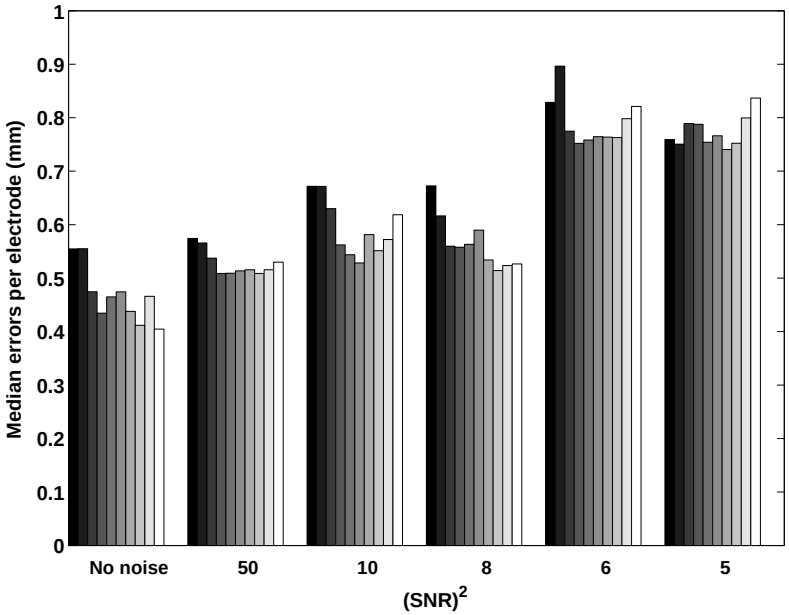

(b)

FIGURE 5.25: Median errors per electrode with respect to the gold standard, for clinical X-ray sequences for the normal dose and five levels of SNR, where median errors are illustrated for (a) all tracked CS electrodes, and (b) only for the successfully tracked CS electrodes using the View-angle independent technique. Different grey scale colour bars are used to distinguish the CS catheter electrodes, starting from the proximal (black colour) and moving to the distal electrode (white colour).

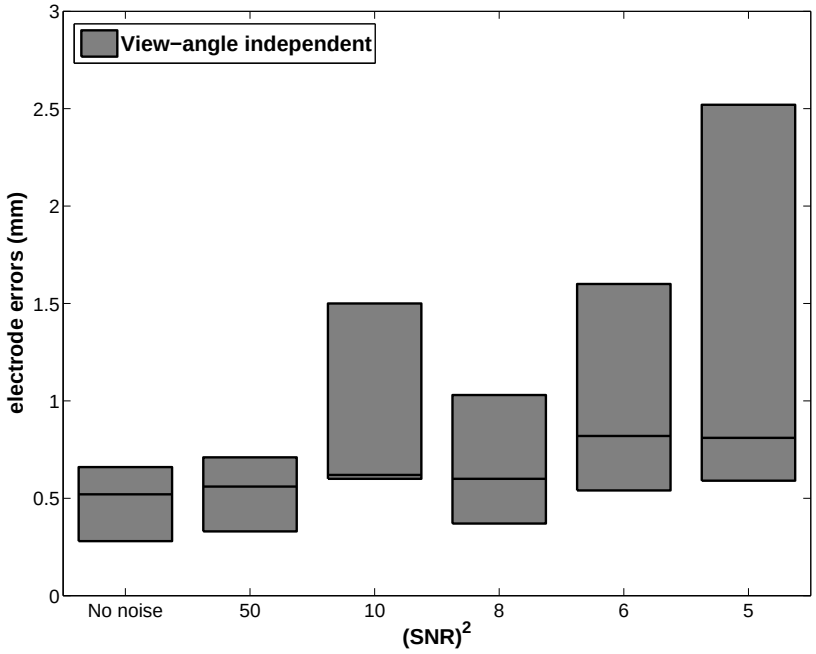

(a)

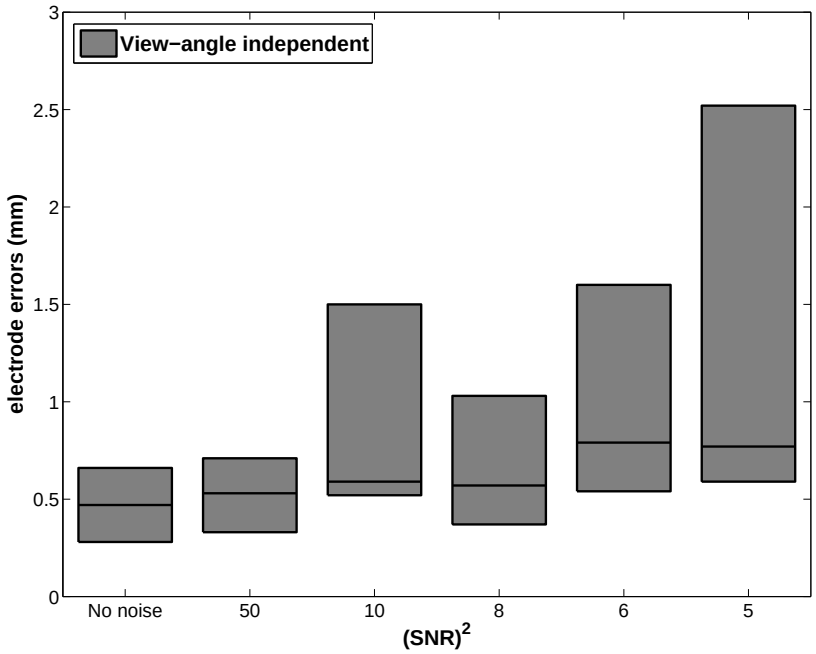

(b)

FIGURE 5.26: Illustration of the 25^{th} percentile, median and 75^{th} percentile, values over (a) all CS catheter electrodes in the data sets (b) only successfully tracked CS catheter electrodes for each noise level using the View-angle independent technique on clinical datasets.

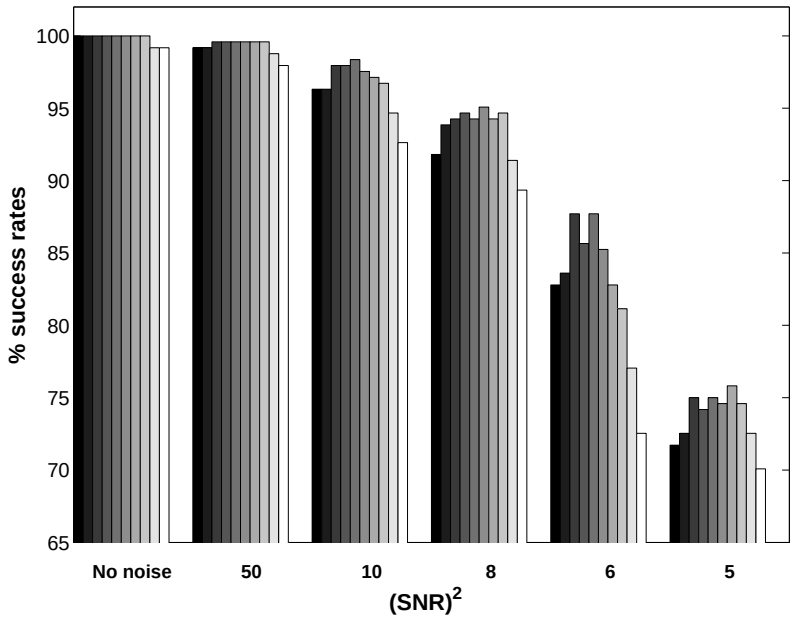

FIGURE 5.27: CS catheter tracking technique percentage success rates (%), for clinical X-ray sequences for the normal dose and five different levels of SNR using the View-angle independent technique. Success cases are considered to be the ones where the median errors per electrode are below 2mm.

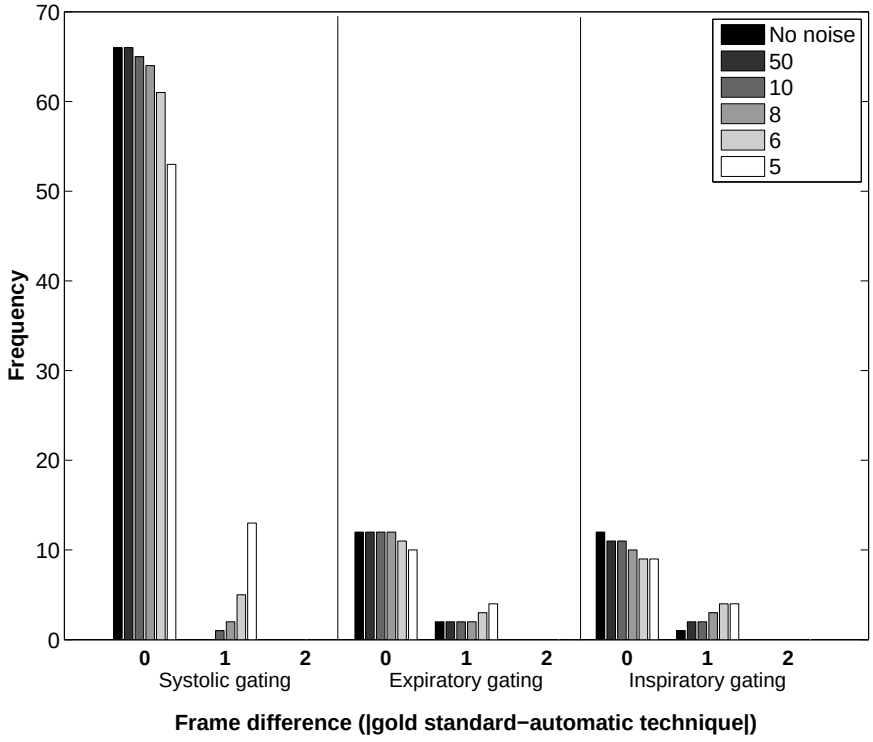

FIGURE 5.28: Distributions of frame difference errors for end-systolic, EX, and EI gating for the uncorrupted and all different levels of SNR^2 X-ray sequences using the PCA-view-angle independent technique on clinical images.

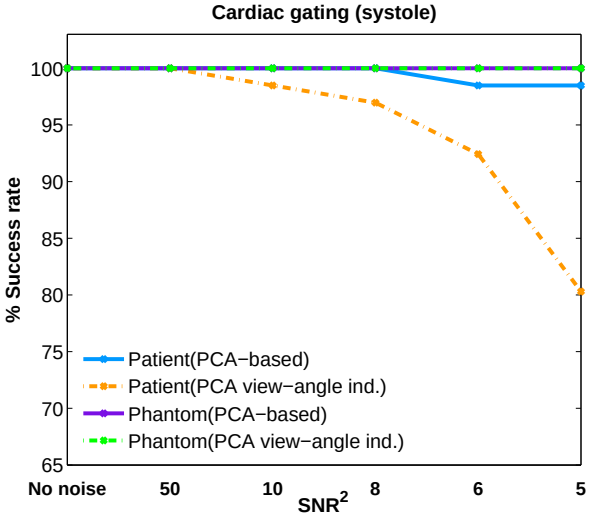

(a)

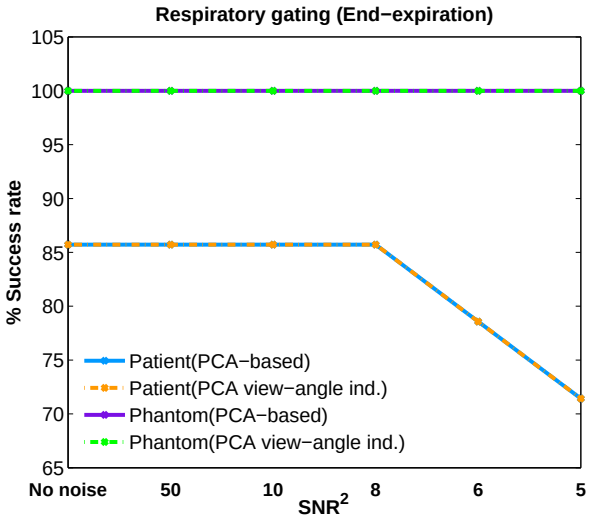

(b)

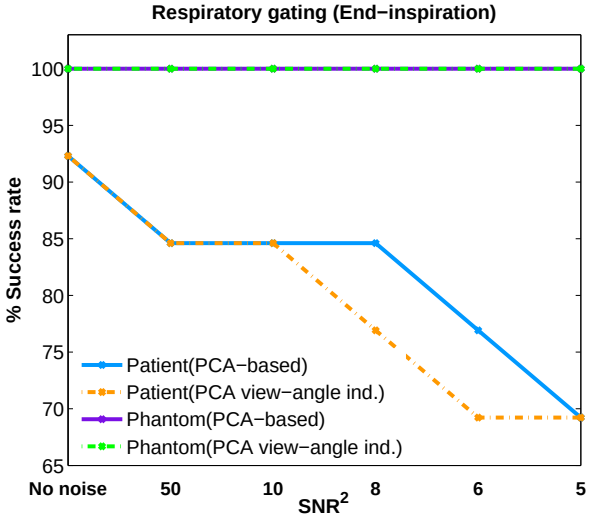

(c)

FIGURE 5.29: Percentage success rates for (a) end-systolic, (b) EX and (c) EI gating for the uncorrupted and all noise corrupted X-ray sequences compared for the PCA view-angle independent and the previous Tracked-PCA technique on patient and phantom sequences. In (a) all lines overlap at No noise and at SNR $\sqrt{50}$, the Phantom(PCA-based) and Phantom(PCA view-angle ind.) lines completely overlap and the Patient(PCA-based) overlaps with the Phantom lines at No noise and at $SNRs$ $\sqrt{50}$ to $\sqrt{8}$. In (b) the Phantom lines completely overlap, as do the Patient lines. In (c) the two phantom lines completely overlap and the Patient lines overlap at No noise and $SNRs$ $\sqrt{50}$ to $\sqrt{10}$.

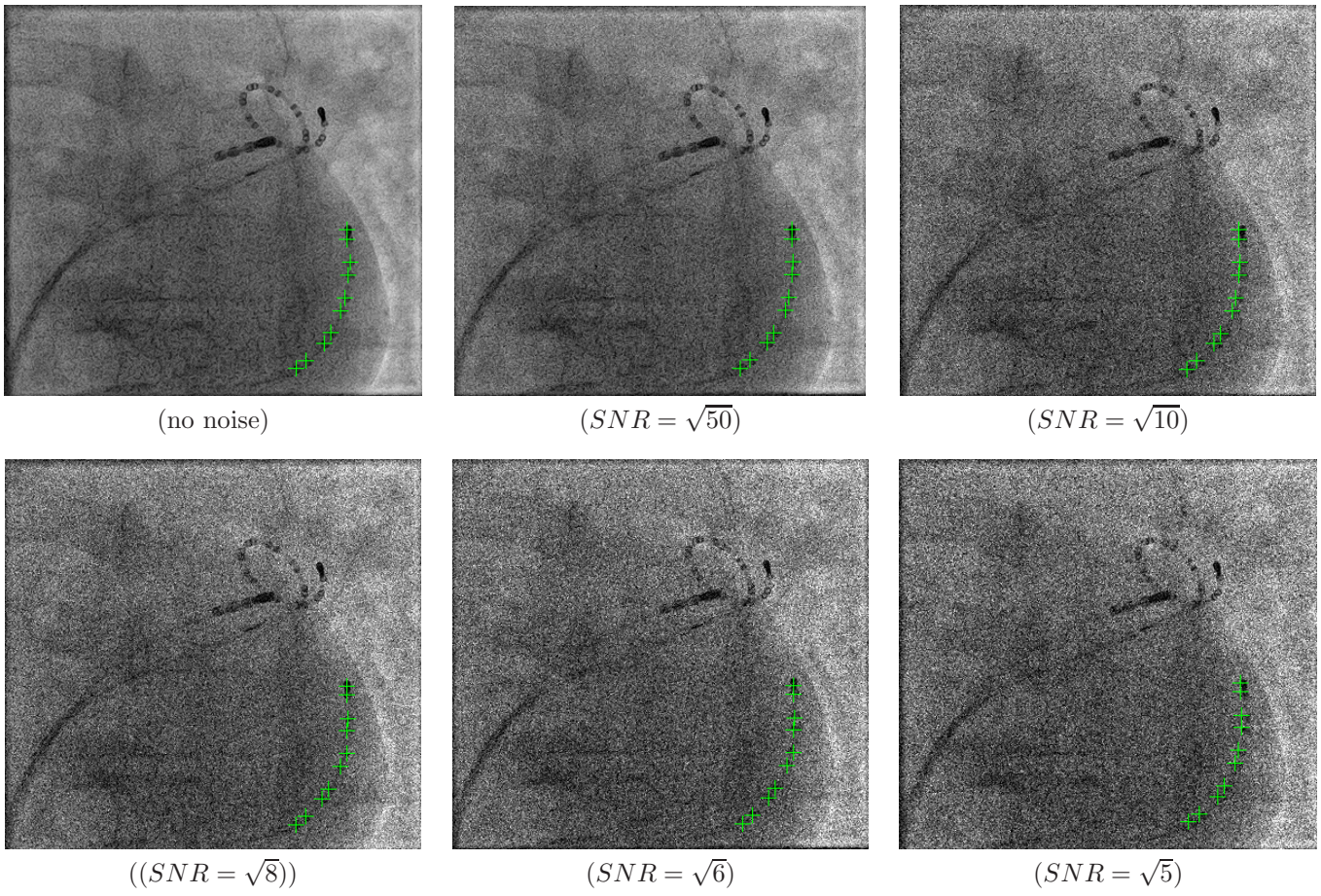

FIGURE 5.30: The View-angle independent CS catheter tracking technique is illustrated in green crosses on an uncorrupted X-ray image during the ablation stage of a procedure to treat AF; and on the same X-ray image corrupted with different levels of Poisson noise.

gating technique can potentially minimise patient exposure to radiation by allowing the use of lower dose fluoroscopy

5.5.1 Tracked-PCA technique

The application of the novel framework of the Tracked-PCA technique that involved the formation and application of a statistical model of the motion of the CS catheter, was demonstrated for automatic gating in normal and very low dose clinical X-ray fluoroscopy sequences. Using the statistical model on unmodified fluoroscopy images for retrospective image-based gating, it was demonstrated that the method is able to detect cardiac and respiratory phases from these X-ray fluoroscopy images. For the application of the technique to normal dose images, success rates for end-systolic gating, EX and EI respiratory gating were established. For the cardiac gating validation, systole was chosen as opposed to diastole for validation since the manual ground truth is more reliable for end-systole where rapid motion can be used as the visual cue. For the application of the technique to rotational gating and to phase matching for 3D reconstruction, where the motion gating accuracy objective is set to 0.1s, success rates of 100.0%, 86.9% and 92.1%, were established, for end-systolic, EX and EI gating, respectively. Therefore, in at most 14.0% of the cases over all gating tasks the technique fails to achieve the motion gating accuracy objective set in this thesis. Since both applications usually use the diastolic phases of the heart, the technique was also validated on end-diastolic cardiac gating, and success rates of 100% have been established. These experiments illustrate that the method is just as accurate on diastolic frames, so it is appropriate to use the systolic results to validate the two applications. For the application of the technique to motion compensation, where the motion gating accuracy objective is set to 1s, success rates of 100% were established for all respiratory gating tasks.

A comparative quantitative validation was performed on the ten clinical fluoroscopy sequences, to investigate whether the Tracked-PCA method was superior to simply using the Cartesian coordinates of the electrode positions alone. The tracking data for the proximal and distal electrodes were employed using the same gating technique. Results indicate that the Tracked-PCA method outperforms both of these comparative techniques for all the three gating tasks. The method was further comparatively validated by comparing it against the phase correlation technique [192]. The results indicate that the phase correlation technique performs the worst of the tested methods. For each of the X-ray imaging sequences used, X-ray imaging was performed at three frames per second. When performing measurements for frequency domain imaging at such low frame rates, the phase results can be impacted by phase drift or noise, and hence this is a possible reason for the poor performance of the phase correlation method. In general, the energy change measured by phase correlation could also be caused by the motion of catheters or contrast agent injection. As the method uses the overall motion of moving objects, the cardiac

and respiratory cycle motions detected by this method could be incorrect when the clinician manipulates the catheters or injects contrast agent.

For a more comprehensive validation, and more precisely for investigating whether the dimensionality reduction technique used (PCA) was superior to others, the technique was comparatively validated by comparing it against other dimensionality reduction techniques. These include the ICA, Laplacian eigenmaps and ISOMAP techniques. These techniques have some differences to the statistical PCA technique used for the development of the Tracked-PCA method. Firstly, the PCA is a linear dimensionality reduction technique. The technique is linear in that the new variables are a linear combination of the original. PCA is adequate if the data fits a Gaussian distribution. On the other hand, although ICA is a linear dimensionality reduction technique like PCA, the ICA is performed by assuming that the subcomponents are non-Gaussian signals and that they are statistically independent from each other. Laplacian eigenmaps and ISOMAP are non-linear dimensionality reduction techniques. While for linear dimensionality reduction techniques it is assumed that the data is close to a lower dimensional linear subspace, for the non-linear ones the low dimensional surface is embedded non linearly. Most non-linear methods, such as the Laplacian eigenmaps and ISOMAP techniques, aim to embed data that originally lies in a high dimensional space into a lower dimensional space, while preserving characteristic properties, such as the neighbourhood information. In addition to the fact that the comparative methods are more complicated to implement than PCA, the results also illustrate that all of them perform worse than PCA.

The method was also validated in clinical cases where a quadripolar CS catheter is used instead of the commonly used decapolar CS catheter by including in the tracking data only the last four electrodes of the catheter. The results illustrate that the performance of the developed technique is unchanged in cases where the quadripolar CS catheter is used and consequently, the method is still applicable in these cases.

Application of the model-based approach to very low dose X-ray sequences in near-real time was also demonstrated in this chapter. Cardiac and respiratory motions were extracted from the corrupted sequences. Figure 5.13 illustrates that this method is robust even when the motion is estimated from the very low dose X-ray sequences. In particular, for the application of the technique to rotational gating and to phase matching for 3D reconstruction, where the motion gating accuracy objective is set to 0.1s, the technique achieved success rates for end-systolic, EX and EI gating of 92.9%, 73.7% and 71.8%, respectively, even at the low SNR value of $\sqrt{2}$. For the application of the technique to motion compensation, where the motion gating accuracy objective is set to 1s, success rates of 100% were established for all gating tasks even at the lowest SNR values of $\sqrt{1}$. The technique is robust and accurate even when the motion-gating accuracy is set to be within 0.1s. Therefore, the technique could potentially be used for all three targeted clinical applications that this thesis seeks to address.

Furthermore, this accurate and robust method is able to detect the CS catheter in every frame of the X-ray sequences with a few millimetres accuracy. Even in cases with the lowest SNR values, median errors per electrode did not exceed 1.3 mm for the successfully tracked CS electrodes. When the computation of median errors included all CS electrodes irrespective of whether they were unsuccessfully tracked or not, the median errors per electrode did not exceed 1.8mm for the application of the technique to SNR values down to $\sqrt{2}$. As mentioned in Section 1.6, the tracking algorithms should be able to achieve these accuracies within this tolerance at least 90% of the time. The clinical experiments conducted in this chapter show that the Tracked-PCA technique can meet the accuracy objective at SNR levels of $\sqrt{5}$ and above. Within the constraints of these objectives, the achievable dose reduction factor for this technique is between $\frac{1}{10}$ and $\frac{1}{25}$ of the normal dose images, indicating the clinically significant robustness of the technique to noise.

Success rates calculated for the Tracked-PCA catheter tracking technique are higher than those calculated for the Real-time tracking technique both for the higher dose and the low dose X-ray sequences. Even though the Tracked-PCA technique performs better than the Real-time tracking technique, the Real-time tracking technique is robust and also performs very well in higher dose images. In the clinical scenario, the Real-time tracking technique will be used to form the PCA model from high dose X-ray images. Subsequently, the X-ray dose would be reduced and the Tracked-PCA technique would be employed for the catheter detection, enabling the subsequent procedure to be carried out at very low X-ray dose.

5.5.2 HML-based technique

A validation of the novel and robust to varying image-content retrospective HML-based method, for the purpose of image-based automatic cardiac and respiratory motion gating of normal and very low dose images, has been presented in this chapter. The technique was applied on the total of the 10 RFA and 18 CRT clinical X-ray fluoroscopy sequences. For the application of the technique to normal dose images, average success rates for end-systolic cardiac gating, EX and EI respiratory gating were established over all datasets. For the application of the technique to rotational gating and to phase matching for 3D reconstruction, success rates of 94.0%, 100% and 97.9% were established, for end-systolic, EX and EI, respectively. Therefore, in at most 6.0% of the cases over all gating tasks the technique fails to achieve the motion gating accuracy objective set in this thesis. For the application of the technique to motion compensation, success rates of 100% were established for all gating tasks.

A comparative quantitative validation was performed on the 10 RFA clinical fluoroscopy sequences, to investigate whether the proposed technique was superior to the previously developed

Tracked-PCA technique. The results indicate that the proposed technique outperforms the results of the previously developed technique for respiratory gating. While the Tracked-PCA technique outperforms the HML-based technique in cardiac gating, it relies on the tracking of a specific catheter, the CS catheter. The proposed HML-based technique does not have the constraint of the presence of the CS catheter in the X-ray images, instead it is robust to varying image-content. Thus, it is robust to typical EP X-ray images that can contain a varying number of different types of EP catheters and may include contrast agent injection.

The HML-based technique was also validated on very low dose X-ray sequences. Figure 5.17 illustrates that the technique is robust even when the motion is extracted from the very low dose rate X-ray sequences. The method remains accurate and robust, especially for respiratory gating, even on the high levels of Poisson noise. i.e. where SNR^2 was 2, indicating a dose reduction of more than 25 times. In particular for the application of the technique to rotational gating and to phase matching for 3D reconstruction, end-systolic, EX and EI gating success rates of 77.0%, 88.8% and 92.1%, respectively, were achieved for the application of the technique to the low SNR value of $\sqrt{2}$. For the application of the technique to motion compensation, success rates of 100% were established for all gating tasks even at the lowest SNR value of $\sqrt{1}$. The results demonstrate that the technique would be robust and accurate when potentially applied to motion gating of 3D rotational X-ray angiography (3DRXA) sequences, phase matching for 3D reconstruction and motion compensation by integrating respiratory motion into MRI-derived roadmaps fused with live X-ray fluoroscopy, the three clinical applications that the proposed frameworks were intended to target throughout this thesis.

5.5.3 Masked-PCA technique

The application of the novel framework of the Masked-PCA technique has been demonstrated in clinical datasets for the purposes of retrospective motion gating. Similar to the HML-based technique, the Masked-PCA technique is robust to varying image-content. The technique was developed to increase the cardiac gating accuracy and robustness of the HML-based technique. Validation of the technique on the 10 clinical EP X-ray sequences, from 10 different patients who underwent RFA procedures for the treatment of AF, and 18 clinical electrophysiology X-ray sequences, from 9 different patients that underwent CRT procedures for bi-ventricular pacing, is demonstrated in this chapter. For the application of the technique to motion gating of 3DRXA sequences and to phase matching for 3D reconstruction, end-systolic, EX and EI gating success rates of 99.6%, 97.9% and 97.0% were established for the total of the 28 X-ray sequences in normal dose. Therefore, in at most 3.0% of the cases over all gating tasks the technique fails to achieve the motion gating accuracy objective set in this thesis. For the application of the technique to motion compensation, success rates of 100% were established for all gating tasks, again for the total of the

28 X-ray sequences in normal dose. A comparative quantitative validation was performed on the total of the 28 clinical fluoroscopy sequences in normal dose, to investigate whether the proposed technique was superior to the previously developed robust to varying image-content HML-based technique (Section 5.4.3) and to the phase correlation technique [192]. The results indicate that the proposed Masked-PCA technique outperforms the previously developed robust to varying image-content technique for cardiac gating. It was found to have significantly fewer errors than the HML technique. It was also found that there is statistically no significant difference between the HML-based technique and Masked-PCA technique for respiratory gating. Additionally, the proposed technique outperforms the phase correlation technique for all three gating tasks. As already mentioned in Section 5.5.1, in using the phase correlation method the energy change could be caused by the motion of catheters, pacing leads or contrast agent injection. As the method uses overall motion of moving objects, the cardiac and respiratory motions detected by this method could be incorrect when the clinician manipulates the catheters or pacing leads, or injects contrast agent. This might be a reason for the poor performance of the phase correlation technique on clinical data.

The technique has also been validated on very low dose X-ray sequences. Figure 5.23c illustrates that the technique is robust even when the motion is extracted from the very low dose X-ray sequences, i.e. where SNR^2 was 2, indicating a dose reduction of more than 25 times. End-systolic, EX and EI success rates of 89.1%, 88.8% and 86.8%, respectively, were established for the application of the technique to motion gating of 3DRXA sequences and to phase matching for 3D reconstruction even at the low SNR value of $\sqrt{2}$. Similarly, gating success rates were computed to be 77.0%, 88.8% and 92.1% using the HML-based comparative technique for its application to motion gating of 3DRXA sequences and to phase matching for 3D reconstruction, showing a significant increase in performance using the Masked-PCA technique for cardiac motion gating. Furthermore, for the application of the technique to motion compensation, success rates of 100% were established for all gating tasks, for the total of the 10 RFA X-ray sequences even at the lowest SNR value of $\sqrt{1}$.

The previously proposed Tracked-PCA method (Section 5.4.2) involved the formation of a statistical model of the motion of a coronary sinus catheter based on PCA of tracked electrode locations from standard monoplane X-ray fluoroscopy images. The application of the model was demonstrated for the purposes of cardiac and respiratory gating of X-ray fluoroscopy images in normal and very low dose X-ray fluoroscopy images. Applying the Tracked-PCA method on the same 10 RFA X-ray sequences at SNR^2 of 2, end-systolic, EX and EI gating success rates were computed to be 92.9%, 73.7% and 71.8%, respectively. EX and EI success rates have been significantly improved as a result of the Masked-PCA motion gating technique. Although end-systolic gating success rates at normal dose have been slightly decreased, by 1.6%, as a result of the Masked-PCA technique there is no constraint of the presence of the CS catheter in the

X-ray images, as required for the previously developed Tracked-PCA technique. Instead, unlike most previously developed motion gating techniques, the Masked-PCA is robust to varying image-content. Thus, it is robust to typical EP X-ray images that can contain a varying number of different types of EP catheters and may include contrast agent injection.

5.5.4 View-angle independent technique

In this chapter, the validation of the View-angle independent technique for near-real time gating and catheter tracking in clinical images has been presented. Using the model on unmodified clinical images for near-real time cardiorespiratory motion gating, end-systolic, EX and EI gating success rates of 100.0%, 85.7% and 92.3%, were established, respectively, for the application of the technique to motion gating of 3DRXA sequences and to phase matching for 3D reconstruction. Therefore, in at most 15.0% of the cases over all gating tasks the technique fails to achieve the motion gating accuracy objective set in this thesis. Additionally, for the application of the technique to motion compensation, success rates of 100% were established for all gating tasks. For very low dose applications, gating success rates of 80.3%, 71.4% and 69.2% were established even at the lowest SNR value of $\sqrt{5}$, for the application of the technique to motion gating of 3DRXA sequences and to phase matching for 3D reconstruction. For the application of the technique to motion compensation, success rates of 100% were established for all gating tasks, again even at the lowest SNR value of $\sqrt{5}$.

The technique is able to gate CS catheter electrode positions in the two views to reconstruct the 3D position of the CS catheter and then to track the catheter in very low dose X-ray images at the new angle. The algorithm was able to detect the coronary sinus catheter with median errors not exceeding 0.9mm, well below the acceptable value in clinical practice which is 2mm [93], even in images corrupted with Poisson noise of SNR down to $\sqrt{5}$. The computation of median errors included all CS electrodes irrespective of whether they were unsuccessfully tracked or not.Unlike most previously developed motion gating techniques, the main novelty of the View-angle independent technique is that it is X-ray system view-angle independent. Therefore, it is applicable and robust in cases where the angulation of the scanner is changed between frames.

5.5.5 Comparison of techniques

The validation of the novel frameworks developed in this thesis on clinical datasets indicates an exceptionally good cardiorespiratory motion gating performance, with success rates ranging between 85.7%-100.0% for the application of the four techniques at normal dose to motion gating of 3DRXA sequences, phase matching for 3D reconstruction and motion compensation. Although as expected the accuracy of the motion gating is reduced when applied to clinical

data sets, compared to phantom datasets, the results demonstrate a promising performance of the technique to the three clinical applications that this thesis seeks to address. In both normal and very low dose scenarios, the Tracked-PCA outperforms the alternative techniques for cardiac motion gating, with a minimum motion gating % success rate of 92.9% even for the application of the technique to SNR values of $\sqrt{2}$. Although the Tracked-PCA technique is superior to the HML-based and Masked-PCA techniques for cardiac gating, the framework of the technique precludes it being used in datasets where the CS catheter is not present in the images. On the other hand, again in both normal and very low dose scenarios, the HML-based and Masked-PCA techniques indicate a superior performance over the Tracked-PCA technique for EX and EI gating with minimum success rates of 88.8% and 92.1%, respectively, for the HML-based technique and 88.8% and 86.8%, respectively, for the Masked-PCA technique. After checking that the data distribution was normally distributed, an f-test was conducted under the null hypothesis that there was no difference in the techniques. Experiments indicate that there is no statistically significant difference between the HML-based technique and Masked-PCA technique for respiratory gating. Even though the above techniques demonstrate a very promising performance for the potential clinical applications, one major limitation of these and other model-based approaches is the requirement to build a separate model for each X-ray view. Therefore, the X-ray system view-angle independent technique was developed for the purposes of motion gating in cases where the angulation of the scanner is changed between frames, establishing minimum end-systolic, EX and EI success rates of 80.3%, 71.4% and 69.2% at the lowest SNR value of $\sqrt{5}$.

The PCA-based CS catheter detection methods, Tracked-PCA and View-angle independent methods, can detect the CS catheter position without defining a ROI in the X-ray image. These novel CS catheter detection algorithms have been validated on clinical experiments and similar to their validation on phantom datasets, they have been demonstrated to achieve accuracies within the 2mm clinical tolerance, a criterion for suitability for deployment in the clinical workflow. Therefore, in terms of clinical application, the techniques can potentially be used for performing 2D-3D registration of 3D cardiac data (CT or MRI) to X-ray fluoroscopy, using catheters that are reconstructed in 3D from sequential biplane X-ray images. The techniques will be suitable for providing image registration for 3D dynamic compensation. In particular, they will be suitable for the updating of 3D roadmaps to significantly improve the accuracy of fluoroscopy overlays for cardiac procedures or for the off-line fusion of cardiac image data for application in biophysical modelling research.

For the applications involving RFA data, the frame rates that are commonly used during these procedures are the lowest frame rate that is available on the X-ray system, i.e. three frames per second. Higher frame rates are not routinely used in order to minimise radiation dose. It is accepted that, as a result, the temporal resolution of manually identifying specific points in

the cardio-respiratory cycle will be limited by the frame rate. However, since this resolution is the required resolution during clinical procedures, and since it is known from the phantom experiments, illustrated in Chapter 4 that the method works equally well on higher frame rate images, it is appropriate for effective clinical translation of the algorithms to be validated at low frame rates.

A significant advantage of the Tracked-PCA technique on low dose clinical images is that it can operate within a few seconds per image sequence. Specifically, the technique is implemented with execution time between 0.06 and 0.1 seconds per frame, depending on the step size. Although the application of the technique to motion gating suffers from a time lag of 1 sample interval, this will not be the case for its application to 3D dynamic compensation, because there is no need to identify peaks/troughs in the extracted signals. Therefore, the technique is fast enough to be potentially applied for real-time 3D dynamic compensation. On the other hand, the View-angle independent technique is implemented with execution time between 0.41 and 1.43 seconds per frame. Although the execution time of the application of the technique to clinical datasets is slightly faster than for phantom datasets, real-time motion compensation is again not currently feasible. However, as also mentioned previously, code optimisation was not the focus of this work and would need to be considered for real-time clinical application.

For the validation of the experiments presented in this chapter a different gold standard method for cardiac gating was chosen compared to the one used for the validation of the techniques on phantom datasets. This involved manual detection of systolic and diastolic frames. Manual detection was performed by different observers and the average inter observer variation was computed as a proportion of the cardiac cycle. For the RFA and CRT procedures, four and three experienced observers were used, respectively, to manually detect systolic frames. A 0% and 1.91×10^{-4} % average variation was established between observers for the RFA and CRT procedures, respectively. This non zero value for the CRT procedures was generated by 7 peaks of 1 frame difference. This very small variation indicates that the ground truth is sufficient for the computed experiments.

The techniques developed and validated throughout this thesis are workflow-friendly and do not require any additional fiducial markers or contrast agent. They will be particularly useful for registration and overlay of pre-procedural images with X-ray fluoroscopy for guidance and biophysical modelling. Most importantly, the techniques are robust-to-noise. Therefore, they have the potential to greatly reduce radiation dose in image-guided cardiac catheter procedures and outweigh the radiation risk by the benefit of the interventional procedure. As a consequence, radiation to patients and staff will decrease significantly, therefore accomplishing the main objective behind the work of this thesis.

5.5.6 Conclusion

As already mentioned in Chapter 4, application of the techniques to clinical datasets introduces uncertainties and therefore, accuracy and precision established in phantom datasets will not necessarily follow through in clinical practice. The uncertainties introduced involve: the imaging field of view, the anatomical region of interest, variations in image quality due to the patient's anatomy, the presence of non-rigid structures in the field of view, and other factors that are outside the control of a phantom-based assessment. Additionally, in patient images some of the electrodes on the CS catheter might move out of the field of view so that the complete CS catheter body is not visible throughout the procedure. This was expected to compromise the accuracy and precision of the CS catheter detection algorithms when applied to clinical data. Additionally, images from patient data differ from phantom data in more ways with the most significant being the non-repeating motion of the heart throughout the cardiorespiratory cycle. This might introduce motion artefacts and potential phase mismatch issues between images of the heart compromising the ability of the techniques for performing 2D-3D registration of 3D cardiac data (CT or MRI) to X-ray fluoroscopy, using catheters that are reconstructed in 3D from sequential biplane X-ray images, a potential significant clinical application of the proposed algorithms. Furthermore, patient images usually have lower contrast than images of phantoms and so imaging of the heart often involves the injection and perfusion of contrast agent into the blood stream for better vessel and chamber visibility.

Even though the above uncertainties and complications exist in clinical practice, the comprehensive validation of the techniques on clinical datasets, demonstrated in this chapter, illustrates that their robustness, accuracy and precision should not compromise their clinical translation, even though they are less accurate/robust than when applied on phantom data. Consequently, it will not compromise their potential use in the targeted clinical applications that this thesis seeks to address. All in all, the developed motion gating techniques are a key component of the three clinical applications. The next chapter (Chapter 6) demonstrates how the basic motion gating techniques can be extended into these applications to be useful in clinical practice.

Chapter 6

Clinical applications

Contents

6.1 Introduction

There has been very limited clinical translation of currently available motion gating techniques. A likely reason for this lack of translation is a lack of accuracy and robustness of the techniques proposed to date. A second reason is that the most accurate motion gating techniques currently available interrupt and complicate the clinical workflow. This thesis seeks to address the current limitations of motion gating techniques to foster the uptake of such techniques in clinical practice.

To achieve this goal, novel and effective methods have first been devised, in Chapters 3, 4 and 5, to improve on the accuracy and robustness of the alternative motion gating techniques proposed to date. Following this, these techniques should be translated to clinical applications. In this chapter, preliminary experiments on the application of these techniques to different clinical tasks are demonstrated. In particular, the clinical applications that the gating techniques are used in are: 3D catheter reconstruction, motion gating of 3D rotational X-ray angiography (3DRXA) and motion compensation by integrating respiratory motion into MRI-derived roadmaps fused with live X-ray fluoroscopy.

First, the Tracked-PCA, Masked-PCA and HML-based techniques are demonstrated for the purpose of 3D reconstruction of optically opaque objects seen in the X-ray fluoroscopic images. Approximately 80% of EP catheter laboratories are monoplane. In order to reconstruct optically opaque objects seen in X-ray images in 3D, like vessels, interventional devices and more importantly catheters, at least two oblique views must be acquired and phase-matched to the same cardiorespiratory phase. The acquisition of these images is called sequential biplane imaging. Performing 2D-3D registration of 3D cardiac data (CT or MRI) to X-ray fluoroscopy using interventional devices is one of the clinical applications of gating [89]. For this application the devices are catheters and pacing leads and there is therefore a need for them to be reconstructed in 3D from sequential biplane X-ray images. This kind of registration is suitable for providing guidance of cardiac catheterisation procedures or for the off-line fusion of cardiac image data for applications in biophysical modelling research [90].

Furthermore, in this chapter it is shown how the novel View-angle independent approach can be used for motion gating of 3DRXA. Motion gating of sequences where the angulation of the scanner is changed between frames is a particularly important clinical application of motion gating as current methods are limited to breath-holding for respiration and either no gating for cardiac motion or arresting the heart using adenosine or rapid pacing [100].

Finally, an extension of the methods to motion compensation is demonstrated. Throughout this thesis, even though the whole cycle is detected using the proposed techniques, for evaluation, only peaks and troughs were used, where the gold standard is well-defined. The obtained signal can potentially be used not only for gating but also for real-time dynamic compensation. Since a pre-operative compensation for different phases of cardiac/respiratory motion can be performed, and the results simply recalled based on the current phase of the system, the image-based phase detection should be most useful for dynamic roadmapping applications for cardiac interventions. In this chapter, the clinical application of the Tracked-PCA technique for real-time respiratory motion compensation and the extension using the View-angle independent technique to unseen images taken at any arbitrary projection are demonstrated, by prospectively driving the motion of the 3D MRI roadmaps fused onto live X-ray fluoroscopy.

6.2 Catheter 3D reconstruction

6.2.1 Methods

Catheters and pacing leads are reconstructed in 3D by the back projection from biplane X-ray images of corresponding point pairs that lie along the devices. In particular, identifiable point pairs correspond to the catheter electrodes and the tip of the pacing leads for catheter and pacing leads reconstruction, respectively. The method was tested on sequential biplane X-ray sequences to determine the optimal phase-matched frame pairs for the reconstruction of these interventional devices. The frame pairs were chosen by first using one of the gating methods to find all the frames that were at the same phase, e.g. EX/end-systole. The optimal frame pairs were then chosen from this set using the backprojection distance metric. The metric is calculated by first back-projecting corresponding points on the catheter or pacing lead from the two views, to yield two projection lines. The midpoint of the shortest line segment between the two lines is then reprojected, which traces the midpoint from the source back to the two 2D images. The distance between the original plane point and the reprojected point, the reprojection error, is then calculated. The biplane pair which minimised this distance, defined as the minimal reprojection error, was assumed to yield the best catheter or pacing lead reconstruction.

6.2.2 Experiments

6.2.2.1 Testing using sequential biplane reconstruction

It was quantitatively assessed how well the chosen biplane pairs matched by computing the minimal reprojection errors arising from the Tracked-PCA frame matching technique and comparing these against the minimal reprojection errors arising from manual frame matching by an experienced observer [231]. Testing was done on RFA cases using the CS catheter. Additionally, minimal reprojection errors arising from the Masked-PCA and HML-based automatic frame matching gating techniques were computed. For these techniques, testing was done on RFA and CRT X-ray sequences using the CS catheter and the tip of the ventricular pacing lead reconstruction, respectively.

6.2.3 Results

6.2.3.1 Testing using sequential biplane reconstruction

Tracked-PCA technique. The minimal reprojection errors arising when the Tracked-PCA method was applied to the sequential biplane RFA X-ray sequences introduced in Chapter 5, comprising a total of 244 frames, to determine the optimal phase-matched frame pairs for catheter reconstruction, are illustrated in Figures 6.1a and 6.1b. Biplane X-ray images were acquired from two different angle views using the monoplane X-ray system. Typically, one was the anteroposterior (AP) view and the other was the left/right anterior oblique (LAO/RAO) 30° view. Minimal reprojection errors (mm) arising from the automatic frame matching and from manual frame matching are illustrated in black and white bars, respectively. Under each bar the matched frame pairs (AP/LAO) for each processed case are displayed. It can be seen from the results that in Case 1 (EX/end-systole and EI/end-systole) the frame pair numbers only agree for LAO. In Case 3 (EX/end-systole) only the AP frame numbers agree, and in the rest there is a disagreement of (AP/LAO) frame pair numbers. The average minimal reprojection errors of EX/end-systole frame pairs and EI/end-systole frame pairs were calculated to be 2.8 mm and 0.538 mm, respectively. Comparing the minimal reprojection errors arising from the automatic technique against the minimal reprojection errors arising from manual frame matching, which were calculated to be 3.51 mm and 3.06 mm for EX/end-systole and EI/end-systole respectively, it can be seen that the automatic technique is much more accurate than the manual technique.

Masked-PCA and HML-based techniques. The Masked-PCA and HML-based techniques were tested on the three RFA sequential biplane X-ray sequences, comprising a total of 244 frames, and the three CS angiography biplane sequences carried out during CRT procedures, comprising a total of 438 frames. The optimal phase-matched images to reconstruct either the CS catheter or the tip of the right-ventricular pacing lead were determined by the automatic gating method. The minimal reprojection errors arising from this technique are shown in Figure 6.2. Cases 1–3 illustrate the RFA biplane sequences while Cases 4–6 illustrate the CRT biplane sequences. Minimal reprojection errors (mm) arising from the automatic Masked-PCA frame matching and the minimal reprojection errors from manual frame matching are illustrated in black and white, respectively. Minimal reprojection errors arising when the HML-based technique was applied are illustrated in gray, on the same figure. The results show that both the Masked-PCA and the HML-based frame matching outperform the manual frame matching.

Using the Masked-PCA technique, average minimal reprojection errors of 1.64mm and 0.54mm were computed for EX/end-systole and EI/end-systole frame pairs, respectively, for catheter reconstruction from RFA biplane X-ray sequences. Reconstruction of the tip of the right-ventricular pacing lead from CRT biplane X-ray sequences produced average minimal reprojection errors

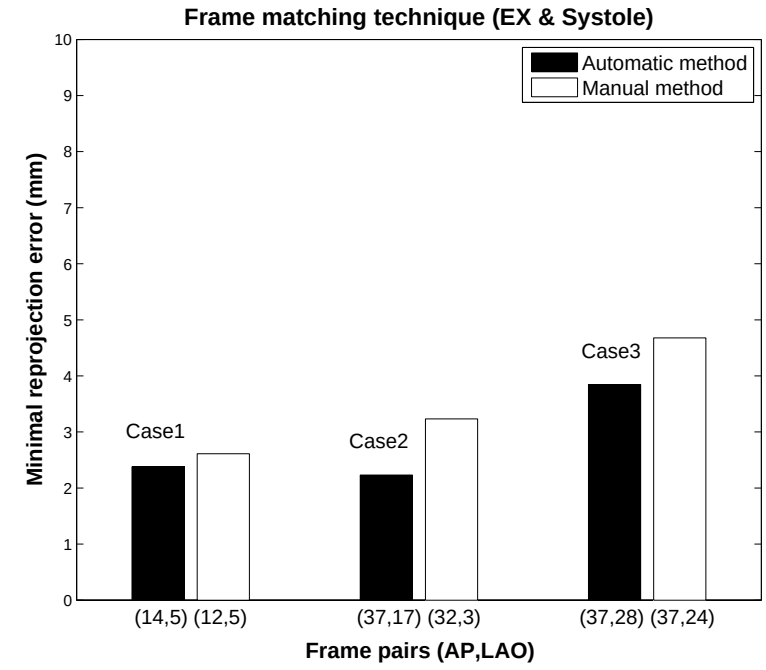

(a)

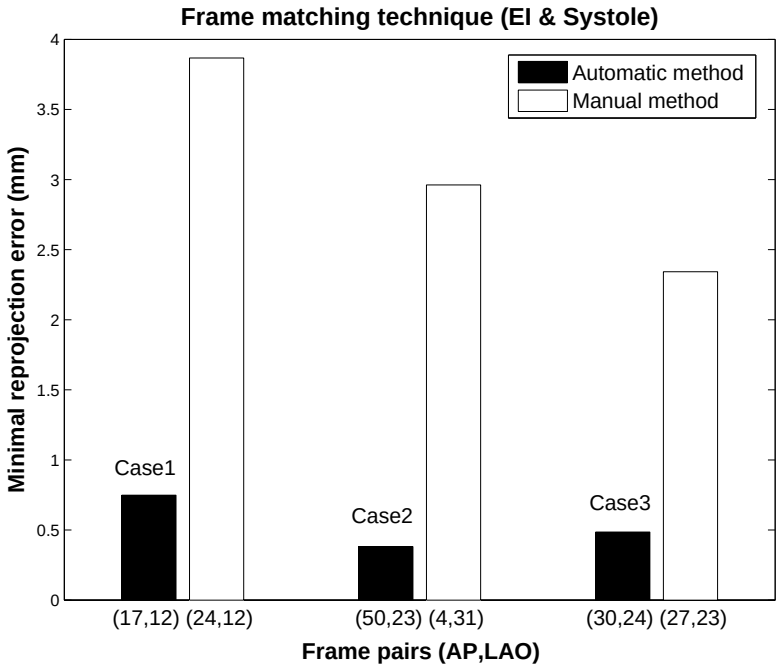

(b)

FIGURE 6.1: Computation of (a) EX/end-systole and (b) EI/end-systole minimal reprojection errors (mm) for the automatic Tracked-PCA technique compared to manual gating on the three RFA X-ray sequences. The matched frame pairs (AP, LAO) are displayed.

of 0.32mm and 0.40mm, respectively. Comparatively, using the HML-based technique, average minimal reprojection errors of 1.64mm and 1.60mm were computed, respectively, for RFA biplane X-ray sequences and 0.46mm and 0.47mm, respectively, for CRT biplane X-ray sequences. Average minimal reprojection errors arising from manual frame matching were computed to be 3.51mm and 3.06mm for EX/end-systole and EI/end-systole, respectively, for the RFA sequences and 2.96mm and 2.36mm, for the CRT sequences. Although the comparative HML-based automatic frame matching technique shows a better performance than the manual frame matching technique, the results demonstrate that the Masked-PCA technique performs better than the HML-based technique.

Under each bar the matched frame pairs (AP and LAO) for each processed case are displayed. It can be seen from the results that, in Case 1 (EX/end-systole and EI/end-systole) all frame pair numbers agree for LAO; but only the automatic techniques agree for AP. In Case 3, for EX/end-systole, the frame pair numbers agree for both AP and LAO between the automatic techniques. In Case 4, for EX/end-systole, the frame pair numbers only agree for LAO between the automatic techniques and for EI/end-systole agree for both AP and LAO between the automatic techniques. In Case 6, for EI/end-systole, only the automatic techniques agree. In the rest there is a disagreement of frame pair numbers for both AP and LAO.

6.3 Motion gating of rotational X-ray angiographic images

6.3.1 Methods

The framework of the proposed View-angle independent method for cardiorespiratory motion gating and CS catheter detection applied to 3D rotational angiography sequences was explained in Chapter 3, Section 3.4.2. The process involves the formation of a statistical model of catheter motion in the *training* view (Section 3.4.2.1), and then its application on the *current* view (Section 3.4.2.2). Unlike in previous chapters, the test data are rotational sequences and the *current* view changes each frame.

For the phantom datasets, the exact view-angles for each frame were not available in the DICOM headers. Instead, initial estimates for the angles were computed by assuming a constant rotation speed. These were refined by including a search over the angles ($\pm 5^\circ$ from the initial estimate in steps of 1°) in the exhaustive search for the PCA weights.

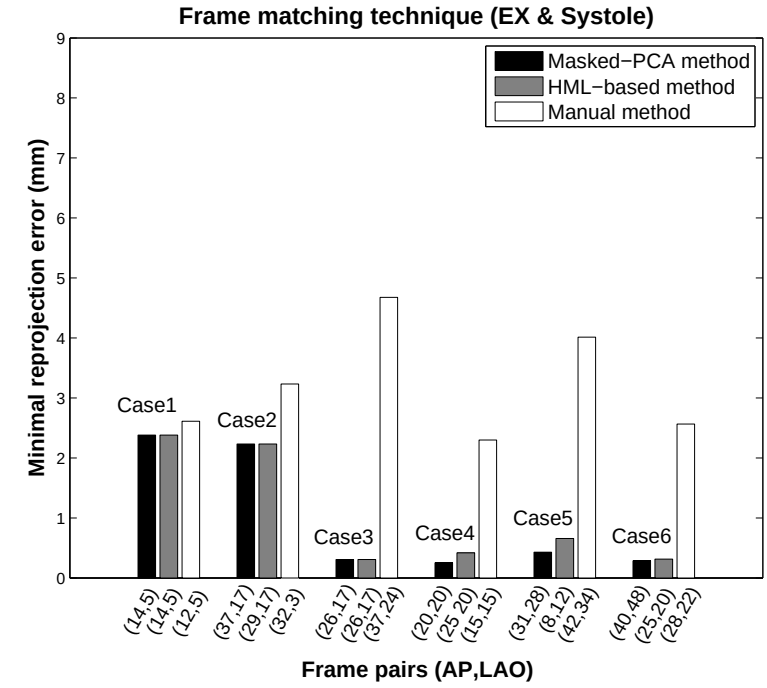

(a)

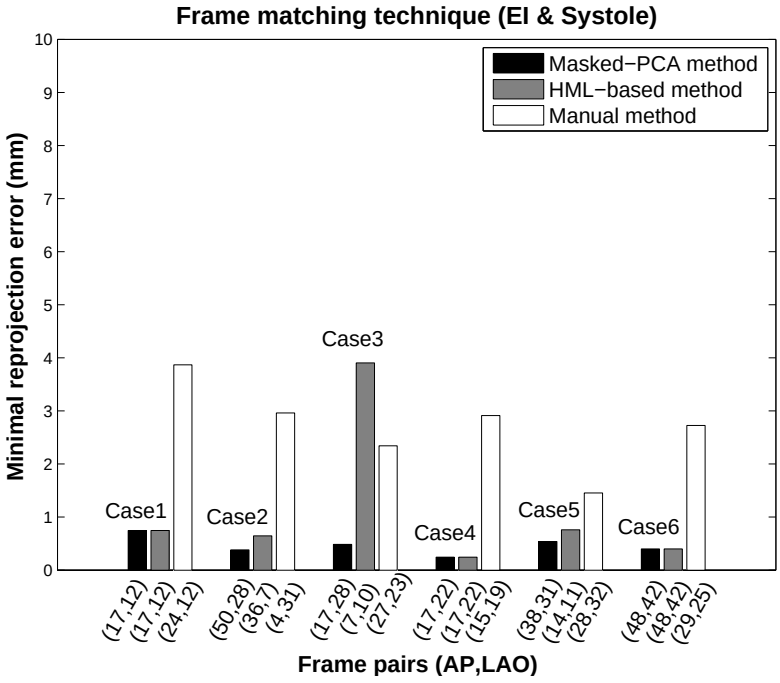

(b)

FIGURE 6.2: Computation of (a) EX/end-systole and (b) EI/end-systole minimum reprojection errors (mm) for the automatic Masked-PCA and HML-based techniques and manual technique for six X-ray fluoroscopy sequences. The matched frame pairs (AP, LAO) are displayed.

6.3.2 Experiments

6.3.2.1 Application to rotational sequences at normal dose

The technique was validated on 3 clinical rotational X-ray angiography sequences (341 frames) and 2 phantom rotational X-ray sequences (540 frames). For the patient sequences the statistical model was formed on a monoplane X-ray sequence acquired for each patient in the AP view. For the application of the technique on the phantom rotational sequences, the model was formed on monoplane X-ray sequences in AP and RAO30° views in turn.

Catheter tracking validation. Similar to the catheter tracking validation performed in Chapters 4 and 5, to validate the performance of the CS catheter tracking, median errors per electrode were calculated. Tracking failures were considered to be those cases where the electrode error was above 2 mm [93].

Gating validation. To validate the gating technique, the same kind of frame difference analysis was performed as in Chapters 4 and 5 again with the same gold standard methods.

6.3.2.2 Application to rotational sequences at low dose

The X-ray images were corrupted by applying Poisson noise as described in Section 4.3.5.1. SNR values of $\sqrt{50}$, $\sqrt{10}$, $\sqrt{8}$, $\sqrt{6}$ and $\sqrt{5}$ were used. Similar to the validation performed in Chapters 4 and 5, the CS catheter tracking was validated in terms of median errors per electrode, and gating was validated using frame difference analysis.

6.3.3 Results

6.3.3.1 Application to rotational sequences at normal and low dose

Figures 6.3 and 6.4 illustrate the results of the CS catheter tracking technique on normal dose X-ray images at different view-angles from (a) a patient and (b) a phantom example X-ray sequence, respectively. The results illustrate that this novel view-angle independent technique can successfully track the CS catheter in X-ray sequences where the angulation of the scanner is changed between frames.

Quantitative validation of CS catheter tracking. Figures 6.5a and 6.6a illustrates median errors per electrode for the View-angle independent CS catheter tracking on the uncorrupted images and the images corrupted with Poisson noise at the 5 SNR levels for patient and phantom

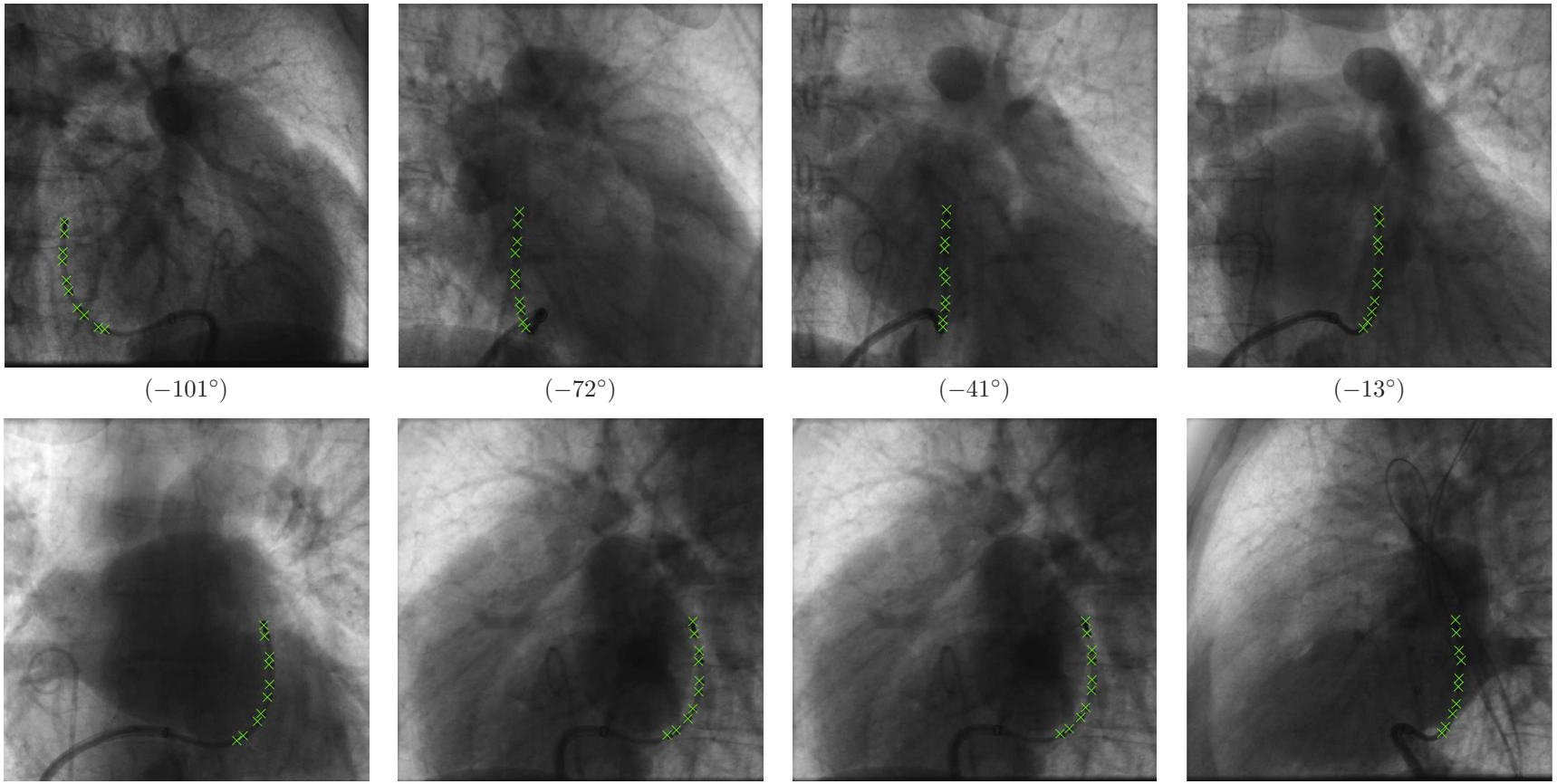

FIGURE 6.3: The View-angle independent CS catheter tracking technique is illustrated in green colour crosses on 3DRXA clinical images of evenly sampled view-angles.

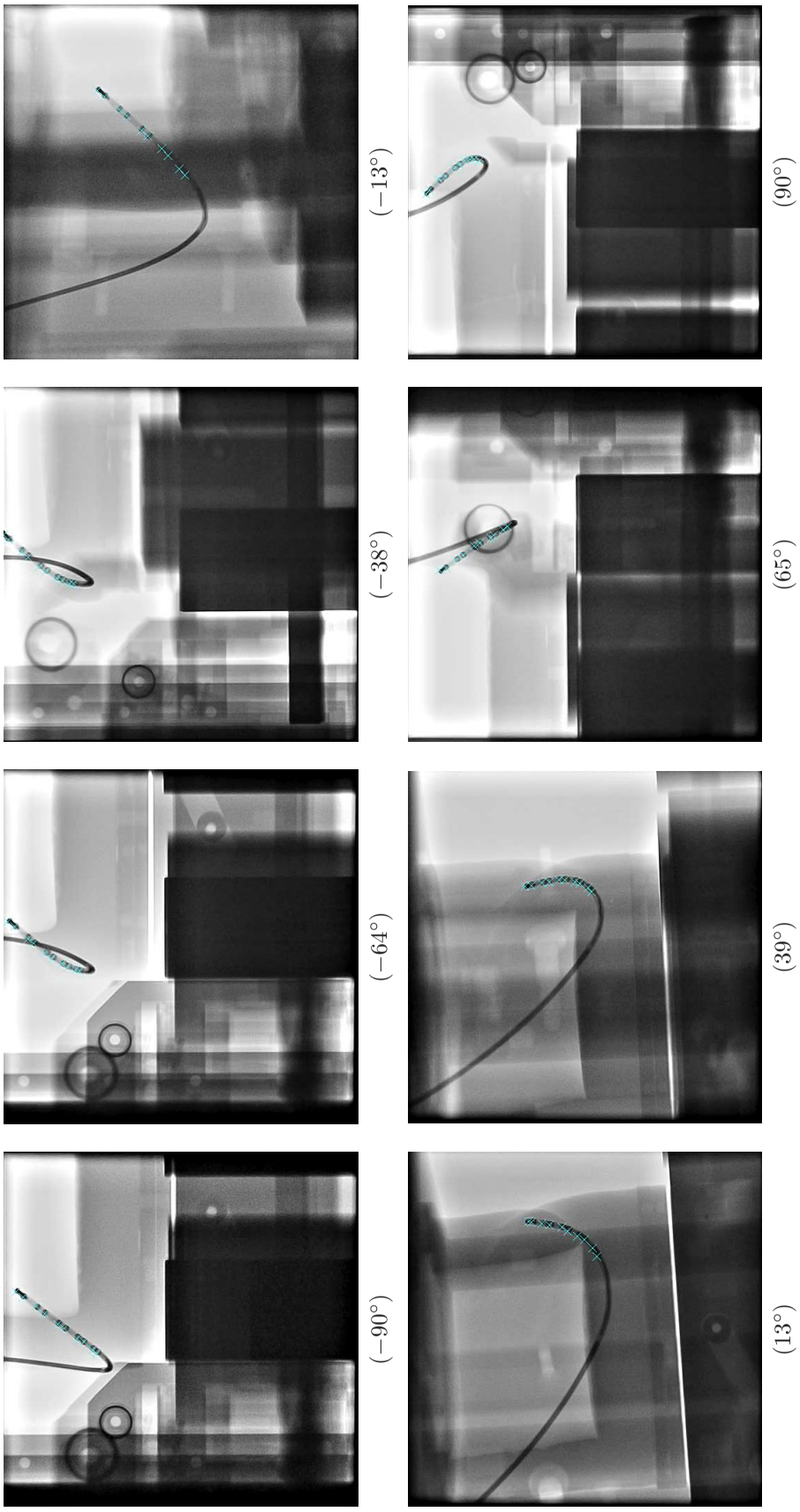

FIGURE 6.4: The View-angle independent CS catheter tracking technique is illustrated in cyan colour crosses on 3DRXA phantom images of evenly sampled view-angles.

X-ray images, respectively. Errors are calculated with respect to the gold standard detection. Since the technique is designed to track each of the ten CS catheter electrodes, errors were calculated for each electrode and are shown in different grey scale colours, starting from the proximal (black colour) and moving to the distal (white colour) electrode. For the technique to be acceptable in clinical practice, failure cases were considered to be the ones where median errors per electrode were above 2mm [93]. For a more comprehensive validation, in Figures 6.5b and 6.6b median errors were calculated and are shown only for the successfully tracked CS catheter electrodes, again for patient and phantom X-ray images, respectively. Figure 6.7 shows the range of the errors in terms of the 25^{th} percentile, median and 75^{th} percentile, over all electrodes, and for successfully tracked electrodes, for each noise level. Success rates were also calculated and are shown as percentages (%) in Figures 6.8a, b for patient and phantom X-ray images, respectively.

Quantitative validation of cardiorespiratory motion gating. For both cardiac and respiratory gating, the absolute frame difference was computed for the phantom procedures. For patient procedures the absolute frame difference was computed only for cardiac gating as patients were in breath-hold. Figures 6.9a and 6.9b illustrate the frame difference errors in frequency distribution bar charts, i.e. the number of peaks or troughs with 0, 1 or 2 frames separation from the gold standard for the patient and phantom rotational sequences, for all gating tasks and noise levels. The results indicate a 100% cardiac gating success rate when the technique is applied to normal dose images. Using the corrupted clinical images for 'near-real time' cardiorespiratory motion gating, the technique is accurate to within 0.1s with a success rate of 60.0% for end-systolic gating, while end-systolic, EX and EI of 62.0%, 66.7% and 50.0%, respectively, for the phantom cases, were established at SNR of $\sqrt{5}$. No false positives or negatives (i.e. extra/fewer detected peaks/troughs) over the processed sequences were found. The results demonstrate that the proposed technique is robust and accurate in tracking the CS catheter and is doing a faultless job in extracting cardiorespiratory motion from any view-angle, over the range of 180° from LAO 90° to RAO 90°, in normal dose scenarios for rotational acquisitions. Regarding the application of the technique to low dose rotational datasets, the outcome shows that the performance of the technique is adversely affected in both CS catheter tracking and motion extraction at the lowest SNR value of $\sqrt{5}$.

6.4 Motion compensation

6.4.1 Methods

6.4.1.1 Clinical application to motion compensation

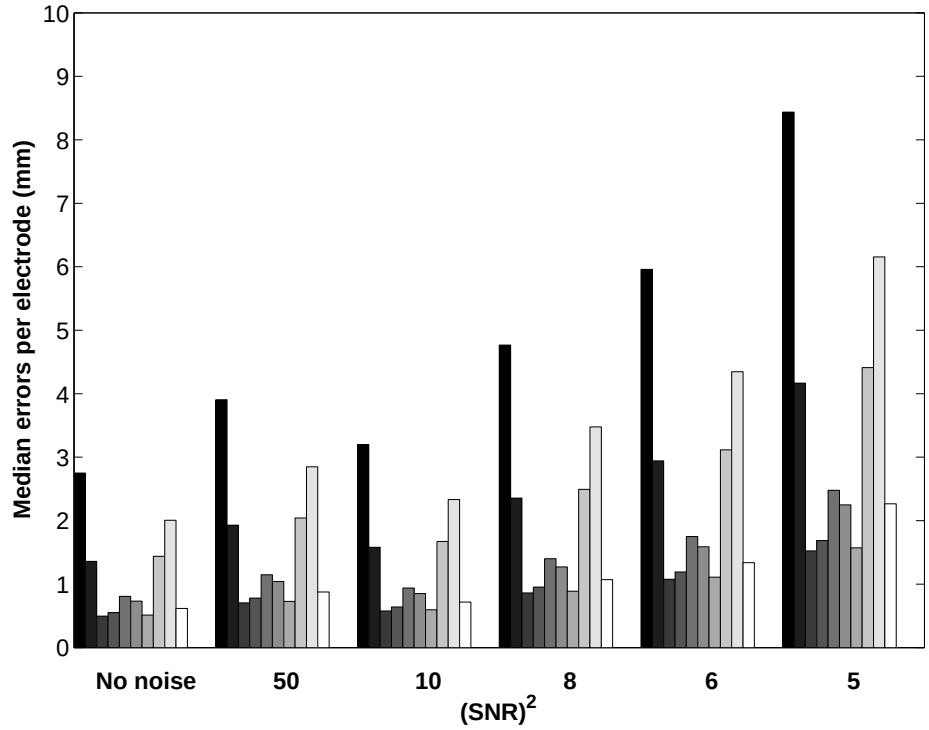

(a)

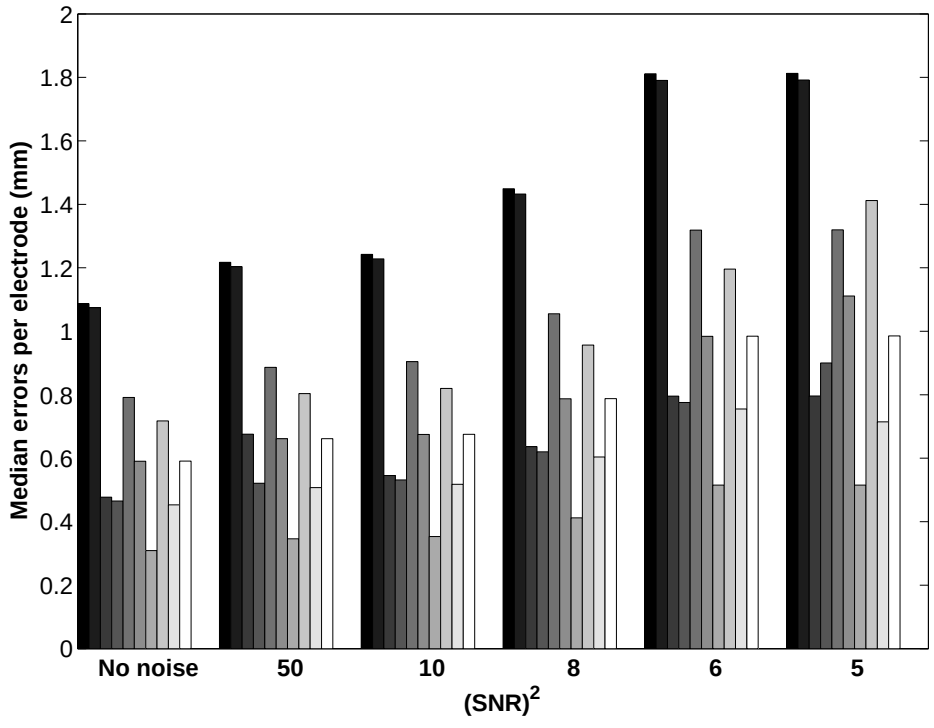

(b)

FIGURE 6.5: Median errors per electrode with respect to the gold standard, for clinical rotational X-ray sequences for the normal dose and five levels of SNR, where median errors are illustrated for (a) all tracked CS electrodes, and (b) only for the successfully tracked CS electrodes using the View-angle independent technique. Different grey scale colour bars are used to distinguish the CS catheter electrodes, starting from the proximal (black colour) and moving to the distal electrode (white colour).

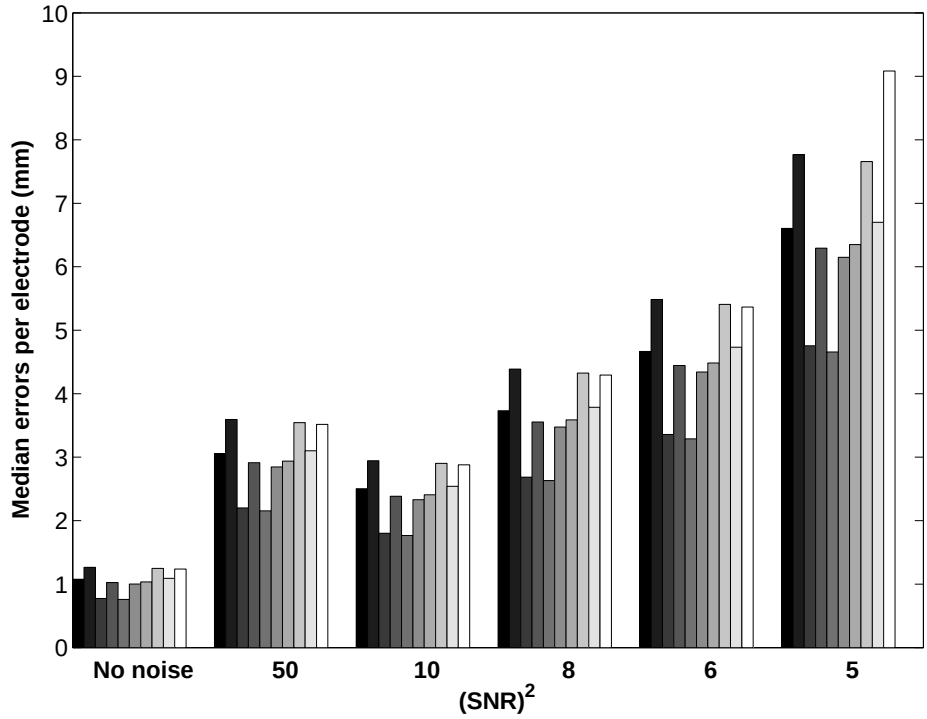

(a)

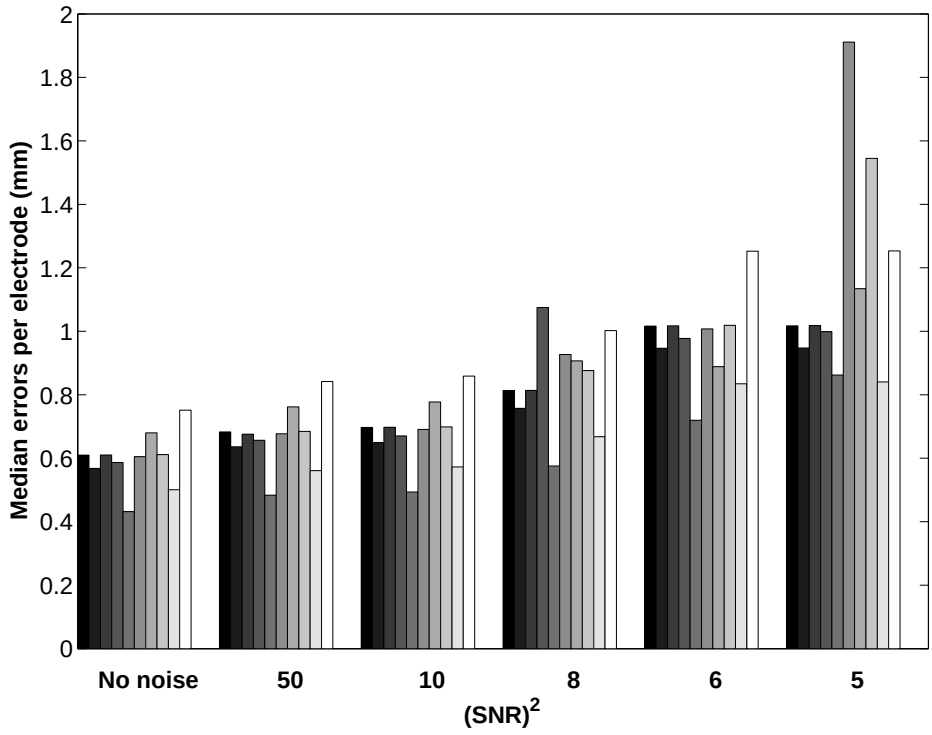

(b)

FIGURE 6.6: Median errors per electrode with respect to the gold standard, for phantom rotational X-ray sequences for the normal dose and five levels of SNR, where median errors are illustrated for (a) all tracked CS electrodes, and (b) only for the successfully tracked CS electrodes using the View-angle independent technique. Different grey scale colour bars are used to distinguish the CS catheter electrodes, starting from the proximal (black colour) and moving to the distal electrode (white colour).

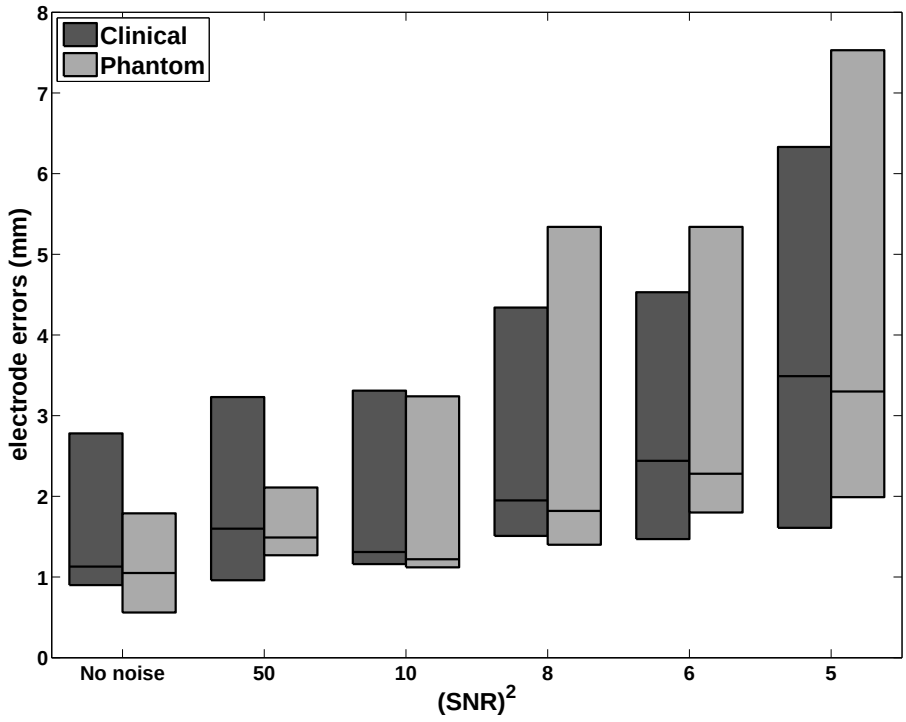

(a)

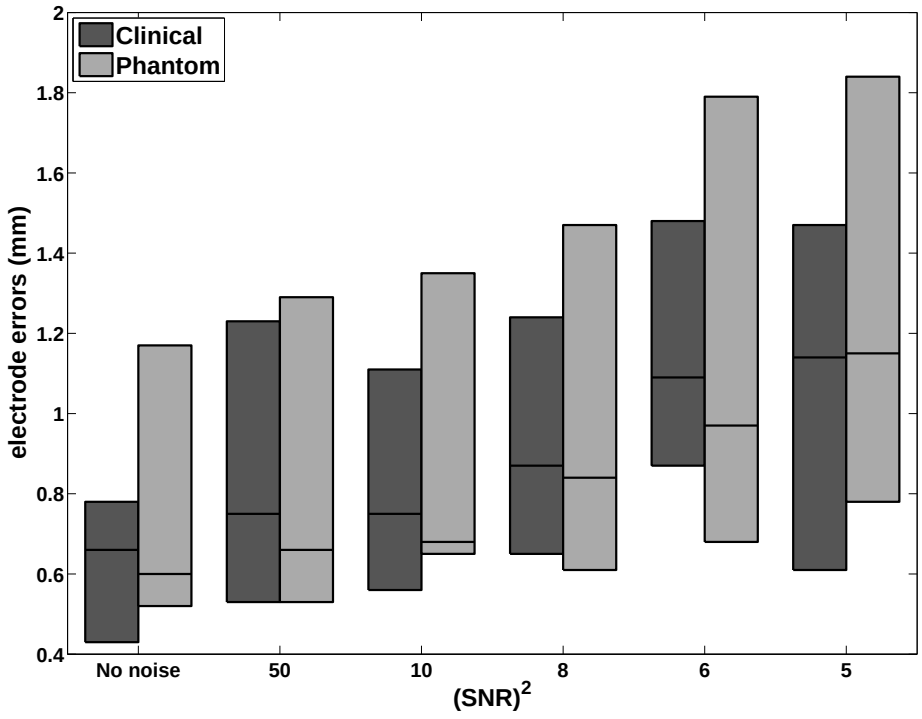

(b)

FIGURE 6.7: Illustration of the 25^{th} percentile, median and 75^{th} percentile values over (a) all CS catheter electrodes in both phantom and clinical data sets and (b) only successfully tracked CS catheter electrodes, for each noise level using the View-angle independent technique.

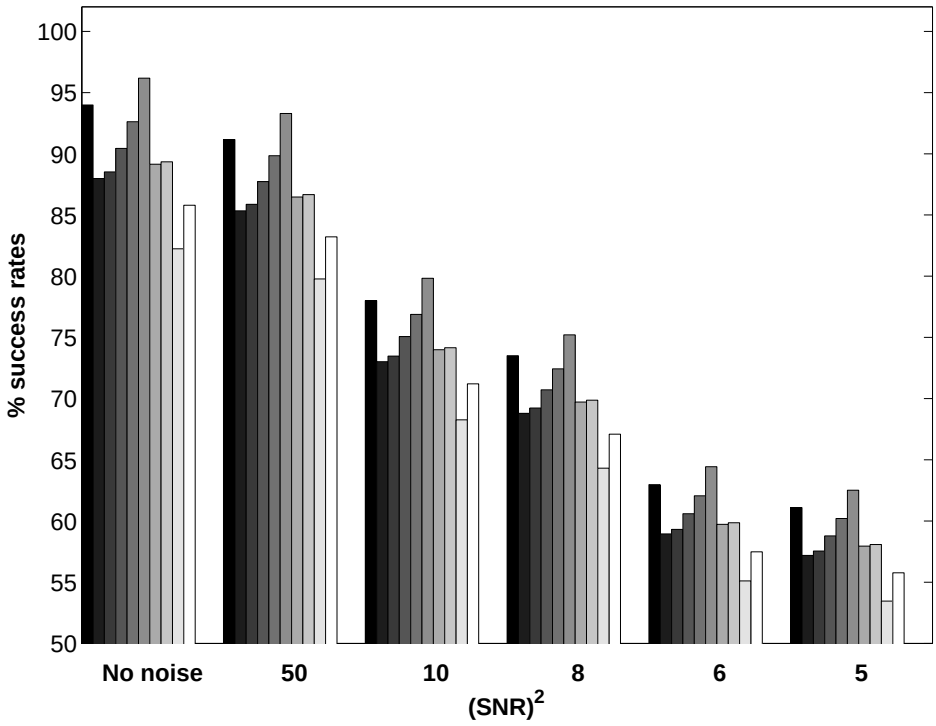

(a)

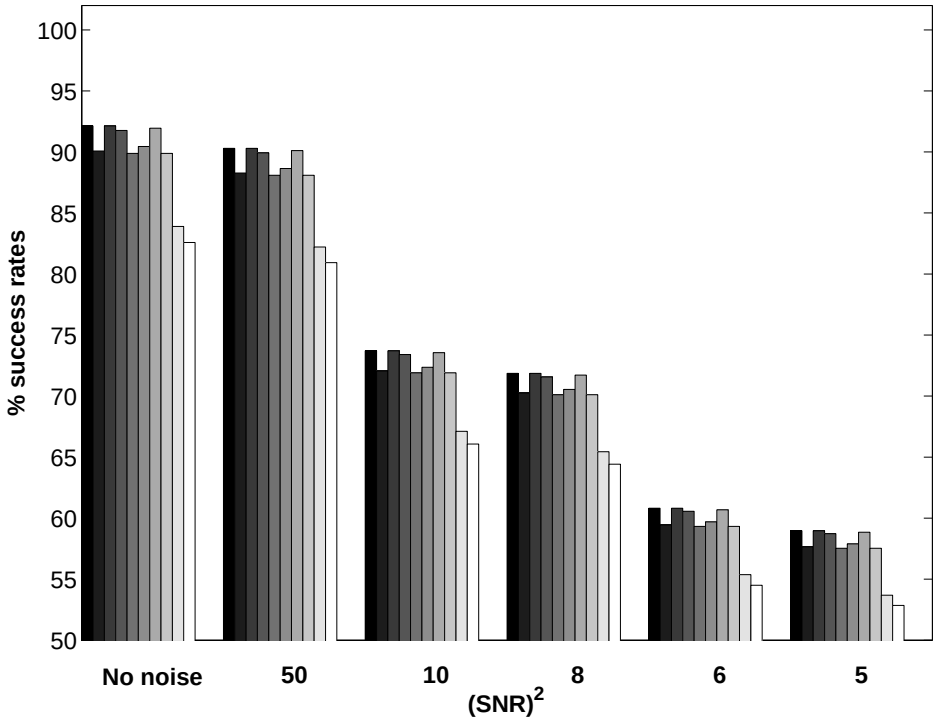

(b)

FIGURE 6.8: CS catheter tracking technique percentage success rates (%), for (a) clinical and (b) phantom rotational X-ray sequences for the normal dose and five different levels of SNR using the View-angle independent technique. Success cases are considered to be the ones where the median errors per electrode are below 2mm.

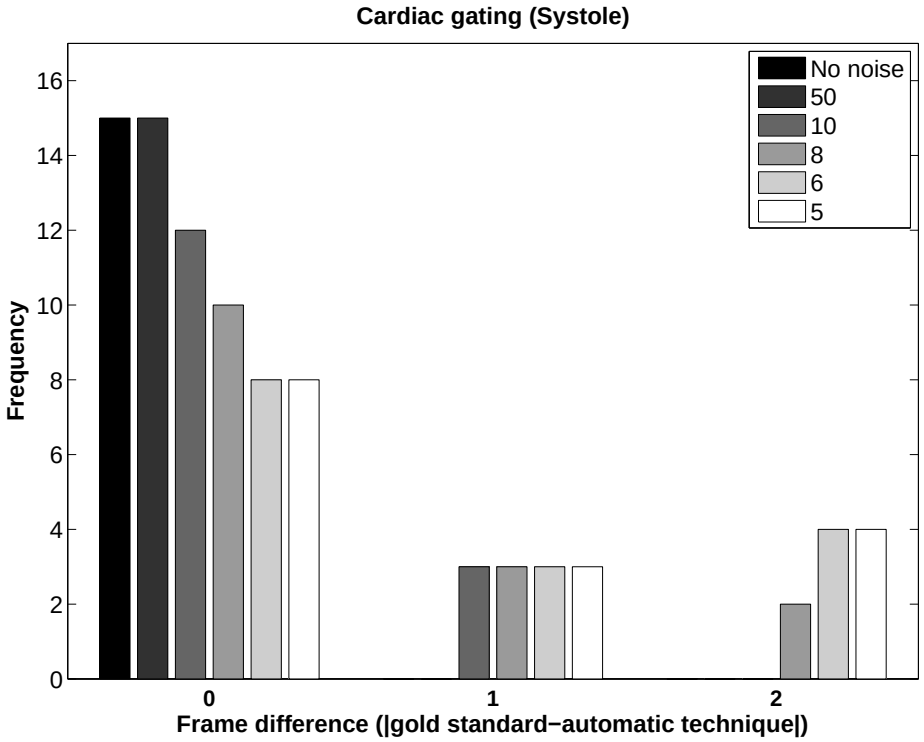

(a)

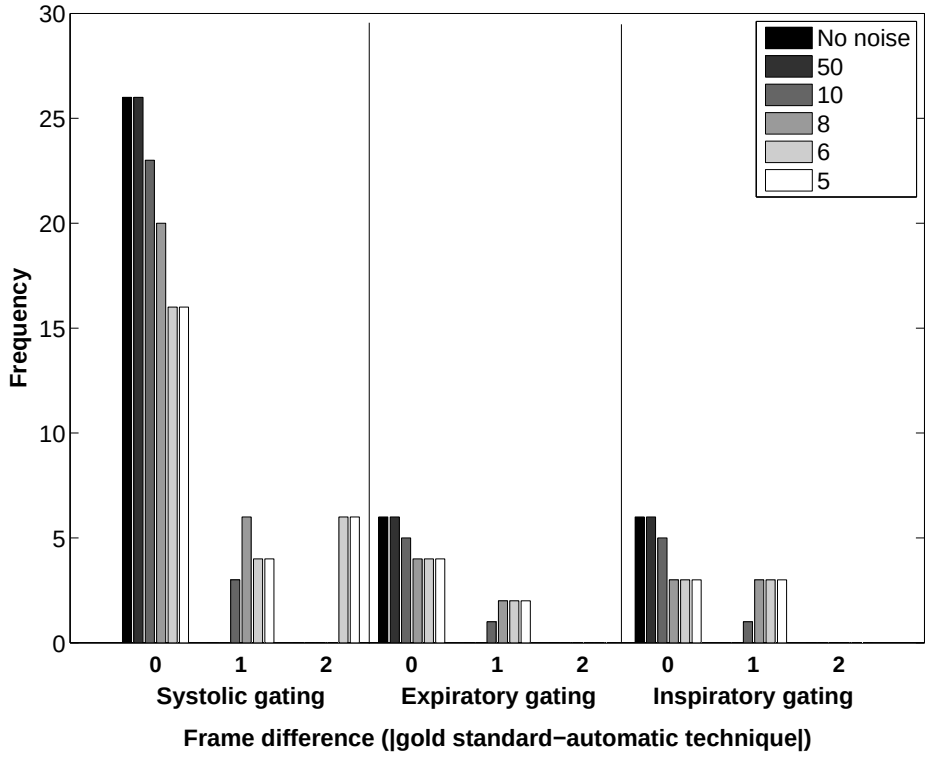

(b)

FIGURE 6.9: Frequency distributions of frame difference errors for cardiac gating for the uncorrupted and all five different SNR^2 X-ray images using the View-angle independent technique on (a) clinical rotational and (b) phantom datasets.

Respiratory motion compensation in the *training* view. In this section it is shown how the Tracked-PCA technique allows clinical application of real-time motion compensation in the *training* view. For this application, the fast multi-scale blob detector was used to detect all possible electrode-like objects in the X-ray images in the *training* view. The weights for the first two PCs, w_1 and w_2, that give a catheter position most similar to the detected blobs are determined. The framework of this is explained in detail in Chapter 3, Section 3.1.2.3. To compensate for respiratory motion, a 3D roadmap registered and overlaid onto an end-expiration and end-diastolic frame of an X-ray sequence is updated along the superior-inferior (head-to-foot) vector of the patient by the variation of w_2 throughout the X-ray sequence. The magnitude of the w_2 variation must be scaled to an appropriate level for the respiratory motion in the image. Here, this is done by matching the scaling for the 1^{st} half respiratory cycle of the image sequence to a separate measure derived using diaphragm tracking. The derived signal was scaled by a 1D motion scaling factor, which was set to 0.6 as in [243]. How to set the scaling is not considered in detail in this thesis, but one possibility is that manual motion scaling would be required in the clinical setting. Finally, the 3D heart roadmap is translated along the head-to-foot vector of the patient by the resulting 1D displacement.

Respiratory motion compensation at any view-angle. In this section it is shown how the View-angle independent technique allows clinical application of real-time motion compensation in a new image taken at any angle (*current* view). This works in the same way as in the *training* view, except that the weights, $\hat{w}_1$ and $\hat{w}_2$, now represent the cardiorespiratory phase of the image in the new view. They are estimated using the framework in Chapter 3, Section 3.4.2.2, which determines the weights that give epipolar lines in the new view most similar to the detected blobs. The resulting weights indicate the cardiorespiratory phases and the blobs nearest to the epipolar lines give the catheter location in the new image.

To compensate for cardiorespiratory motion, the 3D roadmap is translated along the superior-inferior (head-to-foot) vector of the patient by the variation of the 2^{nd} weight, w_2. Again, manual motion scaling is required.

6.4.2 Experiments

6.4.2.1 Clinical protocol

Pre-procedural image acquisition and segmentation. A high resolution free-breathing whole heart MRI scan was acquired (3D balanced turbo field echo (TFE), respiratory gated at end-expiration, cardiac triggered and gated at end-diastole). The image segmentation was performed using a shape model-based automatic segmentation algorithm [244]. This automatically

segmented the four cardiac chambers, the great vessels and the CS, taking less than 30 seconds. Manual adjustments were carried out, especially for the left atrium and CS due to anatomical variability. Furthermore, the tracheal bifurcation was manually segmented. The whole segmentation process took less than 5 minutes. Surface models were generated for each anatomical structure. Anatomical MR imaging was performed prior to the procedure for 5 patients undergoing RFA procedures for the treatment of AF.

Fluoroscopy overlay. The interventional guidance platform that was used was a prototype based on the commercial EP Navigator software (Philips Healthcare, Best, The Netherlands), illustrated in Figure 6.10a. This platform allowed for the manual registration of pre-procedural anatomical volumetric data onto live X-ray fluoroscopy to guide the cardiologist during the interventions. The initial registration of the MR derived anatomical models and the X-ray image was performed manually from X-ray images in EX and end-diastole using a combination of the CS catheter placed in the CS vessel and the tracheal bifurcation as corresponding features. The registration was assessed by experienced observers.

6.4.2.2 Motion compensation in both the *current* and the *training* views

Clinical application of motion compensation was done using the Tracked-PCA technique in the *training* view, where the model is built, using 4 clinical X-ray sequences (244 frames) of patients undergoing RFA procedures for the treatment of AF. This application is demonstrated using the leave-one-out cross-validation approach. This involves using a single frame from the original X-ray sequence as the validation data, and the remaining frames as the training data to build the statistical CS catheter model, for each of the frames in turn. The technique was validated on the end-diastolic frames (found manually) of the X-ray imaging sequences (73 frames). Additionally, by the use of the View-angle independent technique motion compensation was done in the *current* view, on 1 sequential biplane clinical X-ray sequence (AP and LAO30° views, 50 frames, 2 runs in total) from a patient undergoing an RFA procedure for the treatment of AF. Again, the technique was validated on the end-diastolic frames of the X-ray imaging sequences (9 frames). MR anatomical imaging was performed prior to these procedures.

Validation. To validate the motion compensation technique, the accuracy of the registration between the 3D roadmap and the 2D X-ray images was assessed and the improvement of the registration accuracy after motion correction was obtained. This was done by computing the 2D target registration errors (TREs) arising at the trachea bifurcation and the CS vessel at end-diastolic frames of the imaging sequences. Using the trachea bifurcation the TREs were easily computed as it is well visualised by X-ray fluoroscopy. However, the CS vessel is not visible in the X-ray fluoroscopy images. To compute the TRE the CS catheter is used, which acts as

TABLE 6.1: Average and maximum TRE (mm) values over all validation frames using the trachea bifurcation as a reference structure with and without motion compensation. The sequence type determines whether the sequence is a monoplane (M) or sequential biplane (SB) sequence.

With motion compensation		
Sequence type	Average error (mm)	Maximum error (m)
M	0.38	1
M	0.45	1.27
M	0.47	1.03
SB	0.36	1.09
SB	0.5	1.36
Without motion compensation		
M	0.56	1.45
M	0.59	1.68
M	0.69	1.28
SB	0.66	1.25
SB	0.67	1.75

a surrogate for the position of the centreline of the CS vessel since it is rigidly placed within this structure during the procedure. The TRE was computed as the distance error between the predicted position and the correct position of the two reference structures in the end-diastolic X-ray images. Specifically, two 2D B-spline curves were used to annotate the two structures in the projection of the 3D MR model and the X-ray fluoroscopy. The TRE was defined as the average 2D distance between the two B-spline curves.

6.4.3 Results

6.4.3.1 Motion compensation in the *current* and *training* views

The computed average and maximum TRE values over all validation frames are illustrated for each validation sequence in Tables 6.1 and 6.2 before and after motion correction using the trachea bifurcation and the CS, respectively. The sequence type determines whether the sequence is a monoplane or sequential biplane acquisition. Motion compensation of monoplane sequences was performed using the Tracked-PCA technique. Therefore, motion compensation was performed on the same view-angle in which the model was built. Motion compensation of sequential biplane sequences was performed using the View-angle independent technique. Therefore, it was performed on a different view-angle from the one in which the model was built.

Figure 6.10 illustrates a 3D MR model registered and overlaid onto an end-expiratory and end-diastolic frame of an example X-ray fluoroscopy sequence. The 3D model consists of the trachea (TR), the left atrium (LA), the right atrium (RA) and the coronary sinus (CS) vessel. In Figure 6.10a the platform used for the motion compensation is illustrated. The 3D anatomical structures are labelled. In Figure 6.10b, the 3D model is more transparent to allow for registration evaluation. Figure 6.11 illustrates the overlay of the 3D MR model of the trachea and the CS

TABLE 6.2: Average and maximum TRE (mm) values over all validation frames using the CS vessel as a reference structure with and without motion compensation. The sequence type determines whether the sequence is a monoplane (M) or sequential biplane (SB) sequence.

With motion compensation		
Sequence type	Average error (mm)	Maximum error (mm)
M	0.81	3.57
M	1.08	9.46
M	0.08	4.19
SB	1.24	7.19
SB	1.17	6.93
Without motion compensation		
M	7.43	20.96
M	7.08	25.15
M	7.43	20.96
SB	7.77	21.29
SB	7.32	21.42

vessel structures used for validation purposes on a different frame of the same example X-ray sequence without and with motion correction. In Figures 6.11a and 6.11b, the B-spline curves of the annotation of the trachea bifurcation are illustrated before and after motion correction, respectively, in both the 3D MR model, in green colour, and the X-ray fluoroscopy image, in blue colour. In Figures 6.11c and 6.11d the B-spline curves of the annotation of the CS are illustrated before and after motion correction, respectively, again in both the 3D MR model, in green colour, and the X-ray fluoroscopy image, in blue colour.

The execution time of the respiratory motion compensation in the *current* view was between 0.38 and 0.44 seconds per frame, and less than a second per image sequence in the *training* view. The X-ray imaging was performed at 3 frames per second per image sequence. Although the motion compensation is not sufficiently fast for real-time application, code optimisation could allow real-time application of the technique.

6.5 Discussion

In this chapter, preliminary experimental validation of the proposed techniques to more challenging clinical tasks is demonstrated. Initially, the clinical application of motion gating for performing 2D-3D registration of 3D cardiac data (CT or MRI) to X-ray fluoroscopy using interventional devices is considered. The 3D reconstruction of the interventional devices, required by the registration, has been demonstrated. The three developed methods: Tracked-PCA, HML-based and Masked-PCA, described in this thesis were tested using sequential biplane image sequences. Applying them on biplane image sequences the optimal phase-matched frame pairs

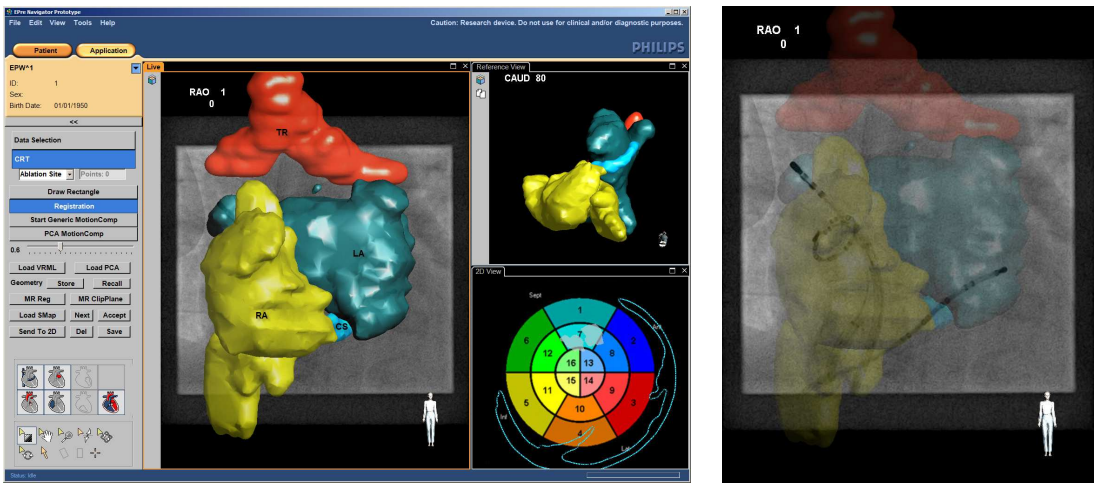

(a) (b)

FIGURE 6.10: Registration and overlay of a 3D MR model, consisting of TR, LA, RA and CS, onto an end-expiratory and end-diastolic frame of an example X-ray fluoroscopy sequence. In (a) the platform used for motion compensation is illustrated along with labelling of the anatomical 3D structures. In (b) the transparency of the 3D model is increased to allow for registration evaluation.

were determined to use for catheter and/or pacing lead reconstruction. It is illustrated in Figures 6.1 and 6.2 that the minimal reprojection errors arising from the automatic techniques are much more accurate than the minimal reprojection errors arising from manual frame matching.

Additionally, the application of a novel and potentially clinically useful View-angle independent gating technique has been demonstrated for the purpose of near-real-time cardiorespiratory gating of rotational X-ray fluoroscopic images. The technique was validated on 3 clinical rotational X-ray angiography sequences (341 frames) and 2 phantom rotational X-ray sequences (540 frames) at normal and low dose. For phantom images at normal dose, end-systolic, EX and EI gating success rates of 100% were established. For 3DRXA patient images, an end-systolic gating success rate of 100% was found. The technique was able to track the CS catheter with median errors not exceeding 1.0mm for successfully-tracked electrodes. On the other hand, for the application of the technique to the images corrupted by Poisson noise at the lowest SNR values of $\sqrt{5}$, an end-systolic gating success rate of 60.0% was computed for the clinical cases. Additionally, end-systolic, EX and EI success rates of 62.0%, 66.7% and 50.0%, respectively, for the phantom cases, were established. These outcomes show a deterioration of the performance of the technique in both CS catheter tracking and motion extraction at the lowest SNR values of $\sqrt{5}$. Furthermore, for the application of the technique to the noise corrupted sequences, the results illustrate that the technique is able to track the CS catheter with median errors not exceeding 2.0mm for successfully-tracked electrodes on both clinical and phantom datasets. As mentioned in Section 1.6, the tracking algorithms should be able to achieve these accuracies within this tolerance at least 90% of the time. The clinical and phantom experiments conducted in this chapter show that the View-angle independent technique can meet the accuracy objective

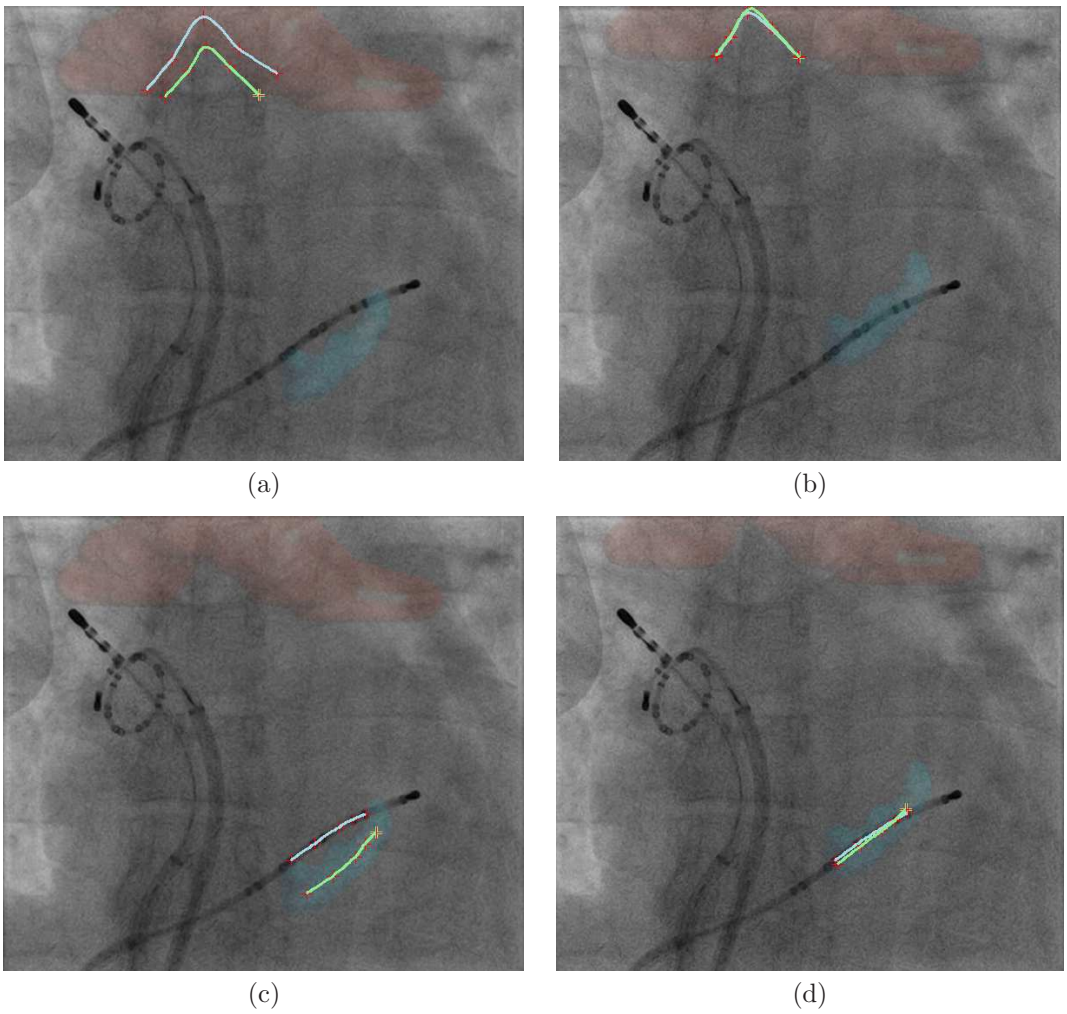

FIGURE 6.11: Overlay of a 3D MR model of the trachea and CS vessel onto X-ray fluoroscopy without and with motion correction. The B-spline curves of the annotation of the trachea bifurcation and the CS are illustrated in (a) and (c), respectively, before motion is corrected, in both the 3D MR model, in green colour, and the X-ray fluoroscopy image, in blue colour. The B-spline curves of the annotation of the trachea bifurcation and the CS are illustrated in (b) and (d), respectively, after correcting for the motion.

at SNR levels of $\sqrt{50}$ and above. However, even at normal dose and at the SNR level of $\sqrt{50}$, success rates fall below 90% for some electrodes. Therefore, within the constraints of these objectives, the rotation gating technique is not currently sufficiently robust and accurate in lower dose X-ray images.

To the author's knowledge the only view-angle independent work in the literature is proposed by Lehmann *et al.* [190]. This technique is capable of measuring coronary motion from the 2D projection images acquired during rotational angiography, with the aim of developing an image-based cardiac gating strategy specifically for 3D coronary angiography. The technique is described in Chapter 2, Section 2.3.3. Although it has the advantage of being view-angle independent, its robustness as a function of angle is not fully tested as the authors analysed data from only two views. Clinically, where small field-of-view X-ray image intensifier detectors

are used in coronary angiography, the background structures may move in and out of the field of view and it is important that the effect of this on the SIC measurement be minimised. An additional drawback of this technique is that it can only gate the cardiac motion of the heart. The utility of the technique in 3D coronary angiography has been demonstrated in an animal study. The success of the animal experiment is encouraging, but further analysis of 3D clinical angiograms is necessary.

On the other hand, validation of the View-angle independent technique, proposed in this thesis, for the purposes of motion gating and CS tracking in any view-angle, over the range of 180°, is demonstrated in this section. Experiments involve normal dose scenarios for rotational clinical and phantom acquisitions. As in earlier chapters, the main reason for the algorithm's catheter tracking and gating failures is the ineffectiveness of the blob detection algorithm at view-angles that distort the solid circular shape of the CS catheter electrodes, resulting in their misdetection. This occurs frequently in rotational sequences, which explains the reduced performance of the rotational gating technique compared to gating results in earlier chapters.

Finally, the clinical application of motion compensation in the *training* and *current* views is demonstrated, using the Tracked-PCA and View-angle independent techniques, respectively. Initially, motion compensation is demonstrated on images in the *training* view, where the model is built, using the Tracked-PCA technique, by integrating respiratory motion into MRI-derived roadmaps fused with live X-ray fluoroscopy. Motion compensation is then demonstrated on images taken at any arbitrary projection, using the View-angle independent technique. Anatomical localisation is crucial for the safety, accuracy and effectiveness of catheter guidance during EP procedures. The respiratory motion compensation was validated on 1 sequential biplane and 4 monoplane sequences. 2D TREs were calculated for validation using the trachea bifurcation and the CS vessel as reference structures and these were found to be 0.55mm and 1.03mm on average, respectively, after motion compensation. These values are well within the clinical accuracy requirement.

The experiments illustrate a promising outcome of the View-angle independent and Tracked-PCA techniques to potentially compensate for respiratory motion by updating 3D roadmaps overlaid on live X-ray fluoroscopy using images taken at any arbitrary projection thereby enhancing image guidance for cardiac interventions.

6.6 Conclusion

This chapter introduces a preliminary study of the application of the techniques devised and proposed in this thesis to more challenging clinical tasks. These tasks include 3D optically opaque object reconstruction, motion gating of 3DRXA and motion compensation. Even though

the experiments performed in this chapter demonstrate a very promising clinical translation of the proposed techniques, many of the addressed components need a more thorough and scientifically more rigorous validation before the integration of the techniques into clinical practice. Even though the final aim would be the application of the proposed methods in clinical routine, the focus of this thesis has been the development and the feasibility evaluation of such novel techniques, rather than evaluation of their clinical translation.

Chapter 7

Conclusions

Contents

A summary of the original contributions developed and validated in this thesis is presented in Section 7.1. Although examples of clinical applications of the proposed methods have been given in Chapter 6, Section 7.2 summarises the impact that the proposed techniques could have on clinical practice. In Section 7.3, an analysis of the current limitations of the proposed methods is provided, along with possible future directions that may help fulfil or extend beyond the thesis objectives. The chapter ends with concluding remarks, Section 7.4.

7.1 Summary

This thesis focused on and aims to address the problem of cardiac and respiratory motion in image-guided cardiac catheterisation procedures. Cardiac and respiratory motion causes misalignments between the static previously acquired roadmaps used for guidance and the intra-procedure moving anatomy, resulting in misleading guidance information. A viable solution to this problem is represented by cardiorespiratory motion gating/compensation techniques. However, to date these techniques remain mostly a research topic with very limited clinical uptake. The main reasons behind this lack of clinical translation lie in the lack of accuracy and robustness of the techniques proposed to date, and the increase in overall procedure time and radiation dose they bring to the interventional procedure. The underlying objective behind the work presented in this thesis is to address the limitations of previously proposed cardiorespiratory

motion gating/compensation techniques by devising novel and effective robust-to-noise methods that address the lack of accuracy/robustness and facilitate their clinical application.

The Tracked-PCA motion gating technique proposed in Chapter 3, and validated in both phantom and clinical datasets in Chapters 4 and 5 has proven to be accurate and robust in the extraction of cardiorespiratory motion information and CS catheter tracking even in very low dose X-ray fluoroscopic sequences. In particular, the application of the technique to clinical datasets is accurate to within 0.1s with a success rate of 92.9%, 73.7% and 71.8%, for end-systolic, EX and EI gating respectively, even at the low SNR value of $\sqrt{2}$. The proposed framework includes the formation of a novel statistical model of the motion of a CS catheter based on principal component analysis of tracked electrode locations from standard monoplane X-ray fluoroscopy images. The application of the model was demonstrated for the purposes of retrospective cardiac and respiratory gating of normal dose X-ray fluoroscopy images, and it was shown that a modification of the technique allows near real-time application in very low dose scenarios. Along with cardiorespiratory motion determination, this technique is able to track the CS catheter throughout the X-ray images.

The technique has proven to be more accurate than the recently proposed state-of-the-art techniques, i.e. the phase correlation [192] and real-time tracking [95, 96, 209] techniques, for motion estimation and CS catheter tracking, respectively. The gating success rates of the technique were computed to be 100.0%, 86.9% and 92.1% as opposed to 35.2%, 10.7% and 20.7% computed using the phase correlation technique for end-systolic, EX and EI, respectively, at normal dose. Additionally, the CS catheter tracking success rates per electrode did not fall below 90% at the SNR level of $\sqrt{5}$, which is the acceptable tolerance set in the objectives of this thesis, while at the same SNR level the Real-time tracking technique success rates were varying between 20-60% for the 10 CS catheter electrodes. The gain in accuracy is due to the robust framework used for the formation of the model during the calibration phase. The model provides sufficient constraints on the electrode locations to enable tracking to be successful even in very low dose X-ray images, and consequently, robust and accurate in the extraction of cardiorespiratory motion information.

The second novel contribution of this thesis is the HML-based technique, also proposed in Chapter 3, and validated in both phantom and clinical datasets in Chapters 4 and 5. This technique further facilitates clinical application since it is robust to varying image-content. Therefore, it is robust to typical EP X-ray images that can contain a varying number of different types of EP catheters and may include contrast agent injection. Unlike the Tracked-PCA technique, the HML-based technique is applicable to more types of minimally invasive procedures, such as CRT, where the CS catheter is not present in the X-ray images. Particularly, the technique is accurate to within 0.1s with success rates of 77.0%, 88.8% and 92.1%, for end-systolic, EX and EI gating, respectively, for its application to the low SNR value of $\sqrt{2}$. EX and EI gating success rates were significantly improved compared to the Tracked-PCA technique, which were found

to be 73.7% and 71.8%, respectively at the same SNR level. However, this robust to varying image content motion-gating technique came with a compromise of the end-systolic success rate obtained using the Tracked-PCA technique.

As the performance of the methods is essential in order to foster their clinical translation, a third motion gating technique was developed and presented in this thesis, in an attempt to increase the cardiac gating accuracy and robustness of the HML-based technique. The PCA statistical method is used in combination with other image processing operations to make the proposed Masked-PCA technique suitable for cardiorespiratory gating. Similar to the HML-based technique, this developed technique does not rely on specific catheters being present in the image data or the localisation of these devices, and makes no assumptions about the nature of the motion present in the images. The technique proved to be accurate to within 0.1s with success rates of 89.1%, 88.8% and 86.8%, for end-systolic, EX and EI, respectively, at the low SNR value of $\sqrt{2}$. Thus, the end-systolic gating success rates have significantly improved from 77.0% using the HML-based technique to 89.1% using the Masked-PCA technique, while respiratory gating success rates remain similar.

For both the HML-based and Masked-PCA techniques, the whole sequence must be collected before processing. Therefore, the techniques are intended for retrospective analysis. Both techniques are demonstrated for the purpose of motion gating on low dose images. As illustrated in the validation chapters of this thesis (Chapter 4 and Chapter 5), they are both robust-to-noise.

Finally, a View-angle independent motion gating technique was developed. This technique aimed to address the major limitation of the above and other model-based approaches proposed to date, which is the requirement to build a separate model for each X-ray view. The Tracked-PCA technique was significantly extended to make it X-ray system view-angle independent and therefore much more clinically useful. This approach is based on forming a PCA-based model of the CS catheter in a first or *training* view and then using this to determine both the cardiac and the respiratory phases in near-real time in any arbitrary second or *current* view. For the application, the method uses the epipolar constraint and a Euclidean distance/angle-based cost function. Using the model on images of the lowest SNR value of $\sqrt{5}$, the accuracy of the technique was found to be within 0.1s with success rates of 80.3%, 71.4% and 69.2%, for end-systolic, EX and EI, respectively. Even though the technique facilitates gating in cases where the angulation of the C-arm is changing it has the disadvantage of a lower robustness to decreasing the radiation dose.

Along with cardiorespiratory motion determination, this technique is able to track the CS catheter throughout the X-ray images, again in any arbitrary subsequent view. In particular, the success rates per electrode were computed to vary between 70-80%, at the SNR value of $\sqrt{5}$. Although success rates were decreased as compared to the Tracked-PCA technique, which were

found to be more than 90%, results are still better than the success rates computed using the Real-time tracking technique, which were found to vary between 20-60% for the 10 CS catheter electrodes.

7.2 Clinical impact

In this section, the potential impact of the proposed methods in terms of clinical applications is summarised.

Cardiac and respiratory motions provide a significant limitation to image-guided interventions applied to organs such as the heart.. As a result, misalignments are caused between the pre-procedure image-derived roadmap and the underlying cardiac anatomy. To guide diagnostic catheterization, structural heart interventions, and electrophysiology procedures it is essential to incorporate physiological motion into fused roadmaps.. Cardiac and respiratory motion gating techniques have been proposed as a solution by gating the X-ray acquisition at specific correct phases, i.e. EX/end-diastolic, and therefore eliminating the motion. For cardiorespiratory motion gating, the most commonly used approach is to limit image acquisition to the most quiescent cardiac and respiratory phase, which is usually end-diastole for cardiac motion and end-expiration for respiratory motion, and reject data acquired outside of the "cardiorespiratory gating window". Nevertheless, such techniques alone may be insufficient to adequately compensate for the respiratory motion. This is because they typically only provide relative information about cardiac and respiratory motion, which can be used to determine the cardiac and respiratory phases (systole or diastole and inspiration or expiration for the cardiac and respiratory motions, respectively) but not any absolute motion information, such as displacement, rotation, etc. Therefore, their usefulness for the purpose of cardiorespiratory motion correction is very limited.

In addition to generating gating information, the Tracked-PCA and View-angle independent techniques were able to track the position of the CS catheter throughout the sequence in normal and very low dose scenarios. For the Tracked-PCA technique the tracking is restricted to the view-angle where the statistical model was built. On the other hand, for the View-angle independent technique the gated electrode positions in the two views were used to reconstruct the 3D position of the CS catheter and then to track the catheter in very low dose X-ray images at the new angle. Correct CS electrode annotation is clinically useful in EP procedures for relating signals measured at the electrodes to locations on the anatomy. Additionally, for rotational acquisitions, the electrodes can be removed by replacing them with adjacent background prior to 3D reconstruction in an attempt to reduce motion artefacts.

The Tracked-PCA and View-angle independent techniques developed in this thesis are robust-to-noise, and therefore have the potential to greatly reduce radiation dose in image-guided cardiac catheter procedures. In fact, within the constraints of the thesis objectives, the achievable dose reduction factor is between $\frac{1}{10}$ and $\frac{1}{25}$ for the Tracked-PCA technique and around $\frac{1}{10}$ of the normal dose images for the View-angle independent technique, indicating the robustness of the techniques to noise. As a consequence, radiation to patients and staff will decrease significantly.

The research carried out in this thesis draws motivation from the clinical requirements in image-guided cardiac catheterisation procedures to overlay preoperatively acquired 3D anatomical data onto intra-operative X-ray. A second application for this work is the fusion of electroanatomical mapping (EAM) data acquired using electrophysiological (EP) mapping and navigation systems such as *EnSite* and *Carto* with preoperative data for biophysical modelling [90], using X-ray as an intermediary. Performing 2D/3D registration of 3D cardiac data (CT, MRI or EAM) to X-ray fluoroscopy using optically opaque objects seen in X-ray images, like vessels, interventional devices and more importantly catheters, is one essential clinical application of gating. As already mentioned in Chapter 6, interventional devices such as catheters and pacing leads must be reconstructed in 3D from biplane X-ray images. However, a biplane system is less common than a monoplane system in the clinical setting due to its much higher cost, and involves increased radiation exposure for both the patient and the clinician. In order to reconstruct interventional devices seen in X-ray images in 3D using a monoplane system, at least two oblique views must be acquired and phase-matched to the same cardiorespiratory phase. In this thesis, the Tracked-PCA, HML-based and Masked-PCA algorithms were demonstrated for the purpose of this application (Section 6.2).

The role of 3D image guidance for interventional procedures and minimally invasive surgeries is increasing for the treatment of vascular disease. Currently, most interventional procedures are guided by 2D X-ray fluoroscopy, but 3D rotational X-ray angiography (3DRXA) has the potential to offer clinicians quantitative volumetric information about anatomical structures that can be registered and overlaid onto X-ray fluoroscopy images, which is particularly suited to the clinical workflow [84]. The greatest challenge to the development of 3DRXA is the selection of an appropriate reconstruction strategy. Motion gating is required for the reconstruction of 3D coronary angiography data because the heart is beating during image acquisition. In order to decrease motion artefacts in the reconstructed volume, projections obtained when cardiac motion is minimal, and when the heart is at a similar phase in the motion cycle, must be selected for reconstruction. One technique for cardiac gating is by synchronising the fluoroscopic images with the electrocardiogram, indicating the phase of the cardiac cycle and inferring the extent of cardiac motion. Projection images acquired during a definite phase of the cardiac cycle are typically selected for reconstruction. However, as already mentioned in Chapter 2 of this thesis, this is normally an optional extra when purchasing an X-ray system and requires extra hardware.

Consequently, current methods are limited to breath-holding for respiration and either no gating for cardiac motion or arresting the heart using adenosine or rapid pacing [100]. Image-based gating would be advantageous in 3DRXA because it is a direct indicator of motion, rather than an inference. The View-angle independent motion gating technique could be used for motion gating of 3DRXA. Motion gating of sequences where the angulation of the scanner is changed between frames is a particularly important clinical application. Early-stage validation of this View-angle independent technique for the purposes of motion gating of any view-angle, over the range of 180°, in normal and low dose scenarios for rotational clinical and phantom acquisitions was demonstrated in Section 6.3 of this thesis.

The techniques proposed in this thesis illustrate application to motion compensation using gating, by gating the X-ray acquisition at specific correct phases, and therefore eliminating the motion. Even though only the peaks and troughs were used for gating, the proposed techniques are capable of detecting the whole cycle, and therefore, could potentially be used for real-time dynamic compensation. This thesis demonstrates preliminary experiments (Section 6.4) on the application of the proposed techniques to prospective motion compensation in both the *training* view where the model is built, using the Tracked-PCA technique, and in the *current* view, on images taking at any arbitrary projections using the View-angle independent technique, by integrating respiratory motion into MRI-derived roadmaps fused with live X-ray fluoroscopy. The 2D target registration errors (TREs) calculated for validation using the trachea bifurcation and the CS vessel as reference structures were found to be 0.55mm and 1.03mm on average, with maximum values of 1.36mm and 9.46mm, respectively, after motion compensation. These values are well within the clinical accuracy requirement.

7.3 Current limitations and future directions

In this section, the main limitations of the proposed methods are analysed. For each limitation, possible solutions that could represent future investigations are discussed and presented so that the clinical objectives are met or exceeded.

Real-time implementation of the Tracked-PCA motion gating technique on low dose X-ray images. The low dose technique as described in Chapter 3, Section 3.1.2.3 is developed to gate previously unseen frames based on a statistical model formed from normal dose images during a calibration phase. The gating technique is almost prospective, but would suffer from a time lag of 1 sample interval because of the need to identify peaks/troughs in the extracted signals. Therefore, the gating is in near real-time. Alternatively, it could be combined with a 'predict-ahead' technique [245] to eliminate the time lag. This would allow real-time gating.

Real-time implementation of the View-angle independent technique. In Chapter 3, Section 3.4 it is mentioned that the View-angle independent approach is based on forming a PCA-based model of the CS catheter in a first or *training* view and then using this to determine both the cardiac and the respiratory phases, in near real-time, in any arbitrary second or *current* view. Regarding the algorithm's performance on the different experiments, depending on the step size, the execution time was between 0.44 and 1.73 seconds per frame running in Matlab on Windows 7 with a 3.4 GHz Intel Core i7 CPU and 8 GB of RAM. Hence, real time implementation is not actually met. However, code optimisation was not the focus of this work and would need to be considered for real-time application. This includes the translation of the code to the C/C++ environment, as this will favour quicker execution times. Additionally, a decrease in execution time will favour real-time motion compensation in the secondary view in sequences where X-ray imaging is performed at three frames per second or faster.

Blob detection and CS catheter tracking. The Tracked-PCA and View-angle independent techniques make use of the blob detection algorithm implemented by Ma *et al.* [95, 96, 209] to detect blobs throughout the X-ray images. However, results indicate that this blob detection algorithm fails in low dose images and consequently this worsens the proposed algorithms' performance. Future work should aim to develop a new more accurate blob detection algorithm in an attempt to increase the % success rates of the techniques. This could be done by implementing a learning-based detection method such as the one proposed by Brost *et. al* [203]. The authors illustrate that learning-based approaches can reach a better performance if the training set is sufficiently comprehensive to capture all relevant catheter features encountered in clinical practice and that they are usually superior with respect to suppressing interfering structures that are not of interest. Additionally, for the Tracked-PCA and View-angle independent techniques the CS catheter tracking works by determining the weights for the first two PCs that give a catheter position most similar to the detected blobs. Euclidean distance-based and Euclidean distance/angle-based cost functions are designed for the Tracked-PCA and View-angle independent techniques, respectively. Future work could investigate closer integration of the blob detection code with the cost functions used for gating very low dose X-ray images, with a view to improving the success rate of the technique still further. For this application the effect of a more explicit catheter detection could be investigated, by including temporal constraints into the cost functions, i.e. the electrode will not move drastically between consecutive frames. Additionally, for a more comprehensive validation of the View-angle independent technique, a comparison to the technique proposed by Lehmann *et al.* [190], the only technique found in the literature that is also applicable to cases where the angulation of the scanner is changed between frames, should be done.

Clinical evaluation. The motivation of this thesis was to devise novel techniques to foster the uptake of cardiorespiratory motion gating techniques in clinical practice. Nevertheless,, the focus of this thesis was the development and the feasibility evaluation of such novel techniques, rather than their clinical evaluation. In fact, the results presented constitute a preliminary evaluation on a rather small sample of clinical imaging data. Specifically, for the application of the View-angle independent gating technique to rotational X-ray angiographic patient procedures, the validation was done only for cardiac gating as patients were in breath-hold. This might give better results than would otherwise be obtained when using patient data where both types of motion, cardiac and respiratory, are present. However, as current methods are limited to using breath-hold it is indeed difficult to obtain such patient data. For a more comprehensive validation, further extensive evaluation on additional patient data is required to test the robustness of the proposed methods. Such extensive evaluation was out of the scope of this thesis and should be a focus of future work.

Gold standard cardiac gating. In order to quantatively validate the cardiac gating methods, manual gating of the cardiac cycle at end-systole was performed by an experienced observer, by visually detecting the end of contraction of the left ventricle from the fluoroscopic left heart border shadow. Manual gating of the cardiac cycle at end-systole was further validated by another 4 observers who were trained to identify the end-systolic frames throughout the X-ray sequences. The end-systolic frame number was recorded and compared with the corresponding end-systolic frame number from the automatic detection. End-systole was chosen as opposed to diastole for validation since the manual ground truth is more reliable for end-systole where rapid motion can be used as the visual cue. The validity of this gold standard method might be discussed. Although five individual observers were asked to manually detect systolic frames and statistical analysis proved that the variability between the results obtained was extremely low, as indicated in Chapter 5, this does not completely exclude the possible presence of a human error. In the future, more observers could be included or a different gold standard strategy investigated.

Retrospective motion gating techniques. In this thesis, the HML-based technique has been applied to cardiac and respiratory signal extraction only retrospectively after all the images were acquired, which is not suitable for dynamic overlays. Future work could look at increasing robustness and developing the clinical translation of the technique. Specifically, this work could be extended to extract cardiorespiratory signals using hierarchical manifold learning (HML) from live X-ray sequences in real-time. This could be achieved by extracting the signals using incremental HML. Fischer *et al.* [191] proposed such a technique but with ISOMAP, which is a different manifold learning technique. Specifically, incremental HML could update the embedding without recomputing unchanged information. The eigendecomposition would not get computed

from scratch, but updated from the previous solution, assuming that the new point does not change the manifold and thus the eigenvectors and eigenvalues drastically. However, at least one full breathing cycle must be observed in a training phase of images at the beginning of the procedure before the mapping can give correct results. Therefore, a change of the C-arm angulation or the table position would invalidate the mapping, which must be relearned after each system movement. Similarly, this could be done for the Masked-PCA technique using an incremental PCA technique, developed accordingly.

Algorithms' validation. Currently, the validation framework of the techniques compares absolute frame differences between the techniques and the gold standard methods. It is understandable that for a normal heart rate, with sequences of 3 frames per second, it will not be too difficult to get an absolute frame difference of zero, and a frame difference of one might be considered too big. However, the techniques were also validated in sequences of 30 frames per second, where their performance is much more realistically measured. Future work might focus on computing a model that can interpolate the cardiac and respiratory traces in an attempt to provide a sub-sample value for the cardiac and respiratory phases, which would result in more meaningful comparisons.

HML-based cardiac gating performance. The HML-based technique illustrated a slightly lower cardiac gating performance than the other techniques presented in this thesis. Investigations show that the reason for optimising end-systolic gating on the specified patches is because of the inclusion of the heart border, a structure that carries significant cardiac motion information. Further work could look at modifying the technique by giving more emphasis to the importance of the heart border structure in an attempt to improve the end-systolic gating success rate.

Motion compensation. To perform motion compensation, the magnitude of the w_2 variation must be scaled to an appropriate level for the respiratory motion in the image. In this thesis, this was done by matching the scaling for the 1^{st} half respiratory cycle of the image sequence to a separate measure derived using diaphragm tracking. The derived signal was scaled by a 1D motion scaling factor, which was set to 0.6 as in [243]. How to set the scaling is not considered in detail in this thesis, but one possibility is to manually scale the motion in the clinical setting. Both this and the diaphragm method require manual input, but for an ideal clinical translation a fully automated workflow is preferred. One possibility is that the manual scaling could be replaced by calibrating the scaling using information extracted from a training sequence, perhaps using the y-translation of the electrodes.

7.4 Concluding remarks

The use of cardiorespiratory motion gating techniques is becoming more popular in catheterisation procedures, in order to provide overlays and for X-ray fluoroscopic fusion. As pointed out in this thesis, several reasons can explain the current lack of translation of motion gating techniques from research to the clinic. These include their lack of accuracy/robustness and proper validation on clinically realistic data. Most importantly the motion gating techniques proposed to date require high contrast X-ray images. This requires an increase in the radiation dose to the patients and the clinicians or the use of contrast agent, which can cause adverse reactions for the patient that range from mild to severe. Consequently, the clinicians might be reluctant to adapt and integrate such techniques in routine cardiac catheterisation procedures. The motion gating techniques proposed in this thesis not only show promising performance but also deal with the problem of radiation dose. As demonstrated in Chapters 4 and 5, the techniques have the advantage of being robust-to-noise. Therefore, they do not fail even on the very low dose images where $(SNR)^2$ was 5, representing a dose reduction of 10 times. Adapting and integrating the proposed techniques in routine cardiac catheterisation procedures has the potential to greatly reduce radiation dose. As a consequence radiation to patients and staff will decrease significantly.

It is the goal of the author to design and develop a software platform that will eventually be deployed routinely in the clinical environment to provide motion gating using the approaches presented in this thesis. A technique will be developed and embedded in this intelligent hybrid system that, based on the assessed X-ray sequence, could automatically detect the most appropriate method that should be used for motion gating. The Tracked-PCA technique will be used for cardiac gating of X-ray images where the CS catheter is present, while retrospective cardiac gating using Masked-PCA is the best option where the CS catheter is absent from the images. Where retrospective gating is acceptable, Masked-PCA will be used for respiratory gating regardless of image content, whereas Tracked-PCA is necessary if 'near real-time' gating is needed. The View-angle independent technique must be used for both cardiac and respiratory gating of sequences where the angulation of the scanner is changed between frames. The motion gating techniques will be fully automated, accurate, and robust and use only data from the clinical protocol, thereby providing the cardiologists with improved visual information to help guide the safe and accurate placement of catheters, while introducing minimal disruption to the clinical workflow.

Bibliography

[1] S. Yusuf, M. Flather, J. Pogue, D. Hunt, J. Varigos, L. Piegas, A. Avezum, J. Anderson, M. Keltai, A. Budaj, K. Fox, and L. Ceremuzynski, "Variations between countries in invasive cardiac procedures and outcomes in patients with suspected unstable angina or myocardial infarction without initial ST elevation," *The Lancet*, vol. 352, no. 9127, pp. 507–514, 1998.

[2] J. Fajadet and A. Chieffo, "Current management of left main coronary artery disease," *European Heart Journal*, vol. 33, no. 1, pp. 36–50, 2012.

[3] O. Birim, A. Bogers, and A. Kappetein, "Comparing cost aspects of coronary artery bypass graft surgery with coronary artery stenting.," *The Journal of Cardiovascular Surgery*, vol. 53, pp. 641–650, 10 2012.

[4] G. Lee, P. Sanders, and J. Kalman, "Catheter ablation of atrial arrhythmias: state of the art," *The Lancet*, vol. 380, no. 9852, pp. 1509–1519, 2012.

[5] T. Nitta, Y. Ishii, and S. Sakamoto, "Surgery for atrial fibrillation: recent progress and future perspective," *General Thoracic and Cardiovascular Surgery*, vol. 60, no. 1, pp. 13–20, 2012.

[6] M. MacDonald, *Your Body: The Missing Manual*. O'Reilly Media, Inc., 2009.

[7] I. Philip, P. Jeremy, and J. Michelle, *The Cardiovascular System at a Glance*. John Wiley and Sons, 2012.

[8] K. Robert, *Anatomy and Physiology: Understanding the Human Body*. Jones and Bartlett Publishers, 2005.

[9] M. Robert, *The Gross Physiology of the Cardiovascular System*. Tucson, AZ: Racquet Press, 1993.

[10] F. Martini, *Anatomy and Physiology*. Rex Bookstore, Inc., 2007.

[11] F. Netter and S. Colacino, *Atlas of human anatomy*. Ciba-Geigy Corporation, 1989.

[12] C. Starr, C. Evers, and L. Starr, *Biology Today and Tomorrow with Physiology*. Cengage Learning, 2009.

[13] R. Anderson, *The gross physiology of the cardiovascular system*. Robert Anderson, 1993.

[14] M. Antz, K. Otomo, M. Arruda, B. Scherlag, J. Pitha, C. Tondo, R. Lazzara, and W. Jackman, "Electrical conduction between the right atrium and the left atrium via the musculature of the coronary sinus," *Circulation*, vol. 98, no. 17, pp. 1790–1795, 1998.

[15] R. Ponti, S. Ho, J. Salerno-Uriarte, M. Tritto, and G. Spadacini, "Electroanatomic analysis of sinus impulse propagation in normal human atria," *Journal of Cardiovascular Electrophysiology*, vol. 13, no. 1, pp. 1–10, 2002.

[16] M. Vassalle, J. Karis, and B. F. Hoffman, "Toxic effects of ouabain on purkinje fibers and ventricular muscle fibers," *American Journal of Physiology–Legacy Content*, vol. 203, no. 3, pp. 433–439, 1962.

[17] G. Lines and B. Nielsen, *Computing the electrical activity in the heart*, vol. 1. Springer, 2007.

[18] J. Shaw-Dunn, "Essentials of human anatomy and physiology," *Journal of Anatomy*, vol. 179, p. 206, 1991.

[19] H. Huikuri, A. Castellanos, and R. Myerburg, "Sudden death due to cardiac arrhythmias," *New England Journal of Medicine*, vol. 345, no. 20, pp. 1473–1482, 2001.

[20] H. Calkins, J. Sousa, R. El-Atassi, S. Rosenheck, M. de Buitleir, W. Kou, A. Kadish, J. Langberg, and F. Morady, "Diagnosis and cure of the Wolff-Parkinson-White syndrome or paroxysmal supraventricular tachycardias during a single electrophysiologic test," *New England Journal of Medicine*, vol. 324, no. 23, pp. 1612–1618, 1991.

[21] B. Phibbs, *The human heart: a basic guide to heart disease*. Lippincott Williams and Wilkins, 2007.

[22] J. Willerson, H. Wellens, J. Cohn, and D. Holmes, *Cardiovascular Medicine*. Springer, 3rd ed., 2007.

[23] V. Fuster, L. Rydén, D. Cannom, H. Crijns, A. Curtis, K. Ellenbogen, J. Halperin, J.-Y. Le Heuzey, G. Kay, J. Lowe, S. Olsson, E. Prystowsky, J. Tamargo, and S. Wann, "ACC/AHA/ESC 2006 guidelines for the management of patients with atrial fibrillation—executive summarya report of the american college of cardiology/american heart association task force on practice guidelines and the european society of cardiology committee for practice guidelines (writing committee to revise the 2001 guidelines for the management of patients with atrial fibrillation) developed in collaboration with the european heart rhythm

association and the heart rhythm society," *Journal of the American College of Cardiology*, vol. 48, no. 4, pp. 854–906, 2006.

[24] H. Calkins, J. Brugada, D. Packer, R. Cappato, S. Chen, H. Crijns, R. Damiano, D. Davies, D. Haines, M. Haissaguerre, Y. Iesaka, W. Jackman, P. Jais, H. Kottkamp, K. Kuck, B. Lindsay, F. Marchlinski, P. McCarthy, J. Mont, F. Morady, K. Nademanee, A. Natale, C. Pappone, E. Prystowsky, A. Raviele, J. Ruskin, and R. Shemin, "HRS/EHRA/ECAS expert consensus statement on catheter and surgical ablation of atrial fibrillation: Recommendations for personnel, policy, procedures and follow-up a report of the heart rhythm society (HRS) task force on catheter and surgical ablation of atrial fibrillation developed in partnership with the european heart rhythm association (EHRA) and the european cardiac arrhythmia society (ECAS); in collaboration with the american college of cardiology (ACC), american heart association (AHA), and the society of thoracic surgeons (STS). endorsed and approved by the governing bodies of the american college of cardiology, the american heart association, the european cardiac arrhythmia society, the european heart rhythm association, the society of thoracic surgeons, and the heart rhythm society.," *Europace*, vol. 9, no. 6, pp. 335–379, 2007.

[25] R. Hart, O. Benavente, R. McBride, and L. Pearce, "Antithrombotic therapy to prevent stroke in patients with atrial fibrillation: A meta-analysis," *Arch. Intern. Med.*, vol. 154, p. 1449, 1994.

[26] S. Stewart, C. Hart, D. Hole, and J. McMurray, "A population-based study of the long-term risks associated with atrial fibrillation: 20-year follow-up of the renfrew/paisley study," *The American Journal of Medicine*, vol. 113, no. 5, pp. 359–364, 2002.

[27] W. Wattigney, G. Mensah, and J. Croft, "Increasing trends in hospitalization for atrial fibrillation in the united states, 1985 through 1999 implications for primary prevention," *Circulation*, vol. 108, no. 6, pp. 711–716, 2003.

[28] R. Klabunde, *Cardiovascular physiology concepts*. Lippincott Williams and Wilkins, 2011.

[29] G. Moe, W. Rheinboldt, and J. Abildskov, "A computer model of atrial fibrillation," *American Heart Journal*, vol. 67, no. 2, pp. 200–220, 1964.

[30] W. Garrey, "The nature of fibrillary contraction of the heart: its relation to tissue mass and form," *Am J Physiol*, vol. 33, pp. 397–414, 1914.

[31] K. Konings, C. Kirchhof, J. Smeets, H. Wellens, O. Penn, and M. Allessie, "High-density mapping of electrically induced atrial fibrillation in humans," *Circulation*, vol. 89, no. 4, pp. 1665–1680, 1994.

[32] M. HaIssaguerre, P. JaIs, D. Shah, A. Takahashi, M. Hocini, G. Quiniou, S. Garrigue, A. Le Mouroux, P. Le Métayer, and J. Clémenty, "Spontaneous initiation of atrial fibrillation by ectopic beats originating in the pulmonary veins," *New England Journal of Medicine*, vol. 339, no. 10, pp. 659–666, 1998. PMID: 9725923.

[33] M. Allessie, W. Lammers, J. Smeets, F. Bonke, and J. Hollen, "Total mapping of atrial excitation during acetylcholine-induced atrial flutter and fibrillation in the isolated canine heart," *Atrial Fibrillation. Molndal, Sweden: Lindgren and Soner*, pp. 44–62, 1982.

[34] D. Wilber, C. Pappone, P. Neuzil, A. De Paola, F. Marchlinski, A. Natale, L. Macle, E. Daoud, H. Calkins, B. Hall, V. Reddy, G. Augello, M. Reynolds, C. Vinekar, C. Y. Liu, S. Berry, and D. Berry, "Comparison of antiarrhythmic drug therapy and radiofrequency catheter ablation in patients with paroxysmal atrial fibrillation: A randomized controlled trial," *Jama*, vol. 303, no. 4, pp. 333–340, 2010.

[35] G. Bleeker, J. Bax, P. Steendijk, M. Schalij, and E. van der Wall, "Left ventricular dyssynchrony in patients with heart failure: pathophysiology, diagnosis and treatment," *Nature Clinical Practice Cardiovascular Medicine*, vol. 3, no. 4, 2006.

[36] C.-M. Yu and Q. Zhang, "Assessment of LV systolic dyssynchrony in heart failure beyond a snapshot," *JACC: Cardiovascular Imaging*, vol. 4, no. 5, pp. 457–459, 2011.

[37] S. Higgins, J. Hummel, I. Niazi, M. Giudici, S. Worley, L. Saxon, J. Boehmer, M. Higginbotham, T. De Marco, and E. Foster, "Cardiac resynchronization therapy for the treatment of heart failure in patients with intraventricular conduction delay and malignant ventricular tachyarrhythmias," *Journal of the American College of Cardiology*, vol. 42, no. 8, pp. 1454–1459, 2003.

[38] D. Kass, "An epidemic of dyssynchronybut what does it mean?," *Journal of the American College of Cardiology*, vol. 51, no. 1, pp. 12–17, 2008.

[39] J. Bax, G. Bleeker, T. Marwick, S. Molhoek, E. Boersma, P. Steendijk, E. Van Der Wall, and M. Schalij, "Left ventricular dyssynchrony predicts response and prognosis after cardiac resynchronization therapy," *Journal of the American College of Cardiology*, vol. 44, no. 9, pp. 1834–1840, 2004.

[40] T. Nagakura, M. Takeuchi, H. Yoshitani, H. Nakai, T. Nishikage, M. Kokumai, S. Otani, M. Yoshiyama, and J. Yoshikawa, "Hypertrophic cardiomyopathy is associated with more severe left ventricular dyssynchrony than is hypertensive left ventricular hypertrophy," *Echocardiography*, vol. 24, no. 7, pp. 677–684, 2007.

[41] S. Ghio, C. Constantin, C. Klersy, A. Serio, A. Fontana, C. Campana, and L. Tavazzi, "Interventricular and intraventricular dyssynchrony are common in heart failure patients, regardless of qrs duration," *European Heart Journal*, vol. 25, no. 7, pp. 571–578, 2004.

[42] W. Abraham and D. Hayes, "Cardiac resynchronization therapy for heart failure," *Circulation*, vol. 108, no. 21, pp. 2596–2603, 2003.

[43] C. Leclercq and D. Kass, "Retiming the failing heart: principles and current clinical status of cardiac resynchronization," *Journal of the American College of Cardiology*, vol. 39, no. 2, pp. 194–201, 2002.

[44] C.-M. Yu, E. Chau, J. Sanderson, K. Fan, M.-O. Tang, W.-H. Fung, H. Lin, S.-L. Kong, Y.-M. Lam, and M. Hill, "Tissue doppler echocardiographic evidence of reverse remodeling and improved synchronicity by simultaneously delaying regional contraction after biventricular pacing therapy in heart failure," *Circulation*, vol. 105, no. 4, pp. 438–445, 2002.

[45] K. Cleary and T. Peters, "Image-guided interventions: technology review and clinical applications," *Annual Review of Biomedical Engineering*, vol. 12, pp. 119–142, 2010.

[46] T. Peters, "Image-guidance for surgical procedures," *Physics in Medicine and Biology*, vol. 51, no. 14, p. R505, 2006.

[47] R. Mueller and T. Sanborn, "The history of interventional cardiology: Cardiac catheterization, angioplasty, and related interventions," *American Heart Journal*, vol. 129, no. 1, pp. 146–172, 1995.

[48] J. Meyer, "Werner forssmann and catheterization of the heart, 1929," *The Annals of Thoracic Surgery*, vol. 49, no. 3, pp. 497–499, 1990.

[49] M. Goerig and K. Agarwal, "Werner forssmann: The typical man before his time," *AINS*, vol. 43, no. 02, pp. 162–165, 2008.

[50] A. Manolis, V. Vassilikos, T. Maounis, H. Melita-Manolis, L. Psarros, A. Haliasos, and D. Cokkinos, "Detection of myocardial injury during radiofrequency catheter ablation by measuring serum cardiac troponin i levels: procedural correlates," *Journal of the American College of Cardiology*, vol. 34, pp. 1099–1105, 10 1999.

[51] C. Pappone, S. Rosanio, G. Oreto, M. Tocchi, F. Gugliotta, G. Vicedomini, A. Salvati, C. Dicandia, P. Mazzone, V. Santinelli, S. Gulletta, and S. Chierchia, "Circumferential radiofrequency ablation of pulmonary vein ostia a new anatomic approach for curing atrial fibrillation," *Circulation*, vol. 102, no. 21, pp. 2619–2628, 2000.

[52] K. Nademanee, J. McKenzie, E. Kosar, M. Schwab, B. Sunsaneewitayakul, T. Vasavakul, C. Khunnawat, and T. Ngarmukos, "A new approach for catheter ablation of atrial fibrillation: mapping of the electrophysiologic substrate," *Journal of the American College of Cardiology*, vol. 43, pp. 2044–2053, June 2004.

[53] S. Cazeau, C. Alonso, G. Jauvert, A. Lazarus, and P. Ritter, "Cardiac resynchronization therapy," *Europace*, vol. 5, no. s1, pp. S42–S48, 2003.

[54] F. Philippon, "Cardiac resynchronization therapy," *Journal of Cardiac Surgery*, vol. 19, no. 3, pp. 270–274, 2004.

[55] N. Wijesekera, M. Duncan, and S. Padley, "X-ray computed tomography of the heart," *British medical bulletin*, vol. 93, no. 1, pp. 49–67, 2010.

[56] R. Ionasec, I. Voigt, B. Georgescu, Y. Wang, H. Houle, F. Vega-Higuera, N. Navab, and D. Comaniciu, "Patient-specific modeling and quantification of the aortic and mitral valves from 4-D cardiac CT and TEE," *IEEE Transactions on Medical Imaging,*, vol. 29, no. 9, pp. 1636–1651, 2010.

[57] C. Stehning, P. Boernert, and K. Nehrke, "Advances in coronary MRA from vessel wall to whole heart imaging.," *Magnetic Resonance in Medical Sciences: MRMS: an official journal of Japan Society of Magnetic Resonance in Medicine*, vol. 6, no. 3, pp. 157–170, 2006.

[58] V. Mor-Avi, L. Sugeng, and R. Lang, "Real-time 3-Dimensional echocardiography an integral component of the routine echocardiographic examination in adult patients," *Circulation*, vol. 119, no. 2, pp. 314–329, 2009.

[59] M. Orlov, P. Hoffmeister, G. Chaudhry, I. Almasry, G. Gijsbers, T. Swack, and C. Haffajee, "Three-dimensional rotational angiography of the left atrium and esophagus—a virtual computed tomography scan in the electrophysiology lab," *Heart Rhythm*, vol. 4, no. 1, pp. 37–43, 2007.

[60] K. Rhode, Y. Ma, J. Housden, R. Karim, C. Rinaldi, M. Cooklin, J. Gill, M. O'Neill, T. Schaeffter, J. Relan, M. Sermesant, H. Delingette, N. Ayache, M. Kruger, W. Schulze, G. Seemann, O. Dossel, and R. Razavi, "Clinical applications of image fusion for electrophysiology procedures," in *Biomedical Imaging (ISBI), 2012 9th IEEE International Symposium on*, pp. 1435–1438, 2012.

[61] S. Shpun, L. Gepstein, G. Hayam, and S. Ben-Haim, "Guidance of radiofrequency endocardial ablation with real-time three-dimensional magnetic navigation system," *Circulation*, vol. 96, no. 6, pp. 2016–2021, 1997.

[62] M. Earley, R. Showkathali, M. Alzetani, P. Kistler, D. Gupta, D. Abrams, J. Horrocks, S. Harris, S. Sporton, and R. Schilling, "Radiofrequency ablation of arrhythmias guided by non-fluoroscopic catheter location: a prospective randomized trial," *European Heart Journal*, vol. 27, no. 10, pp. 1223–1229, 2006.

[63] M. Daccarett, N. Segerson, J. Günther, G. Nolker, K. Gutleben, J. Brachmann, and N. Marrouche, "Blinded correlation study of three-dimensional electro-anatomical image integration and phased array intra-cardiac echocardiography for left atrial mapping," *Europace*, vol. 9, no. 10, pp. 923–926, 2007.

[64] C. Fantoni, M. Kawabata, R. Massaro, F. Regoli, S. Raffa, V. Arora, J. Salerno-Uriarte, H. Klein, and A. Auricchio, "Right and left ventricular activation sequence in patients with heart failure and right bundle branch block: a detailed analysis using three-dimensional non-fluoroscopic electroanatomic mapping system," *Journal of Cardiovascular Electrophysiology*, vol. 16, no. 2, pp. 112–119, 2005.

[65] D. Packer, "Three-dimensional mapping in interventional electrophysiology: techniques and technology.," *Journal of Cardiovascular Electrophysiology*, vol. 16, no. 10, p. 1110, 2005.

[66] D. Bhakta and J. Miller, "Principles of electroanatomic mapping," *Indian Pacing and Electrophysiology Journal*, vol. 8, no. 1, p. 32, 2008.

[67] W. Saliba, V. Reddy, O. Wazni, J. Cummings, J. Burkhardt, M. Haissaguerre, J. Kautzner, P. Peichl, P. Neuzil, and V. Schibgilla, "Atrial fibrillation ablation using a robotic catheter remote control systeminitial human experience and long-term follow-up results," *Journal of the American College of Cardiology*, vol. 51, no. 25, pp. 2407–2411, 2008.

[68] R. Hunter and R. Schilling, "Long-term outcome after catheter ablation for atrial fibrillation: safety, efficacy and impact on prognosis," *Heart*, vol. 96, no. 16, pp. 1259–1263, 2010.

[69] M. Koa-wing, P. Kojodjojo, L. Malcome-Lawes, T. Salukhe, N. Linton, A. Grogan, D. Bergman, P. Lim, Z. Whinnett, and K. McCarthy, "Robotically assisted ablation produces more rapid and greater signal attenuation than manual ablation," *Journal of cardiovascular electrophysiology*, vol. 20, no. 12, pp. 1398–1404, 2009.

[70] S. Ito, "X-ray fluoroscopic system," 2010.

[71] J. Kennedy, S. Trenholme, and I. Kasser, "Left ventricular volume and mass from single-plane cineangiocardiogram. a comparison of anteroposterior and right anterior oblique methods," *American Heart Journal*, vol. 80, no. 3, pp. 343–352, 1970.

[72] C. Linte, P. Lang, M. Rettmann, D. Cho, D. Holmes III, R. Robb, and T. Peters, "Accuracy considerations in image-guided cardiac interventions: experience and lessons learned," *International journal of computer assisted radiology and surgery*, vol. 7, no. 1, pp. 13–25, 2012.

[73] L. Lickfett, M. Mahesh, C. Vasamreddy, D. Bradley, V. Jayam, Z. Eldadah, T. Dickfeld, D. Kearney, D. Dalal, B. Lüderitz, R. Berger, and H. Calkins, "Radiation exposure during catheter ablation of atrial fibrillation," *Circulation*, vol. 110, no. 19, pp. 3003–3010, 2004.

[74] S. De Buck, F. Maes, J. Ector, J. Bogaert, S. Dymarkowski, H. Heidbuchel, and P. Suetens, "An augmented reality system for patient-specific guidance of cardiac catheter ablation procedures," *IEEE Transactions on Medical Imaging*, vol. 24, pp. 1512–24, 2005.

[75] L. F. Gutiérrez, R. d. Silva, C. Ozturk, M. Sonmez, A. M. Stine, A. N. Raval, V. K. Raman, V. Sachdev, R. J. Aviles, M. A. Waclawiw, E. R. McVeigh, and R. J. Lederman, "Technology preview: X-ray fused with magnetic resonance during invasive cardiovascular procedures," *Catheterization and Cardiovascular Interventions*, vol. 70, no. 6, pp. 773–782, 2007.

[76] K. Rhode, M. Sermesant, D. Brogan, S. Hegde, J. Hipwell, P. Lambiase, E. Rosenthal, C. Bucknall, S. Qureshi, J. Gill, R. Razavi, and D. Hill, "A system for real-time XMR guided cardiovascular intervention," *IEEE Transactions on Medical Imaging*, vol. 24, no. 11, pp. 1428–1440, 2005.

[77] H. Yu, R. Fahrig, and N. Pelc, "Co-registration of X-ray and MR fields of view in a hybrid XMR system," *Journal of Magnetic Resonance Imaging*, vol. 22, no. 2, pp. 291–301, 2005.

[78] L. Brzozowski, A. Ganguly, M. Pop, Z. Wen, R. Bennett, R. Fahrig, and J. Rowlands, "Compatibility of interventional X-ray and magnetic resonance imaging: Feasibility of a closed bore XMR (CBXMR) system," *Medical Physics*, vol. 33, no. 8, pp. 3033–3045, 2006.

[79] J. Sra, G. Narayan, D. Krum, and M. Akhtar, "Registration of 3D computed tomographic images with interventional systems implications for catheter ablation of atrial fibrillation," *Journal of Interventional Cardiac Electrophysiology*, vol. 16, no. 3, pp. 141–148, 2006.

[80] S. Knecht, H. Skali, M. O'neill, M. Wright, S. Matsuo, G. Chaudhry, C. Haffajee, I. Nault, G. Gijsbers, and F. Sacher, "Computed tomography–fluoroscopy overlay evaluation during catheter ablation of left atrial arrhythmia," *Europace*, vol. 10, no. 8, pp. 931–938, 2008.

[81] J. Ector, S. D. Buck, W. Huybrechts, D. Nuyens, S. Dymarkowski, J. Bogaert, F. Maes, and H. Heidbuechel, "Biplane three-dimensional augmented fluoroscopy as single navigation tool for ablation of atrial fibrillation: accuracy and clinical value," *Heart Rhythm*, vol. 5, no. 7, pp. 957–964, 2008.

[82] E. Krestel, *Imaging systems for medical diagnostics: fundamentals and technical solutions*. Siemens Aktiengesellschaft, 1990.

[83] P. Hertrich, *Practical Radiography*. John Wiley and Sons, 2005.

[84] J. Li, M. Haim, B. Movassaghi, J. Mendel, G. Chaudhry, C. Haffajee, and M. Orlov, "Segmentation and registration of three-dimensional rotational angiogram on live fluoroscopy to guide atrial fibrillation ablation: A new online imaging tool," in *Heart Rhythm* (2, ed.), pp. 231–237, 2009.

[85] A. Al-Ahmad, L. Wigstrom, D. Sandner-Porkristl, P. Wang, P. Zei, J. Boese, G. Lauritsch, T. Moore, F. Chan, and R. Fahrig, "Time-resolved three-dimensional imaging of the left atrium and pulmonary veins in the interventional suite—a comparison between multisweep

gated rotational three-dimensional reconstructed fluoroscopy and multislice computed tomography," *Heart Rhythm*, vol. 5, no. 4, pp. 1547–5271, 2008.

[86] M. Prummer, J. Hornegger, G. Lauritsch, L. Wigstrom, E. Girard-Hughes, and R. Fahrig, "Cardiac C-arm CT: a unified framework for motion estimation and dynamic CT," *Medical Imaging, IEEE Transactions on*, vol. 28, no. 11, pp. 1836–1849, 2009.

[87] K. Rhode, D. L. G. Hill, P. Edwards, J. Hipwell, D. Rueckert, G. Sanchez-Ortiz, S. Hegde, V. Rahunathan, and R. Razavi, "Registration and tracking to integrate X-ray and MR images in an XMR facility," *Medical Imaging, IEEE Transactions on*, vol. 22, pp. 1369–1378, November 2003.

[88] J. Sra, G. Narayan, D. Krum, A. Malloy, R. Cooley, A. Bhatia, A. Dhala, Z. Blanck, V. Nangia, and M. Akhtar, "Computed tomography-fluoroscopy image integration-guided catheter ablation of atrial fibrillation," *Journal of Cardiovascular Electrophysiology*, vol. 18, no. 4, pp. 409–414, 2007.

[89] M. Truong, T. Gordon, R. Razavi, G. Penney, and K. Rhode, "Analysis of catheter-based registration with vessel-radius weighting of 3D CT data to 2D X-ray for cardiac catheterisation procedures in a phantom study," in *Statistical Atlases and Computational Models of the Heart. Imaging and Modelling Challenges*, vol. 7085 of *Lecture Notes in Computer Science*, pp. 139–148, Springer Berlin Heidelberg, 2012.

[90] M. Sermesant, R. Chabiniok, P. Chinchapatnam, T. Mansi, F. Billet, P. Moireau, and N. Ayache, "Patient-specific electromechanical models of the heart for the prediction of pacing acute effects in CRT: A preliminary clinical validation.," *Medical Image Analysis*, vol. 16, no. 1, pp. 201–215, 2012.

[91] M. Sermesant, J.-M. Peyrat, P. Chinchapatnam, F. Billet, T. Mansi, K. Rhode, H. Delingette, R. Razavi, and N. Ayache, "Toward patient-specific myocardial models of the heart," *Heart Failure Clinics*, vol. 4, no. 3, pp. 289–301, 2008. Function Follows Form.

[92] R. Kerckhoffs, *Patient Specific Modeling of the Cardiovascular System*. Springer, 2010.

[93] M. Esteghamatian, Z. Azimifar, P. Radau, and G. Wright, "Real-time 2D-3D MR cardiac image registration during respiration using extended kalman filter predictors," in *Signal Processing, 2008. ICSP 2008. 9th International Conference on*, pp. 1325–1328, October 2008.

[94] A. King, R. Boubertakh, K. Rhode, Y. M. Y.L., P. Chinchapatnam, G. Gao, T. Tangcharoen, M. Ginks, M. Cooklin, J. Gill, D. Hawkes, R. Razavi, and T. Schaeffter, "A subject-specific technique for respiratory motion correction in image-guided cardiac catheterisation procedures," *Medical Image Analysis*, vol. 13, no. 3, pp. 419–431, 2009a.

[95] Y. Ma, A. King, N. Gogin, G. Gijsbers, C. Rinaldi, J. Gill, R. Razavi, and K. Rhode, "Clinical evaluation of respiratory motion compensation for anatomical roadmap guided cardiac electrophysiology procedures," *IEEE Transactions on Biomedical Engineering*, vol. 59, no. 1, pp. 122–131, 2012.

[96] Y. Ma, A. King, N. Gogin, G. Gijsbers, C. Rinaldi, J. Gill, R. Razavi, and K. Rhode, "Comparing image-based respiratory motion correction methods for anatomical roadmap guided cardiac electrophysiology procedures," in *Functional Imaging and Modeling of the Heart* (D. Metaxas and L. Axel, eds.), vol. 6666 of *Lecture Notes in Computer Science*, pp. 55–62, Springer Berlin Heidelberg, 2011.

[97] K. Bhatia, A. Rao, A. Price, R. Wolz, J. Hajnal, and D. Rueckert, "Hierarchical manifold learning," in *Medical Image Computing and Computer-Assisted Intervention – MICCAI* (N. Ayache, H. Delingette, P. Golland, and K. Mori, eds.), vol. 7510 of *Lecture Notes in Computer Science*, pp. 512–519, Springer Berlin Heidelberg, 2012.

[98] R. Manzke, A. Lutz, M. Schenderlein, A. Bornstedt, R. Chan, K. Dietmeyer, and V. Rasche, "A new PVA-based dynamic cardiac phantom for evaluation of functional MR imaging methods at 3T," in *ISMRM Proceedings*, 2010.

[99] M. Truong, A. Aslam, M. Ginks, C. Rinaldi, R. Rezavi, G. Penney, and K. Rhode, "2D-3D registration of cardiac images using catheter constraints," in *Computers in Cardiology, 2009*, pp. 605–608, September 2009.

[100] C. Kriatselis, S. Nedios, S. Akrivakis, M. Tang, M. Roser, J.-H. Gerds-Li, E. Fleck, and M. Orlov, "Intraprocedural imaging of left atrium and pulmonary veins: A comparison study between rotational angiography and cardiac computed tomography," *Pacing and Clinical Electrophysiology*, vol. 34, no. 3, pp. 315–322, 2011.

[101] D. Ruijters, R. Homan, P. Mielekamp, P. van de Haar, and D. Babic, "Validation of 3D multimodality roadmapping in interventional neuroradiology," *Physics in Medicine and Biology*, vol. 56, no. 16, p. 5335, 2011.

[102] K. McLeish, D. Hill, D. Atkinson, J. Blackall, and R. Razavi, "A study of the motion and deformation of the heart due to respiration," *Medical Imaging, IEEE Transactions on*, vol. 21, no. 9, pp. 1142–1150, 2002.

[103] K. Nieman, M. Oudkerk, B. Rensing, P. van Ooijen, A. Munne, R.-V. van Geuns, and P. de Feyter, "Coronary angiography with multi-slice computed tomography," *The Lancet*, vol. 357, no. 9256, pp. 599–603, 2001.

[104] M. Paling and J. Brookeman, "Respiration artifacts in MR imaging: reduction by breath holding," *Journal of Computer Assisted Tomography*, vol. 10, no. 6, pp. 1080–1082, 1986.

[105] G. S. Mageras and E. Yorke, "Deep inspiration breath hold and respiratory gating strategies for reducing organ motion in radiation treatment," *Seminars in Radiation Oncology*, vol. 14, no. 1, pp. 65–75, 2004. High-Precision Radiation Therapy of Moving Targets.

[106] D. Mah, J. Hanley, K. Rosenzweig, E. Yorke, L. Braban, C. Ling, S. Leibel, and G. Mageras, "Technical aspects of the deep inspiration breath-hold technique in the treatment of thoracic cancer," *International Journal of Radiation Oncology Biology Physics*, vol. 48, no. 4, pp. 1175–1185, 2000.

[107] K. Rosenzweig, J. Hanley, D. Mah, G. Mageras, M. Hunt, S. Toner, C. Burman, C. Ling, B. Mychalczak, and Z. Fuks, "The deep inspiration breath-hold technique in the treatment of inoperable non–small-cell lung cancer," *International Journal of Radiation Oncology Biology Physics*, vol. 48, no. 1, pp. 81–87, 2000.

[108] K. Sixel, M. Aznar, and Y. Ung, "Deep inspiration breath hold to reduce irradiated heart volume in breast cancer patients," *International Journal of Radiation Oncology Biology Physics*, vol. 49, no. 1, pp. 199–204, 2001.

[109] J. Wong, M. Sharpe, D. Jaffray, V. Kini, J. Robertson, J. Stromberg, and A. Martinez, "The use of active breathing control (ABC) to reduce margin for breathing motion," *International Journal of Radiation Oncology Biology Physics*, vol. 44, no. 4, pp. 911–919, 1999.

[110] E. Barnes, B. Murray, D. Robinson, L. Underwood, J. Hanson, and W. Roa, "Dosimetric evaluation of lung tumor immobilization using breath hold at deep inspiration," *International Journal of Radiation Oncology Biology Physics*, vol. 50, no. 4, pp. 1091–1098, 2001.

[111] C. Biancia, E. Yorke, C. Chui, P. Giraud, K. Rosenzweig, H. Amols, C. Ling, and G. Mageras, "Comparison of end normal inspiration and expiration for gated intensity modulated radiation therapy (IMRT) of lung cancer," *Radiotherapy and Oncology*, vol. 75, no. 2, pp. 149–156, 2005.

[112] K. Herfarth, J. Debus, F. Lohr, M. Bahner, B. Rhein, P. Fritz, A. Hoss, W. Schlegel, and M. Wannenmacher, "Stereotactic single-dose radiation therapy of liver tumors: results of a phase I/II trial," *Journal of Clinical Oncology*, vol. 19, no. 1, pp. 164–170, 2001.

[113] H. Timinger, S. Krueger, J. Borgert, and R. Grewer, "Motion compensation for interventional navigation on 3D static roadmaps based on a dynamic motion model," *International Congress Series*, vol. 1268, p. 1055, 2004.

[114] H. Timinger, S. Krueger, K. Dietmayer, and J. Borgert, "Motion compensated coronary interventional navigation by means of diaphragm tracking and elastic motion models," *Physics in Medicine and Biology*, vol. 50, no. 3, p. 491, 2005.

[115] A. Khamene, J. Warzelhan, S. Vogt, D. Elgort, C. Chefd Hotel, J. Duerk, J. Lewin, F. Wacker, and F. Sauer, "Characterization of internal organ motion using skin marker positions," in *Medical Image Computing and Computer-Assisted Intervention – MICCAI* (C. Barillot, D. Haynor, and P. Hellier, eds.), vol. 3217 of *Lecture Notes in Computer Science*, pp. 526–533, Springer Berlin Heidelberg, 2004.

[116] V. Kini, P. Keall, S. Vedam, D. Arthur, B. Kavanagh, R. Cardinale, and R. Mohan, "Preliminary results from a study of a respiratory motion tracking system: Underestimation of target volume with conventional CT simulation," *International Journal of Radiation Oncology Biology Physics*, vol. 48, no. 3, p. 164, 2000.

[117] C. Ramsey, D. Scaperoth, and D. Arwood, "Clinical experience with a commercial respiratory gating system," *International Journal of Radiation Oncology Biology Physics*, vol. 48, no. 3, pp. 164–165, 2000.

[118] S. Vedam, P. Keall, V. Kini, and R. Mohan, "Determining parameters for respiration-gated radiotherapy," *Medical Physics*, vol. 28, no. 10, pp. 2139–2146, 2001.

[119] E. Ford, G. Mageras, E. Yorke, K. Rosenzweig, R. Wagman, and C. Ling, "Evaluation of respiratory movement during gated radiotherapy using film and electronic portal imaging," *International Journal of Radiation Oncology Biology Physics*, vol. 52, no. 2, pp. 522–531, 2002.

[120] P. Keall, G. Starkschall, H. Shukla, K. Forster, V. Ortiz, C. Stevens, S. Vedam, R. George, T. Guerrero, and R. Mohan, "Acquiring 4D thoracic CT scans using a multislice helical method," *Physics in Medicine and Biology*, vol. 49, no. 10, p. 2053, 2004.

[121] C. Nelson, G. Starkschall, P. Balter, M. Fitzpatrick, J. Antolak, N. Tolani, and K. Prado, "Respiration-correlated treatment delivery using feedback-guided breath hold: a technical study," *Medical Physics*, vol. 32, no. 1, pp. 175–181, 2004.

[122] R. Berbeco, S. Nishioka, H. Shirato, G. Chen, and S. Jiang, "Residual motion of lung tumours in gated radiotherapy with external respiratory surrogates," *Physics in Medicine and Biology*, vol. 50, no. 16, p. 3655, 2005.

[123] A. George, M. Sonmez, R. Lederman, and A. Faranesh, "Robust automatic rigid registration of MRI and X-ray using external fiducial markers for XFM-guided interventional procedures," *Medical Physics*, vol. 38, no. 1, pp. 125–141, 2010.

[124] R. Ehman, M. McNamara, M. Pallack, H. Hricak, and C. Higgins, "Magnetic resonance imaging with respiratory gating: techniques and advantages," *American journal of roentgenology*, vol. 143, no. 6, pp. 1175–1182, 1984.

[125] D. Atkinson, M. Burcher, J. Declerck, and J. Noble, "Respiratory motion compensation for 3-D freehand echocardiography," *Ultrasound in Medicine and Biology*, vol. 27, no. 12, pp. 1615–1620, 2001.

[126] S. Jiang and K. Doppke, "Dosimetric effect of respiratory motion on the treatment of breast cancer with tangential fields," *Medical Physics*, vol. 28, no. 1228, 2001.

[127] P. Giraud, S. Helfre, V. Servois, B. Dubray, C. Beigelman-Grenier, G. Zalcman-Liwartoski, C. Straus-Zelter, S. Neuenschwander, J. Rosenwald, and J. Cosset, "Evaluation of intrathoracic organs mobility using CT gated by a spirometer," *Radiotherapy Oncology*, vol. 56, 2000.

[128] T. Zhang, H. Keller, M. J. O'Brien, T. Mackie, and B. Paliwal, "Application of the spirometer in respiratory gated radiotherapy," *Medical Physics*, vol. 30, no. 12, pp. 3165–3171, 2003.

[129] M. Van Herk, C. Scheider, J. Sonke, E. Damen, and K. DeJaeger, "Respiration-correlated CT of lung cancer patients," *Radiotherapy Oncology*, vol. 64, pp. 80–81, 2002.

[130] L. Dietrich, S. Jetter, T. Tucking, S. Nill, and U. Oelfke, "Linac-integrated 4D cone beam CT: first experimental results," *Physics in Medicine and Biology*, vol. 51, no. 11, p. 2939, 2006.

[131] T. Kleshneva, J. Muzik, and M. Alber, "An algorithm for automatic determination of the respiratory phases in four-dimensional computed tomography," *Physics in Medicine and Biology*, vol. 51, no. 16, p. N269, 2006.

[132] S. Ahn, B. Yi, Y. Suh, J. Kim, S. Lee, S. Shin, and E. Choi, "A feasibility study on the prediction of tumour location in the lung from skin motion," *The British Journal of Radiology*, vol. 77, no. 919, pp. 588–596, 2004.

[133] J. Hoisak, K. Sixel, R. Tirona, P. Cheung, and J.-P. Pignol, "Correlation of lung tumor motion with external surrogate indicators of respiration," *International Journal of Radiation Oncology Biology Physics*, vol. 60, no. 4, pp. 1298–1306, 2004.

[134] Y. Tsunashima, T. Sakae, Y. Shioyama, K. Kagei, T. Terunuma, A. Nohtomi, and Y. Akine, "Correlation between the respiratory waveform measured using a respiratory sensor and 3D tumor motion in gated radiotherapy," *International Journal of Radiation Oncology Biology Physics*, vol. 60, no. 3, pp. 951–958, 2004.

[135] D. Gierga, J. Brewer, G. Sharp, M. Betke, C. Willett, and G. Chen, "The correlation between internal and external markers for abdominal tumors: implications for respiratory gating," *International Journal of Radiation Oncology Biology Physics*, vol. 61, no. 5, pp. 1551–1558, 2005.

[136] H. Yan, F.-F. Yin, G.-P. Zhu, M. Ajlouni, and J. Kim, "The correlation evaluation of a tumor tracking system using multiple external markers," *Medical Physics*, vol. 33, no. 11, pp. 4073–4084, 2006.

[137] D. Gierga, G. Sharp, J. Brewer, M. Betke, C. Willett, and G. Chen, "Correlation between external and internal markers for abdominal tumors: implications for respiratory gating," *International Journal of Radiation Oncology Biology Physics*, vol. 57, no. 2, pp. S186–S187, 2003.

[138] H. Shirato, T. Harada, T. Harabayashi, K. Hida, H. Endo, K. Kitamura, R. Onimaru, K. Yamazaki, N. Kurauchi, and T. Shimizu, "Feasibility of insertion/implantation of 2.0-mm-diameter gold internal fiducial markers for precise setup and real-time tumor tracking in radiotherapy," *International Journal of Radiation Oncology Biology Physics*, vol. 56, no. 1, pp. 240–247, 2003.

[139] K. Kitamura, H. Shirato, S. Shimizu, N. Shinohara, T. Harabayashi, T. Shimizu, Y. Kodama, H. Endo, R. Onimaru, and S. Nishioka, "Registration accuracy and possible migration of internal fiducial gold marker implanted in prostate and liver treated with real-time tumor-tracking radiation therapy (RTRT)," *Radiotherapy and Oncology*, vol. 62, no. 3, pp. 275–281, 2002.

[140] C. Nelson, G. Starkschall, P. Balter, R. Morice, C. Stevens, and J. Chang, "Assessment of lung tumor motion and setup uncertainties using implanted fiducials," *International Journal of Radiation Oncology Biology Physics*, vol. 67, no. 3, pp. 915–923, 2007.

[141] P. Kellman, C. Chefd'hotel, C. Lorenz, C. Mancini, A. Arai, and E. McVeigh, "Fully automatic, retrospective enhancement of real-time acquired cardiac cine MR images using image-based navigators and respiratory motion-corrected averaging," *Magnetic Resonance in Medicine*, vol. 59, no. 4, pp. 771–778, 2008.

[142] R. Van der Weide, C. Bakker, and M. Viergever, "Localization of intravascular devices with paramagnetic markers in MR images," *Medical Imaging, IEEE Transactions on*, vol. 20, no. 10, pp. 1061–1071, 2001.

[143] Y. Wang, P. Rossman, R. Grimm, S. Riederer, and R. Ehman, "Navigator-echo-based real-time respiratory gating and triggering for reduction of respiration effects in three-dimensional coronary MR angiography.," *Radiology*, vol. 198, no. 1, pp. 55–60, 1996.

[144] R. Ehman and J. Felmlee, "Adaptive technique for high-definition MR imaging of moving structures.," *Radiology*, vol. 173, no. 1, pp. 255–263, 1989.

[145] C. Wachinger, M. Yigitsoy, and N. Navab, "Manifold learning for image-based breathing gating with application to 4D ultrasound," in *Medical Image Computing and Computer-Assisted Intervention – MICCAI 2010* (T. Jiang, N. Navab, J. Pluim, and M. Viergever,

eds.), vol. 6362 of *Lecture Notes in Computer Science*, pp. 26–33, Springer Berlin Heidelberg, 2010.

[146] C. Wachinger, M. Yigitsoy, E.-J. Rijkhorst, and N. Navab, "Manifold learning for image-based breathing gating in ultrasound and MRI," *Medical Image Analysis*, vol. 16, no. 4, pp. 806–818, 2012.

[147] D. Manke, K. Nehrke, P. Bornert, P. Rosch, and O. Dossel, "Respiratory motion in coronary magnetic resonance angiography: a comparison of different motion models," *Journal of Magnetic Resonance Imaging*, vol. 15, no. 6, pp. 661–671, 2002.

[148] D. Manke, K. Nehrke, and P. Bornert, "Novel prospective respiratory motion correction approach for free-breathing coronary MR angiography using a patient-adapted affine motion model," *Magnetic Resonance in Medicine*, vol. 50, no. 1, pp. 122–131, 2003.

[149] K. Nehrke and P. Bornert, "Prospective correction of affine motion for arbitrary MR sequences on a clinical scanner," *Magnetic Resonance in Medicine*, vol. 54, no. 5, pp. 1130–1138, 2005.

[150] S. De Winter, R. Hamers, M. Degertekin, K. Tanabe, P. Lemos, P. Serruys, J. R. T. C. Roelandt, and N. Bruining, "A novel retrospective gating method for intracoronary ultrasound images based on image properties," in *Computers in Cardiology, 2003*, pp. 13–16, September 2003.

[151] H. Zhu, K. Oakeson, and M. Friedman, *Retrieval of cardiac phase from IVUS sequences*, vol. 5035. International Society for Optics and Photonics, 2003.

[152] K. Karadayi, T. Hayashi, and Y. Kim, "Automatic image-based gating for 4d ultrasound," in *Engineering in Medicine and Biology Society, 2006. EMBS'06. 28th Annual International Conference of the IEEE*, pp. 2388–2391, IEEE, 2006.

[153] D. Ballard, "Generalizing the hough transform to detect arbitrary shapes," *Pattern Recognition*, vol. 13, no. 2, pp. 111–122, 1981.

[154] M. Van Horn, W. Snyder, G. Braden, and D. Herrington, "Intracoronary ultrasound catheter motion compensation using the generalized hough transform," in *Computers in Cardiology*, pp. 293–296, IEEE, 1994.

[155] G. Isguder, G. Unal, M. Groher, N. Navab, A. Kalkan, M. Degertekin, H. Hetterich, and J. Rieber, "Manifold learning for image-based gating of intravascular ultrasound (IVUS) pullback sequences," in *Medical Imaging and Augmented Reality* (H. Liao, P. Edwards, X. Pan, Y. Fan, and G.-Z. Yang, eds.), vol. 6326 of *Lecture Notes in Computer Science*, pp. 139–148, Springer Berlin Heidelberg, 2010.

[156] A. King, C. Jansen, K. Rhode, D. Caulfield, R. Razavi, and G. Penney, "Respiratory motion correction for image-guided cardiac interventions using 3-D echocardiography," *Medical Image Analysis*, vol. 14, no. 1, pp. 21–29, 2010.

[157] A. King, K. Rhode, Y. Ma, C. Yao, C. Jansen, R. Razavi, and G. Penney, "Registering preprocedure volumetric images with intraprocedure 3-D ultrasound using an ultrasound imaging model," *IEEE Transactions on Medical Imaging*, vol. 29, no. 3, pp. 924–937, 2010c.

[158] D. Peressutti, E. J. Rijkhorst, D. C. Barratt, G. P. Penney, and A. P. King, "Estimating and resolving uncertainty in cardiac respiratory motion modelling," in *Biomedical Imaging (ISBI), 2012 9th IEEE International Symposium on*, pp. 262–265, May 2012.

[159] D. Peressutti, G. Penney, R. Housden, C. Kolbitsch, A. Gomez, E.-J. Rijkhorst, D. Barratt, K. Rhode, and A. King, "A novel bayesian respiratory motion model to estimate and resolve uncertainty in image-guided cardiac interventions," *Medical Image Analysis*, vol. 17, no. 4, pp. 488–502, 2013.

[160] M. Georg, R. Souvenir, A. Hope, and R. Pless, "Manifold learning for 4D CT reconstruction of the lung," in *Computer Vision and Pattern Recognition Workshops, 2008. CVPRW'08. IEEE Computer Society Conference on*, pp. 1–8, IEEE, 2008.

[161] G. Carnes, S. Gaede, E. Yu, J. Van Dyk, J. Battista, and T.-Y. Lee, "A fully automated non-external marker 4D-CT sorting algorithm using a serial cine scanning protocol," *physics in Medicine and Biology*, vol. 54, no. 7, p. 2049, 2009.

[162] K. Eck, J. Bredno, and T. Stehle, "Absolute alignment of breathing states using image similarity derivatives," in *Medical Imaging*, vol. 5744, pp. 79–86, 2005.

[163] C. Chavarrias, J. Vaquero, A. Sisniega, A. Rodriguez-Ruano, M. Soto-Montenegro, and M. Desco, "Validation of a retrospective respiratory gating method for small-animal CT scanners," in *Nuclear Science Symposium Conference Record, 2008. NSS'08. IEEE*, pp. 4303–4305, IEEE, 2008.

[164] T. Farncombe, "Software-based respiratory gating for small animal conebeam CT," *Medical Physics*, vol. 35, no. 5, pp. 1785–1792, 2008.

[165] J. Hu, S. Haworth, R. Molthen, and C. Dawson, "Dynamic small animal lung imaging via a postacquisition respiratory gating technique using micro-cone beam computed tomography¡ sup¿ 1¡/sup¿," *Academic Radiology*, vol. 11, no. 9, pp. 961–970, 2004.

[166] J.-J. Sonke, L. Zijp, P. Remeijer, and M. van Herk, "Respiratory correlated cone beam CT," *Medical Physics*, vol. 32, no. 4, pp. 1176–1186, 2005.

[167] R. Manzke, T. Kohler, T. Nielsen, D. Hawkes, and M. Grass, "Automatic phase determination for retrospectively gated cardiac CT," *Medical Physics*, vol. 31, no. 12, pp. 3345–3362, 2004.

[168] G. Klein, B. Reutter, E. Botvinick, T. Budinger, and R. Huesman, "Fine-scale motion detection using intrinsic list mode PET information," in *Mathematical Methods in Biomedical Image Analysis, MMBIA, IEEE Workshop on*, pp. 71–78, IEEE, 2001.

[169] R. Bundschuh, A. Martinez-Moeller, M. Essler, M.-J. Martinez, S. Nekolla, S. Ziegler, and M. Schwaiger, "Postacquisition detection of tumor motion in the lung and upper abdomen using list-mode PET data: a feasibility study," *Journal of Nuclear Medicine*, vol. 48, no. 5, pp. 758–763, 2007.

[170] P. Bruyant, M. King, and P. Pretorius, "Correction of the respiratory motion of the heart by tracking of the center of mass of thresholded projections: a simulation study using the dynamic MCAT phantom," *Nuclear Science, IEEE Transactions on*, vol. 49, no. 5, pp. 2159–2166, 2002.

[171] F. Büther, M. Dawood, L. Stegger, F. Wubbeling, M. Schafers, O. Schober, and K. Schafers, "List mode–driven cardiac and respiratory gating in pet," *Journal of Nuclear Medicine*, vol. 50, no. 5, pp. 674–681, 2009.

[172] D. Visvikis, O. Barret, T. Fryer, A. Turzo, F. Lamare, C. Cheze Le Rest, and Y. Bizais, "A posteriori respiratory motion gating of dynamic PET images," in *Nuclear Science Symposium Conference Record, IEEE*, vol. 5, pp. 3276–3280, IEEE, 2003.

[173] J. He, G. O'Keefe, S. Gong, G. Jones, T. Saunder, A. Scott, and M. Geso, "A novel method for respiratory motion gated with geometric sensitivity of the scanner in 3D PET," *Nuclear Science, IEEE Transactions on*, vol. 55, no. 5, pp. 2557–2565, 2008.

[174] K. Thielemans, S. Rathore, F. Engbrant, and P. Razifar, "Device-less gating for PET/CT using PCA," in *Nuclear Science Symposium and Medical Imaging Conference (NSS/MIC)*, pp. 3904–3910, 2011.

[175] A. King, C. Tsoumpas, C. Buerger, V. Schulz, P. Marsden, and T. Schaeffter, "Real-time respiratory motion correction for simultaneous PET-MR using an MR-derived motion model," in *Nuclear Science Symposium and Medical Imaging Conference (NSS/MIC), 2011 IEEE*, pp. 3589–3594, IEEE, 2011b.

[176] A. King, C. Buerger, C. Tsoumpas, P. Marsden, and T. Schaeffter, "Thoracic respiratory motion estimation from MRI using a statistical model and a 2-D image navigator," *Medical Image Analysis*, vol. 16, no. 1, pp. 252–264, 2012.

[177] B. Martin-Leung, K. Eck, I. Stuke, J. Bredno, and T. Aach, "Mutual information based respiration detection," *Computer Assisted Radiology and Surgery. Proceedings of the 17th International Congress and Exhibition*, vol. 1256, no. 0, pp. 1085–1092, 2003.

[178] T. Netsch, P. Rosch, A. van Muiswinkel, and J. Weese, "Towards real-time multi-modality 3-D medical image registration," in *Computer Vision, 2001. ICCV 2001. Proceedings. Eighth IEEE International Conference on*, vol. 1, pp. 718–725, IEEE, 2001.

[179] T. Moser, J. Biederer, S. Nill, G. Remmert, and R. Bendl, "Detection of respiratory motion in fluoroscopic images for adaptive radiotherapy," *Physics in Medicine and Biology*, vol. 53, no. 12, p. 3129, 2008.

[180] R. I. Berbeco, H. Mostafavi, G. C. Sharp, and S. B. Jiang, "Towards fluoroscopic respiratory gating for lung tumours without radiopaque markers," *Physics in Medicine and Biology*, vol. 50, no. 19, p. 4481, 2005.

[181] A. Condurache, T. Aach, K. Eck, J. Bredno, and T. Stehle, "Fast and robust diaphragm detection and tracking in cardiac X-ray projection images," in *Proceedings of SPIE Medical Imaging*, vol. 5747, pp. 1766–1775, SPIE, 2005.

[182] G. Shechter, C. Ozturk, and J. Resar, "Respiratory motion of the heart from free breathing coronary angiograms," *IEEE Transactions on Medical Imaging*, vol. 23, no. 8, pp. 1046–1056, 2004.

[183] G. Shechter, B. Shechter, J. Resar, and R. Beyar, "Prospective motion correction of X-ray images for coronary interventions," *Medical Imaging, IEEE Transactions on*, vol. 24, no. 4, pp. 441–450, 2005.

[184] M. Schneider, H. Sundar, R. Liao, J. Hornegger, and C. Xu, "Model-based respiratory motion compensation for image-guided cardiac interventions," in *Computer Vision and Pattern Recognition (CVPR), 2010 IEEE Conference on*, pp. 2948–2954, 2010.

[185] A. King, K. Rhode, R. Razavi, and T. Schaeffter, "An adaptive and predictive respiratory motion model for image-guided interventions: Theory and first clinical application," *Medical Imaging, IEEE Transactions on*, vol. 28, pp. 2020–2032, December 2009b.

[186] Y. Zhu, Y. Tsin, H. Sundar, and F. Sauer, "Image-based respiratory motion compensation for fluoroscopic coronary roadmapping," in *Medical Image Computing and Computer-Assisted Intervention – MICCAI 2010* (T. Jiang, N. Navab, J. Pluim, and M. Viergever, eds.), vol. 6363 of *Lecture Notes in Computer Science*, pp. 287–294, Springer Berlin Heidelberg, 2010.

[187] A. Faranesh, P. Kellman, K. Ratnayaka, and R. Lederman, "Integration of cardiac and respiratory motion into MRI roadmaps fused with x-ray," *Medical Physics*, vol. 40, no. 3, 2013.

[188] J. McClelland, D. Hawkes, T. Schaeffter, and A. King, "Respiratory motion models: A review," *Medical Image Analysis*, vol. 17, no. 1, pp. 19–42, 2013.

[189] A. Schweikard, G. Glosser, M. Bodduluri, M. Murphy, and J. Adler, "Robotic motion compensation for respiratory movement during radiosurgery," *Computer Aided Surgery*, vol. 5, no. 4, pp. 263–277, 2000.

[190] G. Lehmann, D. Holdsworth, and M. Drangova, "Angle-independent measure of motion for image-based gating in 3D coronary angiography," *Medical Physics*, vol. 33, no. 5, pp. 1311–1320, 2006.

[191] P. Fischer, T. Pohl, and J. Hornegger, "Real-time respiratory signla extraction from X-ray sequences using incremental manifold learning," in *ISBI*, 2014.

[192] H. Sundar, A. Khamene, L. Yatziv, W. Wein, and C. Xu, "Automatic image-based cardiac and respiratory cycle synchronization and gating of image sequences," in *Medical Image Computing and Computer-Assisted Intervention – MICCAI* (G. Yang, D. Hawkes, D. Rueckert, A. Noble, and C. Taylor, eds.), vol. 5762 of *Lecture Notes in Computer Science*, pp. 381–88, Springer Berlin Heidelberg, 2009.

[193] E. Meijering, W. Niessen, and M. Viegever, "Retrospective motion correction in digital subtraction angiography: a review," *Medical Imaging, IEEE Transactions on*, vol. 18, no. 1, pp. 2–21, 1999.

[194] S. Baert, M. Viergever, and W. Niessen, "Guide-wire tracking during endovascular interventions," *Medical Imaging, IEEE Transactions on*, vol. 22, no. 8, pp. 965–972, 2003.

[195] P. Wang, Y. Zhu, W. Zhang, T. Chen, P. Durlak, U. Bill, and D. Comaniciu, "Hierarchical guidewire tracking in fluoroscopic sequences," in *SPIE Medical Imaging*, pp. 72591L–72591L–8, International Society for Optics and Photonics, 2009.

[196] E. Franken, P. Rongen, M. van Almsick, and B. ter Haar Romeny, "Detection of electrophysiology catheters in noisy fluoroscopy images," in *Medical Image Computing and Computer-Assisted Intervention–MICCAI*, vol. 4191 of *Lecture Notes in Computer Science*, pp. 25–32, Springer Berlin Heidelberg, 2006.

[197] P. Fallavollita, P. Savard, and G. Sierra, "Fluoroscopic navigation to guide RF catheter ablation of cardiac arrhythmias," in *Engineering in Medicine and Biology Society, 2004. IEMBS'04. 26th Annual International Conference of the IEEE*, vol. 1, pp. 1929–1932, IEEE, 2004.

[198] W. Wu, T. Chen, A. Barbu, P. Wang, N. Strobel, S. Zhou, and D. Comaniciu, "Learning-based hypothesis fusion for robust catheter tracking in 2D X-ray fluoroscopy," in *Computer*

Vision and Pattern Recognition (CVPR), 2011 IEEE Conference on, pp. 1097–1104, IEEE, 2011.

[199] L. Yatziv, M. Chartouni, S. Datta, and G. Sapiro, "Toward multiple catheters detection in fluoroscopic image guided interventions," *Information Technology in Biomedicine, IEEE Transactions on*, vol. 16, no. 4, pp. 770–781, 2012.

[200] F. Milletari, N. Navab, and P. Fallavollita, "Automatic detection of multiple and overlapping EP catheters in fluoroscopic sequences," in *Medical Image Computing and Computer-Assisted Intervention – MICCAI 2013* (K. Mori, I. Sakuma, Y. Sato, C. Barillot, and N. Navab, eds.), vol. 8151 of *Lecture Notes in Computer Science*, pp. 371–379, Springer Berlin Heidelberg, 2013.

[201] A. Brost, R. Liao, N. Strobel, and J. Hornegger, "3D respiratory motion compensation during EP procedures by image-based 3-D lasso catheter model generation and tracking," in *Medical Image Computing and Computer-Assisted Intervention–MICCAI* (S. B. Heidelberg, ed.), vol. 5761, pp. 394–401, 2009.

[202] A. Brost, R. Liao, and J. Hornegger, "Respiratory motion compensation by model-based catheter tracking during EP procedures," *Medical Image Analysis*, vol. 14, no. 5, pp. 695–706, 2010a.

[203] A. Brost, A. Wimmer, R. Liao, J. Hornegger, and N. Strobel, "Catheter tracking: Filter-based vs. learning-based," in *Pattern Recognition* (M. Goesele, S. Roth, A. Kuijper, B. Schiele, and K. Schindler, eds.), vol. 6376 of *Lecture Notes in Computer Science*, pp. 293–302, Springer Berlin Heidelberg, 2010b.

[204] A. Brost, R. Liao, J. Hornegger, and N. Strobel, "Model-based registration for motion compensation during EP ablation procedures," in *Biomedical Image Registration* (B. Fischer, B. Dawant, and C. Lorenz, eds.), vol. 6204 of *Lecture Notes in Computer Science*, pp. 234–245, Springer Berlin Heidelberg, 2010c.

[205] A. Brost, W. Wu, M. Koch, A. Wimmer, T. Chen, R. Liao, J. Hornegger, and N. Strobel, "Combined cardiac and respiratory motion compensation for atrial fibrillation ablation procedures," in *Medical Image Computing and Computer-Assisted Intervention – MICCAI 2011* (G. Fichtinger, A. Martel, and T. Peters, eds.), vol. 6891 of *Lecture Notes in Computer Science*, pp. 540–547, Springer Berlin Heidelberg, 2011a.

[206] A. Brost, A. Wimmer, R. Liao, J. Hornegger, and N. Strobel, "Motion compensation by registration-based catheter tracking," in *Proceedings of SPIE Medical Imaging*, vol. 7964, pp. 79641O–79641O, 2011b.

[207] A. Brost, A. Wimmer, R. Liao, J. Hornegger, and N. Strobel, "Constrained 2-D/3-D registration for motion compensation in AFib ablation procedures," *Information Processing in Computer-Assisted Interventions*, pp. 133–144, 2011c.

[208] A. Brost, F. Bourier, A. Wimmer, M. Koch, A. Kiraly, R. Liao, K. Kurzidim, J. Hornegger, and N. Strobel, "Real-time circumferential mapping catheter tracking for motion compensation in atrial fibrillation ablation procedures," in *SPIE Medical Imaging*, pp. 83162V–83162V–6, International Society for Optics and Photonics, 2012.

[209] Y. Ma, A. King, N. Gogin, C. Rinaldi, J. Gill, R. Razavi, and K. Rhode, "Real-time respiratory motion correction for cardiac electrophysiology procedures using image-based coronary sinus catheter tracking," in *Medical Image Computing and Computer-Assisted Intervention–MICCAI* (T. Jiang, N. Navab, J. Pluim, and M. Viergever, eds.), vol. 6361 of *Lecture Notes in Computer Science*, pp. 391–399, Springer Berlin Heidelberg, 2010.

[210] P. Viola and M. Jones, "Robust real-time face detection," *International Journal of Computer Vision*, vol. 57, no. 2, pp. 137–154, 2004.

[211] Y. Ma, G. Gao, G. Gijsbers, C. Rinaldi, J. Gill, R. Razavi, and K. Rhode, "Image-based automatic ablation point tagging system with motion correction for cardiac ablation procedures," in *Information Processing in Computer-Assisted Interventions* (R. Taylor and G.-Z. Yang, eds.), vol. 6689 of *Lecture Notes in Computer Science*, pp. 145–155, Springer Berlin Heidelberg, 2011a.

[212] Y. Ma, N. Gogin, P. Cathier, R. Housden, G. Gijsbers, M. Cooklin, M. O'Neill, J. Gill, C. Rinaldi, R. Razavi, and K. Rhode, "Real-time x-ray fluoroscopy-based catheter detection and tracking for cardiac electrophysiology interventions," *Medical Physics*, vol. 40, no. 7, p. 071902, 2013.

[213] S. Kaeppler, A. Brost, M. Koch, W. Wu, F. Bourier, T. Chen, K. Kurzidim, J. Hornegger, and N. Strobel, "Motion estimation model for cardiac and respiratory motion compensation," in *Information Processing in Computer-Assisted Interventions*, pp. 94–103, Springer, 2012.

[214] K. Bhatia, A. Rao, A. Price, R. Wolz, J. Hajnal, and D. Rueckert, "Hierarchical manifold learning for regional image analysis," *IEEE Transactions on Medical Imaging*, vol. 33, no. 2, pp. 444–461, 2013.

[215] L. Venneri, F. Rossi, N. Botto, M. Andreassi, N. Salcone, A. Emad, M. Lazzeri, C. Gori, E. Vano, and E. Picano, "Cancer risk from professional exposure in staff working in cardiac catheterization laboratory: insights from the national research council's biological effects of ionizing radiation vii report," *American Heart Journal*, vol. 157, no. 1, pp. 118–124, 2009.

[216] T. Koenig, D. Wolff, F. Mettler, and L. Wagner, "Skin injuries from fluoroscopically guided procedures: part 1, characteristics of radiation injury," *American Journal of Roentgenology*, vol. 177, no. 1, pp. 3–11, 2001.

[217] J. Damilakis, M. Koukourakis, A. Hatjidakis, S. Karabekios, and N. Gourtsoyiannis, "Radiation exposure to the hands of operators during angiographic procedures," *European Journal of Radiology*, vol. 21, no. 1, pp. 72–75, 1995.

[218] J. Hirshfeld, S. Balter, J. Brinker, M. Kern, L. Klein, B. Lindsay, C. Tommaso, C. Tracy, L. Wagner, and M. Creager, "ACCF/AHA/HRS/SCAI clinical competence statement on physician knowledge to optimize patient safety and image quality in fluoroscopically guided invasive cardiovascular proceduresa report of the american college of cardiology foundation/american heart association/american college of physicians task force on clinical competence and training," *Journal of the American College of Cardiology*, vol. 44, no. 11, pp. 2259–2282, 2004.

[219] M. Panayiotou, A. King, Y. Ma, C. Rinaldi, J. Gill, M. Cooklin, M. O'Neill, R. Housden, and K. K. S. Rhode, "A statistical model of catheter motion from interventional X-ray images: application to image-based gating," *Physics in Medicine and Biology*, vol. 58, no. 21, pp. 7543–7562, 2013.

[220] M. Panayiotou, A. King, Y. Ma, C. Rinaldi, J. Gill, M. Cooklin, M. O'Neil, and K. Rhode, "Automatic image-based retrospective gating of interventional cardiac X-ray images," in *Engineering in Medicine and Biology Society (EMBC), 2012 Annual International Conference of the IEEE*, pp. 4970–4973, 2012.

[221] T. Lindeberg, "Detecting salient blob-like image structures and their scales with a scale-space primal sketch: A method for focus-of-attention," *International Journal of Computer Vision*, vol. 11, no. 3, pp. 283–318, 1993.

[222] I. Jolliffe, *Principal Component Analysis*. Springer-Verlag New York, 2002.

[223] A. Brost, A. Wimmer, F. Bourier, M. Koch, R. Liao, K. Kurzidim, N. Strobel, and J. Hornegger, "Constrained registration for motion compensation in atrial fibrillation ablation procedures," *IEEE Transactions on Medical Imaging*, vol. 31, no. 4, pp. 870–881, 2011d.

[224] M. Panayiotou, A. King, K. Bhatia, Y. Ma, C. Rinaldi, J. Gill, M. Cooklin, M. O'Neill, R. Housden, and K. Rhode, "Extraction of cardiac and respiratory motion information from cardiac X-ray fluoroscopy images using hierarchical manifold learning," in *Statistical Atlases and Computational Models of the Heart. Imaging and Modelling Challenges* (O. Camara, T. Mansi, M. Pop, K. Rhode, M. Sermesant, and A. Young, eds.), vol. 8330 of *Lecture Notes in Computer Science*, pp. 126–134, Springer Berlin Heidelberg, 2014a.

[225] M. Belkin and P. Niyogi, "Laplacian eigenmaps for dimensionality reduction and data representation," *Neural Computation*, vol. 15, no. 6, pp. 1373–1396, 2003.

[226] J. Ham, D. Lee, and L. Saul, *Semisupervised alignment of manifolds*. The Society for Artificial Intelligence and Statistics, 2005.

[227] A. Frangi, W. Niessen, K. Vincken, and M. Viergever, "Multiscale vessel enhancement filtering," in *Medical Image Computing and Computer-Assisted Interventation — MICCAI* (W. Wells, A. Colchester, and S. Delp, eds.), vol. 1496 of *Lecture Notes in Computer Science*, pp. 130–137, Springer Berlin Heidelberg, 1998.

[228] M. Panayiotou, A. King, R. Housden, Y. Ma, M. Cooklin, M. O'Neill, J. Gill, C. Rinaldi, and K. Rhode, "A statistical method for retrospective cardiac and respiratory motion gating of interventional cardiac x-ray images," *Medical Physics*, vol. 41, no. 7, p. 071901, 2014.

[229] Q. Zhang, A. Pevsner, A. Hertanto, Y.-C. H., K. Rosenzweig, C. Ling, and G. Mageras, "A patient-specific respiratory model of anatomical motion for radiation treatment planning," *Medical Physics*, vol. 34, no. 12, pp. 4772–4781, 2007.

[230] M. Panayiotou, A. King, R. Housden, Y. Ma, M. Cooklin, M. O'Neill, J. Gill, C. Rinaldi, and K. Rhode, "Image-based view-angle independent cardiorespiratory motion gating for X-ray-guided cardiac electrophysiology procedures," in *Statistical Atlases and Computational Models of the Heart. Imaging and Modelling Challenges* (O. Camara, T. Mansi, M. Pop, K. Rhode, M. Sermesant, and A. Young, eds.), Lecture Notes in Computer Science, Springer Berlin Heidelberg, 2015.

[231] D. Hawkes, A. Colchester, and C. Mol, "The accurate 3D reconstruction of the geometric configuration of vascular trees from X-ray recordings," *Physics and Engineering of Medical Imaging. Springer Netherlands*, vol. 119, pp. 250–256, 1987.

[232] G. Penney, J. Weese, J. Little, P. Desmedt, D. Hill, and D. Hawkes, "A comparison of similarity measures for use in 2-d-3-d medical image registration," *Medical Imaging, IEEE Transactions on*, vol. 17, no. 4, pp. 586–595, 1998.

[233] R. Hartley and A. Zisserman, *Multiple View Geometry in Computer Vision*. Cambridge University Press, ISBN: 0521540518, second ed., 2004.

[234] S. Ganapathy, "Decomposition of transformation matrices for robot vision," *Pattern Recognition Letters*, vol. 2, no. 6, pp. 401–412, 1984.

[235] T. Strat, "Recovering the camera parameters from a transformation matrix," *Readings in Computer Vision*, pp. 93–100, 1987.

[236] A. Rougée, C. Picard, C. Ponchut, and Y. Trousset, "Geometrical calibration of X-ray imaging chains for three-dimensional reconstruction," *Computerized Medical Imaging and Graphics*, vol. 17, no. 4, pp. 295–300, 1993.

[237] G. P. Penney, *Registration of Tomographic Images to X-ray Projections for Use in Image Guided Interventions*. PhD thesis, King's College London, University of London, 2001.

[238] I. Mano, H. Goshima, M. Nambu, and M. Iio, "New polyvinyl alcohol gel material for MRI phantoms," *Magnetic Resonance in Medicine*, vol. 3, no. 6, pp. 921–926, 1986.

[239] K. Chu and B. Rutt, "Polyvinyl alcohol cryogel: An ideal phantom material for MR studies of arterial flow and elasticity," *Magnetic Resonance in Medicine*, vol. 37, no. 2, pp. 314–319, 1997.

[240] G. Seymour, *Predictive inference*, vol. 55. CRC Press, 1993.

[241] J. Tenenbaum, V. De Silva, and J. Langford, "A global geometric framework for nonlinear dimensionality reduction," *Science*, vol. 290, no. 5500, pp. 2319–2323, 2000.

[242] D. Langlois, S. Chartier, and D. Gosselin, "An introduction to independent component analysis: Infomax and fastICA algorithms," *Tutorials in Quantitative Methods for Psychology*, vol. 6, no. 1, pp. 31–38, 2010.

[243] Y. Wang, S. Riederer, and R. Ehman, "Respiratory motion of the heart: kinematics and the implications for the spatial resolution in coronary imaging," *Magnetic Resonance in Medicine*, vol. 33, no. 5, pp. 713–719, 1995.

[244] J. Peters, O. Ecabert, C. Meyer, H. Schramm, R. Kneser, A. Groth, and J. Weese, "Automatic whole heart segmentation in static magnetic resonance image volumes," in *Medical Image Computing and Computer-Assisted Intervention – MICCAI 2007* (N. Ayache, S. Ourselin, and A. Maeder, eds.), vol. 4792 of *Lecture Notes in Computer Science*, pp. 402–410, Springer Berlin Heidelberg, 2007.

[245] P. Arnold, F. Preiswerk, B. Fasel, R. Salomir, K. Scheffler, and P. Cattin, *3D organ motion prediction for MR-guided high intensity focused ultrasound*, pp. 623–630. Springer, 2011.

JOURNAL PUBLICATIONS

- M. Panayiotou, A. King, Y. Ma, C. Rinaldi, J. Gill, M. Cooklin, M. O'Neill, R. Housden, and K. K. S. Rhode, "A statistical model of catheter motion from interventional X-ray images: application to image-based gating," *Physics in Medicine and Biology*, vol. 58, no. 21, pp. 7543-7562, 2013.

- M. Panayiotou, A. King, R. Housden, Y. Ma, M. Cooklin, M. O'Neill, J. Gill, C. Rinaldi, and K. Rhode, "A statistical method for retrospective cardiac and respiratory motion gating of interventional cardiac x-ray images," *Medical Physics*, vol. 41, no. 7, p. 071901, 2014.

- M. Panayiotou, K. Rhode, A. King, Y. Ma, M. Cooklin, M. O'Neill, J. Gill, C. Rinaldi, and R. Housden, "Image-based view-angle independent cardiorespiratory motion gating and coronary sinus catheter tracking for X-ray-guided cardiac electrophysiology procedures," submitted to *Physics in Medicine and Biology*.

CONFERENCE PUBLICATIONS

- M. Panayiotou, A. King, Y. Ma, C. Rinaldi, J. Gill, M. Cooklin, M. O'Neil, and K. Rhode, "Automatic image-based retrospective gating of interventional cardiac x-ray images," in *Engineering in Medicine and Biology Society (EMBC), 2012 Annual International Conference of the IEEE*, pp. 4970-4973, 2012.

- M. Panayiotou, A. King, K. Bhatia, Y. Ma, C. Rinaldi, J. Gill, M. Cooklin, M. O'Neill, R. Housden, and K. Rhode, "Extraction of cardiac and respiratory motion information from cardiac X-ray fluoroscopy images using hierarchical manifold learning," in MICCAI workshop *Statistical Atlases and Computational Models of the Heart. Imaging and Modelling Challenges* (O. Camara, T. Mansi, M. Pop, K. Rhode, M. Sermesant, and A. Young, eds.), vol. 8330 of *Lecture Notes in Computer Science*, pp. 126-134, Springer Berlin Heidelberg, 2014a.

- M. Panayiotou, A. King, R. Housden, Y. Ma, M. Cooklin, M. O'Neill, J. Gill, C. Rinaldi, and K. Rhode, "Image-based view-angle independent cardiorespiratory motion gating for X-ray-guided cardiac electrophysiology procedures," in MICCAI workshop *Statistical Atlases and Computational Models of the Heart. Imaging and Modelling Challenges* (O. Camara, T. Mansi, M. Pop, K. Rhode, M. Sermesant, and A. Young, eds.), to appear in *Lecture Notes in Computer Science*.

CONFERENCE ABSTRACT PUBLICATIONS

- M. Panayiotou, A. King, R. Housden, Y. Ma, M. Cooklin, M. O'Neill, J. Gill, C. Rinaldi, and K. Rhode, "Image-based view-angle independent cardiorespiratory motion gating for X-ray-guided cardiac electrophysiology procedures," in *Medical Engineering Centres Annual Meeting and Bioengineering14*, p. 100, 2014.